ALMA MATER STUDIORUM
UNIVERSITÀ DI BOLOGNA

DOTTORATO DI RICERCA IN

FISICA

Ciclo 37

Settore Concorsuale: 02/A2 - FISICA TEORICA DELLE INTERAZIONI FONDAMENTALI

Settore Scientifico Disciplinare: FIS/02 - FISICA TEORICA, MODELLI E METODI MATEMATICI

DARK SECTORS AS AN APPROACH TO BSM SEARCHES. FROM TERRESTRIAL EXPERIMENTS TO ASTROPHYSICAL ONES.

Presentata da: Jaime Hoefken Zink

Coordinatore Dottorato

Alessandro Gabrielli

Supervisore

Silvia Pascoli

Co-supervisore

Ilaria Brivio

Esame finale anno 2025

To my amazing and courageous grandma Marina

Abstract

Neutrino masses, dark matter and the baryon asymmetry of the Universe call for new physics beyond the Standard Model. In recent years, low scale extensions of the Standard Model, the so-called dark sectors, have received significant attention: they postulate the existence of new particles and interactions below the electroweak scale and they communicate with the visible sector via feebly couplings, called portals. The main strength of this approach is that we can get a rich phenomenology from just a few added dark parameters of the theory. Their existence is highly motivated by observed anomalies in a vast range of experiments. We study one particular dark model in detail, the Three Portal model, though we also consider other kinds of realizations of dark sectors. We first present the current status of dark sector parameters. Then, we explain the role of dark sectors in one particular neutrino anomaly: MiniBooNE's low energy excess. We particularly study how a dark photon and one or two heavy neutral leptons from the Three Portal model could explain the anomalous events in MiniBooNE and perform a fitting of the model. Furthermore, we consider this model in hot white dwarfs, so that constraints could be set on the parameter space of the dark photon.

Acknowledgments

The process of my PhD was, for me, a journey of discoveries. On one hand, I encountered many physics topics that ignited my passion for the field: the unveiling of a world filled with new interactions and models, each in some way waiting to be discovered; new mechanisms I never imagined could be computed; and a distant cosmology that reveals itself through the lens of particle physics. On the other hand, I encountered a community of people that reflects the essence of humanity—a scientific community whose support I have felt throughout my career. The former is typically more associated with what a physicist does: working on a specific topic. However, the latter is an essential part of how physics is conducted: within a community. Our field is inherently social; we rely on what others have developed to push boundaries. The understanding of nature is a collaborative endeavor. This is why I would like to take this section to thank all those who played an important role in my research journey.

First of all, I want to thank Prof. Silvia Pascoli. If I were to explicitly mention everything I have learned from Silvia, my thesis would essentially become an acknowledgment to her. Despite her demanding schedule and her many contributions to the physics community, Silvia has always been present, asking deep questions, raising constructive doubts, presenting interesting approaches to diverse problems, and actively supporting my professional growth by seeking valuable opportunities for me to advance as a researcher. However, Silvia's impact on me extends beyond just her mentorship in physics. She has also shown me the crucial and undeniable role of women in physics in the best possible way: by setting an example herself, as a respected and praiseworthy physicist within the community. Furthermore, she has promoted scientific outreach, even in schools, where she has participated personally despite her

tight schedule. Lastly, Silvia has taught me how to balance family life with our demanding career—she is, without a doubt, a courageous mother. For all of these reasons, I want to say: thank you so much, Silvia.

Alongside Silvia, there were many postdoctoral researchers who guided me into the world of research. My early PhD days would not have been the same without the presence of Matheus Hostert. Matheus was incredibly patient with me, helping me gain a deeper understanding of the physics that lay beneath the apparent surface of our research. His passion and enthusiasm for physics played a central role in my development. He also offered me a sincere friendship, which I deeply appreciate and for which I want to thank him: thank you, Matheus.

After my time working with him, I met a researcher who became a dear friend and introduced me to the world of astrophysics: Maura Ramírez-Quezada. Intelligent, efficient, and hard-working, Maura was always available to start a new project or brainstorm ideas. Her skills were not limited to theoretical work; she also excelled at organizing people and using her empathy to support others in their research. For all of this: thank you, Maura—I will definitely keep collaborating with you.

It's hard to categorize the third postdoctoral researcher I met during my PhD. He might fit better in the "friends" section, though our friendship is also rooted in physics and shared interests: Alessandro Granelli. Alessandro shared his passion for physics with me, as well as his love for music. He has a remarkable ability to collaborate, a spirit of service, and is always ready to help. He also invited me to his beloved Tuscany. Visiting his hometown and other Tuscan cities was unforgettable, and I will always cherish those memories. Thank you, Alessandro, my friend.

Among other postdoctoral researchers I have worked with, I would like

to thank Asli Abdullahi for her friendship and work together; Patrick Foldenauer, for his unflagging work as a collaborator and his tenacity in looking for solutions beyond our apparent possibilities. Thank you, Asli and Patrick.

This research journey also involved wonderful PhD students with whom I could share time and knowledge. It would have been impossible to feel at home in Bologna, especially during COVID, without the presence of a very good friend: Daniele Massaro. Daniele was always available and ready to help, for which I am forever grateful. He also became a close friend with whom I shared not only research papers but also aperitivi. I greatly appreciate your trust and friendship, Daniele, as well as your beautiful way of programming. Thank you, Daniele.

The next two friends I met were Francesco Comberiati and Wenbin Feng. Our initial connection was, without a doubt, through football. We soon began sharing food and enjoyable times together. Physics was a part of it, too—our time was full of fruitful conversations. Both showed me the kindness of true friendship, and for that, I want to say: thank you, Francesco and Wenbin.

Our university also gave me the chance to meet PhD students from other fields. I discovered how important it is to be aware of the work of researchers in other areas. Alongside the physics, I also found invaluable friendships. I want to thank Alberto Amadduzzi, Federico Bellisardi, and Pellegrino Piantadosi. Even when the work was hard, there was always a strong motivation to go to the office: meeting these great friends and helping each other progress in our careers and lives. I will never forget my conversations with Albie, having lunch or coffee with Federico, and walking back home with Rino. Thank you, Albie, Federico, and Rino.

As I approached the last year of my PhD, I shared an office with two

good friends: Filippo Fecit and Jacopo Nava. It was impossible to feel alone in that shared space. I have so many good memories with them, along with interesting conversations about physics. Thank you, Filippo and Jacopo.

Another important group of people to me were the Early Stage Researchers (ESRs) from HIDDeN. In general, I would like to thank the HIDDeN project for the opportunity to grow as a researcher in physics. The experience I gained through this project has been one of the most valuable gifts I have received in recent years. In terms of people within the project, I initially had a great time with Salvador Rosauro and Francesco Costa. We were dedicated to a research challenge that is still in progress. I learned a lot from them, but we also shared more than just physics: from meals to bouldering. I appreciate that time together and hope we will continue working on projects in the future. Thank you, Salva and Francesco.

There are other members of the group who, although not directly involved in my research, were an integral part of this fascinating project, and I want to thank them too: thank you, Giacomo, Valentina, Gioacchino, Mario, Xavier, Virgile, Federica, and Paloma. I also spent a lot of time with two wonderful researchers who came to Bologna to participate in a HIDDeN outreach project: Elina Merkel and Diego Jiménez. I am very grateful to both of them: thank you for the time together, Elina and Diego.

The senior members of HIDDeN were essential to the success of the project and to the development of the ESRs. I particularly want to thank Prof. María Concepción González-García, Prof. Joerg Jaeckel, Prof. Georgia Karagiorgi, and many other members of the ITN. I would also like to acknowledge other professors connected to the project. I want to mention Prof. Filippo Sala, who taught me about humanity and kindness as a physicist; he is devoted to his students and genuinely cares about their growth

as human beings as well as researchers. Thank you, Filippo. I would also like to mention Prof. Jordi Salvadó and Toni Bertólez-Martínez, incredible hosts in Barcelona. Thank you, Jordi and Toni. Finally, HIDDeN would not have been possible without the dedicated support of Rebeca Bello: gracias, Rebeca.

I would also like to thank members of our department at the University of Bologna who helped introduce me to the beautiful Italian language: Massimo and Mario. They work at reception, and thanks to them, many university activities run smoothly. Grazie mille, Massimo e Mario.

Before ending this section, I would like to thank my family for their unconditional support. First, my beloved wife, who always believed in me and showed remarkable patience—being married to a physicist is not easy. She has always supported me and lent me a hand whenever necessary, even waiting long hours for me on some days. Thank you, Helen.

I also want to thank my mother and my sister. My mom has been far away, across the ocean. I couldn't be with her when my grandma passed away, as I was working on my PhD. Thank you, mom. My sister was, along with my wife, my only close family in Europe. She has been incredibly supportive and kind, and for that, I will be eternally grateful. Thank you, Carolita.

Finally, I dedicate this thesis to a second mother to me, a person who guided me through life and gave me endless love: my grandma. After almost 104 years of life, she passed away this year. You still live in my heart—thank you, Grandma Marina.

Contents

Introduction

The Standard Model of particle physics (SM) describes the interactions among the fundamental constituents of matter and is capable of explaining experimental results very accurately. The SM is able to predict a vast quantity of observables from just 19 parameters of the theory: 12 fermion masses, 3 gauge couplings, 4 parameters (3 mixing angles and 1 CP-violating phase) for the quark mixing, 1 Higgs boson mass, 1 vacuum expectation value for the Higgs boson and 1 QCD vacuum angle (related to CP violation in the strong interaction) [1–8]. However, the SM fails to account for notable experimental facts, such as the neutrino oscillations through mass mixing [9–17], the dominant component of matter in the universe (85%): dark matter [18–29], the excess of matter with respect to anti-matter (the baryon asymmetry of the universe) [30–34], the gravitational interactions at the quantum level [35–41], etc. In addition to these fundamental problems, there are experimental results that remain unexplained, such as the muon $(g-2)_\mu$ anomaly [42–48], neutrino experiment anomalies (LSND [49–53], MiniBooNE [54–67]), the Hubble tension between the astrophysical and cosmological measured values of the Hubble constant [68–72], ANITA excess events [73–77], etc. It remains unclear if these anomalies are due to experimental artifacts or less understood systematic errors or instead are indications of new physics beyond the Standard Model (BSM). In the latter

case, they offer an avenue of exploration to consider models of new physics.

The landscape of mdoels BSM is vast. On the one hand, theories have been developed from strong postulates and provide complex frameworks, such as string theory [39, 78–81] or super-symmetric models [82–86]. On the other hand, there is another approach: the construction of simple extensions of the SM that can account for the main observable problems, while being easily testable. If these extensions contemplate new interacting fields that feebly interact with the SM and they are in a sub-GeV scale, we call them "dark sectors". The models proposed in the second approach can be clasified as "scientific" according to Karl Popper: they are falsifiable [87]. Dark sectors are easy to test and falsify due to their small number of extra parameters. They also play a crucial role in the interpretation of experimental anomalies in high energy physics as well as in cosmology and astrophysics. They need to be tested against the experimental results in order to identify their viability.

The present work will take the second approach in extending the SM to a new theory. Our strategy consists in focusing on a specific experimental anomaly, the MiniBooNE low energy excess, see Chapter 2, and in proposing a dark sector model to explain it. We will identify the parameter space required to fit the experimental signature and then we will test the model in completely different and therefore complementary ways. In particular we will concentrate on astrophysical environments in which dark sectors can manifest themselves. We have chosen the cooling of hot white dwarfs as a very sensitive test of dark sector models as will be seen in Chapter 3 and Chapter 4. We will introduce the concept of "dark sectors" starting from a broad description of the main renormalisable portals between them and the SM, and specifically we will review the main aspects of dark photons and heavy neutral leptons. We will then put forward the idea of "rich dark

sectors" in which the principle of minimality is abandoned and a structure with multiple particles and interactions is adopted, in analogy to the SM. The "Three portal model" [88] is a prototype for such SM extensions and introduces a new gauge symmetry, with the associated dark photon, a scalar sector needed to break such symmetry and multiple fermions charged under the new symmetry.

We have structured the thesis in four main chapters. In Chapter 1, we introduce the concept of dark sectors and show the current status of it. In Chapter 2, we will first explain one of the most puzzling anomalies in neutrino physics: MiniBooNE low energy excess. We will comment on many of the dark sector solutions to it, to finally focus on the explanation arising in the "Three portal model" thanks to the simoultaneous presence of heavy neutral leptons and dark photons. In Chapter 3, we will take the same dark photon model from the previous chapter, to analyze its effects in the cooling of hot white dwarfs. The general aim is to find the regions relevant for MiniBooNE low energy excess solution that may be excluded by how white dwarfs lose energy. In Chapter 4, we will adopt a similar approach as that of the previous chapter: we will consider a different dark sector model, with a $L_\mu - L_\tau$ gauge symmetry and we will test it against white dwarf cooling. We will first show the excluded regions relevant to the solution of other two important anomalies: muon $(g-2)_\mu$ and the Hubble tension. Secondly, we will develop more precise tools to analyze the effects for a dark photon ultra light masses and also for resonant masses, i.e., masses that are in resonance with the frequency of the plasma in the star. In final chapter, we will conclude. We refer the reader to the appendices, where some of the most relevant computations are shown step by step.

Chapter 1

Dark sectors

The most important evidence that the Standard Model (SM) of particle physics is incomplete comprises neutrino masses and mixing, and the presence of dark matter (DM) and of a baryon asymmetry in the Universe. They call for extensions of the SM. While for many years the focus has been on high energies, recently great attention has been given to dark sectors at scales below the electroweak one. In order to understand the possible connections between the SM and dark sectors, we will first present a general picture of dark sectors, describing some important fields they can contain: the dark photon, heavy neutral leptons (HNLs) and dark scalars. Subsequently, we will present a specific model for dark sectors that will be taken into account in the next chapters: the "Three portal model".

1.1 Dark sectors

In general, dark sectors can be understood as models that contain sub-GeV new fields that feebly interact with the SM through what we will call portals, which are communicating couplings between the two system of fields. Dark

sector models could be minimal, if a very restricted number of new particles and interactions are considered, e.g. in the case of a single portal, or "rich" if multiple particles and/or generations are accounted for. The latter case is strongly motivated by analogy with the structure of the SM and by the self-consistency of the model, e.g. dark photons and HNLs require a mechanism for their masses.

The dark fields can interact with the SM via renormalizable interactions: i) a vector portal when, in a $U(1)_D$ gauge symmetry extension of the SM, the new gauge X^μ kinetically mixes with a SM vector one. The resulting boson is called a "dark photon"; ii) a scalar portal when a dark Higgs singlet mixes with the SM one; iii) a neutrino portal when new right-handed neutrinos couple on one side with SM neutrinos and on the other with the dark sector. In this case the right handed neutrinos which mix with the SM ones go under the name of heavy neutral leptons (HNLs). An illustrative diagram about these connections can be seen in Fig. 1.1. In what follows, we will analyze each of this elements.

1.1.1 Dark photons

We will start by considering a $U_D(1)$ extension of the SM gauge group. The associated gauge field can mix with the SM ones via kinetic mixing. We note that we will use either A' or Z' to indicate the resulting new gauge massive state. For a more complete review on this, we refer to the reader to [89].

Kinetic Mixing

There is more than one way to couple a dark photon to SM fields. The most important one is through a kinetic mixing of the dark photon to an Abelian spin-1 field. That provides the portal linking the dark and visible sectors [90].

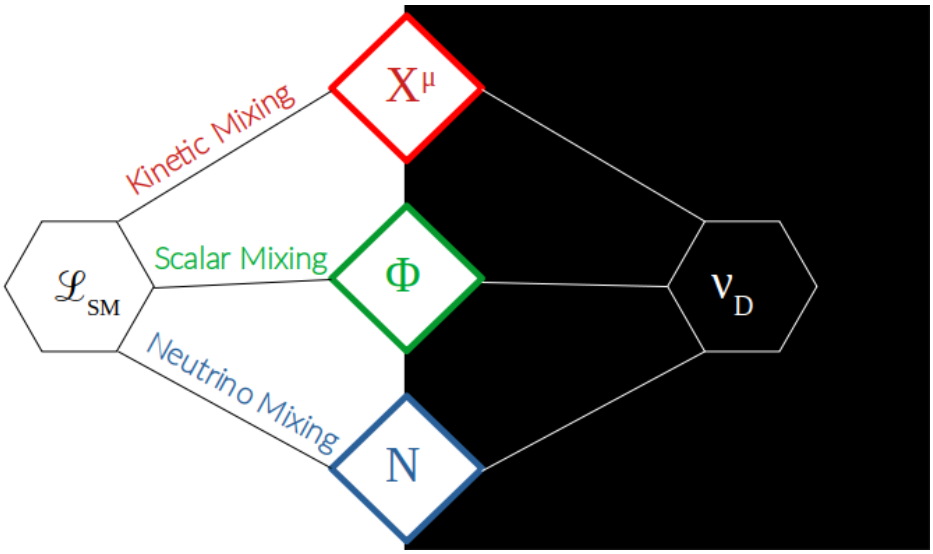

Figure 1.1: Some of the possible portals between dark sectors and the Standard Model: kinetic (through a dark gauge boson X), scalar (through a dark scalar Φ) and neutrino mixing (with the addition of sterile N and dark ν_D neutrino states). Image inspired by an illustration made by Dr. Matheus Hostert.

The relevant Lagrangian density terms read,

$$\mathscr{L}_{kin} = -\frac{1}{4}F_{a\mu\nu}F_a^{\mu\nu} - \frac{1}{4}F_{b\mu\nu}F_b^{\mu\nu} - \frac{\epsilon}{2}F_{a\mu\nu}F_b^{\mu\nu}\,, \tag{1.1}$$

where $F_i^{\mu\nu} \equiv \partial^\mu A_i^\nu - \partial^\nu A_i^\mu$ $(i = a, b)$ are the field strengths of two bosons identified as A_a and A_b, ϵ is a dimensionless quantity that parametrizes the kinetic mixing.

In Eq. (1.1), the fields described by $F_i^{\mu\nu}$ need to be diagonalized, so that the cross term disappears and the physical fields are found. The resulting physical field can be identified with the visible photon and a dark photon, after spontaneous symmetry breaking. These photons are well described by three parameters: the coupling strength of each one plus a mixing parameter [91].

The Lagrangian can be diagonalized as follows

$$\begin{pmatrix} A_a^\mu \\ A_b^\mu \end{pmatrix} = \begin{pmatrix} \frac{1}{\sqrt{1-\epsilon^2}} & 0 \\ -\frac{\epsilon}{\sqrt{1-\epsilon^2}} & 1 \end{pmatrix} \begin{pmatrix} \cos\theta & -\sin\theta \\ \sin\theta & \cos\theta \end{pmatrix} \begin{pmatrix} A'^\mu \\ A^\mu \end{pmatrix} \tag{1.2}$$

The additional orthogonal rotation is always possible and introduces an angle θ which is arbitrary as long as the gauge bosons are massless. This mixing of fields allows the dark sector (DS) and the SM to communicate through the following interaction

$$\begin{aligned} \mathscr{L}_{int} =& e J_\mu A_b^\mu + e' J'_\mu A_a^\mu \,, \\ =& \left[\frac{e' c_\theta}{\sqrt{1-\epsilon^2}} J'_\mu + e \left(s_\theta - \frac{\epsilon c_\theta}{\sqrt{1-\epsilon^2}} \right) J_\mu \right] A'^\mu \,, \\ &+ \left[-\frac{e' s_\theta}{\sqrt{1-\epsilon^2}} J'_\mu + e \left(c_\theta + \frac{\epsilon s_\theta}{\sqrt{1-\epsilon^2}} \right) J_\mu \right] A^\mu \,, \end{aligned} \tag{1.3}$$

where $c_\theta \equiv \cos\theta$ and $s_\theta \equiv \sin\theta$, e is the coupling bewtween electromagnetic currents, J_μ, and the photon and e' is the coupling bewtween dark currents, J'_μ, and the dark photon. Depending on the choice of the mixing angle θ, there are two main limits. The photon could couple just to SM matter, while the dark photon, to both sectors. This is achieved by setting $s_\theta = 0$, so that,

$$\mathscr{L}_{int}^{s_\theta=0} = \left[\frac{e'}{\sqrt{1-\epsilon^2}} J'_\mu - \frac{e\epsilon}{\sqrt{1-\epsilon^2}} J_\mu \right] A'^\mu + e J_\mu A^\mu \,. \tag{1.4}$$

This case is said to exclude milli-charge particles, i.e., particles in the DS that couple slightly to the SM photon. On the other hand, the opposite situation could be achieved by setting $s_\theta = \epsilon$, so that,

$$\mathscr{L}_{int}^{s_\theta=\epsilon} = e' J'_\mu A'^\mu + \left[-\frac{e'\epsilon}{\sqrt{1-\epsilon^2}} J'_\mu + \frac{e}{\sqrt{1-\epsilon^2}} J_\mu \right] A^\mu \,. \tag{1.5}$$

In this second limit, the milli-charge arises and has a coupling strength

of $\sim e'\epsilon$. This coupling is strongly constrained. As can be seen in [92], if these DS particles have masses close to that of the electron, then $\epsilon' \equiv e'\epsilon/e$ is excluded for values $\gtrsim 10^{-15}$ from laboratory (LEP and beam dump experiments), cosmological (BBN) and astrophysical (stellar evolution) bounds. If the milli-charges are very light neutrinos from BSM, the limit is more stringent and excludes $\epsilon' \gtrsim 10^{-21}$.

Mass terms

The main mechanism to give the dark photon a mass is the Higgs one, thanks to a dark scalar that breaks the $U(1)_D$ gauge symmetry. We will focus mainly on this case in the thesis and we will discuss it in details in the next section. Here, we present a more minimal approach for the dark photon mass, the Stueckelberg one.

The Stueckelberg Lagrangian has the following form,

$$\mathscr{L}_{Stu} = -\frac{1}{2}M_a^2 A_{a\mu}A_a^\mu - \frac{1}{2}M_b^2 A_{b\mu}A_b^\mu - M_a M_b A_{a\mu}A_b^\mu \,. \tag{1.6}$$

This was first introduced in [93] with the introduction of a scalar field and as as a mechanism of interaction between QED currents and nuclear forces. The idea was to give mass to an Abelian gauge field. This respected the original symmetry and was also BRST invariant (with the introduction of ghosts fields) [94]. It was originally an alternative to the Higgs mechanism to achieve gauge symmetry breaking without spoiling renormalizability [95]. Eq. (1.6) comes from the following Lagrangian term,

$$\mathscr{L} \supset -\frac{1}{2}\left(\partial_\mu \sigma + M_a A_{a\mu} + M_b A_{b\mu}\right)^2 , \tag{1.7}$$

where σ is the scalar field, which could be an axion. This term assumes there

is a kinetic mixing between the two $U(1)$ gauge fields and makes milli-charge particles from the DS possible.

Because the visible photon does not have mass, under the Stueckelberg mechanism we are forced to set the $\sin\theta$ in Eq. (1.2) equal to 0. In this case the interaction with fermions would be

$$\mathscr{L}_I \supset -\frac{e\epsilon}{\sqrt{1-\epsilon^2}} J_\mu A'^\mu \simeq -e\epsilon J_\mu A'^\mu \,. \tag{1.8}$$

Massless higher order interactions

There is another possibility: that the dark photon is massless. This case is more challenging as the dark photon does not couple directly to any of the SM currents and interacts instead with ordinary matter only through operators of dimension higher than four. This interaction can be expressed through a dimension 5 operator:

$$\mathscr{L}_I = \frac{g_D}{2\Lambda_5} \overline{\psi}^i \sigma_{\mu\nu} \Big(\mathcal{D}_M^{ij} + i\gamma_5 \mathcal{D}_E^{ij} \Big) \psi^j F'^{\mu\nu} \,, \tag{1.9}$$

where $\mathcal{D}_M$ is the magnetic dipole moment, $\mathcal{D}_E$ is the electric dipole moment, g_D is a dark coupling of the dark photon field strength to these dipole moments[1], Λ_5 is the UV-cutoff scale of the term and $\sigma_{\mu\nu} \equiv \frac{i}{4}[\gamma^\mu, \gamma^\nu]$. $\mathcal{D}_E$ is normally not included as it would introduce CP-odd effects. We can turn this term into a dimension 6 one, with the help of the Higgs field and the left-handed doublets:

$$\mathscr{L}_I = \frac{g_D}{2\Lambda^2} \overline{\psi}^i \sigma_{\mu\nu} \Big(\mathcal{D}_M^{ij} + i\gamma_5 \mathcal{D}_E^{ij} \Big) H \psi^j F'^{\mu\nu} + \text{h.c.} \,, \tag{1.10}$$

where H is the Higgs field and ψ^i are left-handed doublets.

[1]The subscript D or d will be used to denote "dark" sectors.

A more general approach to order 5 and 6 terms can be found in [96].

Dark photon and Dark Matter

A lot of attention has been devoted to the connection between dark photons and dark matter as dark sectors provide a very interesting framework for solutions to DM alternative to WIMPs. There are two main cases to regard. DM could be made of particles, mainly fermions, from the dark sector that interact through the dark photon. The other case, more challenging, is to consider the dark photon itself as DM.

DM interacting through a massless dark photon Though this case is not as challenging as the second we will see, there are problems that need to be solved if DM interacts via a massless dark photon: it is a long-range force, while galaxies' dynamics are collisionless and the DM halo is elliptic. According to [97], which works on a dark Abelian gauge group $U(1)_D$ not directly coupled to the SM fields, the dynamics of the early universe impose just few constraints on this massless dark photon case. If the DM fermions, χ, have a mass $m_\chi \sim 1\text{TeV}$, then $\alpha_d \lesssim 10^{-3}$, where $\alpha_d \equiv g_D^2/(4\pi)$, so that the expected relic abundance can be obtained and also the DM can be effectively collisionless in galactic dynamics.

Other effects from cosmology to be considered are those due to what happens after decoupling of DM from SM fields. DM can continue being in a thermal bath slightly coupled to the dark photons in what [98] calls the *Dark-Acoustic-Oscillation* (DAO) regime. This could affect the expansion history of the universe and dark photon perturbations could also alter some cosmological observables, though the most severe constraints come from astrophysics, as we will see.

One of these astrophysical constraints is the ellipticity profile of the halos. The one inferred for the galaxy NGC720, according to [99], sets a limit which comes from the expression for the isotropization timescale of about

$$m_\chi \left(\frac{0.01}{\alpha_d}\right)^{2/3} \gtrsim 300 \text{ GeV}\,. \tag{1.11}$$

This coupling also has an impact on the DM relic density, because DM may annihilate into SM fermions. Heavy fermions are good candidates for DM. Their dominant annihilation is into SM fermions via the exchange of a field S with a coupling α_L, such that,

$$\langle \sigma_{\chi\chi\to\bar{f}f} v\rangle = \frac{2\pi\alpha_L^2}{m_S^2}\,. \tag{1.12}$$

The critical relic density can be produced if

$$2\pi\alpha_L^2 = \left(\frac{10 \text{ TeV}}{m_S}\right)^2 \simeq 0.1\,. \tag{1.13}$$

On the other hand, light DM fields have a high rate in which they annihilate into dark photons

$$\langle \sigma_{\chi\chi\to A'A'} v\rangle = \frac{2\pi\alpha_d^2}{m_\chi^2}\,. \tag{1.14}$$

For $\alpha_d \approx 0.01$ and $m_\chi \lesssim 1$ TeV there is a large cross section. The relic density would be just a fraction of the critical one, so that light dark fermions should have converted into dark photons

$$\Omega_\chi h^2 \approx \frac{2.5\times 10^{-10}\ \text{GeV}^{-2}}{\langle \sigma_{\chi\chi\to A'A'} v\rangle}\,. \tag{1.15}$$

Light DM interacting through a massive dark photon Light DM with masses of the order of MeVs up to GeVs are also a possibility to well

describe DM. The general approach was first developed by [100] for scalar DM candidates and, more recently, by [101] for DM fermions and discovering 9 regimes of different possible interplays between the SM fields, DM and the dark photon. At the beginning, these models were proposed to make predictions more compatible with observations, because the usual WIMP models were predicting cuspy halos [102]. In their simplest form, the main constraints come from the possibility to yield gamma rays in an energy range already tested. Furthermore, a considerable region of the parameter space is excluded due to freeze-out and reannihilation regimes [101].

A possible channel to obtain the relic density if $m_{A'} > 2m_\chi$ is: $\chi\chi \to A' \to \overline{f}f$. The cross section for this light DM is given by,

$$\begin{aligned}\sigma_{\chi\chi\to\overline{f}f} =& \frac{4\pi}{3}\epsilon^2\alpha\alpha_d m_\chi^2\left(1+\frac{2m_e^2}{s}\right)\left(1+\frac{2m_\chi^2}{s}\right) \\ &\times \frac{s}{(s-m_{A'}^2)^2+m_{A'}^2\Gamma_{A'}^2}\frac{\sqrt{1-\frac{4m_e^2}{m_{A'}^2}}}{\sqrt{1-\frac{4m_\chi^2}{m_{A'}^2}}},\end{aligned} \tag{1.16}$$

where α is the fine structure constant, s is the Mandelstam parameter of the interaction and $\Gamma_{A'}$ is the decay width of the dark photon.

The thermal average in the non-relativistic limit and considering $m_e \ll m_\chi$ and $\Gamma_{A'} \ll m_{A'}$ is

$$\sigma_{\chi\chi\to\overline{f}f} \simeq \epsilon^2\alpha\alpha_d\frac{16\pi m_\chi^2}{\left(4m_\chi^2-m_{A'}^2\right)^2}\,. \tag{1.17}$$

When constraining these parameters it is useful to work with the *yield* variable, which is defined as follows

$$y \equiv \epsilon^2 \alpha_d \left(\frac{m_\chi}{m_{A'}} \right)^4 . \tag{1.18}$$

The cross section can be expressed just in terms of this variable, y, and the mass of the DM candidate, m_χ [103].

In terms of this variable, the thermal average is approximately

$$\sigma_{\chi\chi \to \bar{f} f} \simeq \frac{16\pi\alpha y}{m_\chi^2} . \tag{1.19}$$

Another important interaction to keep in mind is the t-channel of DM interacting with electrons. The cross section for this process is

$$\sigma_e = \frac{16\pi\mu_{\chi e}^2 \alpha \alpha_d \epsilon^2}{\left(m_{A'}^2 + \alpha^2 m_e^2\right)^2} \left| F(q^2) \right|^2 . \tag{1.20}$$

where $\mu_{\chi e}$ is the reduced mass of the electron and χ, and $F(q^2)$ is the form factor

$$F(q^2) = \frac{m_{A'}^2 + \alpha^2 m_e^2}{m_{A'}^2 + q^2} , \tag{1.21}$$

where q is the exchange momentum. With the help of this expression, we can find the differential event rate in a DM detector (with N_T the number of target nuclei per unit mass, E the electron energy, $\langle \sigma_e v \rangle$ the thermally averaged cross section, v the χ velocity, ρ_χ the local density of χ)

$$\frac{dR}{d\ln E} \propto \frac{\rho_\chi}{m_\chi} \frac{d\langle \sigma_e v \rangle}{d\ln E} . \tag{1.22}$$

This relation allows us to constraint the parameter ϵ for light DM with the help of direct detection experiments. In general, these limits scale as

$1/m_{A'}$.

DM composed by massive dark photons A condition to be met for very light massive dark photons to be DM is that it is produced non-thermally in the early Universe as a condensate, just as the axion is produced by the misalignment mechanism. By this mechanism, the value of the field is frozen by the fast expanding Universe to the initial value. The rate of expansion must be much larger than the mass, so that the field has no time to relax to the minimum of the potential. One consequence of this is Lorentz-invariance violation, but fortunately it is estimated to be small and undetectable.

In order to have a spin-1 boson candidate for DM, its mass must arise from the Stueckelberg mechanism discussed above in Eq. (1.6) and it must be sufficiently weakly coupled to the Standard Model [104]. Once the Hubble constant value drops below the mass of the dark photon, this DM starts oscillating like a Universe-sized Bose-Einstein condensate and then behaves like cold DM. The oscillation is due to the zero-momentum component of the field in the FRW background

$$\begin{aligned} A'^0 &= 0\,, \\ \ddot{A}'^i + 3H\dot{A}'^i + m_{A'}^2 A'^i &= 0\,, \end{aligned} \tag{1.23}$$

where H is the Hubble constant.

When the discriminant $9H^2 - 4m_{A'}^2$ becomes negative, the field begins to oscillate and we can quantize the different modes and call them particles. Because H has a similar value everywhere, up to perturbations, this transition takes place in the whole universe at the same time (of the rest frame of A'). This is the misalignment mechanism.

There are 2 main constraints in this model. First, a fine tuning of the initial value is needed in order to reproduce the critical density of DM. Second, decays of the dark photon into visible photons and SM leptons must not affect the CMB spectrum. Therefore, $\epsilon < 10^{-9}$ and $m_{A'} < 1$ MeV, which prevents it from a decay into an electron-positron pair, the lightest of the leptons.

The interaction with SM particles is mainly through a dark photon capture by an atom with atomic number Z. The cross section is related to that of the visible photon,

$$\sigma_{A'} = \epsilon^2 \times \sigma_A = \frac{32\sqrt{2}\pi r_e^2}{3}\alpha^2\epsilon^2 Z^5 \left(\frac{m_e}{E_{A'}}\right)^{7/2}, \tag{1.24}$$

where $r_e \equiv \alpha/m_e$ is the classical radius of the electron. Keeping this in mind, the rate of absorption of the dark photon by the detector is

$$\Gamma_{A'} = \frac{\rho_{A'}}{m_{A'}}\sigma_{A'} v_{A'}\,, \tag{1.25}$$

where the energy used to compute $\sigma_{A'}$ should be equal to the dark photon's mass: $E_{A'} \to m_{A'}$ [105].

Production mechanisms If the dark photon itself is DM, it is important to discuss how it may have been produced in early times and the degree of polarization left to the relic DM. That is precisely the aim of this subsection. As we will see in further sections, the polarization must be taken into account in order to set limits properly on dark photons regarded as DM.

First of all, DM dark photons could have been produced through the misalignment mechanism, just as axions. However, unlike these bosons, a nonminimal coupling to the Ricci scalar is needed because a minimal coupling to gravity does not produce the correct relic abundance. The most

important consequence of this mechanism is that it leaves the relics with a fixed polarization within the cosmological horizon. In the case of vector bosons, they are produced with a power spectrum peaked at intermediate wavelengths and not requiring a nonminimal coupling to gravity.

A second scenario is based on tachyonic instabilities arisen when the dark photon couples to a misaligned axion. The axion would have the energy first and, then, its zero mode would transfer it to the transversal and longitudinal components of the dark photon. This production yields a specific helicity, which would also be in the relics, even though further scatterings could change this helicity in some degree.

A third way in which dark photon DM might have been produced is via the decay of topological defects, such as a network of near-global, Abelian-Higgs cosmic strings. In this scenario, there is a really dominant longitudinal polarization production. In general, preferred directions due to production from long strings would be washed out by production through the collapse of smaller closed loops. Therefore, this constitutes a random polarization scenario.

Together with these scenarios, there are other phenomena that could have an effect on the polarization, such as the formation of DM halos. We can account at least for the effect of gravity on this. As shown in [89], if S^a, τ and v^a are the polarization, proper time and 4-velocity respectively and considering $u_a S^a = 0$, we find the following relation from parallel transport,

$$\frac{dS_a}{d\tau} = \Gamma^{\lambda}_{a\nu} S_\lambda \frac{dx^\nu}{d\tau} \,. \tag{1.26}$$

If we just consider motion in a gravitational potential, φ, we find [106],

$$\begin{aligned}\frac{d\mathbf{S}}{dt} =& -\mathbf{S}\frac{\partial\varphi}{\partial t} - 2\mathbf{v}\cdot\mathbf{S}\nabla\varphi - \mathbf{S}\big(\mathbf{v}\cdot\nabla\varphi\big) \\ &+ \mathbf{v}\big(\mathbf{S}\cdot\nabla\varphi\big) + \frac{1}{2}\mathbf{S}\times\big(\nabla\times\mathbf{S}\big)\,.\end{aligned} \tag{1.27}$$

From here, it is useful to define:

$$\mathbf{S}_1 = \big(1+\varphi\big)\mathbf{S} - \frac{1}{2}\mathbf{v}\big(\mathbf{v}\cdot\mathbf{S}\big)\,, \tag{1.28}$$

from which we find the spin-orbit equation,

$$\frac{d\mathbf{S}_1}{dt} = \boldsymbol{\Omega}\times\boldsymbol{S}_1\,, \tag{1.29}$$

where $\boldsymbol{\Omega} \equiv -\frac{1}{2}\nabla\times\boldsymbol{\zeta} - \frac{3}{2}\boldsymbol{v}\times\nabla\varphi$, with $\boldsymbol{\zeta}$ the vector potential. With these results and regarding the virial theorem ($\varphi \sim v^2$), the relative polarization variation is

$$\begin{aligned}\frac{\delta S}{S} \sim& Tv\frac{\varphi}{Rc^2} \\ & 4\times10^{-3}\left(\frac{v}{2\times10^{-3}}\right)^3\frac{T}{13\times10^9 yr}\frac{8\text{ kpc}}{R}\,,\end{aligned} \tag{1.30}$$

where T and R are the typical time and length scales of the problem and c has been restored. The second line is arranged in terms of typical values of our galaxy, just to show the preservation of the initial polarization over its lifetime. We can conclude that a fixed polarization treatment is a sufficient first approximation to the problem.

Phenomenology of the massless dark photon

The phenomenology of the massless case arises from the higher order operator of Eq. (1.9) or Eq. (1.10). Therefore, it depends on the effective scale Λ and the absolute value : $d_M^{ij} = \left|\mathcal{D}_M^{ij}\right|$. Let us see some limits for some relevant quantities related to those parameters.

Limits on the Dipole Scale d_M/Λ^2 There are 3 main sources of constraints for the Dipole Scale: stellar cooling, Big Bang Nucleosynthesis (BBN) and collider physics. The following analysis will regard a value of α_d around $0.1 - 0.01$ and values of Λ up to 12TeV.

From stellar cooling, d_M must be not higher than $10^{-6} - 10^{-5}$ due to the interaction with electrons. To obtain those numbers, there are three main processes of stellar energy loss considered: Compton scattering, pair creation and Bremsstrahlung. The latter provides the most stringent limit. The computations are quite similar to those made for axions. If α'_{ae} is the coupling between the axions and the electrons, [107] makes a combined fit and finds that at 2σ: $\alpha'_{ae} \leq 3.0 \times 10^{-27}$. A proper translation of the axion model to the massless dark photon one of Eq. (1.9) would be

$$\alpha'_{ae} = \frac{1}{2\pi}\left(2 g_D d_M^e \frac{v_h m_e}{\Lambda^2}\right)^2 . \tag{1.31}$$

Therefore, the limit from stellar cooling is

$$\frac{\Lambda^2}{\sqrt{\alpha_d} d_M^e} \gtrsim 4.5 \times 10^6 \text{ TeV}^2 . \tag{1.32}$$

We could also add a constraint from SN 1987A to the dipole scale related to quarks. The limit is set on the coupling between axions and nucleons: $\alpha'_{aN} \leq 1.3 \times 10^{-18}$. This has been done after considering how the length

of the burst constrains the energy losses in the explosion. There is also a relation with the massless dark photon,

$$\alpha'_{aN} = \frac{1}{2\pi}\left(2g_D d_M^q \frac{v_h m_N}{\Lambda^2}\right)^2 . \tag{1.33}$$

So the limit is

$$\frac{\Lambda^2}{\sqrt{\alpha_d} d_M^q} \gtrsim 4.3 \times 10^5 \text{ TeV}^2 . \tag{1.34}$$

The second source of constraints is BBN. This sets a limit of $10^{-4} - 10^{-1}$ on $d_M^{e/\mu}$. This limit is attained after determining the effective number of relativistic species in addition to the SM ones in thermal bath. According to [108], $N_{\text{eff}} = 2.878 \pm 0.278$. The dark photon, with 2 degrees of freedom, must have decoupled before at temperature T_d which is taken to be just above the QCD phase transition: $T_d = 150$ MeV. This decoupling translates in the following,

$$H(T_d) = \frac{T_d^2}{M_{Pl}}\left(\frac{\pi^2}{90} g_*(T_d)\right)^{1/2} > \Gamma_{A'} = n_{A'}\langle\sigma v\rangle , \tag{1.35}$$

where,

$$\begin{aligned} n_{A'} &= \frac{2\zeta(3)}{\pi^2} T^3 , \\ \langle\sigma v\rangle &\simeq \frac{\alpha_d d_M^2 v_h^2}{\Lambda^4} . \end{aligned} \tag{1.36}$$

where $\zeta(3) \approx 1.202$ and σ is the thermally averaged cross section for the dark photon interactions with the standard model particles that are in thermal equilibrium. We also need to relate the effective number of relativistic species to the effective number of degrees of freedom, $g_*(T_d)$ [109],

$$\left(\frac{T_{BBN}}{T_d}\right)^4 = \left(\frac{g_*(T_{BBN})}{g_*(T_d)}\right)^{4/3} < \frac{7}{4}\Delta N_{\text{eff}}. \tag{1.37}$$

Regarding these values and considering $g_*(T_{BBN}) = 43/4$, we finally set the limit

$$\begin{aligned} \frac{\Lambda^2}{\sqrt{\alpha_d} d_M^l} &\geq 6.6 \times 10^3 \text{ TeV}^2 \quad (\text{e and } \mu)\,, \\ \frac{\Lambda^2}{\sqrt{\alpha_d} d_M^q} &\geq 4.3 \times 10^3 \text{ TeV}^2 \quad (\text{s, u, and d})\,. \end{aligned} \tag{1.38}$$

The third and last main source of constraints comes from collider physics (especially the LEP). According to it, $d_M^{e/\mu}$ must be less than $1 - 10^3$. We can search for constraints coming from the atomic physics of transitions in He, for which

$$\frac{\Lambda^2}{\sqrt{\alpha_d} d_M^e} \gtrsim 872 \text{ GeV}^2\,. \tag{1.39}$$

However, the strongest bounds come from macroscopic forces among electrons and electrons and nucleons:

$$\begin{aligned} \frac{\Lambda^2}{\sqrt{\alpha_d} d_M^e} &\gtrsim 1.61 \text{ TeV}^2\,, \\ \frac{\Lambda^2}{\sqrt{\alpha_d}\sqrt{d_M^e d_M^q}} &\gtrsim 1.94 \text{ TeV}^2\,. \end{aligned} \tag{1.40}$$

From laboratory physics, the lack of observation of photons produced after an inverse Bremsstrahlung by the absorption of an axion allows to constrain the coupling of the axion to nucleons. Translating this limit to the massless dark photon, we obtain a limit for the quark sector of the dipole

scale,

$$\frac{\Lambda^2}{\sqrt{\alpha_d} d_M^q} \gtrsim 1.9 \times 10^3 \text{ TeV}^2. \tag{1.41}$$

Collider physics at the LEP constrain the pair annihilation into a photon and a dark photon using the technique *mono-photon plus missing energy* and limits the electronic sector of the dipole scale as follows,

$$\frac{\Lambda^2}{\sqrt{\alpha_d} d_M^e} \gtrsim 1.2 \text{ TeV}^2. \tag{1.42}$$

The same technique is used for the quark sector taking data from the CMS detector at the LHC,

$$\frac{\Lambda^2}{\sqrt{\alpha_d} d_M^q} \gtrsim 4.3 \text{ TeV}^2. \tag{1.43}$$

All of these limits can be found in Fig. (1.2).

Keeping all these stringent limits in mind, there remains the question whether we can still detect a massless dark photon or not. We must look either to processes where SM particles heavier than the e or the μ and the u or d quarks are involved — and the most severe astrophysical bounds do not apply — or physics where the dipole operator is between fermions of different flavors or very high-energy processes where the large scale Λ is partially compensated by the scaling of the dipole and radius operators and the overall contribution is less suppressed.

A UV model for the massless dark photon It is also helpful to search for constraints regarding a particular model. In the following lines, I will present a minimal one, whose more general extension is presented in [110]. Let us have many dark fermions as possible: hadron-like Q and lepton-like χ.

We also have scalars: The L-type scalars are doublets under $SU(2)_L$, while the R-type scalars are singlets under $SU(2)_L$. $S_{L,R}$ carry color indices, while $\varphi_{L,R}$ are color singlets. The Lagrangian is:

$$\begin{aligned}\mathscr{L} \supset & - g_L\big(\varphi_L^\dagger \overline{\chi}_R l_L + S_L^{U\dagger}\overline{Q}_R^U q_L + S_L^{D\dagger}\overline{Q}_R^D q_L\big) \\ & - g_R\big(\varphi_R^\dagger \overline{\chi}_L e_R + S_R^{U\dagger}\overline{Q}_L^U u_R + S_R^{D\dagger}\overline{Q}_L^D d_R\big) + \text{h.c.}\end{aligned} \tag{1.44}$$

Just for simplicity, we will consider $g_L = g_R = g$. There are also mixing terms that generate chirality-changing processes,

$$\mathscr{L} \supset - \lambda_S S_0\big(H^\dagger \varphi_R^\dagger \varphi_L + \tilde{H}^\dagger S_R^{U\dagger} S_L^U + H^\dagger S_R^{D\dagger} S_L^D\big) + \text{h.c.} \tag{1.45}$$

S_0 and H are the Higgs fields with a vev is μ_S and v_h respectively. DS and messenger states are charged under $U(1)_D$ which is unbroken because the dark photon is massless in this model. The scalar messengers are rotated after the Higgs fields acquire their vev. We are regarding that, before SSB, $\varphi_{L\nu}$, S_{Ld}^U and S_{Lu}^D have the same mass, m_S. After rotation, the mass eigenstates are

$$\begin{aligned}\varphi_\pm &= \frac{1}{\sqrt{2}}\big(\varphi_L \pm \varphi_R\big)\,, \\ S_\pm^{U,D} &= \frac{1}{\sqrt{2}}\Big(S_L^{U,D} \pm S_R^{U,D}\Big)\,.\end{aligned} \tag{1.46}$$

with masses,

$$\begin{aligned} m_{\pm} &= m_{\varphi,S}\sqrt{1 \pm \eta_S}\,, \\ \text{where: } \eta_S &\equiv \frac{\lambda_S \mu_{\varphi,S} v_h}{m_S^2}\,. \end{aligned} \tag{1.47}$$

The interaction in the lepton sector that follows from the previous terms is

$$\begin{aligned} \mathscr{L}^{\text{lep}} \supset & - g\varphi^{\dagger}_{L\nu}\left(\overline{\chi}_R \nu_L\right) - \frac{g}{\sqrt{2}}\left(\varphi^{\dagger}_{+} + \varphi^{\dagger}_{-}\right)\left(\overline{\chi}_R e_L\right) \\ & - \frac{g}{\sqrt{2}}\left(\varphi^{\dagger}_{+} - \varphi^{\dagger}_{-}\right)\left(\overline{\chi}_L e_R\right) + \text{h.c.} \end{aligned} \tag{1.48}$$

The hadronic interaction terms have the same form. If χ is stable, its mass has to be less than $m_- + m_e$ ($m_- + m_q$ for the hadronic part, being q the lightest quark). This sets an upper bound

$$\eta_{\varphi,S} < 1 - \left(\frac{M}{m_{\varphi,S}}\right)^2, \tag{1.49}$$

where M is the mass of the heaviest stable dark-sector species and $\eta_{\varphi,S}$ is the mixing parameter in the colorless (color) messengers sector. In general, the model can be generalized by considering different flavor interactions, which could be accounted for by doing the following transformation,

$$\begin{aligned} S_L^{U\dagger}\overline{Q}_R^U q_L &\to S_L^{U_i\dagger}\overline{Q}_R^{U_i}\left(\rho_L^U\right)_{ij} q_L^j\,, \\ S_R^{U\dagger}\overline{Q}_L^U q_R &\to S_R^{U_i\dagger}\overline{Q}_L^{U_i}\left(\rho_L^U\right)_{ij} q_R^j\,. \end{aligned} \tag{1.50}$$

This model can reproduce the terms in the UV - effective Lagrangian of Eq. (1.9) if we match it to the Feynman diagrams of Fig. (1.3), taken from

[111]. After integrating the loop, we can identify the scale Λ

$$\frac{v_h}{\Lambda^2} \simeq \frac{m_{Q^i}}{m_S^2}\,, \tag{1.51}$$

where m_{Q^i} is the heaviest dark-fermion running in the loop. Now, we can re-express the magnetic dipole explicitly in terms of the parameters of the model. For quark flavor transition (i to j) and neglecting SM masses, [112] presents the following computation for the dipole,

$$D_M^{ij} = \rho_{jj}\rho_{ji}^{\dagger}\,\mathrm{Re}\left[\frac{g}{4\pi}\right]^2 F_M(x,\eta_S)\,, \tag{1.52}$$

where,

$$\begin{aligned} x &\equiv m_{Q^i}^2/m_S^2\,,\\ F_M(x,y) &\equiv \frac{1}{2}\big[f(x,y) - f(x,-y)\big]\,,\\ f(x,y) &\equiv \frac{1-x+y+(1+y)\log\left(\frac{x}{1+y}\right)}{\big(1-x+y\big)^2}\,. \end{aligned} \tag{1.53}$$

The limits for this model can be computed and obtained from the SUSY constraints. From the decay of squarks ([113]) and sleptons ([114]) we have respectively

$$\begin{aligned} m_S^i &\gtrsim 940\ \mathrm{GeV}\,,\\ m_\varphi &\gtrsim 290\ \mathrm{GeV}\,. \end{aligned} \tag{1.54}$$

All the limits previously discussed can be analyzed in terms of these new parameters. For stellar cooling,

$$\frac{m_\varphi^2/m_{\chi^e}}{\sqrt{\alpha_D\alpha_L\alpha_R}\left|\rho_{ee}\right|^2 F_M(m_\varphi^2/m_{\chi^e},\eta_\varphi)} \gtrsim 2.1\times 10^6 \text{ TeV}\,, \tag{1.55}$$

where m_{χ^e} is the dark fermion mass associated to the electron. On the other hand, by taking into account the neutrino signal from SN 1987A,

$$\frac{m_\varphi^2/m_{Q^u}}{\sqrt{\alpha_D\alpha_L\alpha_R}\left|\rho_{uu}\right|^2 F_M(m_\varphi^2/m_{Q^u},\eta_S)} \gtrsim 2.0\times 10^5 \text{ TeV}\,, \tag{1.56}$$

where m_{Q^u} is the dark-fermion associated to the light u quark. This relation also holds for d. Additionally, there are other bounds that can be computed from electromagnetic interactions that are possible under this model, but they are not under the scope of the present work.

Future experiments Though the massless dark photon is more stringently limited than the massive one, this case is still worth to be studied. There are some possibilities of studying the massless dark photon in new experiments.

First, experiments studying flavor physics are a good opportunity since the stringent astrophysical constraints do not apply when there are off-diagonal flavor entries for the dipole operator. It could be studied, for example, through Kaon physics at NA62: $K^+ \to \pi^0\pi^+A'$. It could also be measured through decays into invisible states from B-mesons at BaBar and Belle.

Another relevant field for massless dark photons is the Higgs and Z physics, in experiments focused on decays into a visible and dark photon (mono-photon plus missing energy). Again, the stringent astrophysical limits do not apply because the size of the dipole operator is dominated (in the loop diagram) by the heavy-quark contribution, giving raise to the coupling

to the dark photon.

Furthermore, collider experiments at higher energies and luminosities can use the same striking signature of a mono-photon plus missing energy to search for the dark photon in pair annihilations. In this case, the cosmological and astrophysical bounds are as severe as for the massive case.

Finally, two more kinds of experiments are promising. On the one hand, the use of magnons in ferromagnetic materials and their interaction with dark photons ([115] and [116]). On the other hand, gravitational waves emitted during the inspiral phase of neutron star collapse can test the presence of other forces beside gravitation.

Phenomenology of the massive dark photon

The massive photon can be detected directly or indirectly through the following interaction with SM fields,

$$\mathscr{L}_I = -\epsilon e J^\mu A'_\mu \,. \tag{1.57}$$

Any search is done in the parameter space of $m_{A'}$ and ϵ. In the following lines we will be devoted to how we can detect it.

Detection As seen in Fig. (1.4) taken from [111], the massive dark photon can be produced via the electromagnetic current through the following mechanisms:

1. *Bremsstrahlung*: when an electron scatters off a target of nuclei with atomic number Z: $e^- Z \to e^- Z A'$.

2. *Pair annihilation*: for example, for an electron-positron pair: $e^- e^+ \to \gamma A'$.

3. *Meson decays*: decays like $M \to \gamma A'$, where M could be π^0, η, K or D.

4. *Drell-Yan*: this process refers to the annihilation of a quark-antiquark pair into a dark photon, which then decays into pair: $q\overline{q} \to A' \to l^+l^-/h^+h^-$, where l or h refer to a lepton or a hadron, respectively.

In all of these processes, it is important that the dark photon decays into SM fields in order to be detected. If its mass is sufficiently large: $m_{A'} > 2m_e$, it could decay into leptons,

$$\Gamma(A' \to l^+l^-) = \frac{1}{3}\alpha\epsilon^2 m_{A'}\sqrt{1-\frac{4m_l^2}{m_{A'}^2}}\left(1+\frac{2m_l^2}{m_{A'}^2}\right). \tag{1.58}$$

It could also decay into hadrons,

$$\Gamma(A' \to h^+h^-) = \frac{1}{3}\alpha\epsilon^2 m_{A'}\sqrt{1-\frac{4m_\mu^2}{m_{A'}^2}}\left(1+\frac{2m_\mu^2}{m_{A'}^2}\right)R, \tag{1.59}$$

where $R \equiv \sigma_{e^+e^-\to\text{had}}/\sigma_{e^+e^-\to\mu^+\mu^-}$. This ratio is independent of ϵ, which cancels due to being in the numerator and denominator. In case $m_{A'} < 2m_e$, it does not decay into leptons nor hadrons. However, it could also happen that, even though having an enough large mass, it has an invisible decay, due to do it into the DS. The width is given by

$$\Gamma(A' \to \chi\overline{\chi}) = \frac{1}{3}\alpha_d m_{A'}\sqrt{1-\frac{4m_\chi^2}{m_{A'}^2}}\left(1+\frac{2m_\chi^2}{m_{A'}^2}\right). \tag{1.60}$$

This channel dominates if $\alpha_d \gg \alpha\epsilon^2$.

The detection itself can be done by different techniques. The simplest one is to *detect visible final states*. Resonances over a background can be signs of these states. There are 2 main experiments that can detect this: collider experiments, which cover large values of the coupling ($\epsilon > 10^{-3}$), and

beam dump experiments, which are sensitive to lower values ($\epsilon < 10^{-3}$). In both experiments, high luminosities and fluxes are needed, because the dark photon detectable rate is proportional to the fourth power of the coupling involved (ϵ^4). The smallness of the coupling also implies that A' is a long-lived particle (compared to other SM particles).

Another technique is the *missing momentum/energy*. When a dark photon is produced, it could also decay into a not detectable DM pair. In this case, the missing energy and momentum of the process should be a signature of the A'. The main challenge is the high background rejection. Therefore, the detector must be hermetically close and the initial and final state kinematics must be well known in order to compute those missing quantities with high precision. This just depends on the second power of the coupling (ϵ^2).

The third technique we will mention is the *missing mass technique*, which is mainly used to detect invisible particles when the initial state is very well known, like in the process: $e^-e^+ \to \gamma A'$. A characteristic signature is the presence of narrow resonances over a smooth background in the distribution of the missing mass. Detectors must be really hermetic, so that they allow all the other particles in the final state to be detected and a good knowledge of the background.

Constraints on ϵ and $m_{A'}$ The limits really depend on the kind of processes that can take place. First, in the case of decays to visible final states, for which $m_{A'} > 2m_e \approx 1\text{MeV}$, the constraints are set by collider and beam dump experiments. Colliders search for resonances in the invariant mass distribution of e^+e^- or $\mu^+\mu^-$ pairs. Dark photons could be produced by meson decays, Bremsstrahlung, annihilation, Drell-Yan. Important experiments are NA48/2, A1, LHCb, BaBar, KLOE. Beam dump experiments look

for dark photons produced via Bremsstrahlung, meson production and QCD processes. The dark photon is searched for as a displaced vertex with two opposite charged tracks in the decay volume of the experiment. The main experiments are E141 and E137 at SLAC, E774 at Fermilab (e beams) and CHARM at CERN (p beam). Fig. (1.5) shows the current limits.

There is still a region for $\epsilon < 10^{-4}$ and $m_{A'}$ from tens of MeV up to 1 GeV (and also larger masses) that could be searched by Belle-II (at SuperKEKB), LHCb upgrade, NA62++ (at SPS, CERN), NA62(e)++ (at SPS, CERN), FASER/FASER2 (at LHC, CERN), HPS (at Jefferson Laboratory), SeaQuest (at Fermilab), MAGIX (at MESA, Mainz), FCC-ee (future circular e^+e^- collider).

The second regime is when, although $m_{A'} > 1$ MeV, the decays are mainly invisible. In this case techniques like missing momentum, missing energy, and missing mass are used in order to identify a possible massive dark photon decaying into invisible final states. The most stringent limits come from BaBar and NA64(e). Better constraints will be obtained with: NA64(e)++ (at SPS, CERN), Belle-II (at SuperKEKB), KLEVER (at SPS, CERN), PADME (at the Beam Test Facility - BTF - at Laboratori Nazionali di Frascati- INFN). Fig. (1.6) shows the current constraints.

If the dark sector states into which the invisible dark photon decays are taken to be DM, there are new constraints that involve the coupling strength α_d and are related to the direct-detection searches for dark matter. The limits are usually set on the plane y vs m_χ, where y is the yield variable: $y \equiv \epsilon^2 \alpha_d \left(\frac{m_\chi}{m_{A'}}\right)^4$.

The third and last regime takes place when $m_{A'} < 1$ MeV. Experiments that can search for this case are (1) atomic and nuclear experiments, that measure modifications of the Coulomb force due to the dark photon, (2)

axion-like particle (ALP) experiments and helioscopes, in which light shining through a wall (LSW) search for axions and ALPs and that can be adapted to dark photons, (3) astrophysics experiments, which put constraints from the non-observation of anomalous energy transport in stars and (4) cosmology experiments, that could search for the oscillation $\gamma \leftrightarrow A'$, which induces deviations on the black body spectrum in the CMB. The limits are shown in Fig. (1.7).

Phenomenology of the dark photon DM

Many of the limits given above regard the measurement of the dark photon from the results of measurements of the axion or other ALPs. But there is a central property these particles do not share with the dark photon: an intrinsic polarization. When axions of a specific mass are not observed in an experiment, the limits obtained from that are simply imposed on dark photons of similar mass. However, the coupling to experiments has some subtle differences [89]. The aim of this subsection is to give a brief account on that, considering especially haloscopes without B-fields (mainly ADMX, HAYSTAC, CAPP and QUAX) and mostly for massive dark photons that are DM.

There are some problems that make it hard to incorporate the polarization in the computations of the limits. As it is shown in Ref. [89], the polarization distribution highly depends on the production mechanism. Furthermore, this distribution changes as the Earth rotates. Axion experiments are not usually prepared for that. This difficulties have been overlooked by a vast number of studies since [117] first proposed to use axion-like experiments to constrain dark photon models.

Following [89], we need to transform the limits taken from axion-like

experiments to account for the the range of possible angles between the dark photon polarization and the axis or plane that the experiment is sensitive to. We need to transform the current status of the limits for the light dark photon case ($m_{A'} < 0.1$ MeV), shown in Fig. (1.8). These limits are the most general ones, while the previous ones shown were related to a particular kind of decay and for larger masses.

To detect the dark photon, it is important to consider the effect it has on the electric field produced by the SM-photon. After some computations made in [89], if we set the velocity of the dark photon to be zero, we find that the electric field produced by it in the classical limit is

$$|\boldsymbol{E}| = \left| \frac{\chi m_{A'}}{\epsilon} \boldsymbol{A'} \right|, \tag{1.61}$$

where χ is such that the coupling between the visible photon and the dark photon is: $m_{A'}^2 \chi$. This induced field is relevant for experiments exploiting electromagnetic mixing with axions, such as cavity haloscopes, dielectric disks, dish antennae, plasmas, LC circuits, and electric-field radios. However, there are two main differences if we now consider dark photons: they can be polarized in any direction and not necessarily in the external magnetic field's direction (due to the axion's coupling: $\boldsymbol{E} \cdot \boldsymbol{B}$) and their mixing continues even in the absence of a magnetic field. Some experiments might be sensitive to all polarizations lying on a plane (*planar*) and others, just in one direction (*axial*).

For cavity haloscopes, a cylindrical one is only sensitive to the component of the dark photon polarized along the axis parallel to the magnetic field. More complex cavities could be sensitive to more directions, though cavities designed to detect axions are usually not optimized for multiple polarization directions. Therefore, cavities are usually *axial* experiments, so

that in average the power is suppressed by $\langle \cos^2 \theta \rangle = 1/3$.

In the case of dish antennae, the dark photons pass through the dish and their small electric field makes the electrons in the dish oscillate, emitting an ordinary electromagnetic wave perpendicular to the surface. Dish antennae can, at most, only be sensitive to the component of the E field parallel to the disk interface, which makes it a *planar* experiment with a suppression of $\cos\theta$, where θ is the angle between the dark photon polarization and the plane of the interface. If we consider the general rounded disks, after some computations we conclude that the suppression is of 2/3. This is also what happens with dielectric disks.

Plasma haloscopes induce dark photons to convert to photons by matching the plasma frequency with $m_{A'}$. The problem is that the dispersion relation only occurs in the direction of wire alignment. Therefore it will only be sensitive to electric fields aligned with the wire just as the cylindrical cavities.

LC circuits measure the magnetic field, which could be directly produced by the dark photon or indirectly induced by the electric field, causing a current in the conductor. If the system size, r, is much smaller than a Compton wavelength, $m_{A'}^{-1}$, then the electric field will be suppressed; however the magnetic field will not, $|\boldsymbol{E}_{A'}| \sim m_{A'} r |\boldsymbol{B}_{A'}|$. Only polarizations parallel to the conductor can induce a magnetic field. Just polarizations that induce a magnetic field parallel to the readout loop can be detected. That depends on the geometry of the detector: some experiments are *planar*, while other are *axial*.

So, to briefly summarize, we could have *planar* or *axial* experiments. The suppression for those experiments from signals dark photons is 2/3 and 1/3 respectively. Another general problem arises because many experiments

use a method of combination under which it is assumed that the signal will remain constant with time, which is not true if there is a fixed polarization of the dark photons. One would need to account especially for the Earth's rotation.

In Table (1.1), we can see the different haloscope axion experiments and the relevant data to do the transformation from the axion limits to dark photon constraints just as shown in [89]. Up to now, we have mentioned two main difference between dark photons and axions: the absence of a magnetic field in the dark photon case and the nontrivial polarization. Due to the first one, a signal must vanish in the absence of a magnetic field for axions: this does not apply to dark photons. Because of the second difference, there is a factor, $\langle \cos\theta \rangle_{\mathrm{T}}$, that changes the signal strength. [89] computes an additional factor, $\langle \cos\theta \rangle_{\mathrm{T}}^{\mathrm{excl}}$, as the ratio of the axion and dark photon power thresholds that can be excluded at 95% C.L. in the absence of a signal. It encodes how much the exclusion is weakened for the dark photon case. Two assumptions are made: the noise follows a Gaussian distribution and the measured signal equals the median expected noise. More details on the computation can be found in [89]. The results are shown in Fig. (1.9).

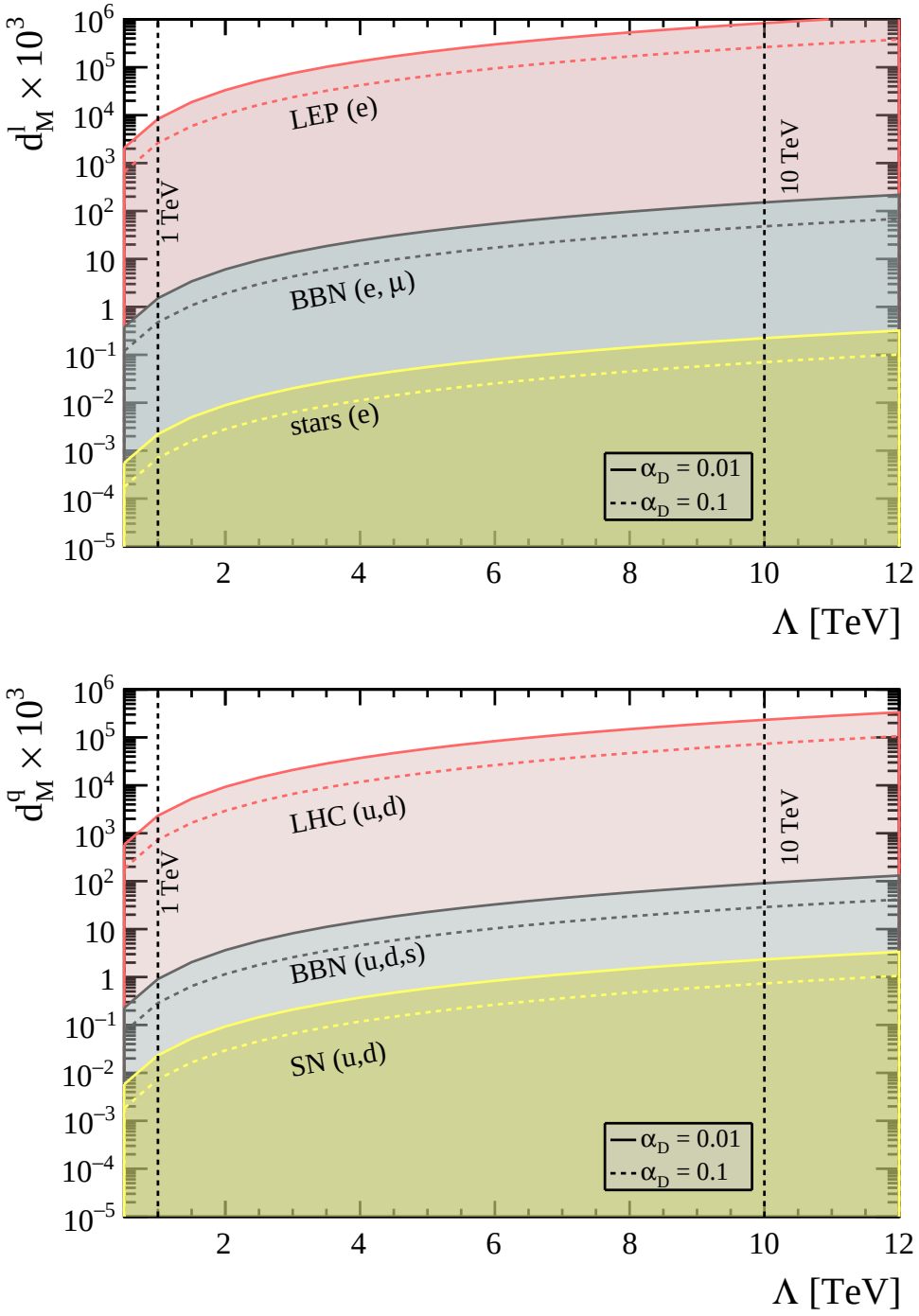

Figure 1.2: Limits for d_M for leptons (above) and quarks (below) considering the three main sources of constraints. Plots taken from [89]

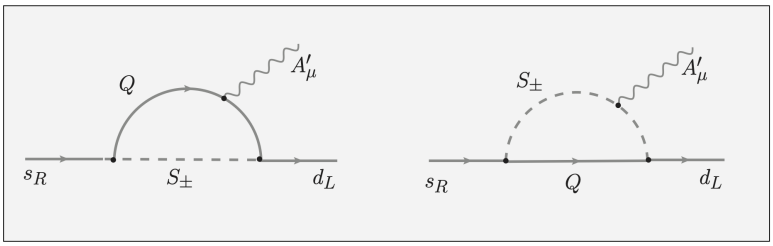

Figure 1.3: Processes taken from the minimal massless dark photon model that match the order 5 terms.

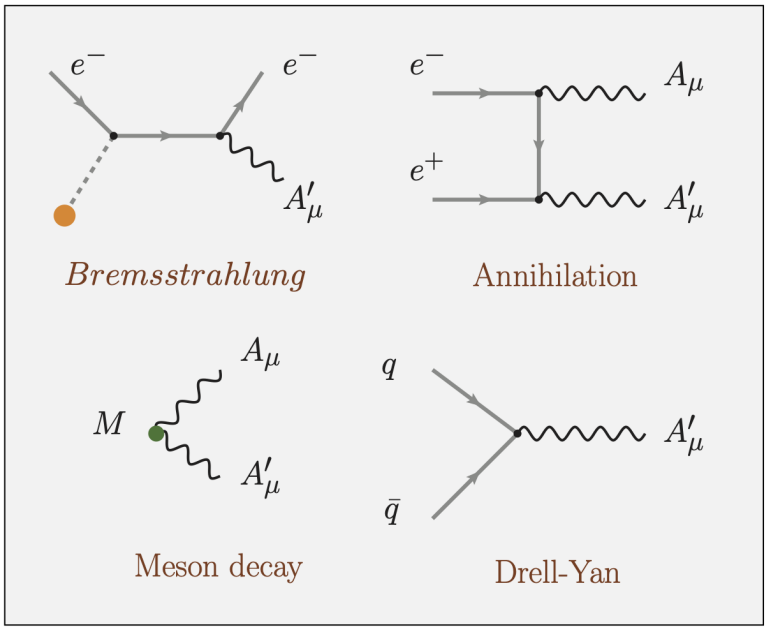

Figure 1.4: Mechanisms by which the massive dark photon can be produced.

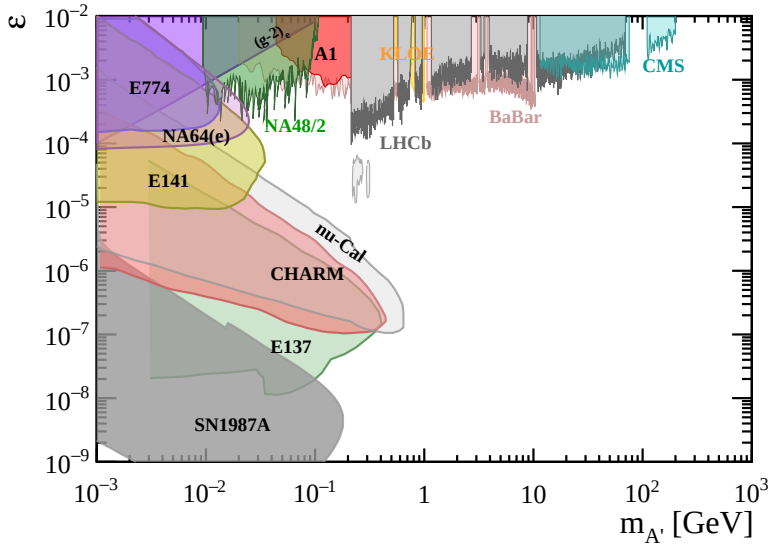

Figure 1.5: Limits for $m_{A'} > 1$MeV from collider and beam dumps experiments. Taken from [89].

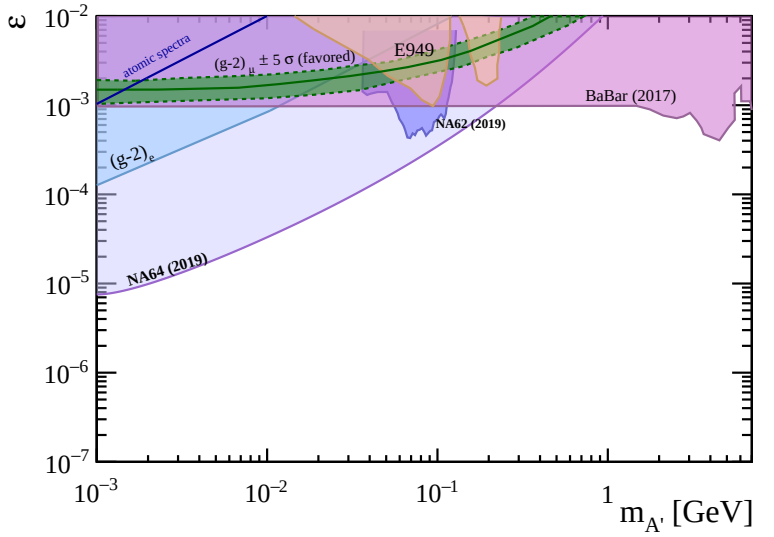

Figure 1.6: Limits for $m_{A'} > 1$MeV in the case of invisible decays. Taken from [89].

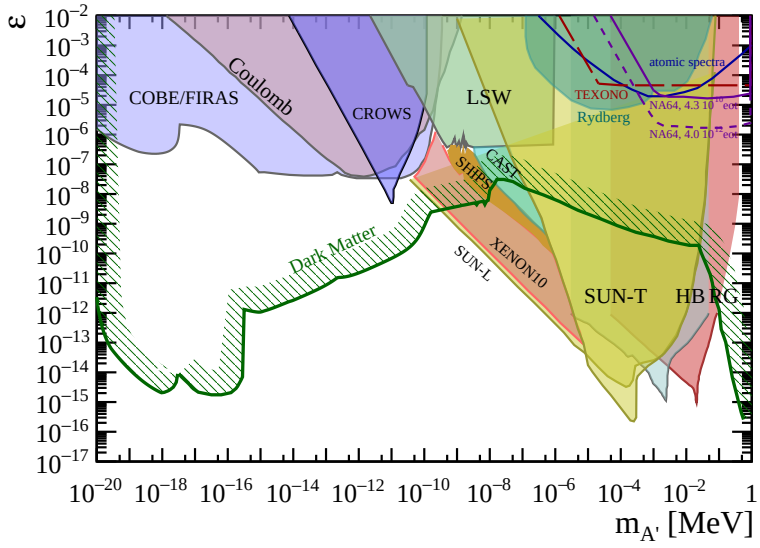

Figure 1.7: Limits for $m_{A'} < 1$MeV. Taken from [89].

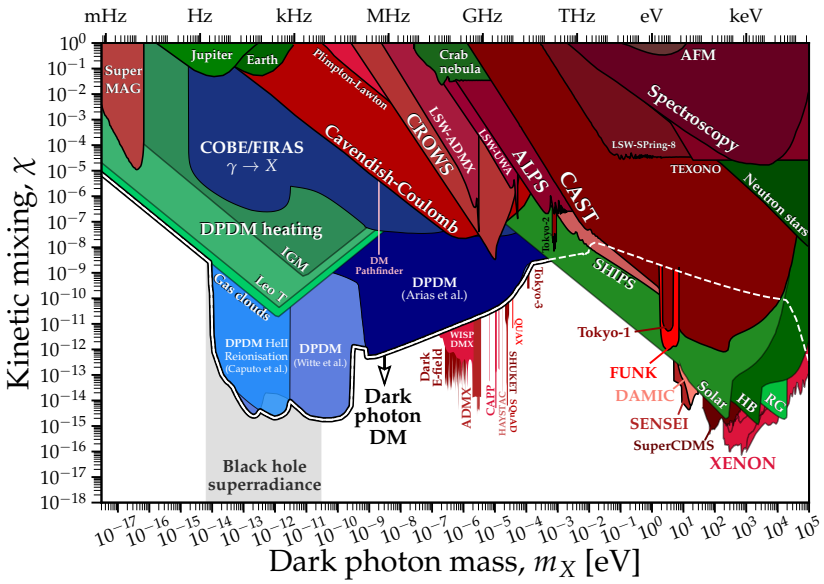

Figure 1.8: Limits for m_χ, which in this case is equivalent to $m_{A'}$. The kinetic mixing χ is equivalent to ϵ. Any bound set by a physical laboratory experiment is shown in red, those set using astrophysical data in green, and those set using cosmological data in blue. The shaded region for $6.5 \times 10^{-15}\text{eV} \leq m_\chi \leq 2.9 \times 10^{-11}\text{eV}$ is excluded, because then the field would spin down stellar mass black holes due to superradiance. Taken from [89].

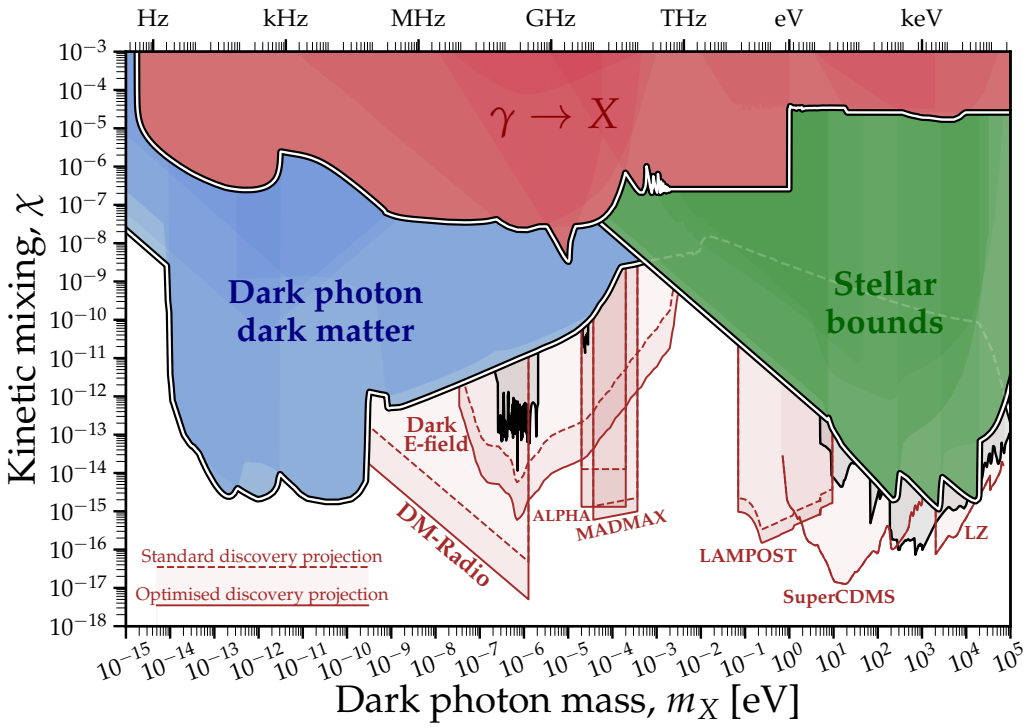

Figure 1.9: Dark photon limits after the transformation from axions. The optimized limits are considering the preferred latitudes after taking into account the rotation of Earth, so that north-axis oriented experiments should be located at a latitude of $\sim \pm 55°$ and zenith-axis oriented at $\sim \pm 35°$. Taken from [89].

Experiment			B [T]	Lat [°]	Meas. time, T	Direction	$\langle\cos^2\theta\rangle_T^{\text{excl.}}$
Cavities	ADMX-1	[118]	7.6	47.66	$\mathcal{O}$(min)	zenith-pointing	∼0.025
	ADMX-2	[119]	6.8	47.66	$\mathcal{O}$(min)	zenith-pointing	∼0.019
	ADMX-3	[120]	7.6	47.66	$\mathcal{O}$(min)	zenith-pointing	∼0.019
	ADMX Sidecar	[121]	3.11[2]	47.66	$\mathcal{O}$(min)	zenith-pointing	∼0.019
	HAYSTAC-1	[122]	9	41.32	$\mathcal{O}$(min)	zenith-pointing	∼0.019
	HAYSTAC-2	[123]	9	41.32	$\mathcal{O}$(min)	zenith-pointing	∼0.019
	CAPP-1	[124]	7.3	36.35	$\mathcal{O}$(min)	zenith-pointing	∼0.019
	CAPP-2	[125]	7.8	36.35	$\mathcal{O}$(min)	zenith-pointing	∼0.019
	CAPP-3	[126]	7.2 and 7.9	36.35	90 s	zenith-pointing	∼0.019
	CAPP-3 [KSVZ]	[126]	7.2	36.35	15 hr	zenith-pointing	0.20
	QUAX-$\alpha\gamma$	[127]	8.1	45.35	4203 s	zenith-pointing	0.023
	†KLASH	[128]	0.6	41.80	$\mathcal{O}$(min)	zenith-pointing	∼0.019
	RBF	[129]	Magnetic field veto				
	UF	[130]	Magnetic field veto				
	ORGAN	[131]	Magnetic field veto				
	RADES	[132]	Magnetic field veto				
LC-circuits	ADMX SLIC-1	[133]	4.5	29.64	$\mathcal{O}$(min)	north-west-facing	∼0.19
	ADMX SLIC-2	[133]	5	29.64	$\mathcal{O}$(min)	north-west-facing	∼0.19
	ADMX SLIC-3	[133]	7	29.64	$\mathcal{O}$(min)	north-west-facing	∼0.19
	ABRACADABRA	[134]	Magnetic field veto[3]				
	SHAFT	[135]	Magnetic field veto				
Plasmas	†ALPHA	[136]	10	Unknown	$\mathcal{O}$(week)	zenith-pointing	0.28–0.33
Dielectrics	†MADMAX	[137]	10	53.57	$\mathcal{O}$(week)	zen/nor-wes-facing	0.26 or 0.62–0.66[4]
	†LAMPOST	[138]	10	Unknown	$\mathcal{O}$(week)	Any-facing	0.61–0.66
	†DALI	[139]	9	28.49	$\mathcal{O}$(month)	Any-facing[5]	0.61–0.66
Dish antenna	†BRASS	[140]	1	53.57	$\mathcal{O}$(100 days)	Any-facing	0.61–0.66
Topological insulators	†TOORAD	[141]	10[6]	Unknown	$\mathcal{O}$(day)	Any-pointing	0.18–0.33

Table 1.1: Summary of axion haloscopes and their parameters relevant for recasting exclusion limits to dark photons. Planned experiments are denoted with a "†".

Latest limits from a dark photon minimal model

Before going to the next section, we will like to present the latest results of the constraints on a dark photon in a minimal model: one that just interacts with SM particles through kinetic mixing with the photon. The results were published in FIPs 2022 [142] and can be seen in Fig. 1.10. For lower dark photon masses, cosmological constraints are the most stringent, while for higher masses they come from XENON and from astrophysics: from the Sun, the horizontal branch stars (HB) and red giants (RG). These astrophysical limits are set by considering the energy loss rate (Sun, HB), the Helium ignition and branch termination (RG).

1.1.2 Heavy neutral leptons (HNLs)

HNLs are a very important ingredient for dark sectors. In the following section, we will discuss what they are and the current status of their searches. Most of the information that will be presented here is taken from [142].

What HNLs are

HNLs are neutral leptons usually regarded in the context of neutrino physics, where they are just new massive neutrino states that are introduced to explain neutrino masses through the seesaw mechanism. These leptons are mixed with neutrinos through an extended mixing matrix. They could be seen as sterile neutrinos, though their masses do not generate neutrino oscillations in the experiments where they are searched for.

HNLs can in general be generated when introducing a Dirac + Majorana mass Lagrangian to assign a mass to neutrinos. The Dirac mass (D) and Majorana mass (M) Lagrangians have the following form:

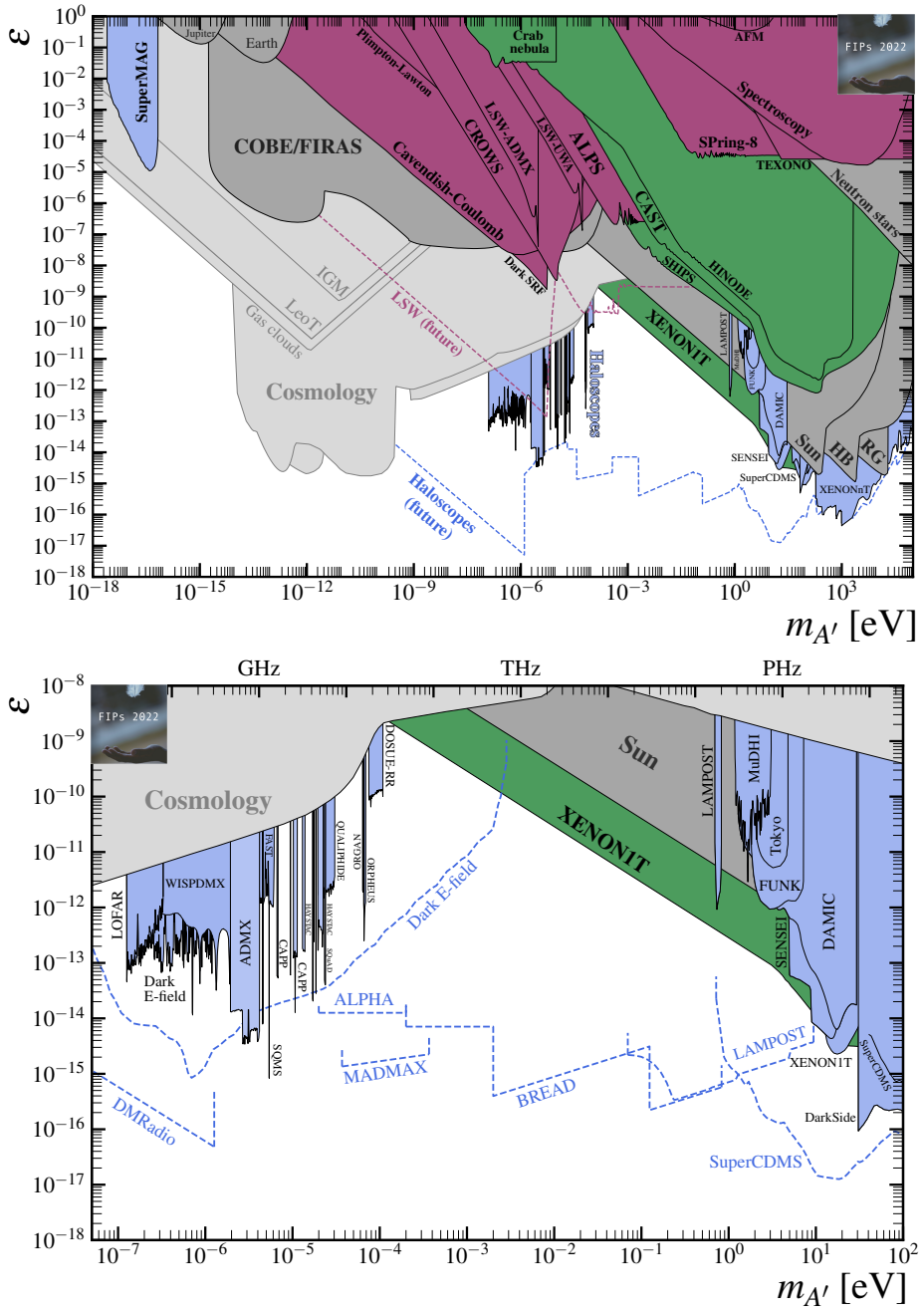

Figure 1.10: Constraints on the dark photon kinetic mixing for a wide mass range ($10^{-18} < m_{A'} \lesssim 10^5$ eV) and a more precise selection ($10^{-7} < m_{A'} < 10^2$ eV). Taken from [142].

$$
\begin{aligned}
-\mathcal{L}_D &= \frac{v}{\sqrt{2}}\lambda_\nu^{ij}\overline{\nu}_{L,i}\nu_{R,j} + \text{h.r.}\,, \\
-\mathcal{L}_M &= \frac{1}{2}M_\nu^{ij}\overline{\nu}_i\nu_j^c + \text{h.r.}\,,
\end{aligned}
\tag{1.62}
$$

where v is the vev of the SM Higgs boson, λ_ν^{ij} are the Yukawa Dirac couplings for the neutrino sector and M_ν^{ij} are the Majorana mass coefficients. We must consider 3 left neutrino states, while we can in general regard n right states. The ν states used for the Majorana Lagrangian can be right or left, though left states would need to come from a dimension-5 effective operator. After this mixing is diagonalized to find the neutrino physical states, the neutrino heavy states would be the HNLs. These leptons can interact through the weak force thanks to the mixing with the light SM states.

Latest searches and limits on HNLs

There are many experiments sensitive to HNLs, especially due to their mixing with SM active neutrinos. A general plot with the main current limits can be seen in Fig. 1.11, together with some of the expected sensitivities that come from future experiments.

Limits on HNL lifetime from BBN Big Bang Nucleosynthesis (BBN) sets very strong limits to any new physics particle candidate. In the case of HNLs, one of the most stringent ones comes from an upper limit to their lifetimes. In general, $c\tau_N^0 \lesssim 3 \times 10^4$ km, where τ_N^0 is the HNL's lifetime in its rest frame [144–149]. The masses can also be constrained: for purely electrophilic and neutrinophilic HNLs, $m_N > 3.7$ MeV [149].

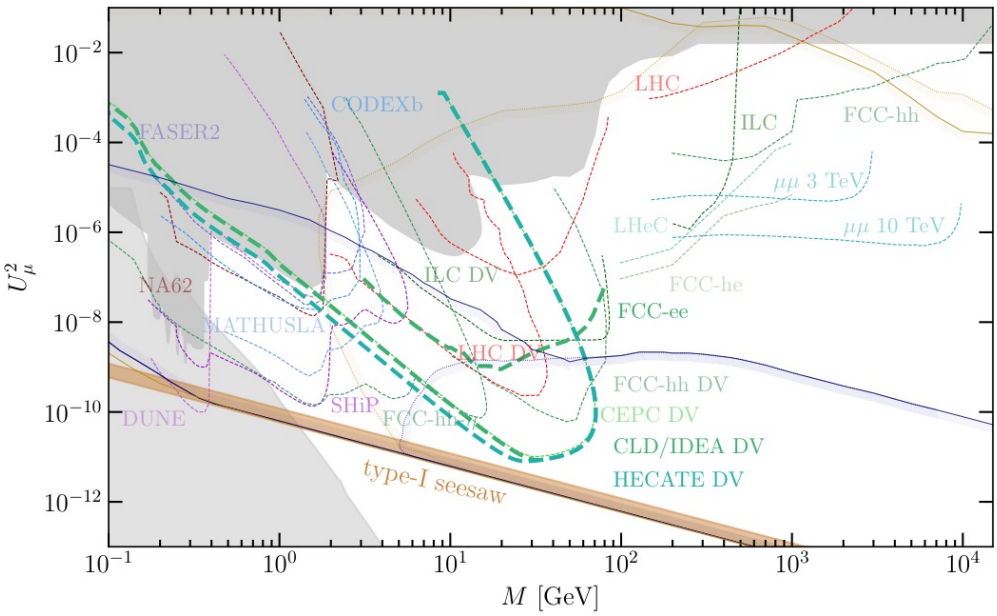

Figure 1.11: Constraints on the mixing (U_μ^2) with the active neutrinos and mass of HNLs (M) from past experiments together with expected sensitivities for future experiments. Taken from [143].

Searches at MicroBooNE MicroBooNE has done a study [150] searching for HNLs and excluding regions on the plane of the mass of the HNL and the mixing of one extra HNL with the muon neutrino, $|U_{\mu 4}|$, assuming that $|U_{e4}| = |U_{\tau 4}| = 0$. The mass range considered was from 260 to 385 MeV. This light HNL mass range allows to look for production of HNLs mainly from the decays of kaons that originate from the interaction between the colliding protons and the targets at BNB and NuMI neutrino beams. This HNLs could decay in the detector, provided that their lifetimes are sufficiently long. The process considered is $K^+ \to \mu^+ N$, where N is the HNL, which would then decay following the process: $N \to \mu^\mp \pi^\pm$. The production rate and decay width are both proportional to $|U_{\mu 4}|^2$, given no other mixings

between the HNL and the SM flavors and regarding the HNLs not to decay before the detector, which is a good approximation for the values considered. These processes are not forbidden given that $m_\mu + m_\pi < m_N < m_K - m_\mu$. Furthermore, if the HNL is of Dirac type, it could just decay into a $\mu^-\pi^+$ pair due to lepton number conservation. The results can be seen in Fig. 1.12.

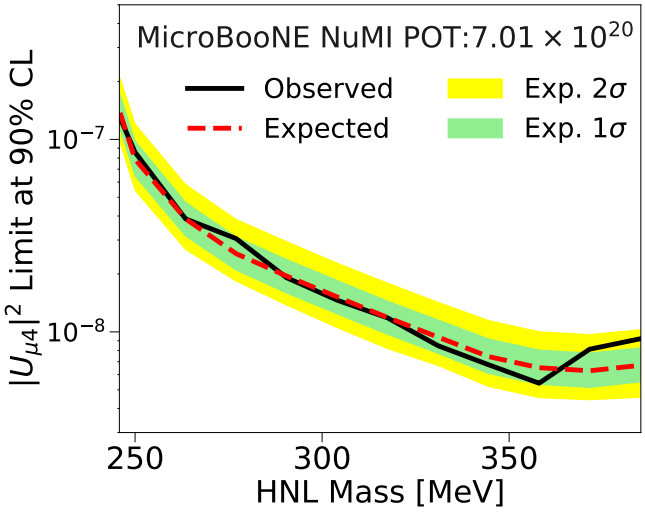

Figure 1.12: Limits at 90% CL from MicrobooNE to $|U_{\mu 4}|$ for $260 < m_N < 385$ MeV. $|U_{e4}|$ and $|U_{\tau 4}|$ are set to 0. Taken from [142].

Future searches at DUNE near detector It will also be possible to study HNLs as products of meson decays in DUNE. The higher energy of the beam will make the mass range of the search much wider, since there is also a production up to the D_s meson ($m_{D_s} = 1.968$ GeV) [151]. The analysis can also be done for different off-axis angles, since this helps in measuring systematic uncertainties because the flux depends on the angle, but the cross section do not.

The modeling of the fluxes has been done using NuShock [152] and can be seen in Fig. 1.13.

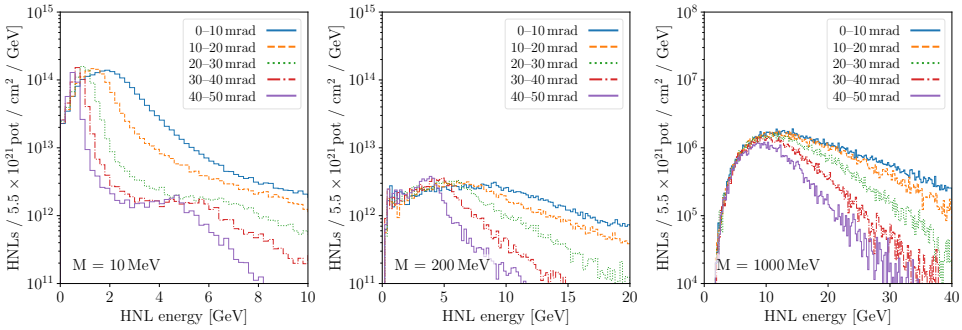

Figure 1.13: Fluxes of HNLs for different masses and angles off-axis of the beam at DUNE Near Detector. Taken from [151].

Backgrounds can be further reduced by selecting events such that the angle θ with respect to the beam is: $\theta < m_N/(E_1 + E_2)$ [153], where E_1 and E_2 are the energies of the two HNL decay product candidates. This cut helps because HNL decays are relatively forward with respect to neutrino interaction products. The results for just one mixing, $U_{\tau 4}$, is shown in Fig. 1.14, where the sensitivities are compared to other experiments' results. As can be seen, DUNE could cover a considerable region of unexplored parameter space.

Searches at neutrino telescopes HNLs can be produced from meson decays in the atmosphere or, alternatively, from upscattering of SM neutrinos that interact with matter: $\nu_\alpha \mathcal{N} \to N\mathcal{N}$. If the HNL only interacts through its mixing with active neutrinos, it will subsequently decay into SM particles and it will be long-lived since the decay rate is proportional to the mixing. The lifetime can be reduced if there are other interactions coming from an effective transition dipole moment operator or a light dark photon that also mediate the decay.

There are three main types of searches for these atmospheric HNLs, de-

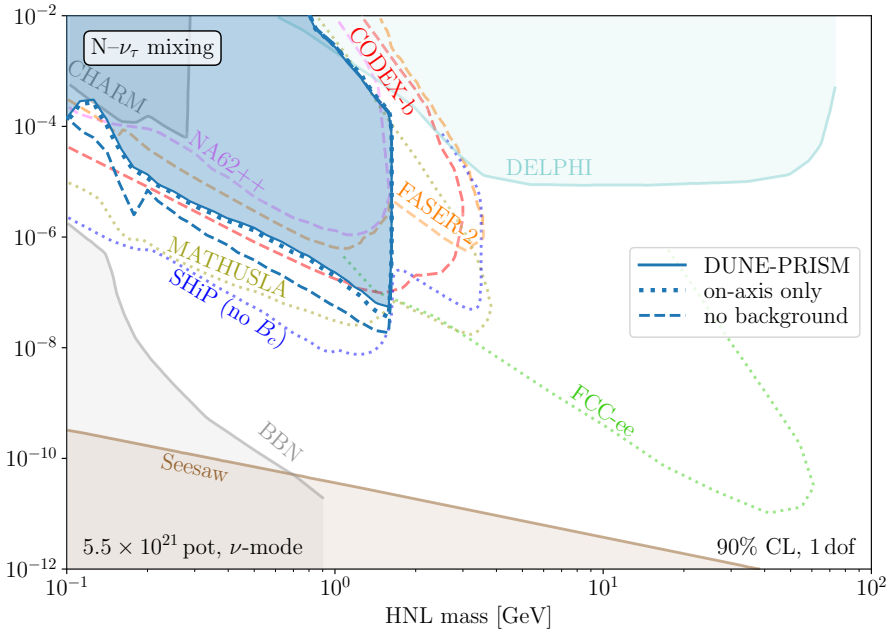

Figure 1.14: Predicted constraints from DUNE Near Detector, together with other existing limits for m_N and $U_{\tau 4}$ (Y-axis). $U_{\mu 4}$ and U_{e4} are set to 0. Taken from [151].

pending on where they are produced [142]:

- Production inside neutrino detectors.
- Production through up-scattering inside the Earth
- Production in the upper layers of the atmosphere

In case of being produced inside neutrino detectors, their signal would be very similar to that of a tau neutrino producing a double-cascade [154]. These events would be expected to be of the order of tens of GeV. Higher energies would imply boosted HNLs that escape the detector before decaying. The best detectors for this case would be Super-Kamiokande (SK), DUNE and Hyper-Kamiokande (HK).

If the HNLs are more long-lived, the ones produced by an upscattering

in the Earth could in principle be visible. The detectable signal would be the energy that is deposited from the HNL decay in the detector. Standard neutrino interactions would be the main background. HNLs of a few MeV produced from solar neutrinos could be detected in Borexino or SK [155, 156]. Other sources of this kinds are atmospheric neutrinos [157], long-baselines like DUNE [158] or even astrophysical neutrinos [159]. This last source could search for masses up to ~ 30 TeV.

The last case is to study the production of HNLs in the upper layers of the atmosphere [160–164]. In this scenario, since the center-of-mass energy coming from cosmic rays is very high, heavier mesons can be produced, such as D and D_s, and MeV - GeV range HNL masses could be searched. A sufficient boost may also help the HNLs to reach the neutrino detectors before decaying. The branching ratios are less than 2×10^{-10} for $m_N = 100$ MeV and 4×10^{-9} for $m_N = 250$ MeV at 90% CL [161].

In Fig. 1.15, we can see the constraints for HNLs produced and detected at SK just through their mixing with the electron neutrino.

Searches at pion decay experiments Searches for rare pion decays, like the experiments PIENU [165] or PEN [166], have also put limits on light HNLs. The PIONEER experiment the Paul Scherrer Institut (PSI) will improve those results. An incoming beam of pions is stopped at an active target (ATAR). The muons that generate from the decay cannot escape the 6-mm-thick target. PIENU looked for the decay channel $\pi^+ \to e^+ N$ by looking at the positron energy spectrum up to 60 MeV. The same procedure was done with muons decaying at rest. Both measurements set constraints on $|U_{e4}|$ and $|U_{\mu 4}|$ respectively. The results can be seen in Fig. 1.16 together with the projections for PIONEER.

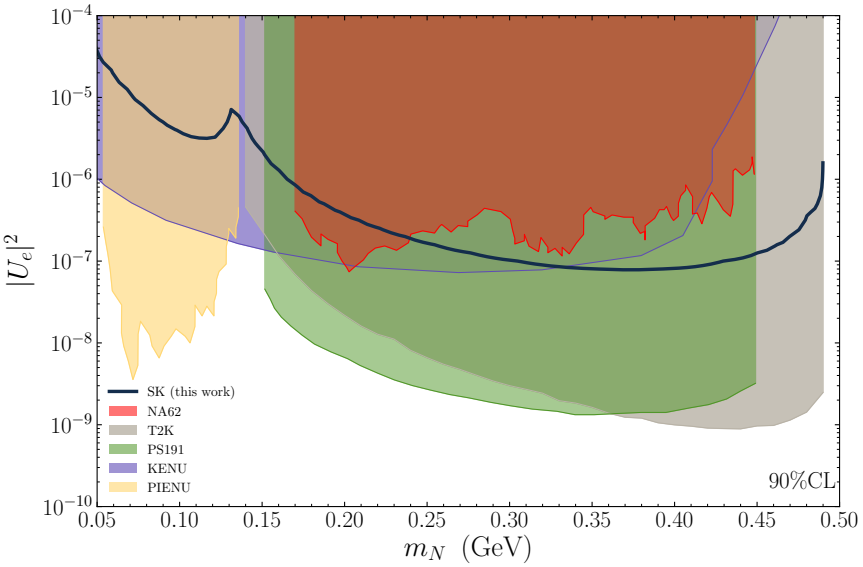

Figure 1.15: Constraints derived from SK atmospheric data on the mixing of HNLs with electron neutrinos ($U_e \equiv U_{e4}$). The HNLs are produced by the decays of mesons. $U_{\mu 4}$ and $U_{\tau 4}$ are set to 0. Taken from [142].

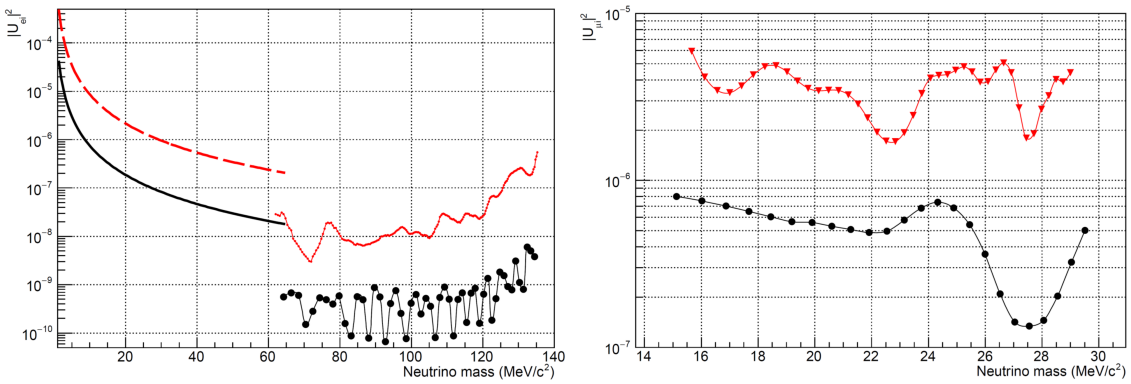

Figure 1.16: Constraints on $|U_{e4}|$ (*left*) and $|U_{\mu 4}|$ (*right*) from PIENU (red) and the expected for PIONEER (black). The HNLs are produced by the decays of pions. The limits are found from the computation of $R^{\text{Exp.}}_{e/\mu}$. Taken from [142].

Searches at BaBar BaBar looked for HNLs mixed with the tau neutrino, setting limits on $|U_{\tau 4}|^2$. The limits vary from 2.31×10^{-2} to 5.04×10^{-6} across $100 < m_N < 1300$ MeV [167]. These constraints are purely kinematical,

i.e., model independent. The collaboration studied decays of the tau lepton through the CC and analyzed the kniematics of the visible decay products, assuming that the HNL could not decay inside the detector. The decay goes through three charged pions and a neutrino. The invariant mass of the pionic system varies with respect of the HNL mass. The range of energies for the pions is

$$E_\tau - \sqrt{m_N^2 + q_+^2} < E_{3\pi} < E_\tau - \sqrt{m_N^2 + q_-^2}\,, \tag{1.63}$$

where,

$$\begin{aligned} q_\pm =& \frac{m_\tau}{2}\left(\frac{m_{3\pi}^2 - m_\tau^2 - m_N^2}{m_\tau^2}\right)\sqrt{\frac{E_\tau^2}{m_\tau^2} - 1} \\ & \pm \frac{E_\tau}{2}\sqrt{\left(1 - \frac{(m_{3\pi} + m_N)^2}{m_\tau^2}\right)\left(1 - \frac{(m_{3\pi} - m_N)^2}{m_\tau^2}\right)}\,, \\ 3m_{\pi^\pm} < & \, m_{3\pi} < m_\tau - m_N\,. \end{aligned} \tag{1.64}$$

As m_M increases, the phase space reduces. The limits can be seen in Fig. 1.17.

Searches at the LHC Another way of looking for HNLs is in collider experiments. The Large Hadron Collider (LHC) has searched for them in the ATLAS [168] and CMS [169] experiments in the range of GeV to a few TeV mass range, by reconstructing the charged leptons and jets, while adding the missing momentum. In [142] we can find the last results from full pp collision data at $\sqrt{s} = 13$ TeV recorded during Run 2 of the LHC (2015 - 2018) corresponding to an integrated luminosity of about 140 fb^{-1}. The HNL phenomenologies covered by these searches are wide:

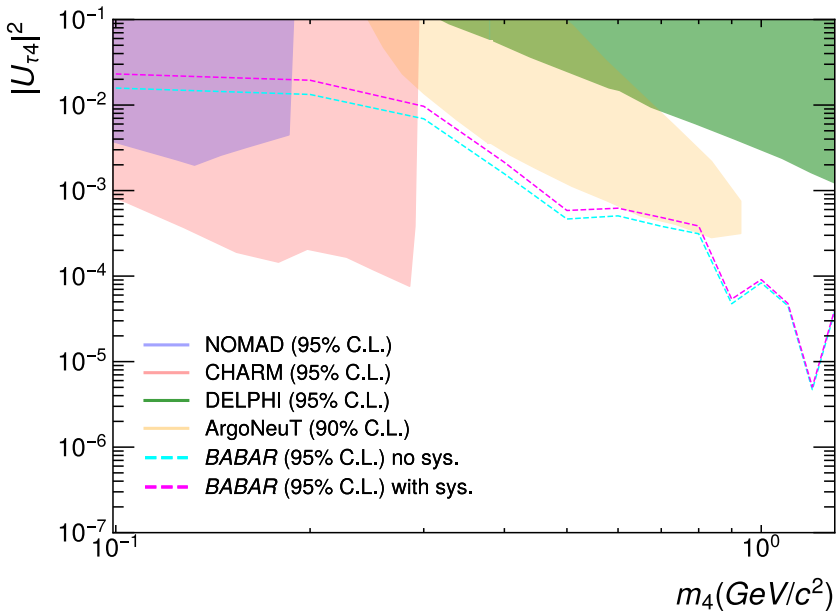

Figure 1.17: Constraints on $|U_{\tau 4}|$ from BaBar. The HNLs are produced by the decays of tau leptons. The limits are at 95% CL. The magenta line is expected to be a very conservative upper limit. Taken from [142].

- HNL production in type-I seesaw models through the Drell–Yan (DY) or a t-channel vector boson fusion (VBF) process [170–172].
- Pair production of HNLs and charged leptons in type-III seesaw models [173].
- HNL pair production in decays of a new heavy dark photon [174].

The DY and the VBF processes' Feynman diagrams can be seen in Fig. 1.18.

For the DY processes, the HNL could decay into 2 charged leptons or a lepton and 2 quarks. Therefore, there could be a di- or trilepton final state that is searched for by the experiment. The masses covered in the searches have been from 1 GeV to 1.6 TeV. Regarding long-lived HNLs, with masses

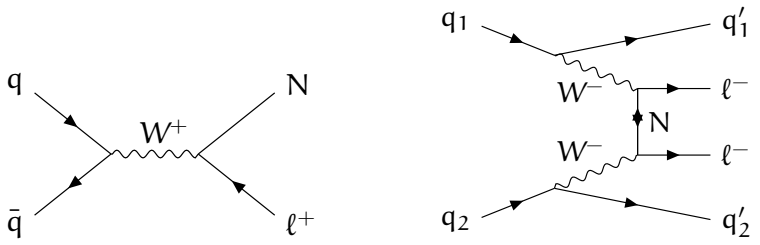

Figure 1.18: Drell-Yan process for production of HNLs (left) and vector boson fusion (right). Taken from [142].

lighter than 20 GeV, it is easier for the DY process to find these topologies due to the displaced vertices. The CMS performed searches for a trilepton final state with a secondary dilepton vertex. The experiment imposed a long-lived constraint, thus they only regarded the lighter masses($\lesssim$ 20 GeV). ATLAS looked for HNLs with events with a displaced dilepton vertex, where the HNL mass was reconstructed from the selected leptons. The results can be seen in Fig. 1.19. The differences in the results are due to the different transverse momentum thresholds in the sinlge-lepton triggers and, in general, different strategies in the selection of events.

For the VBF processes, larger HNL masses are more relevant. The amplitude is proportional to $p_N^2/(p_N^2 - m_N^2)$, where p_N is the 4-momentum of the Majorana HNL mediator. There is a maximum when $p_N^2 \sim m_N^2$. For the energies of the LHC in run 2, the maximum is around a few hundreds of GeV. The searches look for two jets with large rapidity separation, using events with two same-sign muons. This t-channel provides better constraints especially for masses larger than 650 GeV [175, 176]. The limits can be seen in Fig. 1.20.

In the type-III seesaw case, there is an additional fermionic $SU(2)_L$ triplet that gives rise to new HNLs and charged leptons, that can be pair produced via an s-channel, as we can in the diagram in Fig. 1.21.

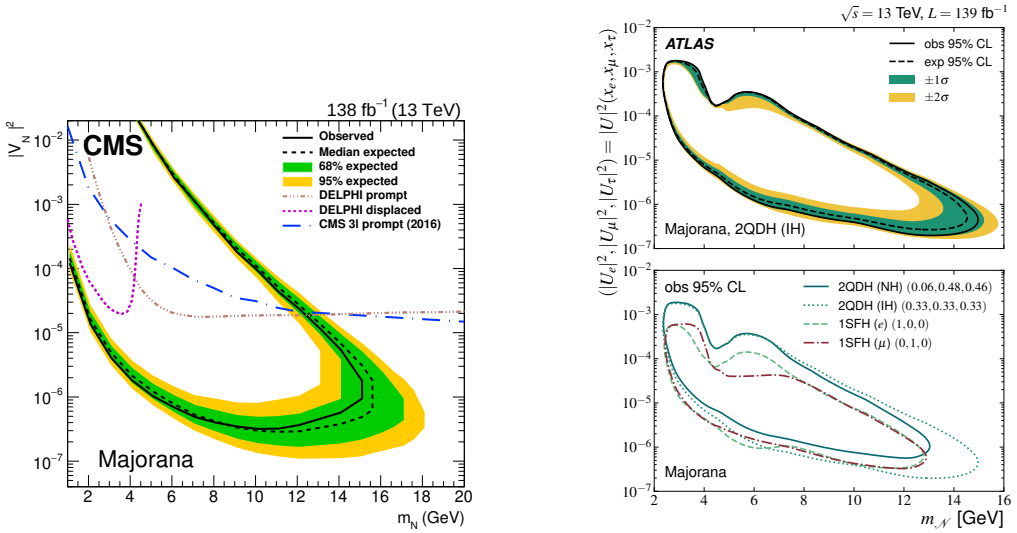

Figure 1.19: Exclusion limits on the mixing between the HNLs and the muon (*left*: CMS, taken from [170]) and with all flavors under a universal mixing assumption (*right*: ATLAS, taken from [171]) in type-I seesaw models as a function of the HNL mass m_N.

The searches at ATLAS looked for three- or four-lepton events. Heavy neutral and charged leptons in type-III seesaw models are excluded up to 910 GeV. The results are presented in Fig. 1.22.

Finally, it is also possible to look for decays of a new heavy dark photon. CMS did this search in the context of a left-right symmetry model (LRSM), where the SM is extended with three extra gauge bosons ($W_R^\pm$ and Z') and three right handed neutrinos under an $SU(2)_R$ symmetry. They considered a large gap between the masses of the Z' and the HNLs, so that the latter are highly boosted, as well as other decay products. The diagram of the process is in Fig. 1.23.

For identifying the event, the two leptons and two quarks are selected and the Z' is reconstructed from these decay products. There are backgrounds from $t\bar{t}$ and l^+l^- production. The exclusion plot is shown with respect to the Z' mass and HNL mass in Fig. 1.24. It considers a lightest HNL mass of 100

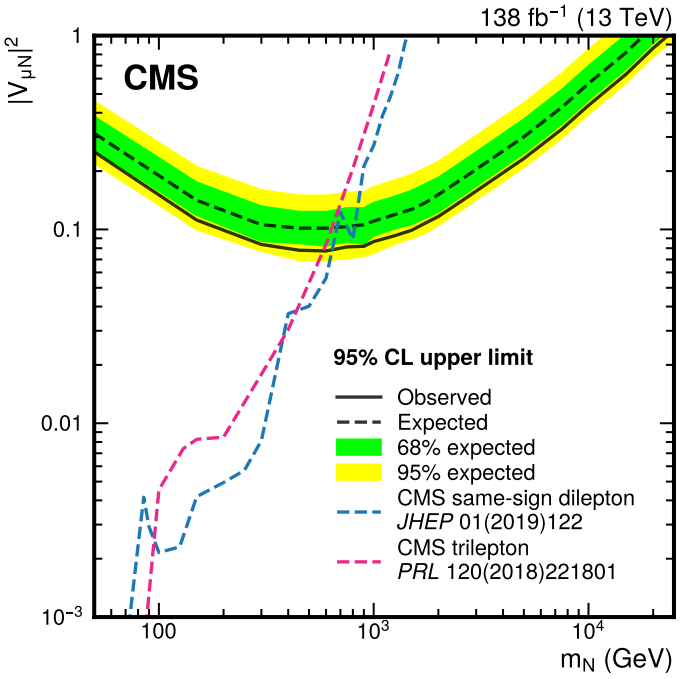

Figure 1.20: Exclusion limits from CMS on the mixing between the HNLs and the muon in type-I seesaw models as a function of the HNL mass m_N. Taken from [172].

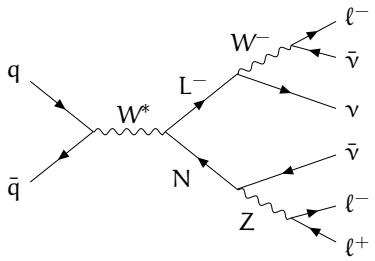

Figure 1.21: Process for production of HNLs and new charged leptons through the W boson. Taken from [142].

GeV.

Future searches at the FCC-ee The Future Circular Collider (FCC) will also look for HNLs, especially on the *ee* collisions (FCC-ee). The energies would be of $\sqrt{s} = 91$ GeV. After an electron - positron collision, a Z boson (SM) is expected to produce an HNL - neutrino pair. The former would

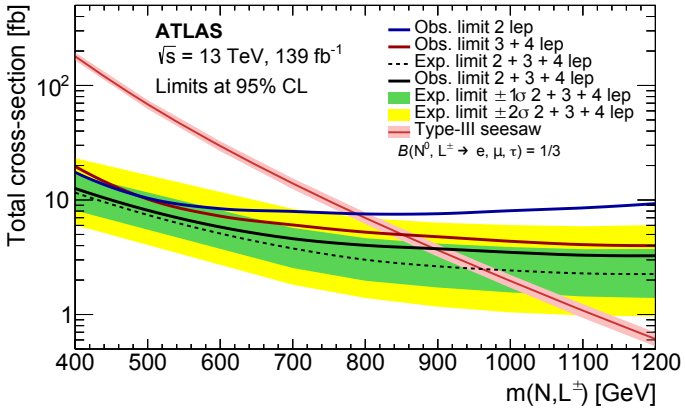

Figure 1.22: Exclusion limits from ATLAS on the production cross section of HNLs and charged leptons for degenerate masses, $m(N, L^{\pm})$. Taken from [173].

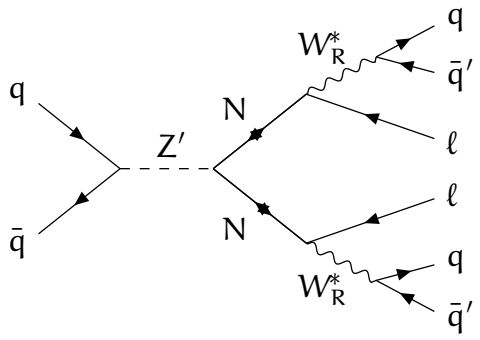

Figure 1.23: Process for production of HNLs through a Z' boson. Taken from [142].

decay mainly into another electron - positron pair plus a neutrino. The cross sections and decay widths depend on the nature of the HNL (Dirac or Majorana) [142]. Right now we just have simulations, since the experiment is still not running. In the absence of other BSM fields, the light HNLs tend to be long-lived. In Fig. 1.25 we can see the lifetimes of the HNLs in the lab frame for different choices of masses, from 30 to 90 GeV. For 30 GeV, the HNLs can even travel 1 m before decaying. Heavier ones travel up to 10 cm, which is still suitable for displaced vertices searches.

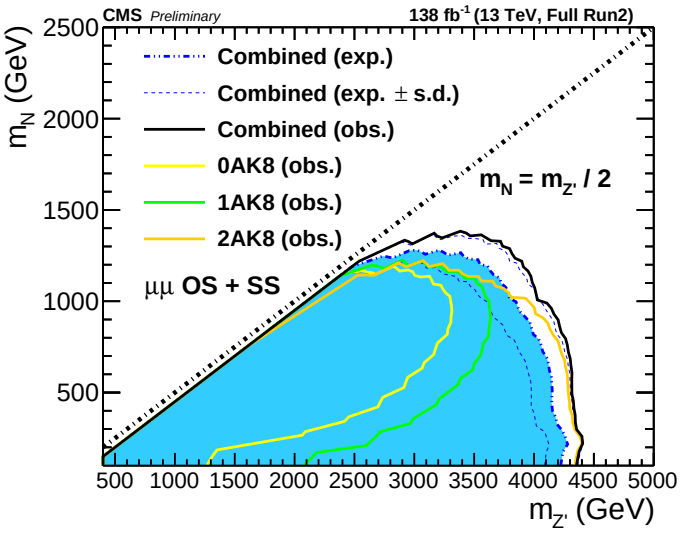

Figure 1.24: Constraints from CMS from dimuon events on LRSM models with respect to the dark photon mass, $m_{Z'}$, and the HNL mass, m_N. Taken from [174].

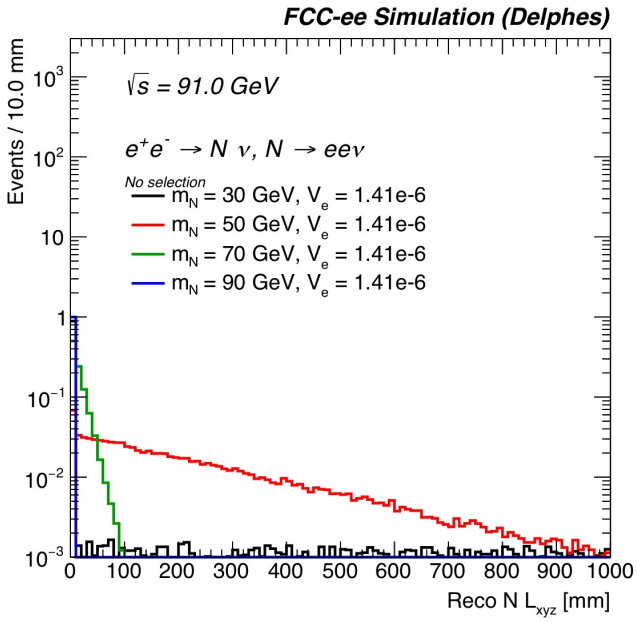

Figure 1.25: Normalized distributions of the reconstructed generated lifetimes of HNLs (L_{xyz}) in mm in the lab frame. The active-sterile mixing used is $|U_{eN}| = 1.41 \times 10^{-6}$. Taken from [143].

Searches at the Big European Bubble Chamber (BEBC) WA66 Data from the BEBC WA66 beam dump experiment at CERN has been used to look for HNLs [177]. The authors in [142] reanalyzed the limits from BEBC and recast the ones from CHARM [178], by considering also a mixing with the tau neutrino, which had no been considered in the previous studies. At BEBC, the dominant source for HNLs is the three-body decay of $D^{\pm}$ and D^0 mesons [177].

The HNLs produced in the beam dump must reach the detector and decay within it. [179] considered just SM particles in the final states: $l^{\mp}\pi^{\pm}$ or $l^{+}l^{-}\nu$, where $l = e, \mu$. The background was computed using the results from WA59 experiment [180]. The reanalysis of BEBC and the recast of CHARM can be seen in Fig. 1.26 for $U_{\tau N}$ and U_{eN}. BEBC WA66 has a better performance even than the much bigger CHARM detector, because the latter has an off-axis beam that makes it receive not only a smaller flux, but also less higher energetic HNLs.

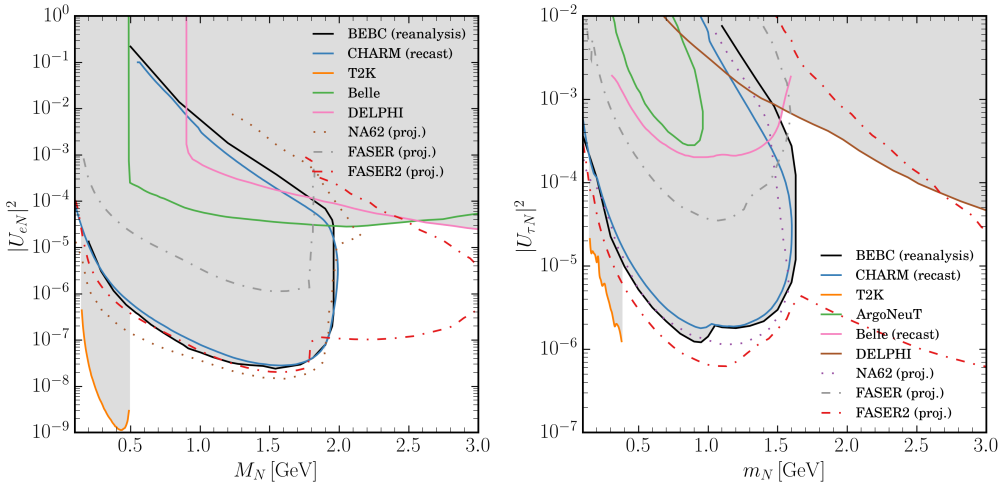

Figure 1.26: 90% CL exclusion region in the HNL mixing with the electron (*left*) and tau (*right*) neutrinos. The limits from BEBC were reanalyzed, while the ones from CHARM recast. There are other important limits, together with the projection at NA62, FASER and FASER2. Taken from [142].

Limits and non-minimal models Many of the previous limits rely on the assumption that the interactions of the HNLs are just under the SM-Weak one through mixing with neutrinos. They often also consider them to be Majorana fermions. Non-minimal models may include forces stronger than the SM-Weak one and Dirac HNLs. This might radically change the picture. For example, the limits set on HNLs below the kaon mass [181] are visibly relaxed when new forces are taken into account [182]. A dark photon could have an effect of more than three orders of relaxation of constraints, as seen in Fig. 1.27.

The effect on the decays of non-minimal models can be categorized in two groups: invisibly-decaying HNLs and visibly-decaying HNLs. The first ones decay into neutrinos and dark particles. In this case, the mediator just talks to dark fields. However, in case the mediator can interact with SM visible fields, then we have the second case. Visible decays can be detected by the following process,

$$\nu_\alpha \mathcal{N} \to \left(N \to \nu_\beta l^+ l^-\right) \mathcal{N} \tag{1.65}$$

In this process, the two leptonic showers can be detected. Depending on the energies, a proton track might also be seen. Fake photon signatures may be misinterpreted in case of an e^+e^- pair, due to the collimated showers produced due to the boost. This is the kind of topology that will be used to explain MiniBooNE on Chapter 2. These decays could also be searched in NA64, where the limits need to be recast in order to account for the different semi-visible decays. This recasting has already been done for NA64 [183], where instead of HNLs the authors considered working with dark matter. Although not mixed with neutrinos, these DM candidates exhibit a relaxation of their limits due to the opened semi-visible channels of decay. In the case

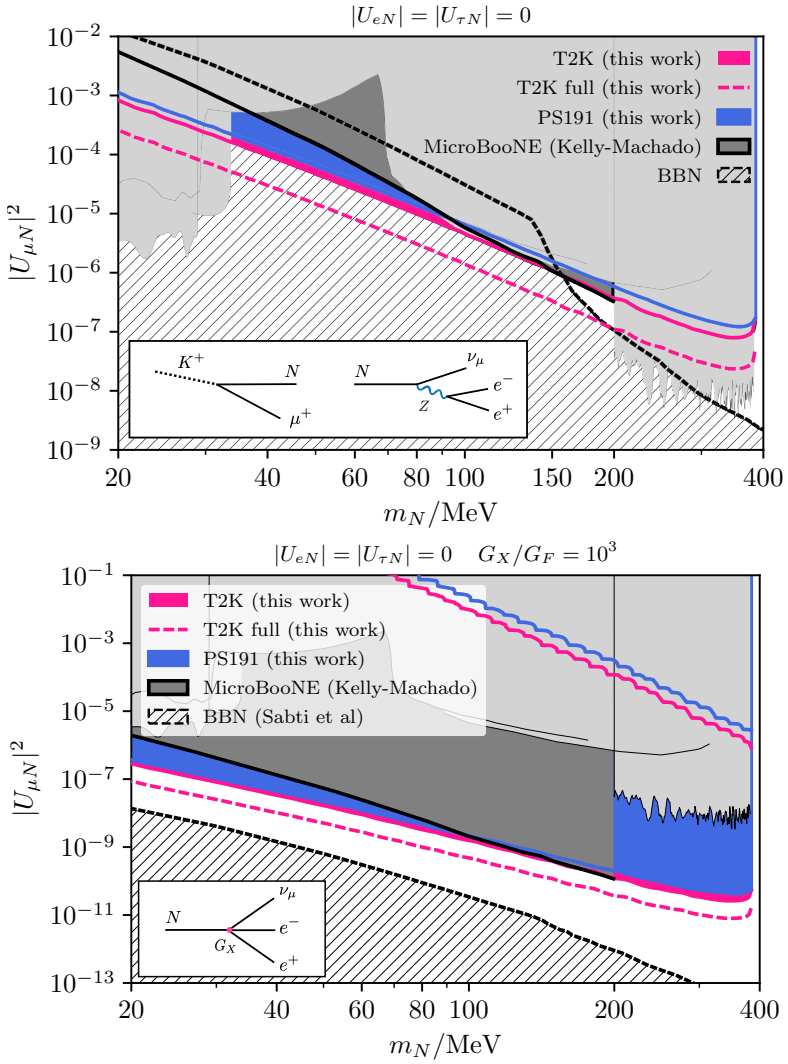

Figure 1.27: Limits on the mass of HNLs from a minimal model (*left*) and from a model that includes an interaction through a dark photon (*right*). Taken from [182].

of just one DM candidate, the results can be seen in Fig. 1.28.

Current status of HNLs

It is important to close this section by having a broader overview on the limits on HNLs. Even though, as we have seen, the constraints are model-

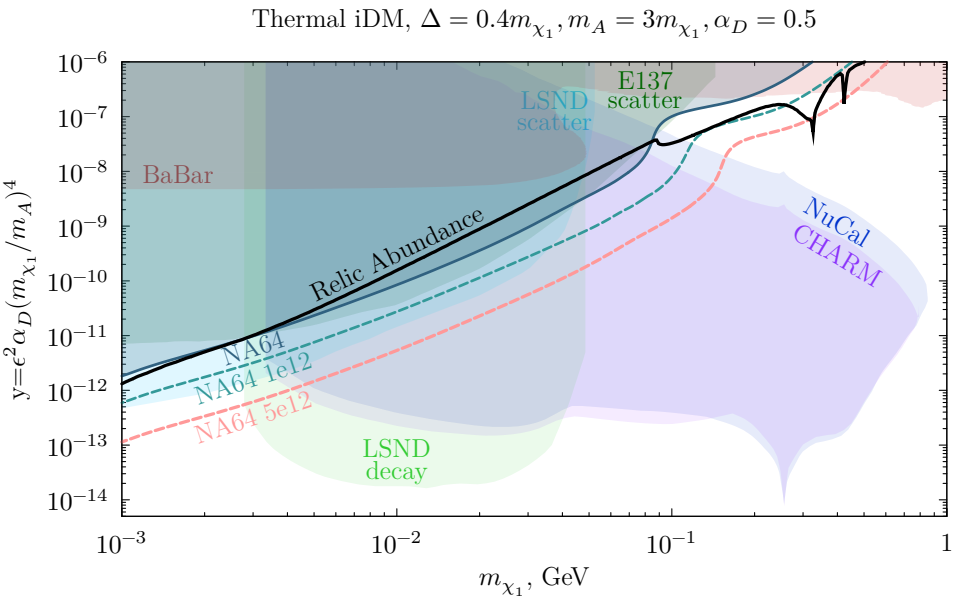

Figure 1.28: Limits on the mass of a thermal DM candidate with respect to a product of couplings and masses: $y \equiv \varepsilon^2\alpha_D\,(m_{\chi_1}/m_{A'})$, where A' is the dark photon mediator, $\alpha_D \equiv g_D^2/(4\pi)$. g_D is the dark coupling of the dark photon to the DM fermions. Two DM fermions are considered, such that: $\Delta \equiv m_{\chi_2} - m_{\chi_1} = 0.4m_{\chi_1}$, $m_{A'} = 3m_{\chi_1}$, $\alpha_D = 0.5$. The plots shows the limits for NA64 together with projections for a different number of electrons on target (EOT). Taken from [183].

dependent, it will be useful to keep in mind some of the allowed regions at least for the minimal model, in which the HNLs partake interaction with the SM through neutrino mixing. We will consider a simplified approach, by which we just turn on the mixing with one particular neutrino active flavor and one HNL is added to the SM. We will follow the notation of [142]: $|U_{\alpha N}| \equiv U_\alpha$. The plots can be seen in Fig. 1.29, Fig. 1.30 and Fig. 1.31.

We can see that for the lowest masses, the most stringent constraints come from BBN, which places a minimum mass for the HNLs. There is also a lower limit to account for the neutrino masses through the type-I seesaw mechanism. As we go to higher masses, from 100 MeV to 1 GeV, collider

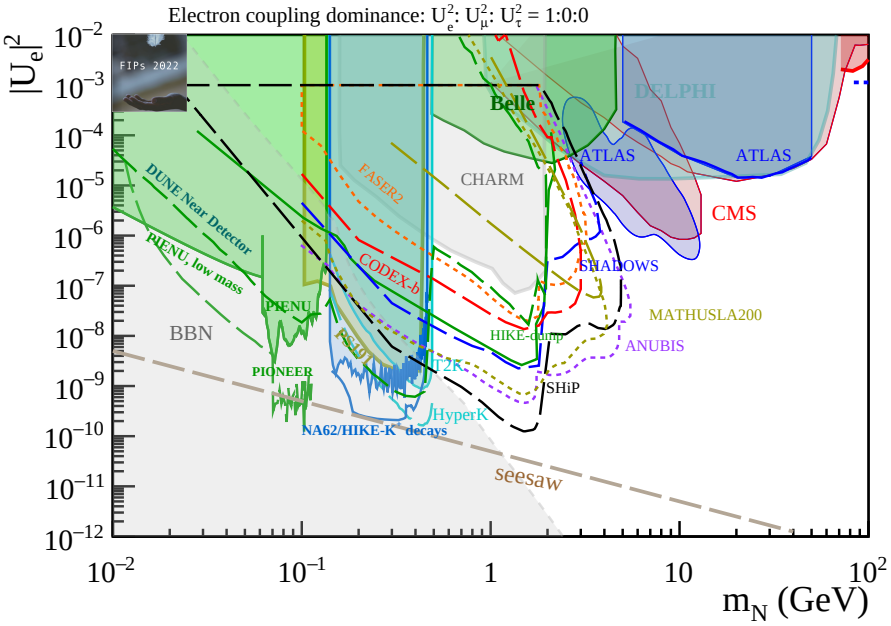

Figure 1.29: Limits on the couplings of HNLs from a minimal model. There is just one mixing activated: U_e. Taken from [142].

or meson decay experiments that put limits on long-lived particles, such as NA62 or FASER2 in the future, have the most stringent constraints to the mixing, especially for the electron and muon cases. As we go to higher masses, from a few to tens of GeV, ATLAS and CMS limit the electron and muon mixings, while DELPHI constrains any mixing. Some of these detectors have not been presented here: they are out of the scope of the present chapter. Just the last searches have been taken into account.

1.1.3 Dark scalars

The last important element of dark sectors are possible scalar extensions. They usually appear as mixed with the SM-Higgs boson, though this is not the only possibility. We will not expand on this topic as in the previous one, since scalars do not play a significant role in the current work. We can

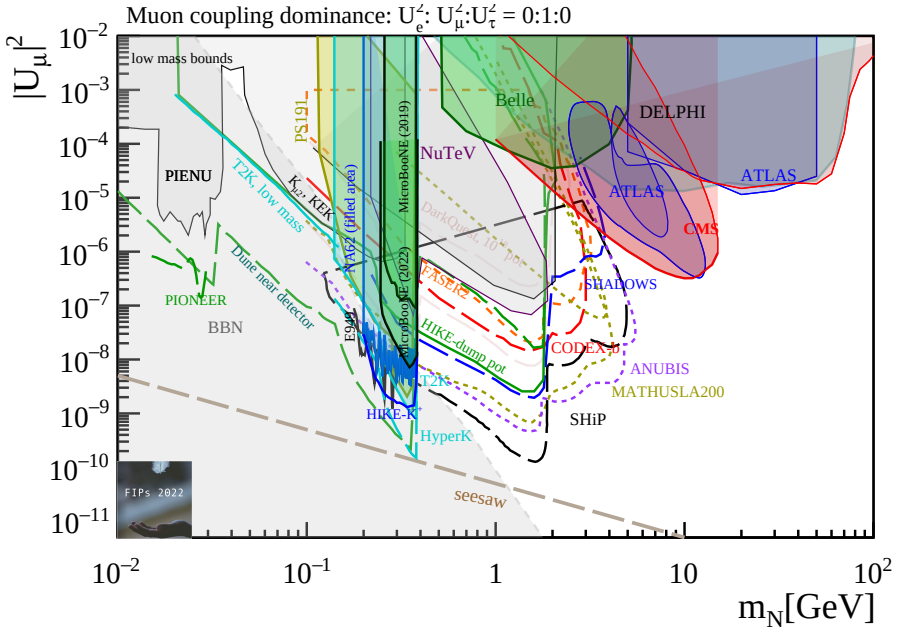

Figure 1.30: Limits on the couplings of HNLs from a minimal model. There is just one mixing activated: U_μ. Taken from [142].

introduce a dark scalar, s, complex singlet and couple it to the Higgs-doublet with the potential [184],

$$V_{\text{scalars}} = V_H(H) + V_{\text{int}}(H,s) + V_s(s)\,, \tag{1.66}$$

where $V_H(H)$ is the SM-Higgs potential, $V_s(s)$ a potential for s and $V_{\text{int}}(H,s)$ is a mixing between both. Due to the mixing, H would not really be the physical SM-Higgs. These last two potentials could be modeled as follows,

$$\begin{aligned} V_{\text{int}}(H,s) &= \frac{\lambda_{Hs}}{2}s^2|H|^2 + \mu_{Hs}s|H|^2\,, \\ V_s(s) &= \frac{m_s^2}{2}s^2 + \frac{\mu_s}{6}s^3 + \frac{\lambda_s}{24}s^4\,. \end{aligned} \tag{1.67}$$

Both scalars could acquire a non-vanishing expectation value due to spon-

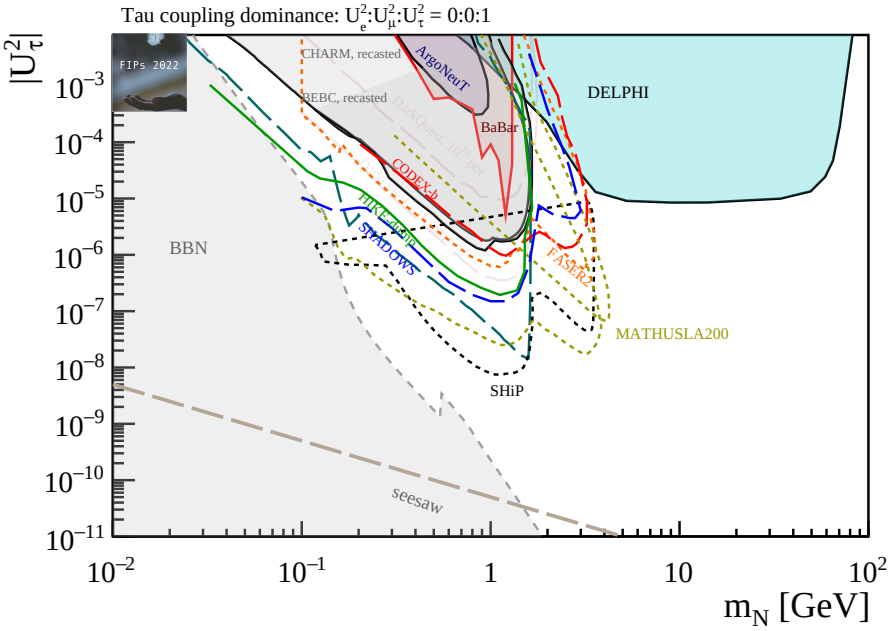

Figure 1.31: Limits on the couplings of HNLs from a minimal model. There is just one mixing activated: U_τ. Taken from [142].

taneous symmetry breaking. Once this happens, if we call h and φ to the SM-Higgs and the dark scalar mass eigenstates respectively, and if θ_s is their mixing angle, then the interactions between the new scalar and the SM fermions, f, has the following form [184],

$$\mathcal{L}_{\varphi-f} = -\sum_f \frac{m_f \sin\theta_s}{v} \varphi \bar{f} f \,, \tag{1.68}$$

where m_f is the mass of the fermions and v is the SM-Higgs vacuum expectation value. $\sin\theta_s$ needs to be small due to experimental constraints. The interactions with the Higgs, apart from the mixing, are through contact interactions of the forms: $\varphi\varphi h$, φhh and $\varphi\varphi hh$ and depend on other parameters than θ_s. We also need to consider a mixing with the weak gauge bosons,

$$\mathcal{L}_{\varphi-WZ} \simeq \left(1+\frac{h+\theta_s\varphi}{v}\right)^2 \left(m_W^2 W^{\mu+}W_\mu^- + \frac{1}{2}m_Z^2 Z^\mu Z_\mu\right) , \tag{1.69}$$

where $m_{W,Z}$ are the masses of the weak gauge bosons. In general, φ can also couple to the gluons and the photon at 1-loop level, though the analysis of these interactions is out of the scope of this work. For more information, we refer the reader to [185–187].

Dark scalars can be detected through their decay modes into SM particles. If its mass is greater than $2m_e$, where m_e is the electron mass, then they predominantly decay into eletron-positron pairs such that:

$$\Gamma_{\varphi\to e^+e^-} = \frac{\sin^2\theta_s m_e^2 m_\varphi}{8\pi v^2}\left(1-\frac{4m_e^2}{m_\varphi^2}\right)^{3/2} . \tag{1.70}$$

For lower masses the decay channel is 1-loop induced into two photons. Depending on the neutrino mass generation, it could also decay into a neutrino pair. Constraints for this boson come from supernovae (SN), since they can be produced in a core-collapse, and from colliders, since they can be produced by meson decays and also by gluon-gluon fusion. In the first case, they can alter the neutrino cooling rate in the SN [188–190]. SN1987A can put limits on scalars with masses less than 100 MeV [191]. In the case of colliders, ATLAS [192] has set constraints on the production of dark scalars that decay into muon pairs. The results can be seen in Fig. 1.32.

There are other experiments in which scalars could be searched, including looking for signatures of gravitational waves due to a phase transition [193], though they are out of the scope of the present analysis. Now we can continue with a specific realization of a dark sector.

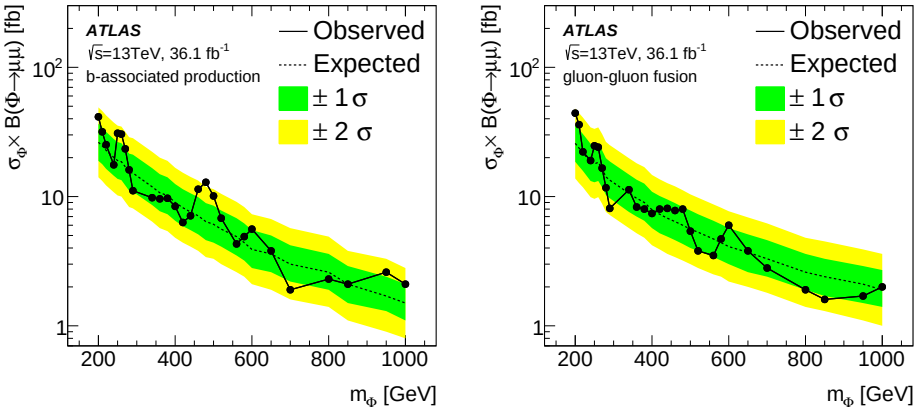

Figure 1.32: Upper limits on scalars produced by the b-quark (*left*) and gluon-gluon fusion (*right*) in ATLAS experiment at CERN to the 95% of C.L. The constraints are set on the total cross section of the scalar production times the branching ratio of its decay into a muon-antimuon pair. Taken from [192].

1.2 Three portal model

Here we will explore the Three portal model [88, 194–196] as a prototype for rich dark sectors. We will abandon the commonly advocated principle of minimality, that introduces a portal at a time, and adopt a structure which resembles that of the SM, the only proven theory of particles and interactions.

1.2.1 Lagrangian

The model has a $U(1)$ extension of the SM, with the associated field X^μ, which is kinetically mixed with the hypercharge boson. It also has a complex singlet dark Higgs scalar Φ charged under $U(1)_D$, where D stands for dark, which breaks the symmetry giving mass to the dark photon and to the HNLs. Finally, the model also includes a set of sterile right handed neutrinos N_R and dark fermions ν_D, charged under the gauge symmetry. The charges of these dark fermions need to cancel the chiral anomalies: this could be attained by

having pairs of oppositely charged ν_D.

The Lagrangian of the model is the following:

$$\begin{aligned}\mathcal{L} \supset & -\frac{1}{4}X^{\mu\nu}X_{\mu\nu} - \frac{\sin\chi}{2}X_{\mu\nu}B^{\mu\nu} + (\mathcal{D}^x_\mu\Phi)^\dagger(\mathcal{D}^\mu_x\Phi) \\ & - V(\Phi,H) + \overline{\nu_N}i\partial\!\!\!/\nu_N + \overline{\nu_D}i\mathcal{D}\!\!\!/^x\nu_D \\ & - \Bigg[(\overline{L}\widetilde{H})Y\nu^c_N + \frac{1}{2}\nu_N M_N\nu^c_N + \overline{\nu_N}(Y_L\nu^c_{D_L}\Phi + Y_R\nu_{D_R}\Phi^*) \\ & + \overline{\nu}_D M_X\nu_D + \text{h.c.}\Bigg],\end{aligned} \tag{1.71}$$

where $D^x_\mu\Phi \equiv \partial_\mu - ig_X X_\mu$.

We will analyze the necessary steps to obtain the physical states after Spontaneous Symmetry Breaking (SSB) of the two Higgs bosons: $SU(2)_L \times U(1)_Y \times U(1)_D \to U(1)_{em}$, by which the bosons acquire a mass to give rise to 4 mass states ($W^\pm$, Z, Z'), being the last one the dark photon.

1.2.2 Spontaneous Symmetry Breaking

To analyze the SSB in the present model, we need to start with the Potential for the two Higgs complex fields: the doublet (H) and the singlet (Φ). The scalar portal arises from the mixing between the two Higgs scalars through a term of the form $\lambda(H^\dagger H)|\Phi|^2$, as follows:

$$V(\Phi,H) = -m^2_\varphi|\Phi|^2 + \lambda_\varphi|\Phi|^4 - m^2_H H^\dagger H + \lambda_H(H^\dagger H)^2 + \lambda(H^\dagger H)|\Phi|^2\,, \tag{1.72}$$

where: $H = \frac{1}{\sqrt{2}}\begin{pmatrix} G^+_1 + iG^+_2 \\ h + iG^0 \end{pmatrix}$ and $\Phi = \frac{1}{\sqrt{2}}(\varphi + iG_\varphi)$.

This potential is minimized under the following conditions:

$$\begin{aligned} H^\dagger H &= \frac{4\lambda_\varphi m_H^2 - 2\lambda m_\varphi^2}{4\lambda_\varphi \lambda_H - \lambda^2} \equiv v_H^2 \,, \\ |\Phi|^2 &= \frac{4\lambda_H m_\varphi^2 - 2\lambda m_H^2}{4\lambda_\varphi \lambda_H - \lambda^2} \equiv v_\varphi^2 \,. \end{aligned} \tag{1.73}$$

It is possible to eliminate the unphysical Goldstone bosons by making appropiate rotations and redefining the gauge fields. In this way, we can directly work in the unitarity gauge, such that:

$$\begin{aligned} H &= \frac{1}{\sqrt{2}} \begin{pmatrix} 0 \\ v_H + h \end{pmatrix} \,, \\ \Phi &= \frac{1}{\sqrt{2}} (v_\varphi + \varphi) \,. \end{aligned} \tag{1.74}$$

After expanding the potential with the above expressions, the second order terms of it are the following:

$$\begin{aligned} V^{(2)}(h,\varphi) &= (\lambda_H v_H^2) h^2 + 2(\frac{1}{2}\lambda v_H v_\varphi) h\varphi + (\lambda_\varphi v_\varphi^2)\varphi^2 \\ &= (h \;\; \varphi) \begin{pmatrix} \lambda_H v_H^2 & \frac{1}{2}\lambda v_H v_\varphi \\ \frac{1}{2}\lambda v_H v_\varphi & \lambda_\varphi v_\varphi^2 \end{pmatrix} \begin{pmatrix} h \\ \varphi \end{pmatrix} \\ &= \frac{1}{2}(h' \;\; \varphi') \begin{pmatrix} m_{h'}^2 & 0 \\ 0 & m_{\varphi'}^2 \end{pmatrix} \begin{pmatrix} h' \\ \varphi' \end{pmatrix} \end{aligned} \tag{1.75}$$

where,

$$
\begin{aligned}
m^2_{h'} &= \lambda_H v_H^2 + \lambda_\varphi v_\varphi^2 - \sqrt{(\lambda_H v_H^2 - \lambda_\varphi v_\varphi^2)^2 + \lambda^2 v_H^2 v_\varphi^2}\,, \\
m^2_{\varphi'} &= \lambda_H v_H^2 + \lambda_\varphi v_\varphi^2 + \sqrt{(\lambda_H v_H^2 - \lambda_\varphi v_\varphi^2)^2 + \lambda^2 v_H^2 v_\varphi^2}\,, \\
\begin{pmatrix} h' \\ \varphi' \end{pmatrix} &= \begin{pmatrix} \cos\theta & -\sin\theta \\ \sin\theta & \cos\theta \end{pmatrix} \begin{pmatrix} h \\ \varphi \end{pmatrix} \\
\tan(2\theta) &= \frac{\lambda v_H v_\varphi}{\lambda_\varphi v_\varphi^2 - \lambda_H v_H^2}\,.
\end{aligned}
\tag{1.76}
$$

In this case, h' and φ' would be the Higgs physical fields, being the first one the SM-Higgs. If we set $\lambda = 0$, we automatically close the portal, such that h' and φ' remain h and φ. As we can see, this model permits to study different portals independently by switching off a portal such as the scalar one.

1.2.3 Gauge Fields

Kinetic Terms

Now we need to study how the vector portal works by means of the kinetic mixing of the hypercharge field, B, with the X field. This mixing term is allowed by the theory and expected to be present. Just considering the Electroweak and Dark sectors, the kinetic terms for the gauge fields in the Lagrangian are:

$$
\mathscr{L}_{\text{kin}} = -\frac{1}{4} B_{\mu\nu} B^{\mu\nu} - \frac{\sin\chi}{2} B_{\mu\nu} X^{\mu\nu} - \frac{1}{4} X_{\mu\nu} X^{\mu\nu} - \frac{1}{2} W^+_{\mu\nu} W^{-\mu\nu} - \frac{1}{4} W^3_{\mu\nu} W^{3\mu\nu}\,. \tag{1.77}
$$

As can be seen, this Lagrangian is very similar to that introduced in

Eq. (1.1) for a generic vector portal. We report it here again for completeness with the notation used in [195].

After some work on the fields B and X, we can get rid of the mixed term:

$$\begin{aligned}
\mathscr{L}_{\text{kin}}^{B,X} &= -\frac{1}{4}(B_{\mu\nu} \quad X_{\mu\nu}) \begin{pmatrix} 1 & \sin\chi \\ \sin\chi & 1 \end{pmatrix} \begin{pmatrix} B_{\mu\nu} \\ X_{\mu\nu} \end{pmatrix} \\
&= -\frac{1}{4}(\overline{B}_{\mu\nu} \quad \overline{X}_{\mu\nu}) \begin{pmatrix} 1/\cos\chi & -\tan\chi \\ 0 & 1 \end{pmatrix} \begin{pmatrix} 1 & \sin\chi \\ \sin\chi & 1 \end{pmatrix} \begin{pmatrix} 1/\cos\chi & 0 \\ -\tan\chi & 1 \end{pmatrix} \begin{pmatrix} \overline{B}_{\mu\nu} \\ \overline{X}_{\mu\nu} \end{pmatrix} \\
&= -\frac{1}{4}\overline{B}_{\mu\nu}\overline{B}^{\mu\nu} - -\frac{1}{4}\overline{X}_{\mu\nu}\overline{X}^{\mu\nu} ,
\end{aligned} \tag{1.78}$$

where,

$$\begin{aligned}
\overline{B}_{\mu\nu} &= \cos\chi B_{\mu\nu} , \\
\overline{X}_{\mu\nu} &= \sin\chi B_{\mu\nu} + X_{\mu\nu} , \\
B_{\mu\nu} &= \sec\chi \overline{B}_{\mu\nu} , \\
X_{\mu\nu} &= -\tan\chi \overline{B}_{\mu\nu} + \overline{X}_{\mu\nu} .
\end{aligned} \tag{1.79}$$

In this way, the kinetic terms are already independent, as they should be to uncover the physical fields. However, the mass terms are still mixed and we need to work on them to find the physical fields after SSB.

Mass Terms

The mass terms for the gauge fields come from the covariant derivatives that act on the Higgs fields. After computing those and just considering the mass terms for the Electroweak and Dark sectors:

$$
\begin{aligned}
(D_\mu H)^\dagger (D^\mu H) + (D^x_\mu \Phi)^\dagger (D^{x\mu} \Phi) \supset & \Big(\frac{g v_H}{2}\Big)^2 W^+_\mu W^{-\mu} + \frac{g^2 v_H^2}{8} W^3_\mu W^{3\mu} \\
& - 2\Big(\frac{g g' v_H^2}{8}\Big) W^3_\mu B^\mu + \frac{g'^2 v_H^2}{8} B_\mu B^\mu \\
& + \frac{1}{2} g_X^2 v_\varphi^2 X_\mu X^\mu \,.
\end{aligned}
\tag{1.80}
$$

This Lagrangian can be worked out and we can obtain the following expression:

$$
\mathscr{L}_{\text{mass}} = \frac{\left(M_Z^{\text{SM}}\right)^2}{2} \begin{pmatrix} W^3_\mu & B_\mu & X_\mu \end{pmatrix} \begin{pmatrix} c_W^2 & -s_W c_W & 0 \\ -s_W c_W & s_W^2 & 0 \\ 0 & 0 & \mu^2 \end{pmatrix} \begin{pmatrix} W^{3\mu} \\ B^\mu \\ X^\mu \end{pmatrix} ,
\tag{1.81}
$$

where,

$$
\begin{aligned}
s_W &\equiv \sin\theta_W \equiv g'/\sqrt{g^2 + g'^2} \,, \\
c_W &\equiv \cos\theta_W \equiv g/\sqrt{g^2 + g'^2} \,, \\
M_Z^{\text{SM}} &\equiv \sqrt{g^2 + g'^2}\, v_H/2 \,, \\
\mu &\equiv \frac{2 g_X v_\varphi}{\sqrt{g^2 + g'^2}\, v_H} \,,
\end{aligned}
\tag{1.82}
$$

where θ_W is the Weinberg angle.

Now we need to replace the fields B_μ and X_μ by $\overline{B}_\mu$ and $\overline{X}_\mu$. After this replacement, a reordering of the fields and using the short notation for trigonometric expressions:

$$\begin{aligned}\mathscr{L}_{\text{mass}} &= \frac{\left(M_Z^{\text{SM}}\right)^2}{2}\begin{pmatrix}\overline{B}_\mu & W_\mu^3 & \overline{X}_\mu\end{pmatrix}\begin{pmatrix}\frac{s_W^2+\mu^2 s_\chi^2}{c_\chi^2} & -\frac{s_W c_W}{c_\chi} & -\mu^2 t_\chi \\ -\frac{s_W c_W}{c_\chi} & c_W^2 & 0 \\ -\mu^2 t_\chi & 0 & \mu^2\end{pmatrix}\begin{pmatrix}\overline{B}^\mu \\ W^{3\mu} \\ \overline{X}^\mu\end{pmatrix} \\ &= \frac{1}{2}\begin{pmatrix}\overline{B}_\mu & W_\mu^3 & \overline{X}_\mu\end{pmatrix} M \begin{pmatrix}\overline{B}^\mu \\ W^{3\mu} \\ \overline{X}^\mu\end{pmatrix}.\end{aligned} \tag{1.83}$$

To diagonalize M, we first note that we can perform the following useful rotation

$$\begin{aligned} R^y(\chi) &\equiv \begin{pmatrix} c_\chi & 0 & -s_\chi \\ 0 & 1 & 0 \\ s_\chi & 0 & c_\chi \end{pmatrix}, \\ R^z(\theta_W) &\equiv \begin{pmatrix} c_W & -s_W & 0 \\ s_W & c_W & 0 \\ 0 & 0 & 1 \end{pmatrix}, \\ V &\equiv R^y(\chi) R^z(\theta_W), \\ V^\dagger M V &= \left(M_Z^{\text{SM}}\right)^2 \begin{pmatrix} 0 & 0 & 0 \\ 0 & 1 & s_W t_\chi \\ 0 & s_W t_\chi & \mu^2/c_\chi^2 + s_W^2 t_\chi^2 \end{pmatrix}. \end{aligned} \tag{1.84}$$

The first diagonal entry corresponds to the photon: it has zero mass. The last step consists in a rotation on the YZ plane that finally diagonalizes the mass matrix:

$$
\begin{aligned}
R^x(\beta) &\equiv \begin{pmatrix} 1 & 0 & 0 \\ 0 & c_\beta & -s_\beta \\ 0 & s_\beta & c_\beta \end{pmatrix} , \\
R^x(\beta)^\dagger (V^\dagger M V) R^x(\beta) &= \begin{pmatrix} 0 & 0 & 0 \\ 0 & M_Z^2 & 0 \\ 0 & 0 & M_{Z'}^2 \end{pmatrix} , \\
\tan(2\beta) &= \frac{2 s_W t_\chi}{1 - s_W^2 t_\chi^2 - \mu^2/c_\chi^2} \, .
\end{aligned}
\tag{1.85}
$$

Now we can compute the physical masses in terms of β:

$$
\begin{aligned}
m_A^2 &= 0 \, , \\
M_Z^2 &= \left(M_Z^{\rm SM}\right)^2 \left(\frac{s_W^2 + c_W^2 c_\chi^2 + \mu^2}{2 c_\chi^2} + \frac{\sqrt{(s_W^2 + c_W^2 c_\chi^2 + \mu^2)^2 - 4 c_\chi^2 \mu^2}}{2 c_\chi^2} \right) \\
&= \left(M_Z^{\rm SM}\right)^2 \Big(1 + s_W t_\chi t_\beta \Big) \, , \\
M_{Z'}^2 &= \left(M_Z^{\rm SM}\right)^2 \left(\frac{s_W^2 + c_W^2 c_\chi^2 + \mu^2}{2 c_\chi^2} - \frac{\sqrt{(s_W^2 + c_W^2 c_\chi^2 + \mu^2)^2 - 4 c_\chi^2 \mu^2}}{2 c_\chi^2} \right) \\
&= \left(M_Z^{\rm SM}\right)^2 \left(1 - \frac{s_W t_\chi}{t_\beta} \right) .
\end{aligned}
\tag{1.86}
$$

After regarding all the transformations made, we finally arrive to the final relation between the initial fields and the physical ones:

$$\begin{pmatrix} B^\mu \\ W^{3\mu} \\ X^\mu \end{pmatrix} = \begin{pmatrix} 1/c_\chi & 0 & 0 \\ 0 & 1 & 0 \\ -t_\chi & 0 & 1 \end{pmatrix} R^y(\chi) R^z(\theta_W) R^x(\beta) \begin{pmatrix} A^\mu \\ Z^\mu \\ Z'^\mu \end{pmatrix},$$
$$\begin{pmatrix} B^\mu \\ W^{3\mu} \\ X^\mu \end{pmatrix} = \begin{pmatrix} c_W & -(s_\beta t_\chi + c_\beta s_W) & (s_\beta s_W - c_\beta t_\chi) \\ s_W & c_\beta c_W & -s_\beta c_W \\ 0 & s_\beta/c_\chi & c_\beta/c_\chi \end{pmatrix} \begin{pmatrix} A^\mu \\ Z^\mu \\ Z'^\mu \end{pmatrix}. \tag{1.87}$$

After these transformations are performed, we can now focus on how are the couplings of these physical fields with the fermions.

1.2.4 Charged Fermions Couplings

Let ψ_i be any fermion charged under the symmetries of the SM or the dark symmetry. The Lagrangian that describes the interactions of these fermions with the vector fields comes from the following term, when ignoring the $SU(3)_c$ gauge fields and the charged current $W^\pm$ fields:

$$\mathscr{L}^f = \overline{\psi}_i i \not{D} \psi_i = \overline{\psi}_i \left[i\not{\partial} - g' \frac{Y}{2} \not{B} - g Q_L^3 \not{W}^3 - g_X Q_X \not{X} \right] \psi_i \,. \tag{1.88}$$

Using the transformations from Eq. (1.87) and considering the relations $Q_e = \frac{Y}{2} + Q_L^3$ and $Y = Y_L P_L + Y_R P_R$, where $P_{R/L} = \frac{1}{2}(1 \pm \gamma^5)$ are the usual projectors onto the left- or right-handed components of the fermion fields, we obtain the following interaction Lagrangian:

$$
\begin{aligned}
-\mathscr{L}_I^f =& \overline{\psi}_i\gamma^\mu\Bigg[\frac{g'}{4}\Big(c_W A_\mu - (s_\beta t_\chi + c_\beta s_W)Z_\mu + (s_\beta s_W - c_\beta t_\chi)Z'_\mu\Big)\Big(Y_L(1-\gamma^5) + Y_R(1+\gamma^5)\Big) \\
&+ \frac{gQ_L^3}{2}\Big(s_W A_\mu + c_\beta c_W Z_\mu - s_\beta c_W Z'_\mu\Big)\big(1-\gamma^5\big) + g_X Q_X\Big(\frac{s_\beta}{c_\chi}Z_\mu + \frac{c_\beta}{c_\chi}Z'_\mu\Big)\Bigg]\psi_i\,.
\end{aligned}
\tag{1.89}
$$

The terms for each vector field is:

$$
\begin{aligned}
\mathscr{L}_{I,A}^f =& -eQ_e\overline{\psi}_i\gamma^\mu\psi_i A_\mu\,, \\
\mathscr{L}_{I,Z}^f =& \overline{\psi}_i\gamma^\mu\Bigg[-\Big\{\frac{e}{2s_W c_W}\Big((c_\beta + s_\beta s_W t_\chi)Q_L^3 + 2s_W(s_\beta t_\chi - c_\beta s_W)Q_e\Big) + g_X Q_X s_\beta/c_\chi\Big\} \\
&+ \frac{e}{2s_W c_W}\Big(c_\beta + s_\beta s_W t_\chi\Big)Q_L^3\gamma^5\Bigg]\psi_i Z_\mu\,, \\
\mathscr{L}_{I,Z'}^f =& \overline{\psi}_i\gamma^\mu\Bigg[\Big\{\frac{e}{2s_W c_W}\Big((s_\beta - c_\beta s_W t_\chi)Q_L^3 + 2s_W(c_\beta t_\chi - s_\beta s_W)Q_e\Big) - g_X Q_X c_\beta/c_\chi\Big\} \\
&- \frac{e}{2s_W c_W}\Big(c_\beta s_W t_\chi - s_\beta\Big)Q_L^3\gamma^5\Bigg]\psi_i Z'_\mu\,.
\end{aligned}
\tag{1.90}
$$

With the values of Q_L^3, Q_e and Q_X (which is 1 for the dark neutrino, ν_D), we can compute the precise interaction Lagrangian for each fermion straightforwardly. Let us see now how are the expressions for neutrinos more explicitly.

1.2.5 Neutrino neutral couplings

For flavor left-handed neutrinos, $Q_L^3 = 1/2$, $Q_e = 0$ and $Q_X = 0$. For those, we also need to add the following term, coming from $\overline{\nu}_D i\not{D}^x \nu_D$: $-\overline{\nu}_D g_X Q_X \not{X} P_L \nu_D$,

such that $X_\mu = \frac{s_\beta}{c_\chi} Z_\mu + \frac{c_\beta}{c_\chi} Z'_\mu$. Taking these terms into account, we finally obtain for the NC interaction with Z:

$$\begin{aligned}
\mathscr{L}_Z^\nu =& - \left(\frac{g}{2c_W} \Big(c_\beta + s_\beta s_W t_\chi \Big) \right) \overline{\nu}_\alpha \gamma^\mu P_L \nu_\alpha Z_\mu - \frac{s_\beta}{c_\chi} \overline{\nu}_D \gamma^\mu P_L \nu_D Z_\mu \,, \\
=& - \frac{c_\beta c_W M_Z^2}{M_W v_H} \overline{\nu}_\alpha \gamma^\mu P_L \nu_\alpha Z_\mu - \frac{s_\beta c_W M_Z M_{Z'}}{M_W v_\varphi} \overline{\nu}_D \gamma^\mu P_L \nu_D Z_\mu \,, \\
=& - M_Z \overline{\nu}_i \left[\frac{c_\beta c_W M_Z}{M_W v_H} U^*_{\alpha i} U_{\alpha j} + \frac{s_\beta c_W M_{Z'}}{M_W v_\varphi} U^*_{Di} U_{Dj} \right] \gamma^\mu P_L \nu_j Z_\mu \,.
\end{aligned} \tag{1.91}$$

If we now consider the neutrinos to be Majorana and following a straightforward prescription, we obtain the final result:

$$\begin{aligned}
\mathscr{L}_Z^\nu =& - \frac{M_Z}{2} \overline{\nu}_i \Big(C_{ij} P_L - C^*_{ij} P_R \Big) \gamma^\mu P_L \nu_j Z_\mu \,, \\
C_{ij} =& \frac{c_\omega}{v_H} U^*_{\alpha i} U_{\alpha j} - \frac{s_\omega}{v_\varphi} U^*_{Di} U_{Dj} \,, \\
c_\omega \equiv& \frac{c_\beta c_W M_Z}{M_W} \,, \\
s_\omega \equiv& - \frac{s_\beta c_W M_{Z'}}{M_W} \,.
\end{aligned} \tag{1.92}$$

Here, we are using the usual convention for trigonometric functions. We could also demonstrate that $s_\omega^2 + c_\omega^2 = 1$. We could do the same process for the interactions through Z':

$$
\begin{aligned}
\mathscr{L}^{\nu}_{Z'} =& -\left(\frac{g}{2c_W}\Big(c_\beta s_W t_\chi - s_\beta\Big)\right)\overline{\nu}_\alpha\gamma^\mu P_L\nu_\alpha Z_\mu - \frac{c_\beta}{c_\chi}\overline{\nu}_D\gamma^\mu P_L\nu_D Z'_\mu\,,\\
=&\frac{s_\beta c_W M^2_{Z'}}{M_W v_H}\overline{\nu}_\alpha\gamma^\mu P_L\nu_\alpha Z_\mu - \frac{c_\beta c_W M_Z M_{Z'}}{M_W v_\varphi}\overline{\nu}_D\gamma^\mu P_L\nu_D Z'_\mu\,,\\
=&M_{Z'}\overline{\nu}_i\left[\frac{s_\beta c_W M_{Z'}}{M_W v_H}U^*_{\alpha i}U_{\alpha j} + \frac{c_\beta c_W M_{Z'}}{M_W v_\varphi}U^*_{Di}U_{Dj}\right]\gamma^\mu P_L\nu_j Z'_\mu\,.
\end{aligned}
\tag{1.93}
$$

Considering the neutrinos as Majorana fields, we finally obtain:

$$
\begin{aligned}
\mathscr{L}^{\nu}_{Z'} =& -\frac{M_{Z'}}{2}\overline{\nu}_i\Big(D_{ij}P_L - D^*_{ij}P_R\Big)\gamma^\mu P_L\nu_j Z'_\mu\,,\\
D_{ij} =&\frac{s_\omega}{v_H}U^*_{\alpha i}U_{\alpha j} + \frac{c_\omega}{v_\varphi}U^*_{Di}U_{Dj}\,.
\end{aligned}
\tag{1.94}
$$

1.2.6 Neutrino Masses

The mass terms of the Lagrangian for the neutrinos are the following:

$$
\begin{aligned}
-\mathscr{L}^{\nu}_{\text{mass}} &= y^\alpha_\nu(\overline{L}_\alpha\cdot\widetilde{H})N^C + \frac{\mu'}{2}\overline{N}N^C + y_N\overline{N}\nu^C_D\Phi + \text{h.c.}\\
&= \frac{y^\alpha_\nu}{\sqrt{2}}\begin{pmatrix}\overline{\nu}_\alpha & \bar{l}_\alpha\end{pmatrix}\begin{pmatrix}v_H\\0\end{pmatrix}N^C + \frac{\mu'}{2}\overline{N}N^C + \frac{y_N}{\sqrt{2}}\overline{N}\nu^C_D v_\varphi + \text{h.c.}
\end{aligned}
\tag{1.95}
$$

Let us define the following,

$$
\begin{aligned}
m_D &= \left[\frac{y^\alpha_\nu}{\sqrt{2}}v_H\right]^{\text{T}}\,,\\
\Lambda &= \left[\frac{y_N}{\sqrt{2}}v_\varphi\right]^{\text{T}}\,.
\end{aligned}
\tag{1.96}
$$

where each vector runs over α and N respectively. Keeping this in mind, the Lagrangian takes the form:

$$\mathscr{L}^{\nu}_{\text{mass}} = -\frac{1}{2}\begin{pmatrix}\overline{\nu_\alpha} & \overline{N} & \overline{\nu_D}\end{pmatrix}\begin{pmatrix}0_{3\times3} & m_D^{\mathrm{T}} & 0\\ m_D & \mu' & \Lambda^{\mathrm{T}}\\ 0 & \Lambda & 0\end{pmatrix}\begin{pmatrix}\nu_\alpha\\ N^C\\ \nu_D^C\end{pmatrix}. \tag{1.97}$$

The mass matrix can be diagonalized by blocks,

$$\widehat{M} = \begin{pmatrix}U_\alpha^{\mathrm{T}} & U_N^{\mathrm{T}} & U_D^{\mathrm{T}}\end{pmatrix}\begin{pmatrix}0_{3\times3} & m_D^{\mathrm{T}} & 0\\ m_D & \mu' & \Lambda^{\mathrm{T}}\\ 0 & \Lambda & 0\end{pmatrix}\begin{pmatrix}U_\alpha\\ U_N\\ U_D\end{pmatrix} = U^{\mathrm{T}}MU\,. \tag{1.98}$$

Just to realize the magnitudes of the masses, we can perform the computation for one generation of neutrinos in each block. First, we see that,

$$\begin{aligned} M' = (R^y_\alpha)^{\mathrm{T}} M R^y_\alpha &= \begin{pmatrix}0 & 0 & 0\\ 0 & \mu' & \sqrt{m_D^2+\Lambda^2}\\ 0 & \sqrt{m_D^2+\Lambda^2} & 0\end{pmatrix},\\ R^y_\alpha &= \begin{pmatrix}c_\alpha & 0 & s_\alpha\\ 0 & 1 & 0\\ -s_\alpha & 0 & c_\alpha\end{pmatrix},\\ \tan\alpha &= \frac{m_D}{\Lambda}\,. \end{aligned} \tag{1.99}$$

Then, we perform a last rotation to diagonalize the mass matrix completely,

$$\widehat{M} = (R^x_\delta)^{\mathrm{T}} M' R^x_\delta = \begin{pmatrix} 0 & 0 & 0 \\ 0 & c^2_\delta \mu' + 2 s_\delta c_\delta \sqrt{m^2_D + \Lambda^2} & 0 \\ 0 & 0 & s^2_\delta \mu' - 2 s_\delta c_\delta \sqrt{m^2_D + \Lambda^2} \end{pmatrix},$$
$$R^x_\delta = \begin{pmatrix} 1 & 0 & 0 \\ 0 & c_\delta & -s_\delta \\ 0 & s_\delta & c_\delta \end{pmatrix},$$
$$\tan(2\delta) = \frac{2\sqrt{m^2_D + \Lambda^2}}{\mu'}. \tag{1.100}$$

Therefore, the masses are

$$\begin{aligned} m_1 &= 0\,, \\ m_2 &= \frac{\mu'}{2}\left(1 + \frac{\mu'}{\sqrt{\mu'^2 + 4m^2_D + 4\Lambda^2}}\right) + 2\frac{m^2_D + \Lambda^2}{\sqrt{\mu'^2 + 4m^2_D + 4\Lambda^2}}\,, \\ m_3 &= \frac{\mu'}{2}\left(1 - \frac{\mu'}{\sqrt{\mu'^2 + 4m^2_D + 4\Lambda^2}}\right) - 2\frac{m^2_D + \Lambda^2}{\sqrt{\mu'^2 + 4m^2_D + 4\Lambda^2}}\,. \end{aligned} \tag{1.101}$$

1.2.7 Neutrino-Higgs interactions

There is another sector which must be considered: the neutrinos with the Higgs fields interactions. The Lagrangian is the following,

$$-\mathscr{L}^{\nu}_{\text{Higgs}} = \frac{y^\alpha_\nu}{\sqrt{2}} \overline{\nu}_\alpha N^C h + \frac{y_N}{\sqrt{2}} \overline{N} \nu^C_D \varphi + \text{h.c.} \tag{1.102}$$

Considering the Majorana nature of neutrino fields, we arrive to the final

form:

$$\begin{aligned}
\mathscr{L}^{\nu}_{\text{Higgs}} &= -\overline{\nu}_i\Big(\big(\Delta_h\big)_{ij}P_R + \big(\Delta_h\big)^*_{ij}P_L\Big)\nu_j h - \overline{\nu}_i\Big(\big(\Delta_\varphi\big)_{ij}P_R + \big(\Delta_\varphi\big)^*_{ij}P_L\Big)\nu_j\varphi\,,\\
\big(\Delta_h\big)_{ij} &= \frac{y^\alpha_\nu}{2\sqrt{2}}\Big(U^*_{\alpha i}U^*_{Nj} + U^*_{\alpha j}U^*_{Ni}\Big)\,,\\
\big(\Delta_\varphi\big)_{ij} &= \frac{y_N}{2\sqrt{2}}\Big(U^*_{Ni}U^*_{Dj} + U^*_{Nj}U^*_{Di}\Big)\,.
\end{aligned} \tag{1.103}$$

If $\lambda \neq 0$, then we need to replace the fields h and φ by the physical ones, h' and φ'. The transformations were already obtained,

$$\begin{aligned}
h &= c_\theta h' + s_\theta\varphi'\,,\\
\varphi &= -s_\theta h' + c_\theta\varphi'\,,\\
\tan(2\theta) &= \frac{\lambda v_H v_\varphi}{\lambda_\varphi v^2_\varphi - \lambda_H v^2_H}\,.
\end{aligned} \tag{1.104}$$

And therefore, the final Lagrangian is

$$\begin{aligned}
\mathscr{L}^{\nu}_{\text{Higgs}} =& -\overline{\nu}_i\bigg[\Big(\big(\Delta_h\big)_{ij}P_R + \big(\Delta_h\big)^*_{ij}P_L\Big)c_\theta - \Big(\big(\Delta_\varphi\big)_{ij}P_R + \big(\Delta_\varphi\big)^*_{ij}P_L\Big)s_\theta\bigg]\nu_j h'\\
&-\overline{\nu}_i\bigg[\Big(\big(\Delta_h\big)_{ij}P_R + \big(\Delta_h\big)^*_{ij}P_L\Big)s_\theta + \Big(\big(\Delta_\varphi\big)_{ij}P_R + \big(\Delta_\varphi\big)^*_{ij}P_L\Big)c_\theta\bigg]\nu_j\varphi'\,.
\end{aligned} \tag{1.105}$$

1.2.8 Phenomenology

We can have a clearer idea of the interactions of the dark photon by doing the following: after defining $\epsilon = \chi \times \cos\theta_W$, the main interactions of the dark photon are can be well approximated as:

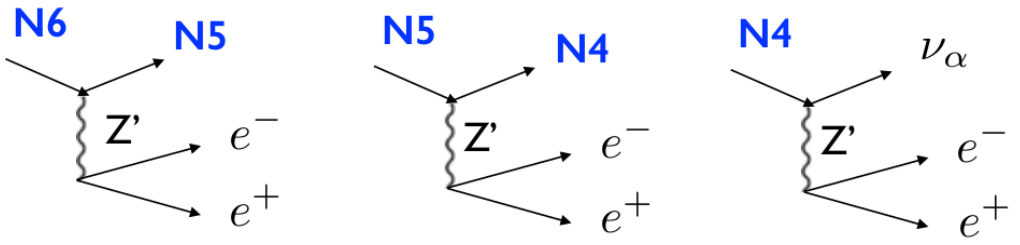

Figure 1.33: Diagrams of the decay of HNLs through the dark photon.

$$-\mathcal{L}_{Z'}^{(\text{int})} \supset \epsilon e Z'_\mu J^\mu_{(\text{EM})} + g_D U^*_{Di} U_{Dj} Z'_\mu J^\mu_{(\nu)} \ , \tag{1.106}$$

where $J^\mu_{(\text{EM})}$ and $J^\mu_{(\nu)}$ stand for the electromagnetic and the neutrino currents respectively, and we are considering that $m^2_{Z'} \ll m^2_Z$. Therefore, electromagnetic and neutrino can both interact through the dark photon, as we can see from the coupled fields in Eq. (1.106). That means that neutrinos can interact with ordinary matter through the dark photon.

The phenomenology of such a model depends critically on the hierarchy of the masses of the new particles, on the couplings and values of the masses and could be very varied. As a specific example, we present the parameters discussed in [88] as this offers an explanation for various anomalies, such as the MiniBooNE low energy excess (LEE), the value of $g-2$ of the muon. We consider a GeV scale for the new physics. Specifically, we fix the dark photon mass around 1.25 GeV and assume that at least 3 of the massive HNLs, N_4, N_5, N_6, are lighter than the dark photon.

We are regarding HNLs of masses of the order of $100s$ MeV. They can mainly decay through the dark photon into lighter neutrino states and an electron-positron pair with decay rates much faster than in the SM (plus HNL mixing).

This would be a major departure from "traditional" BSM through the

opening of three portals that are susceptible of being detected in current experiments. One can expect, for example, displaced vertices and decay chains, for which MicroBooNE, DUNE-ND and T2K would have excellent sensitivity. Also NA62 and SHADOWS could search for signals in kaon decays, while Belle II and BES III can look for signatures in dark photon searches through both invisible and semi-visible decays.

1.2.9 Experimental challenges

In order to better understand the role that models like the Three portal model could play in current particle physics problems, we will mention some of the examples in which these BSM extensions have been used in order to solve some of the current unexplained experimental results.

The MiniBooNE low energy excess

The MiniBooNE experiment sits on the Fermilab Booster Neutrino Beamline (BNB) and employs a 12.2 m diameter Cherenkov detector filled with 818 tons of pure mineral oil, located 541 m away from a beryllium target. It ran in both neutrino mode, with a forward-horn-current (FHC), and anti-neutrino mode, with a reverse-horn-current (RHC). Over a span of 17 years, MiniBooNE observed a large low-energy excess (LEE) of electron-like events. The first excess was reported in neutrino mode, between the years 2007-2009. For a total of 6.46×10^{20} Protons-on-target (POT), an excess of 128.8 ± 43.4 electron-like events was observed over the background with a significance of 3.0σ [57]. This excess was predominantly present in the $200\text{MeV} < E_\nu^{\text{QE}} < 475\text{MeV}$ energy region. It was subsequently observed that an excess of comparable significance (2.8σ) was also present in the anti-neutrino mode, with 78.4 ± 28.5 excess events observed over the back-

ground between the energies $200\text{MeV} < E_\nu^{\text{QE}} < 1250\text{MeV}$ and for 11.27×10^{20} POT [59, 62]. Following these tantalizing hints of new physics, the collaboration increased the data in neutrino mode, nearly doubling the POT, while improving the background analysis and reducing the systematic uncertainties. This led to a substantial increase in the significance of the observations, with the $\sim 3\sigma$ excess rising to 4.7σ [63], and most recently to 4.8σ [65]. The combined neutrino and anti-neutrino mode excess currently stands at $638.0 \pm 52.1(\text{stat.}) \pm 122.2(\text{syst.})$ electron-like events.

The striking 4.8σ excess of low-energy electron-like events (LEE) observed at MiniBooNE [54, 57, 62] challenges our understanding of the neutrino sector at GeV energies. This excess has been scrutinized throughout the literature, with some authors pointing to combinations of effects that could reduce its significance to the order of 3 σ [197, 198]. At this time, it is fair to say that the origin of the LEE remains utterly unknown.

A new generation of experiments with improved particle-identification (PID) capabilities has started to test the origin of the LEE. The first tests came from the MicroBooNE experiment, which used a 170-ton Liquid Argon Time Projection Chamber (LArTPC) in the same beam, the Booster Neutrino Beamline (BNB) as MiniBooNE. Two additional detectors will add to the Short-Baseline Neutrino (SBN) program, the Icarus detector, a 760 ton detector located 600 m from the BNB target, and the Short-Baseline Near Detector (SBND), with a 112-ton active volume at a shorter distance, 110 m away.

We leave the explanation of the role of dark sectors in explaining MiniBooNE excess to Chapter 2.

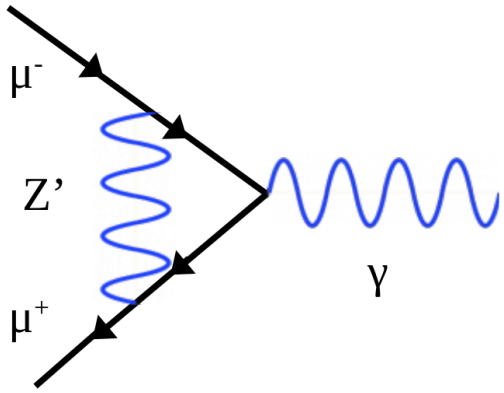

Figure 1.34: Contribution of the dark photon to the anomalous magnetic moment of the muon.

$(g-2)_\mu$ anomaly

There is a longstanding discrepancy between the measured value of $(g-2)_\mu$ and the theoretical prediction at 4.2 σ. Given that $a_\mu \equiv (g-2)_\mu/2$, then $\Delta a_\mu \equiv a_\mu^{\text{exp}} - a_\mu^{\text{th}} = (274 \pm 73) \times 10^{-11}$ [199].

One way to explain this anomaly is through contributions from a dark photon: whether emerging from super-symmetric extensions [200] or just as a sector with weak admixture to photons [201], or by kinetic mixing and a light vector broken symmetry. The dark boson contribution, which is presented in Fig. (1.34), could explain this discrepancy. Taken into account current constraints, this explanation is allowed if dark photons decay semivisibly, i.e. they decay fast into visible particle and some missing energy [196, 202]. If the missing energy is not too much, collider bounds, in particular from BaBar, can be relaxed and a viable region opens up at the $\mathcal{O}$(1GeV) range [196], in the same range needed to explain the MiniBooNE LEE.

1.3 Summary

As we have seen along the present chapter, dark sectors offer rich and vast opportunities to search for physics BSM. The diversity of the realization of many of the fields that can be considered, such as dark photons or HNLs, make constraints quite dependent on the different interactions that are allowed to take place. This variety makes dark sectors a powerful tool to address some of the problems that cannot be explained just by taking the SM into account. In the next chapter, we will show how dark sectors can be used to explain MiniBooNE low energy excess, though the possibilities opened up by these dark extension go far beyond. Let us recapitulate some of the strengths:

- The broad range of masses that can be considered allow to explore different regions in parameter space. The dark photon could be a massless vector or a really heavy one. Although HNLs are constrained from below, still low couplings allow us to explore from very low masses to really heavy ones.

- There are many kinds of interactions that can be explored with dark sectors and that are expressed in the types of portals we can allow: from kinetic mixing of vector fields to neutrino mixing or even scalar interactions. There are also higher dimensional operators that can be explored, such as the transitions magnetic moments of neutrinos and HNLs, topic that will be mentioned in the next chapter.

- The power of dark sectors relies on the possibility of having strong interacting dark fields that talk to the SM through portals characterized by weak interactions, which are suppressed by the couplings themselves

(like the kinetic mixing) or by the mixing with SM fields (like neutrino mixing). This last characteristic is needed not to alter what the SM already explains: strong interactions directly with the SM would imply a visible contribution over the SM one. However, strong interactions just among dark fields is not directly excluded and it allows a broader search into different decay scenarios among dark particles.

- Even though dark sectors do not constitute necessarily dark matter, that does not mean we can also regard them as such or make them be part of how dark matter could interact with the SM.

Now we can continue with the next chapter, where we will consider dark sectors to try to understand what might be missing in the last results of the MiniBooNE experiment.

Chapter 2

Dark sectors and MB-LEE

Significant anomalies in neutrino experiments have persisted for over two decades, with no conclusive resolution in or outside the Standard Model. The most statistically significant of these is the apparent $\nu_\mu \to \nu_e$ conversion of neutrinos and antineutrinos at short baselines in the MiniBooNE experiment [54, 57, 62] and the Liquid Scintillator Neutrino Detector (LSND) [203]. We will search for a possible explanation of such anomaly in a rich dark sector model and we will characterize the required parameter space.

2.1 Introduction

The excess at MiniBooNE, dubbed the low-energy excess (LEE), is characterized by electron-like events in the energy region between 200 MeV and 600 MeV and is coincident in time with the $\langle E_\nu \rangle \sim 800$ MeV neutrino beam. More detailed background studies and data have become available over the years, increasing the significance of the excess to a total of 4.8σ [63, 65]. The origin of LEE has been debated in the literature, with some authors pointing to combinations of effects that could somewhat reduce its signifi-

cance [197, 198]. However, at this time, it is accurate to say that the origin of the LEE remains unknown and that its statistical significance remains strong. Therefore, MiniBooNE LEE is certainly an appropriate scenario to look for hidden physics.

Historically, the most studied BSM explanation to the MiniBooNE LEE has been the 3+1 oscillation model, where an eV-scale sterile neutrino induces short-distance $\nu_\mu \to \nu_e$ oscillations. Other anomalies, including the LSND result and electron-neutrino disappearance gallium experiments [204–210], have also been linked to the LEE under the sterile neutrino hypothesis. This paradigm, however, is in strong tension with cosmology [211–213] and ν_μ-disappearance data [214–216]. In fact, the internal tension in sterile neutrino global fits is significant and driven not by one but multiple experiments [217, 218]. In addition, the LSND and the gallium experiments rely on different principles of operation than MiniBooNE, and, therefore, it is not unlikely that the resolution to each of these anomalies is unrelated. As such, we focus uniquely on the MiniBooNE LEE and its potential solutions in new physics models.

The MiniBooNE detector could not distinguish between the Cherenkov emission of electron and photon showers inside the detector. Therefore, the LEE can be due to multiple kinds of electromagnetic final states, including electrons, photons, and combinations thereof. Therefore, this opens us to rich families of dark sectors BSM. One important class of backgrounds at MiniBooNE arises from photon production in neutrino-nucleus neutral-current (NC) interactions through coherent or resonant processes. Other proposed solutions rely on non-resonant photons, photon pairs, or electron-positron pairs produced inside the detector in coincidence with the neutrino beam. When highly collimated or highly energy-asymmetric, the pairs of

electromagnetic particles can be misreconstructed as a single electron. Several beyond-the-SM explanations have exploited this ambiguity in signal reconstruction. These non-oscillatory explanations are easily embedded in low-scale extensions of the SM, where new dark particles of MeV to GeV masses mediate the production of or decay into electromagnetic activity. We provide an overview of such dark sector physics interpretations of the MiniBooNE LEE and discuss their current status. For a review of broader aspects of short-baseline phenomenology, we point the reader to Ref. [219]. While our discussion is focused primarily on MiniBooNE, our list of particle production modes in neutrino scattering can be applied to other neutrino experiments searching for new physics.

To disentangle the possible nature of the LEE, the Short-Baseline Neutrino (SBN) program at Fermilab is underway and has started to probe a few interpretations of the excess [220, 221]. The program consists of three modern detectors in the Booster Neutrino Beam (BNB), where MiniBooNE was also located. Thanks to the improved particle-identification (PID) capabilities of the Liquid Argon Time-Projection Chambers (LArTPCs), the SBN program has greater discriminating power between electron and photon-like events. The first detector to run in the BNB was the MicroBooNE experiment, a 170 t active-volume detector at 470 m away from the target. Two additional detectors are part of SBN: the Icarus detector, currently in operation and with a much larger fiducial mass of 760 t located 600 m from the BNB target, and the Short-Baseline Near Detector (SBND), with a 112-t active volume at a shorter distance, 110 m away. Recent data from MicroBooNE shows no excess of ν_e events [222–225], but it could not yet fully exclude the 3+1 oscillation picture [67, 226, 227] (see also [228]). The MicroBooNE experiment has also tested the radiative Δ decays hypothesis and

excluded it at the 94% confidence level (C.L.) [229]. The constraint is driven primarily by events with a photon associated with a proton vertex, so non-resonant sources of photons remain largely unconstrained due to the larger backgrounds. Furthermore, LEE explanations based on exotic sources of electron-positron pairs [194, 230–235] or photon pairs [232] are still largely untested.

As a characteristic example of a model where e^+e^- final states explain the LEE, we study the so-called dark neutrino explanation [194, 230]. These models are based on low-scale seesaw mechanisms embedded in a dark sector. The heavy neutral leptons (HNLs) can explain neutrino masses and have new interactions with ordinary matter through light vector or scalar mediators. The mediators enhance the production of HNLs in neutrino-nucleus upscattering and allow them to quickly decay into visible final states inside neutrino detectors. We perform a detailed fit to the MiniBooNE energy distribution for models with a dark photon mediator and one and two HNLs that decay into e^+e^- pairs. This is the first comprehensive fit to the MiniBooNE LEE in the context of an e^+e^- interpretation and will allow other neutrino experiments to perform direct tests of this hypothesis. Our analysis is based on our own simulation of the MiniBooNE experiment in the publicly-available generator `DarkNews` [236].[1]

This chapter is divided as follows. In Section 2.2, we review the MiniBooNE LEE and its properties. In Section 2.3, we discuss the status of different dark sector models proposed to explain the excess. We then turn our focus to dark neutrino models in Section 2.4, where we present the results of our fit to the MiniBooNE energy spectrum. We conclude in Section 2.5.

[1] github.com/mhostert/DarkNews-generator.

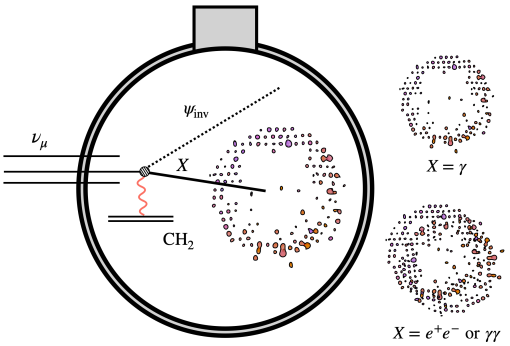

Figure 2.1: Different scenarios where a new particle X can mimic the ν_e appearance signal in the MiniBooNE Cherenkov detector.

2.2 The MiniBooNE low-energy excess

The MiniBooNE experiment was located in the Fermilab BNB and employed a 12.2 m diameter Cherenkov detector filled with 818 tons of pure mineral oil, located 541 m away from the beryllium target. It ran in neutrino mode, with a forward-horn-current (FHC), and anti-neutrino mode, with a reverse-horn-current (RHC). Over a span of 17 years, MiniBooNE observed a large excess of low-energy electron-like events. The first excess was reported in neutrino mode between 2007 and 2009. For a total of 6.46×10^{20} Protons-on-target (POT) in neutrino mode, an excess of 128.8 ± 43.4 electron-like events was observed over the background with a significance of $3.0\,\sigma$ [57]. The excess was predominantly present in the 200 MeV $< E_\nu^{\rm QE} <$ 475 MeV energy region. It subsequently also observed in anti-neutrino mode with a comparable significance of 2.8σ, corresponding to 78.4 ± 28.5 excess events observed over the background in the energy range 200 MeV $< E_\nu^{\rm QE} <$ 1250 MeV for a total of 11.27×10^{20} POT [59, 62]. The experiment then collected nearly double the amount of POT in neutrino mode, improving the background analysis and reducing systematic uncertainties. This led to a substantial increase in the significance of the LEE, with the $\sim 3\,\sigma$ excess rising to $4.7\,\sigma$ [63], and

most recently to $4.8\,\sigma$ [65]. The combined neutrino and anti-neutrino mode excess currently stands at $638.0 \pm 52.1(\text{stat.}) \pm 122.2$ (syst.) electron-like events.

Charged particles in the MiniBooNE detector produce directional Cherenkov light and isotropic scintillation light. Due to the limited PID capabilities of Cherenkov detectors, the signals of electrons, photons, and collimated e^+e^- and $\gamma\gamma$ pairs are too similar to differentiate. Fortunately, the dominant electromagnetic backgrounds at MiniBooNE are constrained with *in-situ* measurements. The beam's intrinsic ν_e content is constrained by ν_μ CC rate measurements. This is particularly relevant at higher energies, where kaon decays at the target dominate the neutrino flux. The kaon production rate was directly measured by SciBooNE [237], which operated at 100 m from the BNB target for a fraction of the total MiniBooNE lifetime. SciBooNE was also used to constrain ν_μ disappearance in the BNB beam in combination with MiniBooNE data [61, 238].

The π^0 production rate is inferred by measuring separated $\gamma\gamma$ pairs [56, 58]. Given the π^0 kinematics and the Monte-Carlo, this allowed MiniBooNE to directly constrain the number of π^0s that decayed to collinear or highly energy-asymmetric photons, as well as the number of photon pairs where one of the photons was absorbed or escaped undetected. In addition, the π^0 and $\pi^\pm$ rates that are measured by MiniBooNE constrain the production of the $\Delta(1232)$ resonance, which in turn constrains the rate of single photon events from radiative $\Delta(1232)$ decay. This constraint, however, is subject to uncertainties on the $\Delta(1232)$ radiative decay branching ratio. Nonetheless, an enhancement of this rate to the level necessary to explain the LEE is in conflict with theoretical predictions [239] and with recent MicroBooNE data [229].

In addition to the low-energy nature of the excess, the most prominent features of the LEE are the following:

1. **Angular spectrum**: The LEE shows a mild preference for forward-going events, although it is still broadly distributed in the angular variable θ_{beam}, the angle of the electron-like shower with respect to the neutrino beam. Approximately 72% of events have a reconstructed angle satisfying $\cos\theta_{\text{beam}} \leq 0.9$.

2. **Radial profile**: The radial distribution of the excess events is consistent with neutrino interactions inside the tank. The significance of the excess also increases when decreasing the radius of the fiducial volume.

3. **Timing**: Most excess events occur within the first 8 ns of bunch timing, coinciding with neutrino scattering events in the detector.

These considerations provide significant constraints on potential LEE mechanisms. Quantifying the constraining power of the aforementioned distributions is challenging outside the collaboration due to the lack of a correlation matrix, but one can conclude that the radial and timing information indicates a preference for a neutrino-induced excess. Additional constraints come from the search for sub-GeV dark matter performed by the MiniBooNE-DM collaboration [64]. The experiment ran in beam-dump mode, directing protons away from the beryllium target and toward the steel absorber at the end of the decay pipe, 50 m away. Consequently, the beam-dump mode had a smaller and softer neutrino flux, allowing non-neutrino signals to be explored. No excess was observed in this search, excluding explanations where new particles are produced in neutral meson decays at the target. Due to suppressed off-target production of charged mesons, reciprocal models with charged mesons are still allowed, up to the signal considerations discussed

above. For a detailed discussion of the role of the angular distribution and of the beam-dump mode data on new-physics interpretations of the LEE, see Ref. [240].

Category	Model	Final state	LEE signal properties			References
			energy dist.	angular dist.	timing	
Flavor transitions	SBL oscillations	e^-	✓	✓	✓	Reviews and global fits [217–219, 241, 242]
	SBL oscillations with invisible sterile decay	e^-	✓	✓	✓	[243, 244]
	SBL oscillations with anomalous matter effects	e^-	✓	✓	✓	[245–250]
	neutrino-flavor-changing bremsstrahlung	e^-	✓	–	✓	[251]
Decays in flight	SBL oscillations with visible sterile decay	e^-	✓	✓	✓	[252–256]
	heavy neutrino decay	γ / e^+e^- / $\gamma\gamma$	✓	✗	✗	[257, 258]
Scattering	neutrino-induced upscattering	γ / e^+e^- / $\gamma\gamma$	✓	✗	✓	DS [88, 194, 196, 230–234, 259], TMM [158, 260–269]
	dark particle-induced upscattering	γ / e^+e^- / $\gamma\gamma$	✓	✗	✓	[270]

Table 2.1: New physics explanations of the MiniBooNE excess categorized by the origin of the electron-like signature and underlying mechanism. Notation: ✓– the model can naturally explain the feature, ✗– the feature poses a strong limitation on the model. SBL stands for "short-baseline".

2.3 New physics explanations

There are four classes of final states that have the potential of explaining the MiniBooNE low-energy excess: e^-, γ, e^+e^- and $\gamma\gamma$. These could be produced by different mechanisms within or beyond the SM. For each of these final states, we discuss how these signals may appear in new-physics models. We summarize our discussion in Table 2.2.

2.3.1 Single electron

The MiniBooNE results have been initially interpreted as an excess of ν_e ($\overline{\nu}_e$) that undergo CC scattering. The electrons (positrons) would be detected as single *fuzzy* Cherenkov rings in the MiniBooNE detector. Such an excess of neutrinos in the beam can be due to a mis-modelling of the flux, or from a BSM phenomenon. One popular new-physics interpretation of the excess is that of short-baseline neutrino oscillation induced by a new sterile neutrino of eV mass. This hypothesis gained significant traction due to the natural connection between the LSND anomaly and the MiniBooNE results, as well as due to other deviations observed in the ν_e disappearance sector, all of which share similar values of L/E. The LSND experiment observed a 3.8σ excess of $\overline{\nu}_e$ in a π decay at rest (DAR) neutrino source. The antineutrinos were detected via inverse-beta-decay (IBD) in the liquid scintillator of the detector. The different operating principles of the two experiments combined with the similar L/E suggested that a common explanation could be found in novel oscillations. We discuss the recent developments regarding this hypothesis below and briefly review some alternatives to pure oscillatory models.

The MicroBooNE detector performed the first test of the LEE under the single-electron hypothesis in LAr using the same beam as MiniBooNE. The

first analysis aimed to constrain the template of the MiniBooNE LEE with three independent ν_e event selections [222–225]. The template is defined as the difference between the central value of the data minus the central value of backgrounds as a function of the reconstructed neutrino energy. This, in turn, can be unfolded into an excess flux of ν_e in the BNB and constrained by MicroBooNE data. We review the findings of this search and comment on important caveats below. In the MicroBooNE's LArTPC detector, protons can be observed as tracks, and the signal contributes to either the $1s1t$ or $1s0t$ topologies.[2] Using a deep-learning-based reconstruction approach, one analysis searched for the exclusive $1e1p$ CCQE channel finding a modest deficit with respect to predictions [223]. A second analysis searched for pionless ν_e scattering using Pandora-based reconstruction in the exclusive channels $1e\mathrm{N}p0\pi$ (N>0) and $1e0p0\pi$ [224]. While a mild deficit was observed in the $1e\mathrm{N}p0\pi$ channel, an excess was present in the $1e0p0\pi$ channel. The latter, however, has a much lower ν_e purity due to photon backgrounds, so it is less sensitive to the single electron hypothesis. The third and highest statistics search was for inclusive $1eX$ ν_e events using the Wire-Cell reconstruction method [225]. Good agreement between data and prediction is observed, and the fixed LEE template is excluded at 3.75σ. Combining all aforementioned channels, except the less-sensitive $1e0p0\pi$ one, MicroBooNE rejects the fixed LEE ν_e template at $> 97\%$ C.L. This translates into an upper limit on the ν_e composition of the MiniBooNE excess, corresponding to $< 51\%$ at 95% C.L.

Two important caveats to the MicroBooNE model-agnostic template analysis were that i) it used a fixed template for LEE and ii) it did not exclude physical models, opting instead to work with a model-agnostic approach. The first point, in particular, is critical as the uncertainties on the tem-

[2] As both electrons and photons are reconstructed as showers, it is customary to use the notation NsMt to specify a topology containing N showers and M tracks.

plate's shape can be large due to the significant systematics and correlations in the MiniBooNE background prediction. In addition, physical models that attempt to explain the anomaly can also have significantly different shapes from the nominal template and still provide a reasonable fit to the data, thanks to the large systematic uncertainties. The significance of the shape uncertainties and the exclusion power of MicroBooNE in the parameter space of 3+1 oscillation models were discussed in detail in Ref. [226]. MicroBooNE has subsequently searched for short-baseline oscillations [271], excluding a considerable part of the sterile neutrino parameter space that can explain the MiniBooNE and LSND results, but not fully ruling out this interpretation. Finally, it has also been pointed out that if the MiniBooNE excess is predominantly composed of antineutrinos (in neutrino mode), the constraints posed by LAr experiments become significantly weaker due to the smaller antineutrino-argon cross sections [272].

We also briefly comment on other measurements of ν_e events at MicroBooNE. In particular, the differential ν_eCC cross section on Argon has been measured using neutrinos from the BNB [273] as well as from the NuMI beam [274, 275]. These measurements still have large statistical and systematic uncertainties, especially in the NuMI neutrino flux prediction, which it can be as large as 20% at the lowest energies ($E_\nu < 300$ MeV). The mean energy of NuMI flux in both analyses is similar to that of Booster neutrinos, and the baseline varies between 679 m, the distance between the NuMI target and MicroBooNE, and 100 m, the distance between the NuMI absorber and MicroBooNE. With increasing statistics, this flux can become an auxiliary tool to explore different L and E configurations, especially relevant for oscillation searches [271].

Sterile-driven short-baseline oscillations

We start the ν_e interpretations of the MiniBooNE excess within the 3+1 model of neutrino oscillations. A mostly-sterile mass eigenstate with $m_4 \gtrsim 1$ eV is introduced, leading to oscillations at $L/E \sim 1$ km/1 GeV, where L is the baseline of the experiment and E the neutrino energy. This interpretation is related to other anomalies in neutrino data, which share similar values of L/E. Of particular relevance is the prediction that the $\nu_\mu \to \nu_e$ appearance signal at MiniBooNE and LSND should be accompanied by ν_e and ν_μ disappearance in sterile-driven oscillation models. We briefly review the status of these two channels below.

Some electron-neutrino and antineutrino experiments have observed a deficit of events compatible with sterile-driven neutrino $\nu_e/\overline{\nu}_e$ disappearance. An overall deficit of $\overline{\nu}_e$ rates at reactor experiments [276], dubbed the reactor antineutrino anomaly (RAA), was observed when incorporating the Huber-Müeller reactor antineutrino flux calculations [277, 278]. Since then, newer calculations of the reactor antineutrino flux have diluted the statistical significance of the RAA [279]. New data on the beta spectrum of ^{235}U and ^{239}Pu collected at the Kurchatov Institute [280] showed that data-driven reactor flux models based on data from ILL [281–284] were overestimating the total number of neutrinos [279, 285]. This interpretation was recently corroborated by the STEREO reactor experiment [286] and resolved the RAA.

Reactor experiments that can measure ratios of event rates at different baselines have better control of the flux systematics. Dedicated searches for sterile neutrinos were performed by the PROSPECT [287, 288], STEREO [286, 289, 290], and DANSS [291] experiments, as well as by the RENO and NEOS collaborations [292]. All these searches reported null results. Neutrino-4 [293], on the other hand, claims evidence for sterile neutrinos at a sig-

nificance of larger than 4σ. The interpretation of their results has been criticized in the literature [294]. In Ref. [295], the authors claim that the Neutrino-4 results can only be reproduced when neglecting the detector energy resolution. Their analysis brings the significance of the excess to as low as 2.2σ, preferring significantly larger and already-excluded mixing angles.

Another anomaly is the deficit of ν_e observed in gallium experiments when exposing the detectors to radioactive sources [296, 297]. This anomaly has been observed in a modern setup by the BEST experiment [298]. These experiments have low sensitivity to the oscillation frequency (Δm^2_{41}) due to poor spatial resolution but they observe an overall significant deficit in the expected ν_e rate. A sterile-driven ν_e disappearance explanation, however, requires large mixing angles with electron-neutrinos, around $|U_{e4}|^2 \sim 0.07$, and is in tension with measurements of the total solar neutrino flux [299]. No consensus has been reached yet on the cause of this anomaly — for recent reviews on the topic, see Refs. [300–302]. Global fits to the reactor and gallium experiment data find that the strongest evidence for anomalous ν_e disappearance comes from BEST and Neutrino-4; no satisfactory agreement among all data in a 3+1 oscillation model was observed [300, 303].

In the muon sector, ν_μ disappearance is not observed by accelerator experiments [61, 238, 304]. The most significant constraint was placed by the MINOS/MINOS+ collaboration [214], surpassing other existing limits by over an order of magnitude. However, their results, especially their sensitivity to averaged-out oscillations, have been questioned in the literature [218, 305]. Despite this, no independent study has been performed to address the issues raised. An independent limit on ν_μ disappearance comes from atmospheric muon-neutrinos that would oscillate due to a sterile-neutrino-induced parametric resonance inside the Earth. This effect is constrained by Ice-

Cube [215, 216] and excludes a significant portion of the sterile neutrino parameter space around $\Delta m^2 \sim 1$ eV^2. In the tau sector, data and constraints on ν_τ appearance are scarce and come mostly from atmospheric neutrino experiments. At accelerators, OPERA set direct limits on $|U_{\tau 4}|^2$ through a search for $\nu_\mu \to \nu_\tau$ appearance [306, 307]. In the future, IceCube [308] and KM3NET [309] could improve on these direct searches. Indirect limits have been obtained with searches for the disappearance of active neutrinos via neutral-current interactions. This strategy was pursued at NOνA [310, 311] and can also be used in the LAr program at FNAL [312]. Other direct probes of sterile neutrinos include searches for anomalous kinks in the beta spectrum of tritium at the KATRIN experiment [313], which are sensitive to the $|U_{e4}|^2$ mixing angle.

Light sterile neutrinos are strongly constrained by cosmology as they would have thermalized with the SM bath in the early Universe and count as additional relativistic species at Big Bang Nucleosynthesis [69, 213, 314]. Extensions to the minimal 3+1 model have proposed to reconcile the model with cosmology [255, 315–325]. The general idea consists of suppressing the production of the light sterile neutrinos in the early Universe. This can be achieved by the so-called secret-interaction mechanism, in which strong self-interactions between sterile neutrinos (or between sterile neutrinos and an ultra-light dark matter background) create a large matter potential for the sterile flavor and suppress their mixing with light neutrinos at early times. Other proposals have also been put forward, showing that lowering the reheating temperature to a few MeV can avoid the thermalization of light sterile neutrinos [318, 326].

It is also possible that short-baseline oscillations are induced by more than just one sterile neutrino. In addition to the even larger number of relativistic

degrees of freedom in the early Universe, this solution is not immune to the tension between appearance and disappearance datasets [327]. Global fits still find a significant internal tension in 3+2 model [218, 328–331].

In conclusion, sterile neutrino models face significant challenges in explaining global neutrino data, and their existence is also in stark contradiction with standard cosmological models. A solution to this conundrum requires additional new physics in the neutrino sector and/or non-standard cosmologies. More data from the SBN program will be essential to test the sterile neutrino interpretation of MiniBooNE directly by means of measurements of the ν_e spectrum at the different baselines of MicroBooNE, SBND, and ICARUS [220, 332].

Anomalous matter effects

The non-standard interactions (NSI) framework provides a phenomenological parameterization of deviations from the ordinary matter potential experienced by neutrinos in matter [333]. While NSIs alone cannot generate new flavor transitions at short baselines, several works in the literature have studied their impact on sterile neutrino-driven oscillations [334]. NSIs can suppress oscillations at large energies, where $2E_\nu V > \Delta m^2_{41}$ with V a new matter potential for neutrinos, relaxing constraints from MINOS/MINOS+ [335] due to the higher energy of the NuMI beam. In addition, the energy of the active-sterile transition resonance used to search for sterile neutrinos at IceCube can be lowered. Even though IceCube is less sensitive to BSM effects at low energies [336], the authors of Ref. [337] conclude that existing IceCube data already rules this possibility out. The new matter potential can be associated with new interactions in the ν_μ and ν_τ sectors [338], with new interactions between sterile neutrinos and ordinary matter [339], or interac-

tions between sterile neutrinos and a dark matter background [340]. The typical values of NSIs required for the aforementioned scenarios are large, typically bigger than a few percent of G_F. They are, therefore, strongly constrained by high-energy neutrino and global data (see [333]).

Anomalous matter potentials can also induce new resonances at short-baseline experiments, akin to the Mikheyev-Smirnov-Wolfenstein (MSW) effect. In this case, the appearance signal can be sharply peaked at the resonant energy and would explain the low energy nature of the MiniBooNE excess. A first proposal was based on an anomalous matter potential sourced by the cosmic neutrino background [248]. However, this idea requires an unrealistic local overdensity of cosmic neutrinos. Ref. [249] also concludes that this scenario is excluded by the different measurements of Δm^2_{31} across the different energy scales of T2K, NOVA, MINOS, and atmospheric experiments. Another possibility is that the matter potential is sourced by ordinary matter and that it exclusively impacts the new sterile neutrino, referred to as a quasi-sterile neutrino in Ref. [250]. In this case, stronger-than-Weak interactions between quasi-sterile neutrinos and matter particles are required to produce the matter potential.

Decaying sterile neutrinos

Heavy, mostly-sterile neutrinos can be produced via mixing in meson decays and subsequently decay in flight into light neutrinos between the source and the detector [252–255]. This decay can proceed through a light scalar particle, for instance, $\nu_4 \to \nu_i \varphi$, with $i < 4$, which can also participate in the secret-interaction mechanism that suppresses ν_4 production in the early Universe. Typically, $m_\varphi + m_{\nu_i} < m_4$ such that ν_4 decays via two-body decays with a lifetime shorter than the short-baseline distances. In some models, the scalar

particle can decay, $\varphi \to \nu_i \overline{\nu}_j$, enhancing the final number of neutrinos [255]. For Dirac neutrinos, the ν_4 and φ decays may be into left(right)-handed (anti)neutrinos, in which case it is referred to as visible or into non-interacting right(left)-handed (anti)neutrinos, in which case it is called invisible since the new decays are unobservable. The visible and invisible types of decay can coexist, depending on the underlying interactions. For Majorana neutrinos, the daughter neutrinos and antineutrinos are always interacting.

In the case of invisible decays, an explanation for the short-baseline anomalies still relies on 3+1 oscillations. However, depending on the experiment energy and baseline, the oscillatory behavior can be damped due to the sterile neutrino decay. Due to the finite lifetime of the sterile state, limits from searches for a sterile-driven resonance in the earth using ν_μ disappearance at IceCube [243, 244] are relaxed. In a dedicated analysis, IceCube has searched for the sterile-driven resonance in invisibly-decaying-sterile neutrino models [341, 342] and found that it actually improves the agreement with data. The null hypothesis of no 3+1 oscillations is disfavored with a p-value of 2.5%, and the hypothesis of 3+1 oscillations without decay is disfavored with a p-value of $\lesssim 1\%$. The best-fit values prefer larger Δm^2_{41} values of $\mathcal{O}(4-10)$ eV^2, as well as large couplings between the scalar and the sterile neutrino, $\alpha_\varphi \simeq 0.6$. A recent global fit to IceCube and global neutrino data finds that invisible sterile decays alleviate the tension in the 3+1 model [343]. Theoretically, these solutions can be easily incorporated in models of singlet scalars coupled to the sterile neutrino; however, the coupling constants preferred by data are large, nearing the non-perturbative regime.

For visible decays, the signal of $\nu_\mu \to \nu_e$ appearance can be mimicked by the $\nu_4 \to \nu_F(\varphi \to \nu_F \overline{\nu}_F)$ decays, where ν_F is the low-energy neutrino flavor state, $|\nu_F\rangle = \sum_{i=1}^{3} U^*_{si} |\nu_i\rangle$. In this case, ν_μ and ν_e disappearance are

proportional to $|U_{e4}|^2$ and $|U_{\mu 4}|^2$, respectively, while the effective appearance signal, if all decays are sufficiently short, is proportional to $|U_{\mu 4}|^2$. Since both appearance and disappearance probabilities depend on the same power of the mixing elements, the global neutrino data tension is significantly reduced and could disappear altogether. In the original proposal [252], the ν_4 decays do not proceed through mixing, but instead from a dimension-five operator $\frac{g_e}{v_h}(\overline{L_e}\tilde{H})\nu_R\varphi$. In that case, appearance signals can still occur without a corresponding ν_e disappearance channel provided $U_{e4} = 0$.

If $U_{e4} \neq 0$, then ν_4 can be produced in ^{8}B decays in the Sun. This is strongly constrained when ν_4 decays to active antineutrinos. Therefore, scenarios where the neutrinos are Majorana or where the scalar is unstable, $\varphi \to \nu_F\overline{\nu}_F$, are in tension with solar antineutrino searches [256]. Dirac neutrinos with a stable φ particle are not subject to these constraints.

We also comment on an alternative, fine-tuned solution to avoid these limits. Consider a model with a lepton-number-charged scalar particle φ_2, which carries $L = 2$. If neutrinos are Dirac and the sterile state is almost degenerate in mass with the scalar, $\epsilon \equiv \frac{m_4 - m_\varphi}{m_4} \ll 1$, then the antineutrinos produced in $\nu_4 \to \overline{\nu}_F\varphi_2$ decays are not observable due to their small energy, below the inverse-beta-decay threshold. The subsequent decays of φ give two interacting visible neutrinos $\varphi \to \nu_F\nu_F$, avoiding solar antineutrino limits altogether. A full analysis is required to determine if the decay couplings can be large enough to overcome the ϵ suppression to the ν_4 lifetime,

$$\Gamma^{\text{Lab}} = \sum_i \frac{m_4^2}{4E_{\nu_4}}|U_{s4}U_{sj}|^2\alpha_\varphi\epsilon^2(2-\epsilon)^2, \tag{2.1}$$

where $\alpha_\varphi = g_\varphi^2/4\pi$. The model, however, still faces strong limits from cosmology [255].

The decaying-sterile neutrino models discussed above have not been directly targeted by MicroBooNE, although the null results of the template analyses and the 3+1 oscillations search can already constrain them. The main difference with respect to the 3+1 oscillations in the sterile decay signal is the softening of the energy dependence of the oscillation and the suppression of ν_μ disappearance. This can weaken the constraining power of the ν_μ sample and wash-out oscillations in the ν_e appearance signal. In particular, ν_e disappearance can be large and suppress the rate of intrinsic ν_e backgrounds while compensating for the additional ν_e rate from the effective $\nu_\mu \to \nu_e$ transition. Given these distinctive features, we encourage a dedicated study of this scenario to assess the sensitivity of MicroBooNE to the decaying-sterile neutrino explanations of the MiniBooNE LEE.

Exotic effects in short-baseline oscillations

Wavepacket decoherence The authors of Ref. [344] pointed out that neutrino-wavepacket decoherence could help explain the lack of $\overline{\nu}_e$-disappearance in reactor experiments in 3+1 oscillation models. The global fit to short-baseline data in Ref. [343] showed that the 4.9σ internal tension of short-baseline data is reduced to 3.6σ when including effects due to the finite size of the neutrino wavepacket. The best-fit result for the size of the wavepacket in that analysis is $\sigma_x \sim 67$ fm, much smaller than the naive expectation of typical inter-atomic distance or the inverse of the detector energy resolution [345]. For comparison, theoretical estimates of the beta-decay-induced antineutrino wavepacket size [346] find $\sigma_x \lesssim 10-100$ pm (see also [347, 348]). For such proposals to be successful, quantum-mechanical decoherence should be more significant than classical averaging from detector resolution.

Energy-dependent mixing angles It has been argued that the possibility of having energy-dependent mixing angles and masses can alleviate the tension between appearance and disappearance experiments in 3+1 oscillation models [349, 350]. As shown in Ref. [350], renormalization group evolution can modify disappearance constraints on the square of mixing elements by factors of $\mathcal{O}(2-3)$ because their energy scales are significantly different from those of LSND and MiniBooNE. The running of the mixing angles also modifies the oscillation at MiniBooNE since the energy scale of detection ($E \sim 3$ GeV) is larger than that of production ($E \sim m_\pi$). Reactors and solar neutrinos constrain $|U_{e4}|$ at energies of $\mathcal{O}(10)$ MeV or less, leaving room for this parameter to run. MINOS/MINOS+ and IceCube, however, are sensitive to the same production scale ($E \sim m_\pi$) but constrain $|U_{\mu 4}|$ at a larger detection energy of about 3 GeV and 1 TeV, respectively. Oscillation searches at MicroBooNE would not be significantly impacted, although the oscillation maximum at the other SBN detectors could be somewhat modified due to the different baselines. The benchmark model proposed in Ref. [350] closely resembles the particle content we discuss in Section 2.4 but does not require any couplings between the new dark particles and the SM other than to neutrinos themselves.

Space-time modifications Altered neutrino dispersion relations have also been discussed to solve the 3+1 oscillation tension. In large extra dimensions, fluctuations of the brane make the path length of active neutrinos larger than that of sterile ones [351–355]. In some cases, the modified dispersion relations lead to resonances in the neutrino flavor evolution. Another realization of such scenarios is through Lorentz violation, parameterized in the SM Extension effective theory, which can modify neutrino flavor evolution

via Lorentz-violating higher-dimensional operators suppressed by powers of $1/M_{\text{planck}}$ [356–358]. Although these models solve some of the issues in the 3+1 oscillation paradigm, they still show tension with global neutrino data due to the steep energy dependence [359].

2.3.2 Single photons

Single photons are an important background in MiniBooNE at low energies. The dominant sources of these events come from misidentified π^0 decays and $\Delta(1232)$ radiative decays [66]. Well-reconstructed two-ring events are measured by MiniBooNE and directly constrain the π^0 rate. While the $\Delta(1232)$ production cross section is also constrained by the π^0 sample, largely made up of resonant events, the radiative branching ratio $\Delta(1232) \to N\gamma$ $(N = n, p)$ is not. An enhancement of this branching by $\mathcal{O}(3)$ factors leads to a remarkable agreement with the LEE. This possibility is constrained by photoproduction experiments, $\gamma p \to \Delta$, and has recently been directly tested by the MicroBooNE experiment. Good agreement with MiniBooNE's estimates was found, excluding this explanation of the LEE at 94% C.L. [229]. It is important to note that while this result excludes the SM Δ hypothesis, it does not necessarily exclude other new physics scenarios that invoke single photons. In particular, the MicroBooNE analysis was not sufficiently sensitive to single photons not accompanied by a hadronic vertex (e.g., coherent emission) due to the significantly larger backgrounds in the $1\gamma 0p$ selection. Single photons can also contribute to the exclusive $1e0p0\pi$ channel of the MicroBooNE ν_e search, where, notably, an excess is already observed [224] In view of that, we proceed to discuss dark sector sources of single photons.

Upscattering via transition magnetic moments

Neutrinos interactions with the material inside or outside the MiniBooNE detector can produce short-lived heavy neutral leptons (HNLs) that subsequently decay visibly inside the fiducial volume. This scenario is referred to as upscattering. One model for upscattering where the HNL decays to a single photon is that of a transition magnetic moment [260–262, 265, 266, 268]. The low-energy Lagrangian is given by

$$\mathscr{L} \supset \frac{\mu_{\rm tr}^{\alpha}}{2}\overline{\nu}_{\alpha}\sigma^{\mu\nu}N_R F_{\mu\nu} + \text{ h.c.}, \tag{2.2}$$

where α is the neutrino flavor index. The interaction above would mediate neutrino-nucleus upscattering that produces the HNL N as well as the subsequent decays of $N \to \nu\gamma$. Depending on the details of the model, the massive particle N may be Dirac or Majorana, although the MiniBooNE angular spectrum prefers the former. An explanation of the LEE can be achieved with $\mu_{\rm tr}^{\mu}$ as small as $\mathcal{O}(10^{-9}\mu_B)$, which corresponds to $\mu_{\rm tr}^{\mu} \sim (1\text{ PeV})^{-1}$. The muon index indicates that muon neutrinos and antineutrinos, which dominate the flux at MiniBooNE, initiate the upscattering process. In what follows, we drop the flavor index and assume $\mu_{\rm tr} = \mu_{\rm tr}^{\mu}$.

In this model, the upscattering cross section and decay rate of the HNL are proportional to $|\mu_{\rm tr}|^2$. Once produced, the HNL can decay into either a single photon or, around 0.7% of the time, into a e^+e^- pair. The total decay rates for a Dirac HNL are given by [182],

$$\Gamma_{N\to\nu\gamma} = \frac{|\mu_{\rm tr}|^2 m_N^3}{16\pi}, \tag{2.3}$$

$$\Gamma_{N\to\nu\ell^+\ell^-} \simeq \frac{\alpha|\mu_{\rm tr}|^2}{48\pi^2} m_N^3 \left[2\log\left(\frac{m_N}{m_\ell}\right) - 3\right], \tag{2.4}$$

where we neglected terms of $\mathcal{O}(m_\ell^2/m_N^2)$ in the dilepton rate. The dilepton mode, while subdominant, provides an alternative signature that may be searched for in $K^+, \pi^+ \to \ell^+ N \to \ell^+ \nu e^+ e^-$ or at low-density neutrino detectors such as ND280 [182]. A detailed fit to the MiniBooNE excess was performed in [268], suggesting to explain both the energy and the angular spectrum of the LEE, the HNL should be as massive as 400 MeV. Ref. [268] also derived constraints on the model from the MINERvA neutrino-electron scattering sideband data. While MINERvA poses strong limits, it is not able to fully exclude the regions of preference, especially at large HNL masses where stringent cuts on the angular spectrum reject most of the signal events.

Several future experiments can probe the TMM scenario, including dark matter direct detection experiments [360], coherent elastic neutrinos-nucleus scattering (CEνNS) measurements [361, 362], double-bang searches at IceCube and large volume neutrino detectors [154, 155, 158, 363, 364], and neutrino detectors at the Forward Facilities of the LHC [365].

The scale of new physics behind the dimension-5 operator above is model-dependent, but a naive estimate for a TMM induced at the one-loop level can be found using

$$\mu_{\rm tr} \simeq \frac{y y' e Q_f}{8\pi^2} \frac{m_f}{M_{\rm UV}^2} \left[\log\left(\frac{M_{\rm UV}^2}{m_f^2} \right) - 1 \right], \tag{2.5}$$

where Q_f and m_f stand for the electric charge and the mass of the charged fermion in the loop, respectively, and $y^{(\prime)}$ is the coupling between left-(right-)handed fermions to the new particle of mass $M_{\rm UV}$. Ref. [366] proposes a leptoquark model as an UV completion to Eq. (2.2), where $f = b$-quark. The leptoquark can be within reach of the LHC with $M_{\rm UV} \gtrsim 1$ TeV for $y = y' = 2$ and $\mu_{\rm tr} \sim 1$ PeV^{-1}.

In general, the UV completion of Eq. (2.2) would also generate large mass terms, $m_D \overline{\nu}_L N_R$ [367–371] (see also [372] for a recent review). In seesaw models, this is undesirable for two reasons: i) neutrino masses would be too large, ii) the mixing between active and heavy neutrinos would be too large. While point number i) can be avoided in inverse seesaw models with approximate conservation of lepton number, point ii) poses a much bigger challenge. The mixing is subject to severe constraints from decay-in-flight and meson peak searches for HNLs. Schematically, for $f = b$, we get

$$U_{\alpha N} \sim \frac{\mu_{\rm tr}}{2} \frac{M_{\rm UV}^2}{e Q_f m_N} \sim 3 \times 10^{-3} \left(\frac{\mu_{\rm tr}}{1 \text{ PeV}^{-1}} \right) \left(\frac{M_{\rm UV}}{1 \text{ TeV}} \right). \tag{2.6}$$

which is prohibitively large. As a result, such models require some fine-tuning to avoid constraints on the mixing angles.

Finally, we note that such transition magnetic moments can also exist between different generations of HNLs [362, 373]. For instance,

$$\mathscr{L} \supset \frac{\mu_{NN'}}{2} \overline{N'_L} \sigma^{\mu\nu} N_R F_{\mu\nu} + \text{ h.c.}, \tag{2.7}$$

where N' may again be a Dirac or Majorana particle. In this case, even relatively light N particles can be produced inside the detector and decay fast enough via $N \to N' \gamma^{(*)}$. For instance, for $m_N = 10$ MeV and $\mu_{\rm tr} \sim (5 \text{ PeV})^{-1}$, the event rate at MiniBooNE is sufficiently large for $\mu_{NN'} \sim (500 \text{ TeV})^{-1}$, provided N' is light enough. Small mass splittings between N and N' can also help ameliorate tensions with the MiniBooNE angular distribution in this case. This is particularly interesting in inverse seesaw models, where lepton number violation is controlled by $M_N - M_{N'}$, though more work is needed to find a self-consistent UV completion of Equations (2.2) and (2.7).

We end this section by noting that HNLs coupled to the SM via mixing

and small TMMs can be long-lived and produced in charged meson decays, $\pi, K \to \ell N$. In this case, the HNL propagates from the target to the detector to decay in flight via $N \to \nu\gamma$ [257]. This signature is severely constrained by the timing information when the HNL mass is larger than ~ 50 MeV. It is also constrained, although not fully excluded, by the corresponding off-shell photon mode $N \to \nu(\gamma^* \to e^+e^-)$ signature at ND280 and PS-191 [182]. The latter, however, does exclude similar models where the dominant branching ratio of the HNL is into e^+e^- [258].

Neutrino-induced inverse-Primakoff scattering

We now turn to another possibility for producing single-photon signatures: neutrino-induced inverse Primakoff scattering (IPS). In this scenario, the neutrino scatters on a nucleus through a virtual scalar particle that undergoes inverse Primakoff scattering, $\varphi^* A \to \gamma A$, with A a nuclear target. The scalar may couple to photons or dark photons (Z'), and either mediator may be exchanged with the nucleus. The MiniBooNE LEE can be explained if a photon is produced in the final state or if a dark photon decays to an e^+e^- pair. In this section, we focus on the former. The process $\nu A \to \nu\gamma A$ has been discussed in Ref.[269] in the context of the dimension-seven Rayleigh operators, $\overline{\nu}\nu F_{\mu\nu}F^{\mu\nu}$ and $\overline{\nu}\nu F_{\mu\nu}\widetilde{F}^{\mu\nu}$. The scenario we discuss here is one of the completions of the operator above, also discussed by the authors.

We discuss a model of a light scalar particle with loop-induced couplings to SM photons. For later convenience, we also include couplings to a dark photon, the mediator of a new $U(1)_D$ gauge symmetry. The low-energy

Lagrangian reads,

$$\begin{aligned}\mathscr{L} \supset & -\frac{1}{4}X_{\mu\nu}X^{\mu\nu} - \frac{\varepsilon}{2c_W}F_{\mu\nu}X^{\mu\nu} - \frac{1}{2}\partial_\mu\varphi\partial^\mu\varphi \\ & - \frac{\alpha}{8\pi}\varphi\left(\frac{c_{\gamma\gamma}}{f_{\gamma\gamma}}F_{\mu\nu}F^{\mu\nu} + \frac{c_{\gamma X}}{f_{\gamma X}}F_{\mu\nu}X^{\mu\nu} + \frac{c_{XX}}{f_{XX}}X_{\mu\nu}X^{\mu\nu}\right),\end{aligned} \tag{2.8}$$

where $A^{\mu\nu} \equiv \partial_\mu A_\nu - \partial_\nu A_\mu$ for $A = X, F$, with X_μ the $U(1)_D$ mediator before diagonalization of the kinetic and mass terms. The scales $f_{\gamma\gamma}/c_{\gamma\gamma}$ and $f_{\gamma X}/c_{\gamma X}$ are constrained by direct searches for new charged particles of by the coupling of φ with SM particles. If the operators above are generated by charged particles with no $U(1)_D$ charge, we expect $c_{\gamma X} \propto \varepsilon$ and $c_{XX} \propto \varepsilon^2$, upon diagonalization of the gauge kinetic terms.

The scalar can also couple to the neutrino sector. A large direct coupling to SM neutrinos is challenging to achieve within a $\mathrm{SU}(2)_L$-invariant model, but a direct coupling to a sterile neutrino ν_s is less constrained. This sterile state ν_s mixes with SM neutrinos, and in terms of the mass eigenstates, $|\nu_s\rangle = \sum_{i=1}^{4} U_{si}^* |\nu_i\rangle$. Having this in mind, we can consider

$$\mathscr{L} \supset c_\nu^{ij}\varphi\overline{\nu_i}P_L\nu_j + \text{h.c.}, \tag{2.9}$$

where all couplings c_ν^{ij} are proportional to $U_{si}^* U_{sj}$. For concreteness, we assume neutrinos to be Dirac.

Using the equivalent photon approximation, we estimate the cross-section for the $\nu A \to \nu\gamma A$ process. In the limit of large m_φ, we find

$$\frac{\mathrm{d}\sigma_{\nu A\to\nu\gamma A}}{\mathrm{d}Q^2\mathrm{d}\hat{s}} \simeq \frac{\alpha^3 Z^2}{64(4\pi)^4}\frac{|c_{\gamma\gamma}|^2}{f_{\gamma\gamma}^2}\frac{\hat{s}}{Q^2}\frac{|c_\nu|^2}{m_\varphi^4}|F(Q^2)|^2, \tag{2.10}$$

where Q^2 is the momentum exchange with the nucleus, $\hat{s} = (k + k_\gamma)^2$ is the center-of-mass energy of the projectile neutrino and the semi-real photon,

and $F(Q^2)$ is the nuclear electromagnetic form factor. The cross section favors large center-of-mass energies thanks to the higher-dimension nature of the interaction and, therefore, produces high-energy photons, in contrast with the low-energy nature of the MiniBooNE excess. It is also suppressed by large powers of α and phase-space factors. This is expected since the full process is a one-loop three-body scattering.

It is easy to see that for typical values of allowed couplings and masses the total cross section is far below the SM neutrino cross section. We have also checked this for small values of m_φ, where the mediator mass no longer suppresses the rate. This is compatible with the findings of [269], which quotes limits on the neutrino polarizability operators of order $c_\nu|c_{\gamma\gamma}|/f_{\gamma\gamma} < 3 \times 10^{-3}$ GeV^{-1}. Clearly, $f_{\gamma\gamma}$ is tied to the GeV scale for allowed couplings of c_ν of $\mathcal{O}(10^{-3})$, and, therefore, requires new large couplings to charged particles below the EW scale, which is highly constrained by direct searches. The situation is much worse in Majoron models where c_ν is proportional to neutrino masses. While a detailed study would be needed to draw definitive conclusions, we deem this model inconsistent with the LEE as i) it produces photons that are too high energy, ii) requires decay constants $f_{\gamma\gamma}$ significantly below the EW scale, signaling a theoretical inconsistency for the couplings required to explain the LEE.

Finally, we mention that IPS can also be initiated by dark particles in the beam. Ref. [270] considered the production of long-lived scalar particles in charged meson decays, $\pi, K \to \ell\nu\varphi$, followed by the IPS of φ on nuclei inside the detector. In this case, the scalar particle interacted with matter through a virtual dark photon through the $c_{\gamma X}$ operator to produce a single photon.

2.3.3 Electron-positron pairs

Another explanation of the excess is an anomalous source of e^+e^- inside the MiniBooNE detector. The importance of these sources is not only that they can explain MiniBooNE LEE, but also that they are related to many interesting dark sector models. The LEE signal is mimicked if the e^+e^- pairs overlap or are highly asymmetric in energy, so only a single electromagnetic shower is resolved [230]. The e^+e^- explanation of the LEE is unique in that it constitutes both a photon-like (overlapping pairs) and electron-like (energy asymmetric pairs) signal. Neutrino interactions in MiniBooNE rarely produce e^+e^- pairs directly. The most common source of these final states is through the production of photons that subsequently convert into overlapping e^+e^- pairs, or the Dalitz decay of $\pi^0 \to e^+e^-\gamma$ with a branching ratio of $\sim 1.2\%$. We are unaware of a publicly available study of Dalitz decays in MiniBooNE, although the rate is small and most often accompanied by an observable additional photon.[270].

New physics sources of e^+e^- arise naturally in models of dark sectors. The new light particles can be produced by the interactions of muon-neutrinos and antineutrinos with nuclei in the detector and subsequently decay to e^+e^-. We will discuss a few examples based on neutrino upscattering to HNLs, neutrino-induced Primakoff scattering, and bremsstrahlung processes.

No dedicated experimental search for an e^+e^- origin of the LEE has been carried out to date, although several constraints have been derived in phenomenological works. The most constraining data comes from the photon-like sideband of the neutrino-electron scattering measurement of MINERvA [374–376], which has been used to place limits on dark neutrinos and transition magnetic moments in Refs. [268, 377]. Another important limit comes from the HNL search with e^+e^- final states in the gaseous Argon TPCs of

ND280 [378], the off-axis near detector of T2K. Ref. [379] has placed limits on dark neutrinos using this dataset using kernel density estimators to calculate the signal prediction across the model parameter space. No dedicated search has been performed yet in the SBN LAr program.

Neutrino-induced boson fusion

As another possibility for producing new particles by neutrino-nucleus scattering inside MiniBooNE, we discuss the neutrino-induced vector boson fusion (VBF) reactions. Like the IPS process discussed in Section 2.3.2, this is a $2 \to 3$ scattering mediated by light particles. The dark photon interactions in Equation (2.8) and the neutrino-scalar interaction of Equation (2.9) could lead to the on-shell production of the scalar particle φ or of the dark photon Z', which subsequently decay to e^+e^-. The topology of the three-body process need not arise from the higher-dimensional operators in IPS. When considering a dark photon, the IPS diagram can proceed through the direct interaction between φ and Z', as considered in Ref. [233]. We leave a detailed study of this cross section to future literature. In what follows, we comment on the total cross section and argue that it can be sufficiently large for the allowed parameter space.

For dark photon masses below the $\mathcal{O}(100)$ MeV scale, the equivalent photon approximation can give a crude estimate of the cross-section for the $\nu A \to \nu Z' A$ process. In the limit of small mediator masses, we find

$$\frac{\mathrm{d}\sigma_{\nu A \to \nu Z' A}}{\mathrm{d}Q^2 \mathrm{d}\hat{s}} \simeq |c_\nu|^2 \alpha_D \frac{\alpha \varepsilon^2 Z^2}{4\pi} \frac{m_{Z'}^2}{\hat{s}^3 Q^2} |F(Q^2)|^2, \tag{2.11}$$

where Q^2 is the momentum exchange with the nucleus, $\hat{s} = 2k_1 \cdot k_\gamma$ is the center-of-mass energy of the projectile neutrino and the semi-real photon, and

$F(Q^2)$ is the nuclear electromagnetic form factor. Contrary to Eq. (2.10), dark photon production prefers low energy exchange and, therefore, can, in principle, lead to low-energy events. We also note that the rate is proportional to the dark photon mass, which is a reflection of the fact that the scalar coupling to the dark photon is proportional to $g_D^2 v_\varphi$, where v_φ is the dark scalar vacuum expectation value.

It is easy to see that for allowed parameters the cross section can be as large as a few percent of the total neutrino cross section in the SM, indicating that as far as the total rate is concerned, it can successfully reproduce the number of events at MiniBooNE. A detailed study of the energy and angular spectra is required to draw any additional conclusions.

Upscattering to heavy neutrinos

In Section 2.3.2, we discussed the production of HNLs through a transition magnetic moment. Now, we will focus on models where HNLs are generated by new light mediators and decay into dilepton pairs instead of a single photon. These scenarios are particularly simple from a model-building point of view and can be linked to consistent low-energy extensions of the SM. The first proposals in Refs. [194, 230] were based on dark photon models with a single HNL. The signature is given by

$$\nu_\mu A \to (N \to \nu Z'^{(*)} \to \nu e^+ e^-) A, \tag{2.12}$$

where A is some nuclear target, Z' the dark photon, and N an HNL. As indicated, the dark photon may be produced on or off its mass shell. If on-shell, the decay chain is typically prompt, and the final states are more forward-going. If the dark photon is off-shell, the HNL will decay via a

three-body process and be longer-lived. In that case, production from the dirt upstream of the detector can be important.

Later studies considered vector mediators of a $B-L$ gauge symmetry [234] and extended scalar sectors [231, 232], where new light scalars play the role of the dark photon in Eq. (2.12). Another logical possibility is that a scalar particle mediates the scattering process, but the decay proceeds through a light dark photon. An advantage of scalar mediators is that the upscattering is predominantly helicity-flipping, leading to less forward production of the HNL. This can lead to much better agreement with the angular distribution at MiniBooNE.

The HNL models that can give the upscattering signature in Eq. (2.12) typically require multiple states for anomaly cancellation and neutrino mass generation. This was explored in Refs. [88, 196] that generalized the dark neutrino signature to a cascade of decays in the dark sector,

$$\nu_\mu A \to (N_i \to N_j Z'^{(*)} \to N_j e^+ e^-) A, \tag{2.13}$$

where N_j is the lighter of the two HNLs and can be much longer-lived than N_i. Phenomenologically, these models are called $3+n$ models, where n stands for the number of HNLs considered. A more detailed explanation of this family of models, dubbed the Three Portal Model, can be found in **??**. In Section 2.4, we study 3+1 and 3+2 models in the context of the MiniBooNE excess. Due to the larger dark photon coupling to heavy neutrinos, the parent HNL decay in 3+2 models can be much faster than in 3+1 models as it does not involve the coupling of the dark photon to light neutrinos.

The UV completions of dark neutrino sectors with dark Abelian gauge symmetry $U(1)_D$ can be separated according to the origin of the coupling between the dark leptons, ν_D, and active neutrinos, ν_α — we refer to this

coupling as the dark neutrino portal. In Ref. [380], a new scalar $\mathrm{SU}(2)_L$ doublet charged under the $U(1)_D$, H_D, realizes the inverse seesaw mechanism in the neutral lepton sector with a vector-like dark neutrino, ν_D. The dark neutrino portal is then given by the Yukawa coupling between active and dark neutrinos, $\overline{L}H_D\nu_D$. Another possibility studied by Refs. [88, 196] was to consider an $\mathrm{SU}(2)_L$-singlet complex scalar Φ as well as a singlet sterile neutrino ν_N. In this case, the dark neutrino portal is generated in a two-step process: the complex scalar couples the dark neutrinos to the sterile states, $\overline{\nu_N}\nu_D\Phi$, while the latter couples to active neutrinos via the usual neutrino portal, $\overline{L}H\nu_N$. Alternatively, when the sterile neutrino is heavy, one may integrate it out to find the higher-dimensional portal coupling $M_N^{-1}(\overline{L}H)(\nu_D\Phi)$, where M_N is the mass of the sterile neutrino.

The new gauge boson X_μ interacts with the SM particles via kinetic mixing with the SM hypercharge boson B_μ. The dark photon mass may be generated by the Stueckelberg or Higgs mechanisms. The latter implies the existence of new scalar particles, such as a single dark Higgs field, Φ, charged under $U(1)_D$. Heavy neutrino fields charged under the new gauge symmetry, referred to as dark neutrinos, can then simultaneously explain the origin of neutrino masses via the seesaw mechanism and the MiniBooNE signature. The latter is possible thanks to their mixing with SM light neutrinos and the interaction with the dark photon.

For concreteness, we present the full model of Ref. [196], which can accommodate the simpler phenomenological model used in Section 2.4. The

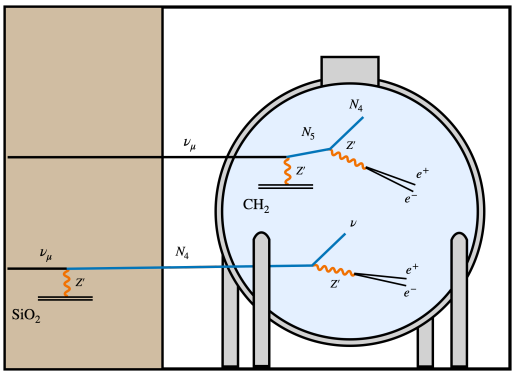

Figure 2.2: The dark neutrino upscattering signature at MiniBooNE for 3+1 models ($N_4 \to \nu e^+ e^-$) and 3+2 models ($N_5 \to N_4 e^+ e^-$). As an example, we show a scattering inside the detector for 3+2 and in the dirt upstream of the detector for 3+1.

Lagrangian is given by,

$$\begin{aligned}\mathscr{L} \supset & -\frac{1}{4}X^{\mu\nu}X_{\mu\nu} - \frac{\varepsilon}{2c_W}X_{\mu\nu}B^{\mu\nu} + (\mathcal{D}_\mu\Phi)^\dagger(\mathcal{D}^\mu\Phi) \\ & - V(\Phi, H) + \overline{\nu_N}i\partial\!\!\!/\nu_N + \overline{\nu_D}i\mathcal{D}\!\!\!/\nu_D \\ & - \Big[(\overline{L}\tilde{H})Y\nu_N^c + \frac{1}{2}\nu_N M_N \nu_N^c + \overline{\nu}_D M_X \nu_D \\ & \quad + \overline{\nu_N}(Y_L\nu_{D_L}^c\Phi + Y_R\nu_{D_R}\Phi^*) + \text{h.c.}\Big]\end{aligned} \tag{2.14}$$

where: $\widetilde{H} \equiv i\sigma_2 H^*$, $\mathcal{D}_\mu\Phi \equiv \partial_\mu - ig_D X_\mu$, and g_D is the coupling constant of the new force. The neutral lepton sector contains a number d of vector-like dark neutrinos $\nu_D = \nu_{D_L} + \nu_{D_R}$ and n sterile states ν_N. Upon diagonalization of the kinetic and mass terms, the gauge boson sector is comprised of the photon A, the SM Z boson, and the dark photon Z'.

One advantage of dark neutrino models is their rich connection to other low-energy phenomenology. For instance, the model of Eq. (2.14) offers a viable solution to the $(g-2)_\mu$ anomaly [381]. Kinetic mixing can explain the deviation from the Standard Model [382], but this solution is already

excluded if the dark photon decays predominantly to e^+e^- or fully invisibly. In the invisible case, BaBar [383] and NA64 [384] exclude the region of preference. However, if the dark photon can decay to several short-lived HNLs, as in dark neutrino models, it becomes a semi-visible particle. That is, it decays to both visible and invisible particles, such as in the reaction $Z' \to (N_i \to N_j e^+e^-)(N_k \to N_l e^+e^-)$, relaxing the constraints above [202, 385]. A simultaneous explanation of the MiniBooNE and $(g-2)_\mu$ anomalies is possible in 3+n models with $n > 1$ and requires ~ 1 GeV, dark photons. Another important connection is to kaon decays, where HNLs can produce multi-lepton signatures, such as $K^+ \to \ell^+(N_i \to N_j e^+e^-)$ [88]. For on-shell dark photons, this decay cascade represents a double bump hunt, where $(p_K - p_\ell)^2 = M_{N_i}^2$ and $(p_{e^+} + p_{e^-})^2 = m_{Z'}$. Finally, similarly to the transition magnetic moment case, large-volume experiments can target the double-bang feature of the upscattering signal [154, 155, 158, 363, 364].

Dark bremsstrahlung

Neutrinos can also bremsstrahlung dark photons or scalars upon scattering with nuclei. These light bosons can then subsequently decay to e^+e^-. The same boson can also mediate the interaction with nuclei, and if it is light, the cross section can be significantly enhanced, similar to the upscattering case. Light bosons will produce collimated e^+e^- pairs to be misreconstructed as single electron events. Ref. [386] considered a similar process initiated by dark matter particles. Here, we are interested in the possibility of bremsstrahlung initiated by neutrinos. The kinetic mixing parameter between the SM and the dark photon is much more constrained.

For concreteness, let us consider a dark photon, Z'. The coupling to matter will be proportional to charge, while the coupling to neutrinos will be

proportional to a dark coupling $g_D U_{Di}^* U_{Dj}$. We can obtain a naive estimate of the dark bremsstrahlung cross section relative to the upscattering one. For dark photons and HNLs much lighter than the energy transfer in the scattering process, we naively expect,

$$\frac{\sigma_{\text{brem}}}{\sigma_{\text{ups}}} \simeq \frac{\alpha_D}{4\pi} \log\left(\frac{s}{m_{Z'}^2}\right), \tag{2.15}$$

which is typically smaller than the upscattering cross sections used in Section 2.3.3. Nevertheless, when α_D is large and $m_{Z'}$ is lighter than 100 MeV, the emission rate could still be large enough to match the number of events of the LEE. The emission cross section is peaked in the forward direction, indicating that it may be challenging to reconcile this model with the angular distribution of the MiniBooNE LEE.

New physics in scattering				
Topology	Model	Diagram	Signal	References
single γ	neutrino upscattering	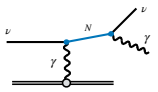	$N \to \nu\gamma$	[158, 260–269]
	neutrino-induced inverse-Primakoff scattering	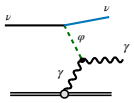	$\varphi^* A \to \gamma A$	[269]
e^+e^-	neutrino upscattering	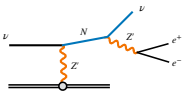	$N \to \nu e^+ e^-$ (on-shell N)	[88, 194, 196, 230–234, 259] ??
	neutrino-induced bremsstrahlung		$Z' \to e^+ e^-$ (off-shell N)	not studied
	neutrino-induced Primakoff scattering	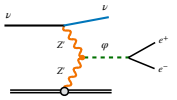	$\varphi \to e^+ e^-$	[233]
	neutrino-induced inverse-Primakoff scattering	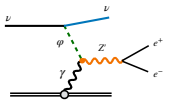	$Z' \to e^+ e^-$	not studied
$\gamma\gamma$	neutrino upscattering	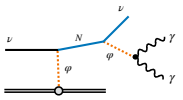	$N \to \nu\gamma\gamma$	[232]
	neutrino-induced Primakoff scattering	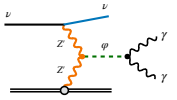	$\varphi \to \gamma\gamma$	not studied

Table 2.2: Examples of new particle production in neutrino-nucleus scattering with electromagnetic final states.

Number of HNLs	Parent HNL m_{3+n} fit	Mass splitting Δ	$m_{Z'}$ fixed	$\lvert V_{\mu h}\rvert^2$ fit	ε fixed	p_{val} ν mode	p_{val} $\overline{\nu}$ mode	p_{val} combined
$n=1$	80 MeV	–	30 MeV	9.0×10^{-10}	8×10^{-4}	34%	6.2%	0.8%
$n=1$	18 MeV	–	200 MeV	6.4×10^{-4}	8×10^{-4}	30%	12%	2.0%
$n=2$	615 MeV	0.3	100 MeV	1.1×10^{-6}	8×10^{-4}	57%	10%	14%
$n=2$	740 MeV	0.5	500 MeV	1.5×10^{-4}	8×10^{-4}	31%	10%	11%
$n=2$	601 MeV	1.0	1.25 GeV	1.3×10^{-3}	8×10^{-4}	29%	4.6%	5.5%
$n=2$	300 MeV	3.0	1.25 GeV	1.9×10^{-4}	8×10^{-4}	28%	4.6%	1.9%

Table 2.3: Best-fit values to the $E_\nu^{\text{CCQE-reco}}$ spectrum at MiniBooNE for the combined fit to ν and $\overline{\nu}$ modes in Figs. 2.3 and 2.7. The number of degrees of freedom for the χ^2 probability p_{val} is 6.8, 6.9, and 15.6 ν mode, $\overline{\nu}$ mode, and the combination, respectively. [60].

2.3.4 Photon pairs

A less explored option is to have dark particles produced in neutrino scattering decay to photon pairs. If the photons are highly collimated, or one of the photons exits the detector before pair converting, the signal appears as an electron-like event at MiniBooNE. This can happen if a scalar boson is produced in the dirt or detector and undergoes $\varphi \to \gamma\gamma$ inside the fiducial volume. The production of the boson can take place either via upscattering, replacing the dark photon of Section 2.3.3 for a scalar, or via IPS and VBF processes with the production of an on-shell scalar particle. In all cases, the scalar decay proceeds via the non-renormalizable interaction between φ and the two photons in Eq. (2.8), giving

$$\begin{aligned}\Gamma_{\varphi\to\gamma\gamma} &= \frac{\alpha^2}{256\pi^3}\frac{|c_{\gamma\gamma}|^2 m_\varphi^3}{f_{\gamma\gamma}^2} \\ &= \frac{1}{5\text{ cm}}\left(\frac{m_\varphi}{200\text{ MeV}}\right)^3\left(\frac{100\text{ GeV}}{f_{\gamma\gamma}/|c_{\gamma\gamma}|}\right)^2 .\end{aligned} \tag{2.16}$$

For the relatively large scalar mass of 200 MeV, the decay constant cannot be significantly larger than 100 GeV, as otherwise direct constraints from beam dumps become prohibitively strong [387]. This, in turn, implies the need for a relatively low-scale UV completion of the two-photon operator, adding further strain on this interpretation.

In the case of upscattering, the same scalar boson may mediate the upscattering process. The HNL produced would decay via $N_4 \to \nu_\ell(\varphi \to \gamma\gamma)$. The scalar should be produced on-shell; otherwise, the HNL decay rate will be too small. In that case, the HNL decay can be regarded as effectively prompt. Like the dark photon decay to e^+e^-, the scalar decay is isotropic, and so, as far as the decay kinematics is concerned, the two scenarios are

similar. One difference, however, is the small fraction of events where one of the photons may escape the fiducial volume before converting to a visible e^+e^- pair, leading to a genuine single photon signal. This upscattering scenario was explored in Ref. [232] and was linked to the $(g-2)_\mu$ anomaly as well; however, in this case, the contribution to the anomalous magnetic moment took place through the Barr-Zee diagram, connecting the decay rate of the $\varphi \to \gamma\gamma$ to the $(g-2)_\mu$ anomaly.

Another possibility to produce $\gamma\gamma$ pairs in MiniBooNE is through the decay of dark particles into neutral pions. One minimal example would a HNL produced via upscattering through a dark boson with axial-vector couplings to quarks. Such scenarios can appear in Z' models where the dark boson mixes with the SM Z via mass-mixing. Contrary to the vectorially coupled dark photon, the axial-vector can mediate $N \to \nu\pi^0$ decays. This scenario requires the π^0 to have significantly different kinematics from the SM π^0 production in order to reproduce the excess, as otherwise it is normalized away by the in-situ π^0 constraint. We leave a detailed study of these two-photon scenarios to future literature.

2.4 Dark neutrino MiniBooNE fit

Having surveyed the MiniBooNE explanations, we now turn to the specific case of dark neutrinos introduced in Section 2.3. This class of models is largely unexplored experimentally, can be embedded in self-consistent low-energy extensions of the SM, and does not contradict cosmological constraints. While they do not explain other anomalies in short-baseline experiments, like the gallium and LSND anomalies, they provide an excellent fit to the MiniBooNE energy spectrum. The signal consists of the decays of

short-lived HNLs produced by neutrinos in the dirt or inside the detector. A schematic of the signature at MiniBooNE is shown in Fig. 2.2. The production requires a new mediator particle to enhance production and shorten the lifetime of the HNLs. In this work, we focus on a dark photon due to the simplicity of the underlying model. Our study covers a similar physics to the one proposed in scalar-mediator and similar models [231–235, 259].

2.4.1 Phenomenological model

We introduce a minimal phenomenological model to describe HNL production and decay via new dark photon interactions. The interactions and particle content we introduce are based on a seesaw extension of the SM with a new $U(1)_D$ gauge symmetry. Examples of UV completions can be found in Refs. [88, 196, 380] and in more detail in Section 1.2.

The minimal particle content consists of a massive dark photon that kinetically mixes with the SM hypercharge and the n heavy neutral leptons that interact through the dark force and mix with light neutrinos. Upon diagonalization of the kinetic and mass terms, the dark photon interactions can be written as

$$\mathscr{L}_{\text{int.}} \supset Z'_\mu \left(g_D \mathcal{J}^\mu_D - e\varepsilon \mathcal{J}^\mu_{\text{EM}} - \varepsilon t_{\text{W}} \frac{m^2_{Z'}}{m^2_Z} \frac{g}{2c_{\text{W}}} \mathcal{J}^\mu_{\text{NC}} \right), \tag{2.17}$$

where it is assumed that $m^2_{Z'} \ll m^2_Z$. The dark current $\mathcal{J}^\mu_{\text{D}}$ can be expressed in general terms based on the neutral lepton mass states,

$$\mathcal{J}^\mu_D \equiv \sum_{i,j=1}^{3+n} V_{ij} \overline{\nu_i} \gamma^\mu \nu_j, \tag{2.18}$$

where n is the total number of heavy neutrino mass states, $V_{ij} \equiv \sum_k Q^D_k U^*_{ki} U_{kj}$

is the interaction vertex and k runs over the number of generations of dark states in the theory. Q_k^D is the dark charge of those, which we will assume to be equal to $+1$ (-1) for neutrinos (antineutrinos), and U is the neutrino mixing matrix. We adopt a similar notation to Ref. [379], extending it to models with two heavy neutrinos. For convenience, we define the dark photon couplings between the low-energy flavor neutrino state, $|\hat{\nu}_\alpha\rangle = \sum_{i=1}^{3} |\nu_i\rangle$, and the upscattered HNLs N_h with $h = 4, 5$. In 3+2 models, assuming unitarity,

$$V_{\alpha h} \equiv U_{Dh} \frac{U_{\alpha 4} U_{D4}^* + U_{\alpha 5} U_{D5}^*}{\sqrt{1 - \sum_\beta (|U_{\beta 4}|^2 + |U_{\beta 5}|^2)}}, \tag{2.19}$$

where $\alpha, \beta \in \{e, \mu, \tau\}$. The equivalent expression for 3+1 models can be recovered by setting all mixing elements $U_{\alpha 5}$ to zero. For simplicity and having the LEE in mind, unless otherwise specified, we will assume that the HNLs mix with the muon neutrino flavor only. In addition, we always assume that $|U_{\mu 4}| = |U_{\mu 5}|$ and $|U_{D4}| = |U_{D5}|$. In our simulations we set $|U_{D4}|$ and $|U_{D5}|$ are taken as $1/\sqrt{2}$, neglecting the small correction from dark-light mixing angles, $|U_{D4}|^2 + |U_{D5}|^2 = 1 - \sum_{i=1}^{3} |U_{Di}|^2$. In this way, $|V_{\mu 4(5)}|$ can be used as a proxy for the parameter $|U_{\mu 4(5)}|$, which is directly constrained by several model-independent HNL limits. Finally, we also define the coupling of HNLs to all light neutrinos, collectively denoted by ν_ℓ,

$$|V_{\ell h}|^2 \equiv \sum_{i=1}^{3} |V_{hi}|^2 \simeq |U_{Dh}|^2 \sum_{\alpha=e}^{\tau} |U_{\alpha 4}|^2. \tag{2.20}$$

In 3+2 models, there must also be two dark flavors, in which case we assume they mix equally with light neutrinos.

We will vary the kinetic mixing parameter, ε, as well as the masses m_4, m_5, and $m_{Z'}$. In the 3+2 model, it will be convenient to define the mass

splitting parameter,

$$\Delta \equiv \frac{m_5 - m_4}{m_4}. \tag{2.21}$$

This parameter controls the mass gap between the two HNL states, and therefore, also the energy release in the $N_5 \to N_4 e^+ e^-$ decays. In what follows, we will assume the physical mass eigenstates to be of pseudo-Dirac nature. This leads to less energetic and less-forward e^+e^- pairs than in the Majorana case.

For large mass splitting in the 3+2 model, the parent HNL can decay invisibly via $N_5 \to N_4 N_4 N_4(\nu_i)$ decays. While this channel is forbidden for $\Delta < 2(1)$, it can also be suppressed by the dark photon coupling matrix, V_{ij}. To thoroughly explore the parameter space of the 3+2 model, we make the assumption that $|V_{4i}| \ll |V_{44}|, |V_{55}| \ll e\varepsilon$, for $i < 4$, allowing us to consider arbitrarily large Δ values without worrying about the invisible decays of N_5. This assumption may seem strong at first, but it can be thought of as the result of a conserved C-symmetry in the dark sector, as discussed in detail in Ref. [385]. Light neutrinos ($C = -1$) and N_4 ($C = -1$) are both odd under C and cannot interact with each other via the dark photon ($C = -1$). On the other hand, N_5 ($C = +1$) is even and can interact with the lighter odd neutral lepton states via the dark photon. In summary, the C symmetry allows the dark photon to mediate transitions between N_5 and the lighter neutral leptons, but not between ν_i and N_4. We further assume that the scalar interactions are sufficiently weak so as not to spoil this structure. Therefore, in what follows, it is understood that N_5 always decays via $N_5 \to N_4 \ell^+ \ell^-$ and $N_5 \to N_4 \pi^+ \pi^-$, even for values of $\Delta > 2$, where $m_5 > 3m_4$.

The relevant decay widths of HNLs into the respective final states are

given by,

$$\Gamma_{N_4\to\nu Z'} = \frac{\alpha_D|V_{\ell 4}|^2}{4}\frac{m_4^3}{m_{Z'}^2}\left(1-\frac{m_{Z'}^2}{m_4^2}\right)^2\left(\frac{1}{2}+\frac{m_{Z'}^2}{m_4^2}\right), \tag{2.22}$$
$$\Gamma_{Z'\to\ell^+\ell^-} = \frac{\alpha\varepsilon^2}{3}m_{Z'}\sqrt{1-\frac{4m_\ell^2}{m_{Z'}^2}}\left(1+\frac{2m_\ell^2}{m_{Z'}^2}\right)$$

in the on-shell dark photon case. In the off-shell dark photon case, the HNLs tend to travel longer distances than in the on-shell case due to the three-body nature of the decay. For off-shell cases, we find,

$$\Gamma_{N_4\to\nu e^+e^-} = \frac{\alpha\alpha_D\epsilon^2|V_{\ell 4}|^2}{48\pi}\frac{m_4^5}{m_{Z'}^4}L\left(m_4^2/m_{Z'}^2\right) \tag{2.23}$$
$$\Gamma_{N_5\to N_4 e^+e^-} = \frac{\alpha\alpha_D\epsilon^2|V_{54}|^2}{48\pi}\frac{m_5^5}{m_{Z'}^4}F\left(m_4^2/m_5^2\right)$$

where $L(x) = \frac{12}{x^4}\left(x-\frac{x^2}{2}-\frac{x^3}{6}-(1-x)\log\frac{1}{1-x}\right)$ and $F(x) = 1+2x-8x^2+18x^3-18x^5+8x^6-2x^7-x^8+24x^3(1-x+x^2)\log(x)$. In both cases, we neglect the charged lepton masses. In the second rate, we neglected higher order terms in $m_4/m_{Z'}$. Note that for small Δ values (large m_4/m_5), neglecting the lepton masses is a bad approximation, and the full width should be calculated. In our analysis, we use the full decay rate provided in `DarkNews`, including Z' and SM Z/W bosons contributions.

2.4.2 DarkNews simulation

We use `DarkNews` [236] to simulate the production of heavy neutrinos by neutrino upscattering in the dirt and inside the MiniBooNE and SBN detectors. The MiniBooNE detector is modeled as a sphere of 6.1 m radius, filled with CH_2. The dirt is modeled as a truncated cone of uniform density filled with SiO_2. The cone z-axis (height) is aligned with the direction of the neu-

trino beam and passes through the center of the MiniBooNE detector. The cone minor and major radii equal 1.047 and 10.28 m, respectively. The total length of the dirt cone is 474 m, extending from the wall of the MiniBooNE vault to the beam absorber. The distance between the MiniBooNE vault wall and the outer shell of the MiniBooNE detector is 6.35 m. The beam flux is assumed not to change with respect to the azimuthal angle. We use the FHC and RHC mode neutrino fluxes from [55], and simulate events using the ν_μ and $\overline{\nu}_\mu$ components of the beam for both modes. The FHC (RHC) data corresponds to $18.75(11.27) \times 10^{20}$ POT.

We calculate the probability of decay inside the MiniBooNE fiducial volume for every heavy neutrino produced to reweight the events accordingly. If their travel direction misses the detector altogether, this probability vanishes. The fiducial volume is defined as a sphere of 5 m radius at the center of the detector. To model reconstruction effects in the detector, we smear the electron-positron pairs using a Gaussian with the true energy of the electrons or positrons as the mean and a σ equals to $0.12 \times \sqrt{E_e^{\text{true}}} + 0.01$ GeV [389].

Our event selection is detailed in Appendix A. To mimic the LEE signature, the e^+e^- must be reconstructed as a single shower. Overlapping and asymmetric events are interpreted as single showers with a "visible" four-momentum $p_{e^+} + p_{e^-}$. We adopt the same criterion for overlapping and energy-asymmetry as the π^0 study of Ref. [198]. With the visible energy E_{vis} of the misreconstructed single shower and its angle θ_{beam} with respect to the neutrino beam, we can calculate $E_\nu^{\text{CCQE-reco}}$, defined as the reconstructed neutrino energy under the hypothesis of CCQE scattering,

$$E_\nu^{\text{CCQE-reco}} = \frac{1}{2} \frac{2m_n E_{\text{vis}} - (m_n^2 + m_e^2 - m_p^2)}{m_n - E_{\text{vis}} + p_{\text{vis}} \cos\theta_{\text{beam}}} \tag{2.24}$$

where m_p, m_n, m_e stand for the proton, neutron, and electron mass, and

$p_{\rm vis} = \sqrt{E_{\rm vis}^2 - m_e^2}$. As a last step, we multiply our final efficiencies by the official single-photon reconstruction efficiency taken from [60], shown in Fig. A.1. This includes the fiducialization of events, requiring $R < 500$ cm, with a 55% efficiency. Since we have already performed the fiducialization in our own simulation, we divide the official efficiencies by this number.

A few examples of our reconstruction efficiencies are shown in Figs. A.5 and A.6 for different values of the parent HNL and dark photon masses in the 3+1 and 3+2 models. These include only reconstruction effects but no geometrical acceptance. The transition between on and off-shell decays is visible in the plots as a sharp drop in efficiency. For on-shell decays, the efficiencies tend to be smaller at large dark photon masses due to the larger separation angles between the e^+e^- pairs for less energetic dark photons.

We also show the total number of e^+e^- pairs expected at the SBN detectors. For that, we use the `DarkNews` implementation of the MicroBooNE, SBND, and ICARUS detectors and the corresponding dirt volumes upstream. Our projections for 6.8×10^{20} POT at MicroBooNE and 15.6×10^{20} POT at SBND and ICARUS [390].

2.4.3 Statistical procedure

We calculate the MiniBooNE χ^2 based on the distribution of $E_\nu^{\rm CCQE-reco}$ using the covariance matrices provided by the MiniBooNE collaboration in [66]. The χ^2 surfaces are obtained by repeating this calculation across two-dimensional grids of model parameters. We do this in two ways: i) for plots of coupling versus mass, we fix all parameters that do not appear in the x and y axes and compute the χ^2 in the ν and $\overline{\nu}$ mode, while ii) for plots of mass versus mass, such as m_4 versus $m_{Z'}$, we fix all parameters except for one mixing angle which we profile over: $U_{\mu 4}$ in the 3+1 model and $U_{\mu 4} = U_{\mu 5}$

in the 3+2 model. This allows us to show the mass parameters that best fit the shape of the LEE, independently of the coupling needed. In this case, we compute the χ^2 using ν mode data only. As in Ref. [60], when quoting the χ^2 probability p_{val} of our best-fit points, we use 6.8, 6.9, and 15.6 degrees of freedom for the neutrino mode, antineutrino mode, and their combination, respectively. This assumes two independent fit parameters, typically $|V_{\mu 4/5}|^2$ and $m_{4/5}$.

In more detail, we vary m_4 and $m_{Z'}$ for the 3+1 model, while in the 3+2 one we vary m_5 and $\Delta = (m_5 - m_4)/m_4$ while fixing $m_{Z'}$ or vary m_5 and $m_{Z'}$ while fixing m_4. In both cases, we profiled over a mixing parameter, setting a maximum value of 10^{-2} for $|U_{\mu 4}|$ (3+1) or for $|U_{\mu 4}|$ and $|U_{\mu 5}|$ (3+2). For the remaining parameters, we use the following default values: $g_D = 2$, $U_{D5} = U_{D4} = 1/\sqrt{2}$, and $\varepsilon = 8 \times 10^{-4}$ ($\varepsilon = 10^{-2}$) for 3+1 (3+2). With our assumptions, the couplings of the dark photon to the HNLs always appear in the combination $\alpha_D^2 |U_{D4}|^4 \varepsilon^2$. Therefore, for different values of each one of these parameters, as long as $|U_{D4}| = |U_{D5}|$, the best-fit regions can be trivially rescaled.

2.4.4 Results

3+1 scenario

Fig. 2.3 shows the regions of preference in the combined ν and $\overline{\nu}$ mode MiniBooNE fit for different values of m_4 and $|V_{\mu 4}|^2$. Both plots set $\varepsilon^2 \alpha_D |U_{D4}|^4 = 5 \times 10^{-8}$ in our benchmark parameters. On the left panel, $|U_{\tau 4}| = 0$, while in the right panel, $|U_{\tau 4}| = 10|U_{\mu 4}|$. The latter helps decrease the HNL lifetime as the coupling $|V_{\ell 4}|^2$ that controls the decay rate is now larger than $V_{mu4}|^2$, which controls the upscattering cross section. Where a discontinuity

is present, it can be attributed to the change of on-shell to off-shell dark photon regimes.

High values of m_4 need higher couplings to produce enough events due to the high threshold for HNL production. On the other hand, when $m_4 < m_{Z'}$ and the dark photon is off-shell in the HNL decay, large couplings are required due to the long decay length of the HNLs. In the off-shell regime, most of the signal stems from HNLs produced in the dirt upstream of the detector. This regime typically produces less energetic e^+e^- pairs than the prompt-decay regime, as the probability of decay inside the MiniBooNE tank is larger for slower HNLs. Furthermore, heavy dark photons tend to produce less forward e^+e^- pairs, further reducing their energy.

Figure 2.5 shows the same regions of preference of the left panel of Fig. 2.3, but exclusively for $m_{Z'} = 30$ MeV. It is then compared with the predictions for the event rates at the three SBN detectors: MicroBooNE, Icarus, and SBND. The orange curves in different dash styles correspond to the parameters where 10^3 e^+e^- pairs would be produced inside the fiducial volume of each detector, considering upscattering in the upstream dirt and inside the detector. This number is presented without any reconstruction or selection efficiencies. The real sensitivity of each experiment will depend on the backgrounds and selection strategy adopted. We leave a detailed study to future work and experimental collaborations.

The best fit of the 3+1 model for $|U_{\tau 4}| = 0$ is given by $|V_{\mu 4}|^2 = 4.8 \times 10^{-7}$, $m_4 = 20$ MeV, and $m_{Z'} = 30$ MeV. We show the prediction for the reconstructed neutrino energy spectrum for this best fit in Fig. 2.4 for neutrino and antineutrino modes. Most events come from coherent scattering on nuclei, although proton-elastic interactions are responsible for about 10% of the total signal. It can also be seen that the rate in neutrino mode is lower than

the data, while in antineutrino mode, it is larger than the data. This is due to the vector nature of the dark photon couplings to quarks. It predicts that the neutrino and antineutrino cross sections on nuclei are the same. This is in mild tension with the MiniBooNE observation that the antineutrino excess is comparatively smaller than the neutrino mode one. The tension is also visible in Table 2.3. The goodness-of-fit is significantly better for neutrino than antineutrino data, so combining the two provides an overall smaller χ^2 probability. Since the excess in neutrino mode is more significant, this mode drives the fit and leads to an overprediction for the number of events in antineutrino mode. In the 3+1 model, the agreement with the data is typically better for long-lived HNL regimes, but it is still at a $\gtrsim 2\sigma$ tension with the combination of the neutrino and antineutrino excess.

Finally, we emphasize that the reconstructed neutrino energy fit has a subleading dependence on the angular distribution and cannot adequately quantify the agreement with the MiniBooNE angular spectrum. A quantitative estimate of this tension, taking into account the correlations between angular bins, is not possible outside the collaboration. Nevertheless, in 3+1 models, we find that virtually all points predict no events in the $\cos\theta \lesssim 0.9$ region. This is due to two main effects: i) for off-shell dark photons, the signal is dominated by dirt production of HNL, so the geometrical acceptance of the detector biases the angular spectrum to be more forward, and i) in the on-shell dark photon regime, the signal is dominated by HNLs produced inside the detector, but the upscattering cross section is predominantly coherent, leading to forward HNL production due to the low momentum exchange with the nucleus. In the next section, we explore $3+2$ scenarios, where HNLs can be short-lived even for off-shell mediators and, therefore, lead to slightly less forward signatures.

Finally, we also explore the effect of simultaneously varying the HNL and mediator masses in Fig. 2.6. The darkest to lightest filled regions show the one, two, and three σ regions of preference, respectively, for the 3+1 model in the plane of m_4 versus $m_{Z'}$. The parameter $|U_{\mu 4}|$ is profiled over with a hard upper bound of $|U_{\mu 4}|^2 < 10^{-4}$. The plot on the right includes one extra mixing, $|U_{\tau 4}|$, which is set to $10 \times |U_{\mu 4}|$. In this case, the upper bound is set on the tau mixing parameter, $|U_{\tau 4}|^2 < 10^{-4}$, explaining why the long-lived region is significantly smaller than in the previous case. The plots are divided in two: a short-lived HNL region ($c\tau_N^0 \leq 10$ cm) shown in shades of blue and a long-lived HNL region ($c\tau_N^0 > 10$ cm) shown in shades of beige, where $c\tau_N^0$ as the decay length of the parent HNL in its rest frame. The two regions correspond to the on-shell and off-shell dark photon cases, respectively. Although we color the regions differently, the fit is done over the entire plane, showing that both on and off-shell regimes can lead to an acceptable fit to the MiniBooNE neutrino energy spectrum.

3+2 scenario

Similarly to the 3+1 scenario, we show the resulting regions of preference in the coupling $|V_{\mu 5}|^2$ versus mass m_5 plane in Fig. 2.7. Each panel corresponds to a fixed value of $\Delta \equiv m_5/m_4 - 1 = 0.3$, 0.5, 1 and 3, going from mildly degenerate to mildly hierarchical masses. In turn, for each panel, we show the resulting preference regions for different fixed values of $m_{Z\prime}$, corresponding to 0.03, 0.06, 0.1, 0.2, 0.5, 0.8 and 1.25 GeV. In these plots, higher values of Δ allow N_5 to be shorter-lived and for it to release more energy into the e^+e^- system. This improves the fit to the excess, up until Δ becomes too large and the decays resemble the 3+1 scenario. The shape of the regions of preference can be understood by noticing that the downward trend at low

m_5 values is caused by long lifetime of N_5, which is typically produced in the dirt and decays more often inside MiniBooNE for larger m_5 due to the steep dependence of the decay rate, $\Gamma \propto m_5^5$. Once N_5 becomes too short-lived to propagate the distance from the dirt to the detector, the regions of preference turn over to then stay flat up to the point where the N_5 production energy threshold is too large. The transition from off-shell to on-shell regions is less noticeable in these plots since HNLs can be short-lived even for off-shell mediators. Nevertheless, it can still be observed as a gap between the two 1σ and 2σ closed regions.

In Fig. 2.9, we can see the distribution of the reconstructed neutrino energy of the best-fit point in the 3+2 model, namely $m_{Z'} = 100$ MeV, $m_5 = 615$ MeV, $\Delta = 0.3$, $|V_{\mu 4}|^2 = |V_{\mu 5}|^2 = 1.1 \times 10^{-6}$, and $\varepsilon = 8 \times 10^{-4}$. Once more, the signal prediction for the neutrino mode undershoots the excess, while the antineutrino signal overshoots it. Overall, Table 2.3 shows that 3+2 models better fit the MiniBooNE energy spectrum, especially for smaller Δ values where the HNL decays produce lower-energy e^+e^- pairs.

Our projections for event rates at the SBN program are shown in Fig. 2.8 for two cases: $m_{Z'} = 30$ and 200 MeV, both for $\Delta = 1$. As before, the contours show the parameter space where we project that 10^3 pairs of e^+e^- will be produced inside the SBND, MicroBooNE, and ICARUS fiducial volumes. As in the 3+1 model, when the signal is dominated by HNL production in the dirt, ICARUS is expected to see as many events as SBND. The smaller neutrino flux at the detector's location is compensated by the greater extent of dirt upstream. It is easy to see that the SBND detector could observe as many as 10^5 e^+e^- pairs with its full exposure.

Turning to mass versus mass plots, Fig. 2.10 shows a fit to neutrino mode data in the plane of Δ versus m_5. We fix $\varepsilon^2 \alpha_D |U_{D5}|^4 = 8 \times 10^{-6}$ and 5×10^{-8},

and impose an upper bound on $|U_{\mu 4}|^2 = |U_{\mu 5}|^2 < 10^{-4}$. The plot exhibits two different shaded colors. The beige color corresponds to N_5 proper decay lengths greater than 10 cm, while the blue one is smaller than 10 cm. The fit is mostly insensitive to the values of Δ once larger than $\Delta \gtrsim 1$. In that case, we recover a scenario similar to the 3+1 model, albeit with a larger coupling on the HNL decay process. Small values of Δ are disfavored due to the longer lifetime and the significant suppression of the energy released in $N_5 \to N_4 e^+ e^-$ decays. Nevertheless, a feature can still be observed at large N_5 masses, where the HNL production occurs by the highest energy neutrinos in the beam at the cost of requiring larger $|V_{\mu 5}|^2$ couplings. We recall that when $1 < \Delta < 2$, the decay process $N_5 \to \nu N_4 N_4$ could, in principle, take place. Similarly for $N_5 \to N_4 N_4 N_4$ when $\Delta > 2$. As discussed in Section 2.4.1, we assume both of these channels to be subdominant due to the structure of the dark photon couplings, which can be easily achieved with symmetry arguments.

The second mass fit is shown in Fig. 2.11. For each panel in the vertical direction, we vary the mass of N_4 to 15, 150, and 250 MeV, while in the horizontal direction, we consider values of ε of 8×10^{-4} and 10^{-2}. We also float $|U_{\mu 4}|^2 = |U_{\mu 5}|^2$, with a hard upper bound of 10^{-4}. As the kinetic mixing increases, more parameter space opens up at large $m_{Z'}$, where the lifetime of the HNL can still be sufficiently short to induce a signal in MiniBooNE. A similar effect happens for lighter N_4, as the mass splitting Δ increases and the N_5 decays faster. The change in regimes from on-shell to off-shell dark photons can be seen in all panels as a feature at intermediate $m_{Z'}$ values.

In summary, the 3+2 model can provide a better fit to the LEE than the 3+1 model when $\Delta \lesssim 1$ due to the lower energy emitted in HNL decays. It still, however, faces two main challenges: the LEE angular distribu-

tion and the tension between neutrino and antineutrino data. While we do show the angular distributions here, we find that 3+2 models tend to predict more events outside the $\cos\theta_{\text{beam}} > 0.9$ region, although the prediction still significantly overshoots the data on the most-forward bin. The values of kinetic mixing, $|V_{\mu 4}|$, and $|V_{\mu 5}|$ can be significantly smaller in this model, even for heavy dark photons, indicating that this scenario is less stringently constrained by other indirect searches for dark photons and HNLs.

2.5 Conclusions

We have reviewed proposed solutions to the low-energy excess of electron-like events at MiniBooNE. Most explanations exploit the limitations in the particle-identification capabilities of the MiniBooNE detector as it cannot distinguish between single $e^{\pm}$, single γ, and collimated or energy-asymmetric e^+e^- or $\gamma\gamma$ pairs. New-physics models that lead to an excess of ν_e and $\overline{\nu}_e$ in the beam, like the popular eV sterile neutrino oscillations, are associated with the single e^- and single e^+ hypothesis and have already been constrained by several experiments, including MicroBooNE, which operated in the same beam as MiniBooNE. Other explanations based on single γ final states, like upscattering to heavy neutrinos with transition magnetic moments or inverse-Primakoff scattering, are far less constrained. The previous single photon search at MicroBooNE is less sensitive to these explanations as it exclusively targets the radiative decays of the $\Delta(1232)$ resonance. Unlike the resonant channel, the single-γ dark sector models predict a dominant coherent-scattering component, which is subject to a larger background due to the absence of a hadronic vertex. We have also discussed proposals based on dark particle decays into e^+e^- and $\gamma\gamma$ pairs inside the detector. These

include dark neutrino models, in which neutrinos interact with nuclei in the detector to produce short-lived heavy neutral leptons. We also comment on a few less explored alternatives to upscattering, including inverse-Primakoff scattering, neutrino-induced vector boson fusion, and dark bremsstrahlung, all of which warrant further study.

After this detailed overview, we have focused on a representative model that advocates HNLs upscattering and subsequent fast decays: the Three Portal model. We have also performed a comprehensive fit to the LEE neutrino energy spectrum. We consider both cases of one HNL (3+1) and two HNLs (3+2) in the spectrum. The 3+2 model is less constrained and can accommodate solutions to the LEE at large mediator masses, where the HNL decays $N_5 \to N_4 e^+ e^-$ proceed via off-shell mediators. In addition, the mass splitting between the parent and daughter HNLs can lead to even lower-energy events, providing a better fit to the LEE. In 3+2 models, we find better fits to the LEE than the best fit in standard sterile-neutrino-driven oscillation hypotheses, with an overall χ^2 probability of 14%. The goodness-of-fit is primarily limited by the tension between the relative number of excess events in neutrino and antineutrino modes. MiniBooNE is compatible with the SM expectation that neutrino cross sections are larger than antineutrino ones; in contrast, the vectorial nature of dark photon interactions predicts they are the same. Another challenge for dark photon models is reproducing the LEE angular spectrum. For dark neutrinos to produce events that are not fully concentrated in the region $\cos\theta_{\rm beam} > 0.9$, the model requires off-shell mediators and large HNL masses, $m_N \gtrsim 400$ MeV. In addition to the uncertainties on the e^+e^- reconstruction, quantifying the agreement with the angular spectrum and its bin-to-bin correlations is not possible with publicly available information, although the prediction significantly overshoots

the excess in the most-forward bin, where only $\sim 32\%$ of the total excess is concentrated. Improvements to the angular spectrum and the neutrino-to-antineutrino ratio can be obtained in models where the upscattering is mediated by a scalar or an axial-vector coupling to quarks. Both possibilities, however, are more severely constrained by other direct searches.

For the first time, our results allow a thorough comparison of the dark neutrino interpretation of MiniBooNE with other experiments' data. Extending existing constraints on dark neutrino models to the slices of parameter space we show here will be crucial to understanding this LEE interpretation status. Looking forward, the SBN program at Fermilab will be able to test the dark neutrino LEE hypothesis using the same beamline in which MiniBooNE operated. As a crude estimate of the reach of each detector, we show the signal event rate expected before reconstruction efficiencies. In the MiniBooNE regions of preference, the number of e^+e^- pairs produced inside the fiducial volume of MicroBooNE can be of $\mathcal{O}(10^3)$, while for SBND and ICARUS, this number can be well above $\mathcal{O}(10^4)$. Despite being located further away from the target, ICARUS can observe as many events as SBND thanks to the larger amount of dirt upstream of the detector, offering the ideal conditions to constrain the parameter space where HNLs are long-lived. A full sensitivity study that contextualizes these event rates on top of SM backgrounds and reconstruction efficiencies in each detector is in order.

We note that our dark neutrino fit is subject to uncertainties in the treatment of the upscattering cross section. These uncertainties are small for light mediators since the signal is dominated by the cleaner coherent neutrino-nucleus scattering channel. However, our `DarkNews` simulation shows that the signal can contain a significant portion of proton-elastic events for heavier mediators, indicating that larger energy transfer regimes can dominate the

upscattering. The tools available to simulate such processes lack a detailed treatment of the nuclear response in these regimes. Future efforts with automated tools like ACHILLES [392] and more comprehensive implementations of dark neutrinos in tools like GENIE [393] will be crucial to support searches for dark particles at next-generation neutrino experiments.

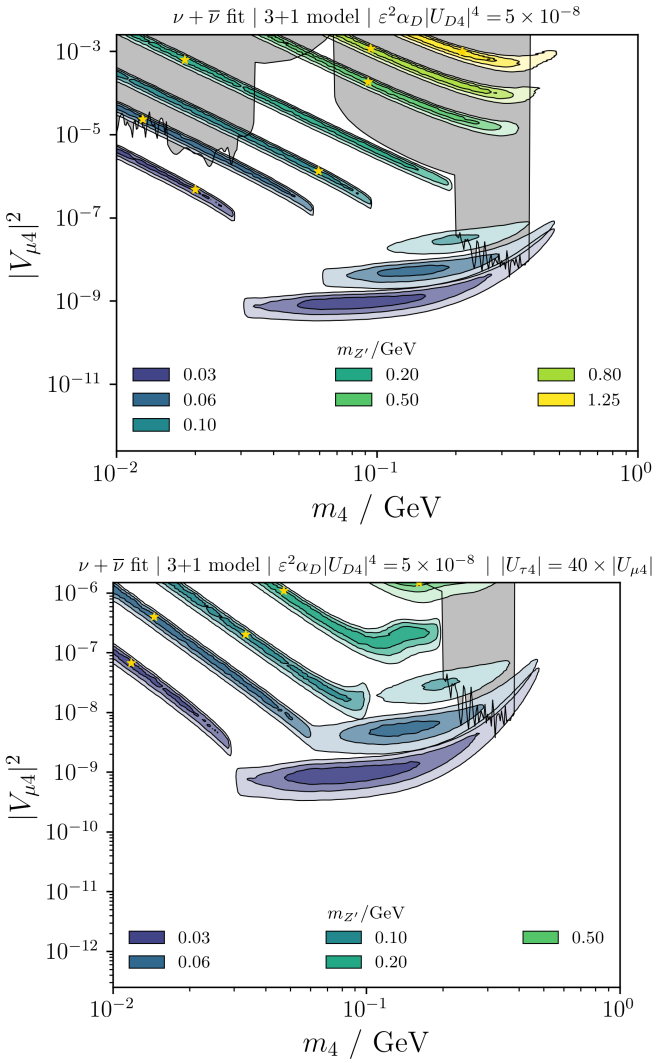

Figure 2.3: The MiniBooNE $E_\nu^{\mathrm{CCQE-reco}}$ best-fit regions in the $|V_{\mu 4}|^2$ and m_4 plane for the 3+1 model. On the first plot, we set $|U_{\tau 4}| = 0$, and on the second $|U_{\tau 4}| = 10|U_{\mu 4}|$. Each color represents a given fixed value of $m_{Z'}$, and the different shading corresponds to the 1σ, 2σ, and 3σ CL regions (2 d.o.f.). Model-independent limits on heavy neutrinos exclude the shadowed region [388]. Other constraints from neutrino scattering and meson decays are not shown.

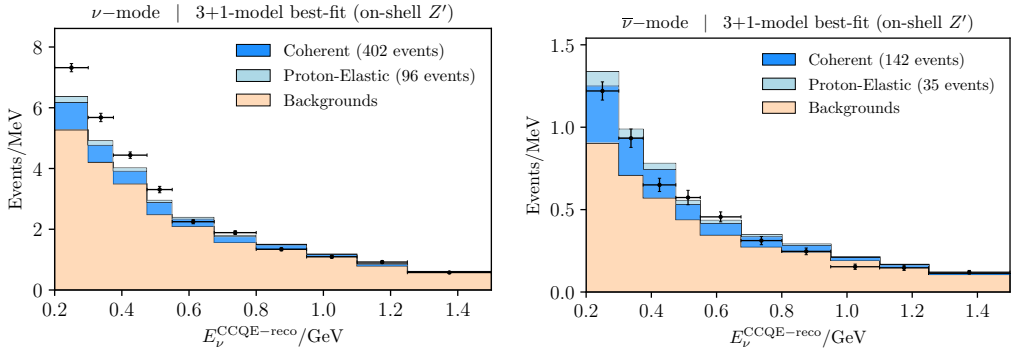

Figure 2.4: The reconstructed neutrino energy $E_\nu^{\mathrm{CCQE-reco}}$ at MiniBooNE for the FHC (ν) mode (upper panel) and the RHC ($\overline{\nu}$) mode (lower panel). The prediction of the best-fit point in the 3+1-model ($|V_{\mu 4}|^2 = 4.8 \times 10^{-7}$, $m_4 = 20$ MeV, $m_{Z'} = 30$ MeV) is shown as a solid blue histogram, separated into events from coherent neutrino-nucleus scattering and proton-elastic neutrino scattering.

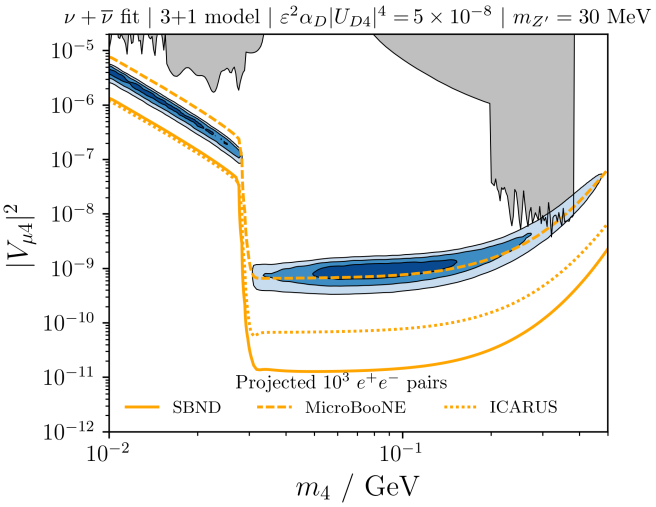

Figure 2.5: Same as Fig. 2.3 showing only the case where $m_{Z'} = 30$ MeV and $|U_{\tau 4}| = 0$. The orange lines indicate where the MicroBooNE (dashed), Icarus (dotted), and SBND (solid) detectors can expect 10^3 e^+e^- pairs from N_5 decays to be produced inside their respective fiducial volumes (before any reconstruction efficiencies).

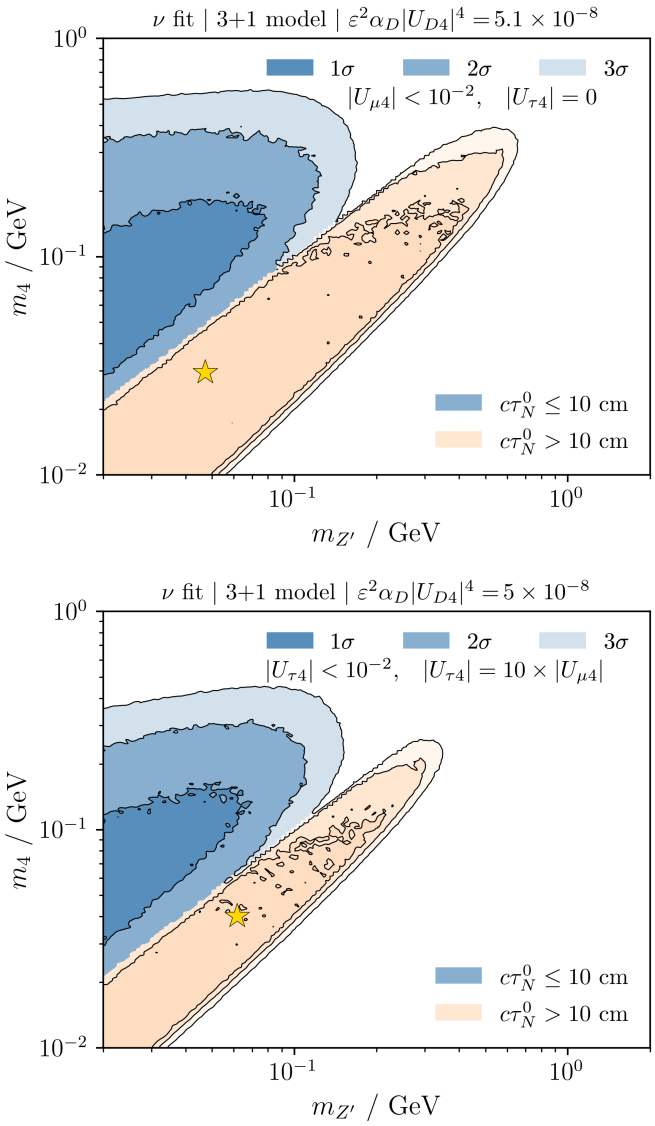

Figure 2.6: The MiniBooNE $E_\nu^{\mathrm{CCQE-reco}}$ best-fit regions in the m_4 and $m_{Z'}$ plane for the 3+1 model without (upper) and with (lower) mixing between N_4 and tau neutrinos. The different regions show the 1σ, 2σ, and 3σ best-fit regions. The coupling $|U_{\mu4}|^2$ is profiled over with an upper bound of $|U_{\mu4}|^2 < 10^{-4}$ (left) and $|U_{\mu4}|^2 < 10^{-4}/10^2$ (right). The dark coupling and kinetic mixing are fixed, as indicated at the top of the panels. We divide the regions into a short-lived and a long-lived regime, where the HNLs decay rapidly, $c\tau_N^0 \leq 10$ cm, and a region where dirt events and displaced vertices are expected, $c\tau_N^0 > 10$ cm, where $c\tau_N^0$ is the HNL proper lifetime.

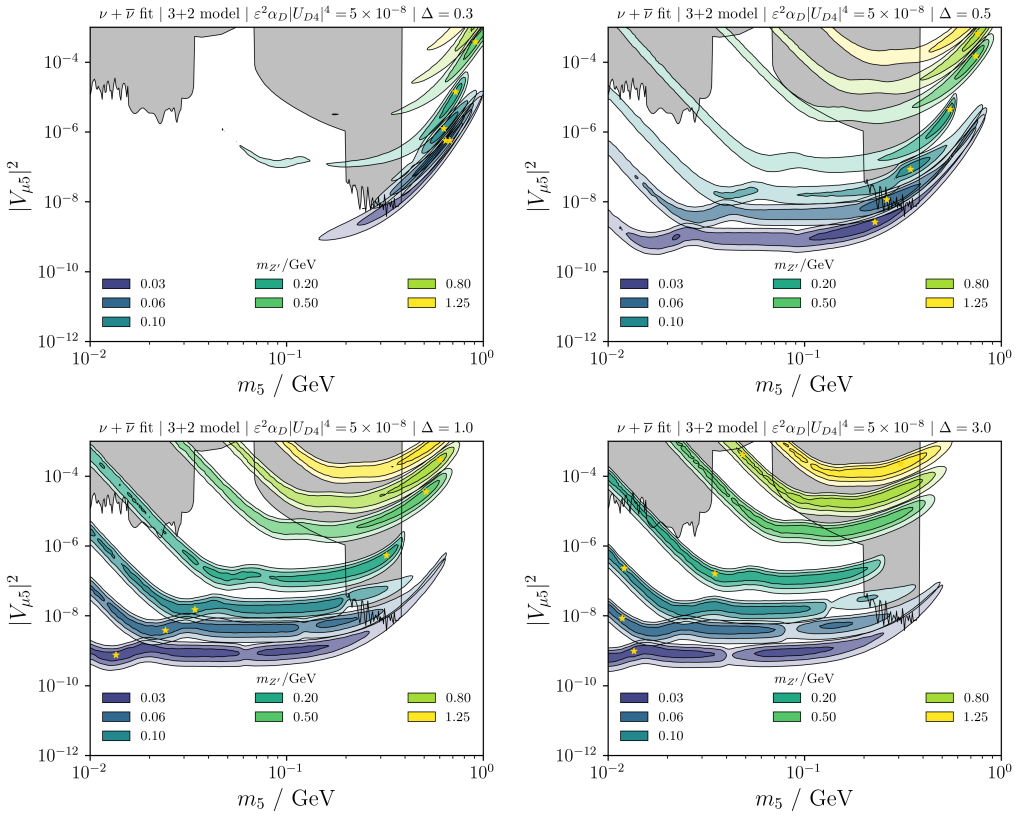

Figure 2.7: The MiniBooNE $E_\nu^{\mathrm{CCQE-reco}}$ best-fit regions in the $|V_{\mu 5}|^2$ and m_5 plane for the 3+2 model. Each panel corresponds to a different value of Δ, as indicated at the top of the panel. Each color represents a given fixed value of $m_{Z'}$, and the different shading corresponds to the 1σ, 2σ, and 3σ CL regions (2 d.o.f.). The 1σ regions in the low-mass and large-coupling regime appear disconnected due to an interpolation artifact. This is due to the strong dependence of the event rate on the HNL lifetime when the signal is dominated by dirt upscattering. Model-independent limits on heavy neutrinos exclude the shadowed region [388]. Other constraints from neutrino scattering and meson decays are not shown.

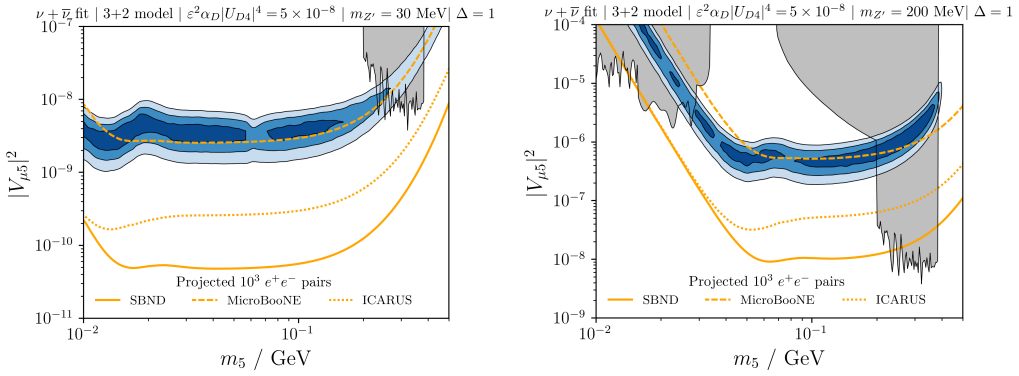

Figure 2.8: Same as Fig. 2.7 but for $m_{Z'} = 30$ MeV (upper) and $m_{Z'} = 200$ MeV (lower). The mass splitting has been fixed to $\Delta = 1$. The orange lines indicate where the MicroBooNE (dashed), Icarus (dotted), and SBND (solid) detectors can expect 10^3 e^+e^- pairs from N_5 decays to be produced inside their respective fiducial volumes (before any reconstruction efficiencies).

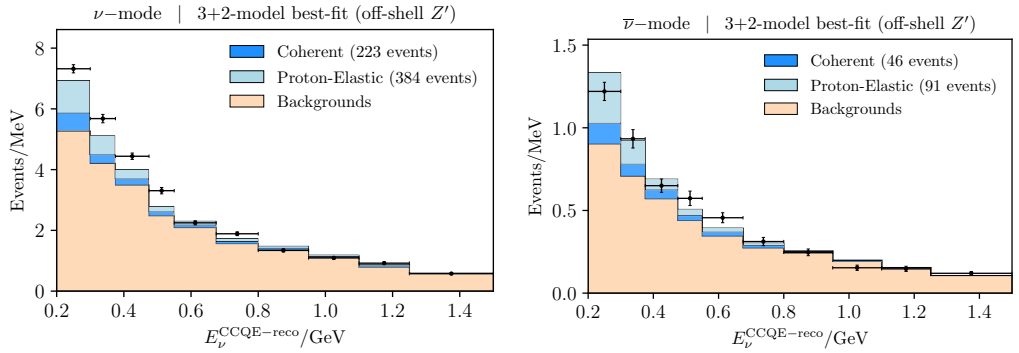

Figure 2.9: The reconstructed neutrino energy $E_\nu^{\mathrm{CCQE-reco}}$ at MiniBooNE for ν mode (upper panel) and $\overline{\nu}$ mode (lower panel). The prediction of the best-fit point in the 3+2-model ($m_{Z'} = 100$ MeV, $m_5 = 615$ MeV, $\Delta = 0.3$, $|V_{\mu4}|^2 = |V_{\mu5}|^2 = 1.1\times10^{-6}$, $\varepsilon = 8\times10^{-4}$) is shown as solid blue histograms, separated into events from coherent neutrino-nucleus scattering and proton-elastic neutrino scattering.

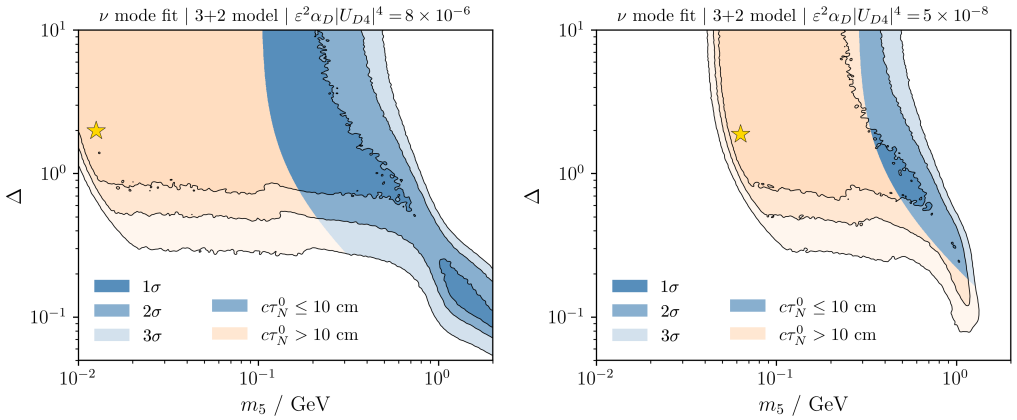

Figure 2.10: The MiniBooNE $E_\nu^{\mathrm{CCQE-reco}}$ best-fit regions in the m_5 and Δ plane for the 3+2 model for two choices of couplings. The different regions show the 1σ, 2σ, and 3σ best-fit regions. The couplings $|U_{\mu4}|^2 = |U_{\mu5}|^2$ are profiled over with an upper bound of $|U_{\mu4}|^2 < 10^{-2}$, which can be tightened by choosing larger dark couplings and kinetic mixing. All the plots consider $m_{Z'} = 1.25$ GeV and couplings as indicated at the top of each panel. We divide the regions into a short-lived and a long-lived regime, where the HNLs decay rapidly, $c\tau_N^0 \leq 10$ cm, and a region where dirt events and displaced vertices are expected, $c\tau_N^0 > 10$ cm, where $c\tau_N^0$ is the HNL proper lifetime.

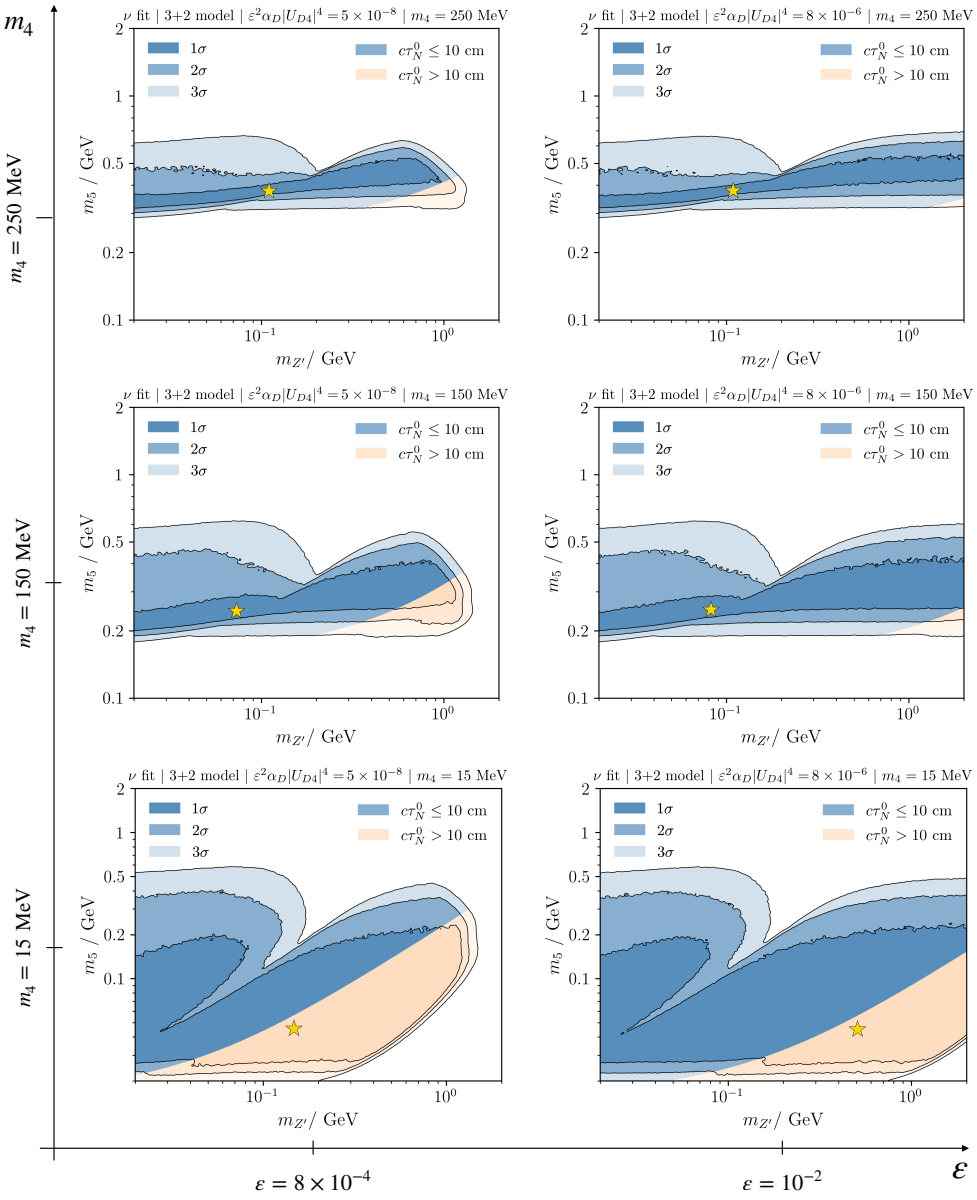

Figure 2.11: The MiniBooNE $E_\nu^{\mathrm{CCQE-reco}}$ best-fit regions in the Δ versus m_5 plane for the 3+2 model with $m_{Z\prime} = 1.25$ GeV. The different regions show the 1σ, 2σ, and 3σ CL regions (2 d.o.f.). From the bottom to the upper rows, we set m_4 equal to 15, 150, and 250 MeV, respectively. In the left and right columns we set ϵ equal to 8×10^{-4} and 10^{-2}, respectively. The couplings $|U_{\mu 4}|^2 = |U_{\mu 5}|^2$ are profiled over with an upper bound of $|U_{\mu 4}|^2 < 10^{-4}$. We divide the regions into a short-lived and a long-lived regime, where the HNLs decay rapidly, $c\tau_N^0 \leq 10$ cm, and a region where dirt events and displaced vertices are expected, $c\tau_N^0 > 10$ cm, where $c\tau_N^0$ is the HNL proper lifetime.

Chapter 3

Heavy dark sectors and white dwarfs

Terrestrial experiments let us search for dark sectors in a more controlled way than astrophysical ones, because we have direct access to the sources. Near detectors, for example, are a powerful tool to measure how the beams evolve in the case of accelerator experiments. However, the energies of astrophysical sources are way more powerful and, in this way, astrophysical experiments can shed light in different ways on our knowledge of hidden sectors. We will devote to one particular case: white dwarfs (WDs) and plasmon decay enhanced by a dark photon, considering the Three Portal model. Since the common masses searched for this model are heavier than the temperatures of WDs [88, 194, 265, 380, 394–400], we will just consider a heavy mediator case, when "heavy" must be understood in terms of the temperatures considered.

3.1 Introduction

White dwarfs provide unique opportunities to study new physics due to their extreme conditions. By analyzing the luminosity emitted by WDs, it is feasible to probe the underlying physics in ways that are impossible in Earth-based laboratories. One particular aspect is the cooling process of young and hot white dwarfs, which is primarily driven by plasmon decay into neutrinos originating from their core [401, 402]. The potential for enhanced cooling through plasmon decay, mediated by new particles, has been explored in the context of models with anomaly-free symmetry, such as $\mathrm{U}(1)_{B-L}$ and $\mathrm{U}(1)_{L_\alpha - L_\beta}$ and which will be considered in Chapter 4. These decay processes contribute to the production of the SM neutrinos [403] and could also lead to the generation of new light particles [404]. Furthermore some studies have shown that there could be other important mechanisms under the assumption of a strong magnetic field [405–410], such as neutrino pair synchrotron emission from electrons [411–416].

The aim of this chapter is to investigate the emission of neutrinos from WDs, with a focus on BSM interactions in the neutrino production rate. Specifically and as mentioned in the first paragraph, we will use the Three Portal model. Since the dark photon is capable of interacting with neutrinos as well as electromagnetic-charged particles, its presence could potentially alter the production of neutrinos through plasmon decay at the early stages of a WD.

The structure of this chapter is organized as follows. In Section 3.2, we provide a concise overview of the physics of white dwarfs. In Section 3.3, we present the emission rate of neutrino production, both within the context of SM interactions and with the modified expressions that include the dark sector. Our results are discussed and presented in Section 3.4, followed by

our conclusions in Section 3.5.

3.2 Theoretical framework

3.2.1 White dwarfs

A white dwarf is a dense star that forms after a normal star has exhausted its nuclear fuel and undergone the final stages of its evolution. This process ejects the outer layers of the star, leaving behind a hot, dense core primarily composed of carbon and oxygen. The core is supported by electron degeneracy pressure, which prevents it from collapsing further and instead causes it to contract and cool over billions of years. White dwarfs are incredibly dense ($\sim 10^6\,\mathrm{kg/m^3}$), with a mass similar to the Sun but a size similar to that of the Earth.

Electrons play a crucial role in determining the equation of state (EoS) and the structure of white dwarfs. In Ref. [417], a theoretical EoS for WDs is obtained by assuming a Wigner-Seitz (WS) cell, which is a uniformly negatively charged spherical cell with a positively charged ion at its centre. Corrections to the electron energy due to the electrostatic potential were also introduced, which are the most significant correction to the EoS. Further corrections, such as considering the non-rigidity of ions within the WS cell and self-interactions, were also taken into account. However, it was determined that these corrections do not significantly affect the behavior of high-density matter.

Initially, white dwarfs have extremely high temperatures before cooling down to become faint objects. There are several stages of cooling that it goes through, with each stage characterized by a different mechanism of energy loss. The equation governing the temperature evolution of WDs depends on

the cooling mechanism and the physical properties,

$$\frac{dT_\star}{dt} = -\frac{L_\gamma}{4\pi R_\star \sigma_{\rm SB} T_\star} - \frac{L_\nu}{4\pi R_\star \sigma_{\rm SB} T_\star}. \tag{3.1}$$

The left-hand side represents the temperature change rate with respect to time, where $T_\star$ is the temperature of the white dwarf. The right-hand side consists of two terms, representing the rates of energy loss due to surface photon radiation (L_γ) and neutrino emission (L_ν), respectively. Here $R_\star$ is the WD radius, and $\sigma_{\rm SB}$ is the Stefan-Boltzmann constant.

The dominant cooling mechanism for newborn WDs is the emission of neutrinos, produced primarily through plasmon decay [401, 402]. The produced neutrinos easily escape the dense core of the WD, carrying away energy and facilitating the loss of thermal energy. The cooling through plasmon decay could in principle be enhanced by strong magnetic fields or through the addition of new fields that could connect SM neutrinos with the electron-positron loop [407–412, 414–416, 418–420]. As the white dwarf continues to cool down, its temperature eventually drops to approximately 10^3 K, at which point it enters the photon cooling stage. In this stage, the white dwarf radiates energy primarily in the form of photons, and its luminosity is dominated by photon radiation. Consequently, this stage is not of interest in the discussion that follows.

The dark photon, Z', as considered by the Three Portal model, can interact with both electromagnetic and dark currents. Its mass is typically assumed to be less than $\mathcal{O}(1\text{GeV})$. When the mass of the dark photon is much smaller than the mass of the Z boson, $M_{Z'}/M_Z \ll 1$, the complicated interactions of the dark photon can be approximated by a simplified form as follows,

$$\mathcal{L}_I \simeq -\epsilon e J_\mu^{\rm EM} Z'^\mu - g_{\rm D} J_\mu^{\rm D} Z'^\mu, \tag{3.2}$$

where $J_\mu^{\rm EM}$ is an electromagnetic current, $J_\mu^{\rm D}$ is a dark current that consists of dark neutrino states: $\bar{\nu}_{\rm D}\gamma_\mu\nu_{\rm D}$, and Z'^μ is a dark photon. This interaction is the main ingredient to compute the BSM contribution to plasmon decay in WDs.

3.3 Neutrino emission rate

3.3.1 Review of emission rate

The release of neutrinos has a significant impact on the energy loss of stars that are extremely hot or dense. The production rate of neutrinos can be greatly affected by the combined effects of the stellar plasma. For instance, photons may decay into pairs of neutrinos ($\gamma \to \nu\overline{\nu}$), carrying away energy [401]. This is made possible by modifying the dispersion relations of the photon due to thermal effects that allow it to decay. Because this arises due to the interaction of the photons with the plasma that surrounds it, they are also called plasmons.

Photon-self energy at finite temperature

To determine the neutrino emissivity due to plasmon decay, we must first compute the self-energy of the photon at a finite temperature, as it plays a crucial role in the emission rate computation. The most comprehensive expression for the photon-self energy at a finite temperature is given as [421, 422],

$$\Pi^{\mu\nu} = 4e^2 \int \frac{d^3k}{(2\pi)^3} \frac{f_e(E_k) + f_{\bar{e}}(E_k)}{2E_k} \times \frac{Q\cdot K(K^\mu Q^\nu + K^\nu Q^\mu) - Q^2 K^\mu K^\nu - (Q\cdot K)^2 g^{\mu\nu}}{(Q\cdot K)^2 - Q^4/4} \tag{3.3}$$

here, $Q = (q_0, \vec{q})$ and $K = (E_k, \vec{k})$ represent the 4-momentum of the photon and electron (or positron), respectively and $Q \cdot K = q_0 E_k - \vec{k}\cdot\vec{q}$. The thermal distribution of the electron (or positron) is denoted by $f_e(E_k)$ (or $f_{\bar{e}}(E_k)$). The self-energy tensor of a thermal photon can be divided into two components: longitudinal and transverse components as follows,

$$\Pi^{\mu\nu} = F P_L^{\mu\nu} + G P_T^{\mu\nu} \tag{3.4}$$

where the projectors are:

$$\begin{aligned} P_T^{\mu\nu} &= \left(\delta^{ij} - \hat{q}^i \hat{q}^j\right)\delta_i^\mu \delta_j^\nu \\ P_L^{\mu\nu} &= \left(- g^{\mu\nu} + \frac{Q^\mu Q^\nu}{Q^2}\right) - P_T^{\mu\nu}. \end{aligned} \tag{3.5}$$

Evaluating the 00-elements of the longitudinal and transverse components of the photon self-energy yields $P_T^{00} = 0$ and $P_L^{00} = \vec{q}^2/Q^2$, respectively. Consequently, we find that $F = Q^2/\vec{q}^2 \Pi^{00}$. Similarly, considering the xx-elements of the transverse and longitudinal components gives $P_T^{xx} = 1$ and $P_L^{xx} = 0$, respectively, leading to $G = \Pi^{xx}$, if x is a transverse direction. As a result, we can express Eq. (3.4) as follows,

$$\Pi^{\mu\nu} = \frac{Q^2}{\vec{q}^2}\Pi^{00} P_L^{\mu\nu} + \Pi^{xx} P_T^{\mu\nu}. \tag{3.6}$$

We identify the first and second terms as $\Pi_L^{\mu\nu}$ and $\Pi_T^{\mu\nu}$, respectively. It is

important to compute these projected quantities because they appear in the propagator of the plasmon:

$$D^{\mu\nu} = \frac{-i\, g^{\mu\lambda}}{Q^2 - F}\, P^{\nu}_{L\lambda} + \frac{-i\, g^{\mu\lambda}}{Q^2 - G}\, P^{\nu}_{T\lambda} \tag{3.7}$$

It is necessary to determine various factors to calculate the photon polarization 4-vectors at finite temperature. This includes the dispersion functions of plasmons as well as the corresponding residual functions ($Z_t(q)$ and $Z_l(q)$), where $q \equiv |\vec{q}|$. In this context, the dispersion relations for photons and plasmons provide the relationship between the frequency ω_t and ω_l and the momentum q of the plasmon. These relations provide information about the energy of the plasmon.

The dispersion function for the plasmon is determined using the longitudinal propagator. The precise form of the propagator is found by considering $D^{00} = \frac{1}{q^2 - \Pi_L(Q)}$. If $\omega_l(q)$ represents the energy of the longitudinally polarized plasmon on-shell, in its vicinity it can be deduced that [421],

$$\lim_{q_0 \to \omega_l(q)} D^{00} = \frac{\omega_l(q)^2}{q^2} \frac{Z_l(q)}{q_0^2 - \omega_l(q)^2} \tag{3.8}$$

and the dispersion relation for ω_l is obtained by setting the denominator equal to zero, meaning that $\Pi_L(\omega_l(q), q) = q^2$. Therefore, we obtain

$$\omega_l(q)^2 = \frac{\omega_l(q)^2}{q^2} \Pi_L(\omega_l(q), q). \tag{3.9}$$

Furthermore, since $\omega_l(q)$ is also the pole of the propagator, the value of $Z_l(q)$ can be easily found from Eq. (3.8)

$$Z_l(q) = \frac{q^2}{\omega_l(q)^2}\left[-\frac{\partial \Pi_L}{\partial q_0^2}(\omega_l(q), q)\right]^{-1} \tag{3.10}$$

Similarly, for the transverse propagator, where x is a transverse direction, we have $D^{xx} = \frac{1}{q_0^2 - q^2 - \Pi_T(Q)}$. The pole of the propagator is given by $\omega_t(q)$, and in its vicinity, the propagator takes the form [421]

$$\lim_{q_0 \to \omega_t(q)} D^{xx} = \frac{Z_t(q)}{q_0^2 - \omega_t(q)^2}, \tag{3.11}$$

the dispersion relation for ω_t is found to be

$$\omega_t(q)^2 = q^2 + \Pi_T(\omega_t(q), q), \tag{3.12}$$

and the residual function $Z_t(q)$ is given by

$$Z_t(q) = \left[1 - \frac{\partial \Pi_T}{\partial q_0^2}(\omega_t(q), q)\right]^{-1}. \tag{3.13}$$

Finally, we can define the plasmon polarization 4-vectors modified due to the effects of the temperature,

$$\begin{aligned} \varepsilon^\mu(q, \lambda = 0) &= \frac{\omega_l(q)}{q}\sqrt{Z_l(q)}(1, 0)^\mu \\ \varepsilon^\mu(q, \lambda = \pm 1) &= \sqrt{Z_t(q)}(0, \varepsilon_\pm(q))^\mu \end{aligned} \tag{3.14}$$

where $\varepsilon_\pm(q)$ are two unit mutually orthogonal vectors on the plane transverse to $\vec{q}$.

During the integration of the self-energy, the quantity $v \equiv k/E_k$, where $k \equiv |\vec{k}|$, may lead to three different temperature regimes: a non-relativistic, relativistic or degenerate regime.

In the non-relativistic limit ($T \ll m_e$) where particles are non-degenerate

$(T \ll m_e - \mu)$, v is equal to 0. On the other hand, in the relativistic limit, where electrons can be considered massless, the parameter v takes on the value of 1. This limit is observed in either a high-density regime ($\mu \gg m_e$) or a high-temperature regime ($T \gg m_e$). Finally, $v = v_F \equiv p_F/E_F$ in the degenerate limit, where $p_F \equiv \left(3\pi^2 n_e\right)^{1/3}$ is the Fermi momentum, $E_F \equiv \mu(T=0)$ is the Fermi energy, and n_e is the number density of electrons. In the degenerate limit, df_e/dk peaks at v_F. In such cases, we can approximate the integrals by extracting this central value, denoted as v_*, from the integral so that [421],

$$\Pi_L = \omega_p^2 \frac{3}{v_*^2}\left(\frac{q_0}{2v_* q}\ln\frac{q_0 + v_* q}{q_0 - v_* q} - 1\right) \tag{3.15}$$

$$\Pi_T = \omega_p^2 \frac{3}{2v_*^2}\left(\frac{q_0^2}{q^2} - \frac{q_0^2 - v_*^2 q^2}{q^2}\frac{q_0}{2v_* q}\ln\frac{q_0 + v_* q}{q_0 - v_* q}\right), \tag{3.16}$$

here, ω_p refers to the plasma frequency, which describes the oscillation of the plasma itself due to changes in the separation of electric charges caused by the motion of the charged particles. This type of oscillation is also referred to as Langmuir waves [423]. It is equal to:

$$\omega_p^2 = \frac{4\alpha}{\pi}\int_0^\infty dk \frac{k^2}{E_k}\left(1 - \frac{1}{3}v^2\right)\left(f_e(E_k) + f_{\bar{e}}(E_k)\right) \tag{3.17}$$

By using the aforementioned approximations in Eq. (3.10) and (3.13), we can express Z_l and Z_t as follows,

$$Z_l^{-1} = \frac{3\omega_p^2}{2v_*^2 q^2}\left(\frac{\omega_l^2}{\omega_l^2 - v_*^2 q^2} - \frac{\omega_l}{2v_* q}\ln\frac{\omega_l + v_* q}{\omega_l - v_* q} - 1\right) \tag{3.18}$$

$$Z_t^{-1} = 1 - \frac{3\omega_p^2}{2v_*^2 q^2}\left(\frac{3}{2} - \frac{3\omega_t^2 - v_*^2 q^2}{2\omega_t^2}\frac{\omega_t}{2v_* q}\ln\frac{\omega_t + v_* q}{\omega_t - v_* q}\right) \tag{3.19}$$

In the computation of the plasmon decay, an additional contribution to the self-energy arises from a diagram containing a γ^5 matrix at one of its vertices. This axial contribution is due to the electroweak sector of neutrinos and must also be calculated. The magnitude of this purely transverse tensor is given by [421]

$$\begin{aligned}\Pi_A(Q) =& \frac{2\alpha}{\pi}\frac{Q^2}{q}\int dk \frac{k^2}{E_k^2}\big[f_e(E_k) - f_{\bar{e}}(E_k)\big] \\ &\times\left(\frac{q_0}{2qv}\ln\frac{q_0 + vq}{q_0 - vq} - \frac{Q^2}{q_0^2 - v^2 q^2}\right)\end{aligned} \tag{3.20}$$

Here α is the fine structure constant. By employing the same approximation as previously mentioned, we can obtain the following expression

$$\Pi_A(Q) = \omega_A \frac{Q^2}{q}\frac{3}{v_*^2}\left(\frac{q_0}{2qv_*}\ln\frac{q_0 + v_* q}{q_0 - v_* q} - 1\right). \tag{3.21}$$

Here, ω_A represents an axial frequency, which is defined as,

$$\begin{aligned}\omega_A &= \lim_{q\to 0}\frac{\Pi_A(\omega_t(q), q)}{q} \\ &= -\frac{2\alpha}{3\pi}\int dk \frac{k^3}{E_k^2}\frac{d}{dk}\big[f_e(E_k) - f_{\bar{e}}(E_k)\big].\end{aligned} \tag{3.22}$$

We now have all the necessary elements to compute the plasmon decay

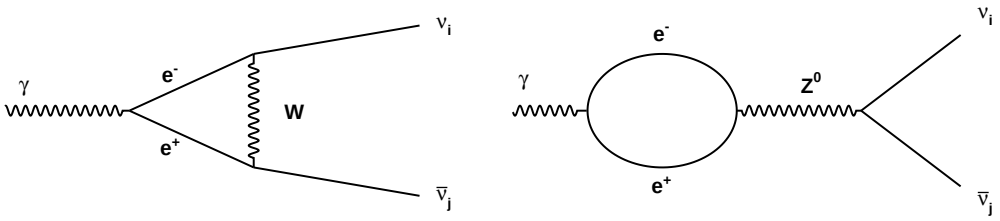

Figure 3.1: Diagrams that contribute to the plasmon decay: trough the charged and neutral currents.

and the neutrino emission rates.

Amplitude and decay width

Figure 3.1 displays the two SM diagrams contributing to plasmon decay. These diagrams can be expressed in a way that includes the previously computed self-energy,

$$\begin{aligned}\mathcal{M} = \frac{G_F}{\sqrt{8\pi\alpha}}\Bigg[&\varepsilon_\mu(\omega_l,q)C_V^{\rm SM}\Big(\Pi_L(\omega_l,q)\Big(1,\frac{\omega_l}{q}\hat{q}\Big)^\mu\Big(1,\frac{\omega_l}{q}\hat{q}\Big)^\nu\Big)\\ &+\varepsilon_\mu(\omega_t,q)g^{\mu i}\Big(C_V^{\rm SM}\Pi_T(\omega_t,q)\Big(\delta^{ij}-\hat{q}^i\hat{q}^j\Big)\\ &+C_A\Pi_A(\omega_t,q)(i\varepsilon^{ijm}\hat{q}^m)\Big)g^{\nu j}\Bigg]\overline{u}(p_1)\gamma_\nu(1-\gamma_5)v(p_2)\end{aligned} \tag{3.23}$$

G_F is the Fermi constant, which appears because $M_W^2(M_Z^2) \gg p^2$. The coefficient $C_V^{\rm SM}$ takes on a value of $2\sin^2\theta_W + 1/2$ for ν_e, and $2\sin^2\theta_W - 1/2$ for other neutrino species. Meanwhile, C_A is equal to $1/2$ for ν_e and $-1/2$ for all others. We are explicitly stating that C_V belongs to the SM to distinguish it from the DS contribution. This is not the case for the axial component, as it remains unaffected by the inclusion of new physics. It should be noted that we assume the masses of the weak bosons to be much larger than the momenta involved in the process. Finally, if $\lambda = l, t$ represents the longitudinal or

transverse polarization, respectively, the above equation can be expressed using shorthand notation

$$\mathcal{M} = \frac{G_F}{\sqrt{2}}\Big(\Gamma^{\mu\nu}_{\lambda}\varepsilon_{\nu}(\vec{q},\lambda)\Big)\overline{u}(p_1)\gamma_{\nu}(1-\gamma_5)v(p_2) \tag{3.24}$$

where a sum over polarization is assumed.

The decay width of the process given a specific polarization λ is,

$$\begin{aligned}\Gamma_{\lambda}(q) = \frac{1}{2\omega_{\lambda}(q)}\int\frac{d^3p_1}{(2\pi)^3}\frac{1}{2p_1}\int\frac{d^3p_2}{(2\pi)^3}\frac{1}{2p_2} \\ (2\pi)^4\delta^{(4)}(P_1+P_2-Q)|\mathcal{M}|^2.\end{aligned} \tag{3.25}$$

The integral can be performed easily since the final states only involve neutrinos, which are independent of the self-energy

$$\Gamma_{\lambda}(q) = -\frac{G_F^2}{12\pi}\frac{\omega_{\lambda}(q)^2-q^2}{\omega_{\lambda}(q)}\Big(\Gamma^{\alpha\mu}_{\lambda}\varepsilon_{\mu}(q,\lambda)\Big)\Big(\Gamma^{\lambda}_{\alpha\rho}\varepsilon^{\rho}(q,\lambda)\Big)^* \tag{3.26}$$

Since the expression is evaluated at $q^0 = \omega_{\lambda}(q)$, it is possible to use the dispersion relations to derive more explicit relations for each polarisation,

$$\Gamma_l(q) = (C_V^{\mathrm{SM}})^2\frac{G_F^2}{48\pi^2\alpha}Z_l(q)\Big(\omega_l(q)^2-q^2\Big)^2\omega_l(q) \tag{3.27}$$

$$\begin{aligned}\Gamma_t(q) = \frac{G_F^2}{48\pi^2\alpha}Z_t(q)\frac{\omega_t(q)^2-q^2}{\omega_t(q)} \\ \times\left((C_V^{\mathrm{SM}})^2\Big(\omega_t(q)^2-q^2\Big)^2 + C_A^2\Pi_A(\omega_t(q),q)^2\right)\end{aligned} \tag{3.28}$$

Emissivity of the plasma

To calculate the Emissivity $\mathcal{Q}$ of the plasma, which represents the rate of energy loss per unit volume, we must integrate the decay rate over the phase space of the photon, with weighting by number density and energy, and sum over the polarization states of the photon as well as the different species of neutrinos. Upon substitution of the previously derived expressions, we obtain the following Emissivity for each type of polarization

$$\mathcal{Q}_T = \sum_\nu (C_V^{\rm SM})^2 \frac{G_F^2}{48\pi^4\alpha} \int_0^\infty dq q^2 Z_t(q) \Big(\omega_t(q)^2 - q^2\Big)^3 n_B(\omega_t(q)) \tag{3.29}$$

$$\mathcal{Q}_A = \sum_\nu C_A^2 \frac{G_F^2}{48\pi^4\alpha} \int_0^\infty dq q^2 Z_t(q) \Big(\omega_t(q)^2 - q^2\Big) \times \Pi_A(\omega_t(q), q)^2 n_B(\omega_t(q)) \tag{3.30}$$

$$\mathcal{Q}_L = \sum_\nu (C_V^{\rm SM})^2 \frac{G_F^2}{96\pi^4\alpha} \int_0^\infty dq q^2 Z_l(q) \Big(\omega_l(q)^2 - q^2\Big)^2 \times \omega_l(q)^2 n_B(\omega_l(q)) \tag{3.31}$$

the sum of the squares of the vector and axial-vector couplings, represented by $C_V^{\rm SM}$ and C_A respectively, overall neutrino species, is given by $\sum_\nu (C_V^{\rm SM})^2 = 3/4 - 2\sin^2\theta_W + 12\sin^4\theta_W \approx 0.911$, while $\sum_\nu C_A^2 = 3/4$. The variable n_B represents the distribution function of the photons within the system.

To calculate the neutrino luminosity, the Emissivity must be integrated over the entire volume of the star. Assuming spherical symmetry, this can be expressed as

$$\mathcal{L}_\Lambda = 4\pi \int_0^{R_\star} \mathcal{Q}_\Lambda(r) r^2 dr \tag{3.32}$$

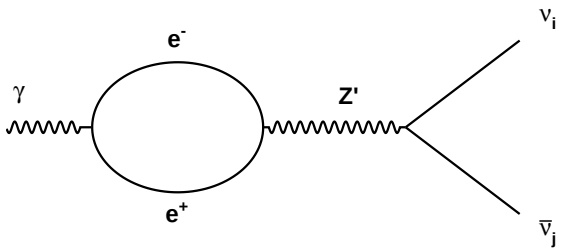

Figure 3.2: Diagram that contributes to the plasmon decay through the dark photon.

where Λ stands for L, T or A. $R_\star$ is the radius of the WD core, which is the volume considered for the plasmon decay. The quantities used to compute the emissivities depend simultaneously on the radius of the WD through its density or p_F, depending on the regime. For high chemical potential, the high degenerate approximation can be used. As we approach the surface of the core, the non-relativistic approximation is used instead.

3.3.2 Emission rate and the dark sector

If dark photons are present and interact with both an electromagnetic current and a current of dark neutrinos, it introduces the possibility of an additional diagram in the system that we sum to the SM ones. The new interaction is analogous to the diagram involving the Z particle, but instead involving the Z' particle, as depicted in Fig. 3.2. In this scenario, the dark final states would be mixed with the light states, which can be expressed in terms of the SM neutrinos.

It is important to note that the plasmon could not produce heavier mass states at the energies characteristic of a WD if we consider those heavy neutral leptons at the MeV scale. The plasma frequencies of a WD are well below those energies.

In this case, we will not use the effective propagator of the dark photo,

$(Q^2 - M_{Z'}^2)^{-1} \sim -M_{Z'}^{-2}$, just to consider a general approach. The amplitude to neutrino mass states i and j, coming from the diagram in Fig. 3.2 is,

$$\begin{aligned}\mathcal{M}_{Z'}^{ij} &= -\varepsilon_\mu(Q) \int \frac{d^4k}{(2\pi)^4} \mathrm{tr}\big[\gamma^\mu S_\beta^F(K)\gamma^\nu S_\beta^F(K-Q)\big] \\ &\times \epsilon e^2 \frac{1}{Q^2 - M_{Z'}^2} \frac{g_\mathrm{D}}{2} U_{i\mathrm{D}}^* U_{j\mathrm{D}} [\overline{u}_j(p_1)\gamma_\nu(1-\gamma_5)v_i(p_2)] \\ &= \frac{G_F}{2\sqrt{4\pi\alpha}} \Big[C_\nu^\mathrm{D} U_{i\mathrm{D}}^* U_{j\mathrm{D}} \Pi^{\mu\nu}\Big] \overline{u}_j(p_1)\gamma_\nu(1-\gamma_5)v_i(p_2)\end{aligned} \tag{3.33}$$

where U represents the mixing matrix for neutrino states, with $U_{i\mathrm{D}}$ denoting the mixing between a dark state D and a light mass state i. Here $S_\beta^F(P)$ is the thermal fermion propagator for the electron/positron at temperature $T \equiv 1/\beta$. The constant C_ν^D is defined as

$$C_\nu^\mathrm{D} = \frac{\sqrt{2\pi\alpha}}{G_F} \frac{\epsilon g_\mathrm{D}}{M_{Z'}^2 - Q^2}. \tag{3.34}$$

When computing the neutrino emission rates, it is convenient to express each contribution in terms of neutrino mass states, i and j, rather than flavour states in order to observe the interference with the dark sector. These mass states may not necessarily be the same, and hence, the summation must be performed over all possible combinations,

$$\begin{aligned} C_{V,ij}^{\mathrm{SM+D}} &= \sum_\alpha C_{V,\alpha}^\mathrm{SM} U_{\alpha i}^* U_{\alpha j} + C_\nu^\mathrm{D} U_{\mathrm{D}i}^* U_{\mathrm{D}j} \\ \big(C_{V,ij}^{\mathrm{SM+D}}\big)^2 &= \Big|\sum_\alpha C_{V,\alpha}^\mathrm{SM} U_{\alpha i}^* U_{\alpha j}\Big|^2 + |C_V^\mathrm{D}\, U_{\mathrm{D}i}^* U_{\mathrm{D}j}|^2 \\ &\quad + \frac{\sqrt{8\pi\alpha}}{G_F} \frac{\epsilon g_\mathrm{D} U_{\mathrm{D}i}^* U_{\mathrm{D}j}}{M_{Z'}^2 - Q^2} \,\mathrm{Re}\left[\sum_\alpha C_{V,\alpha}^\mathrm{SM} U_{\alpha i}^* U_{\alpha j}\right] \end{aligned} \tag{3.35}$$

where $C_{V,\alpha}^{\rm SM}$ is for a particular flavor α. Performing the sums over all possible final mass eigenstates, we compute the decay width,

$$\begin{aligned}\left(C_V^{\rm SM+D}\right)^2 = \sum_\alpha \left(C_V^{\rm SM}\right)^2 + \frac{18\pi\alpha}{G_F^2}\frac{\epsilon^2 g_{\rm D}^2 \left|U_{\rm D}\right|^4}{(M_{Z'}^2 - Q^2)^2} \\ + \frac{\sqrt{8\pi\alpha}}{G_F}\frac{\epsilon g_{\rm D}\left|U_{\rm D}\right|^2}{M_{Z'}^2 - Q^2}\,{\rm Re}\left[\sum_{\alpha,i,j} C_{V,\alpha}^{\rm SM} U_{\alpha i}^* U_{\alpha j}\right].\end{aligned} \tag{3.36}$$

Here, $(C_V^{\rm SM+D})^2 \equiv \sum_{ij}(C_{V,ij}^{\rm SM+D})^2$ has contributions from three terms. The first term represents the SM contribution, while the second term is solely from the DS. The third term represents the interference between the SM and DS amplitudes.

To simplify the computation, the assumption has been made that $U_{{\rm D}i}$ is equal for every i, denoted as $U_{\rm D}$. This implies that the mixing between each light mass state and the dark states is real and equal without any loss of generality. With the inclusion of the dark photon in the plasmon decay, the transverse and longitudinal emissivities are also altered as a consequence,

$$\begin{aligned}\mathcal{Q}_T = 2\frac{G_F^2}{96\pi^4\alpha}\int_0^\infty dq q^2 Z_t(q) \sum_{\alpha\beta}\left(C_V^{\rm SM+D}(\omega_t(q),q)\right)^2 \\ \times\left(\omega_t(q)^2 - q^2\right)^3 n_B(\omega_t(q)),\end{aligned} \tag{3.37}$$

$$\begin{aligned}\mathcal{Q}_L = \frac{G_F^2}{96\pi^4\alpha}\int_0^\infty dq q^2 Z_l(q) \sum_{\alpha\beta}\left(C_V^{\rm SM+D}(\omega_l(q),q)\right)^2 \\ \times\omega_l(q)^2\left(\omega_l(q)^2 - q^2\right)^2 n_B(\omega_l(q)).\end{aligned} \tag{3.38}$$

It is evident from Eq. (3.36), that the dependence on G_F^2/α vanishes for the purely DS contribution. Notice that $\mathcal{Q}_A$ remains unchanged because there is no axial term next to the thermal loop in the dark photon diagram (see Fig.

3.2).

Finally, using Eq. (3.32), Eq. (3.37) and Eq. (3.38), we can compute the WD luminosity due to plasmon decay into neutrinos.

3.4 Results and discussion

To obtain the total luminosity of a WD due to plasmon decay is necessary to obtain the WD radial profiles. This is achieved through the use of the Tolman-Oppenheimer-Volkoff (TOV) equations [424], which describe the hydrostatic equilibrium of a spherically symmetric, non-rotating star coupled to the Salpeter EOS [417]. It is important to note that the following analysis is performed on a hypothetical young WD with 1 solar mass. We fix its temperature to be of the order of 10^8 K, and using the evolutionary sequences given in Ref. [425], this temperature corresponds to a WD of $\sim \mathcal{O}(10^6)$ s old.

It is necessary to establish some limits to determine the parameter space of the Three Portal model that will be explored. One such limit concerns the quantity $\epsilon g_{\rm D}|U_{\rm D}|^2$. Here, $|U_{\rm D}|$ refers to $|U_{\rm Di}|$, where i denotes a massive light neutrino state. Current limits on this element depend on the mass scale of the heavy states, and we want to avoid the heavy states being so light that they can be directly produced by the plasmon.[1] Based on Ref. [426], we can assume that $|U_{\rm D}| \lesssim 10^{-1}$. This would imply high masses for the heavy neutrino states. We are not particularly interested in the specific realization of this as long as the values are not fully excluded. The parameter $g_{\rm D}$ is not a coupling of the dark photon to SM fermionic currents, so limits such as those found in [427] are not relevant for our model. There are no direct constraints on $g_{\rm D}$ neither if we do not consider the dark photon or the HNLs to be

[1] Although this effect might increase the energy lost by plasmon decay.

dark matter, we still need to keep the theory perturbative on $\alpha_{\rm D} \equiv g_{\rm D}^2/4\pi$. Therefore, we can assume that $g_{\rm D} \sim \mathcal{O}(1)$. The excluded regions for ϵ depend heavily on the mass of the dark photon and the number of extra neutrino states. We can assume $\epsilon \lesssim 10^{-2}$ based on [183, 385] which is safe, especially for heavy neutrino mass states of the order of $1 - 10$ GeV [178]. Hence, we can consider $\epsilon g_{\rm D}|U_{\rm D}|^2 \lesssim 10^{-4}$.

On the other hand, for the mass of the dark photon, the limits depend on several conditions: whether the dark photon or the heavy neutral leptons constitute dark matter, the value of ϵ or $g_{\rm D}$ and the mixing matrix of the neutrino sector, U. Here, we will also consider the same parameter space of [183, 385], such that $10\,\text{MeV} \leq M_{Z\prime} \leq 10\,\text{GeV}$. The Lagrangian in Eq. (3.2) is valid as long as $\left(M_{Z\prime}/M_Z\right)^2$ is negligible. Since for $M_{Z\prime} = 10\,\text{GeV}$, this is of the order of 10^{-2}, and its contribution is still negligible.

3.4.1 Luminosity

Figure 3.3 illustrates the total luminosity of the WD attributed solely to plasmon decay. The plot depicts different scenarios. The blue solid (dashed) lines correspond to the longitudinal (transverse) contributions of the SM case. In contrast, the green and pink regions show the longitudinal and transverse contributions of the DS scenario, which includes a dark photon with a mass of $M_{Z'} = 1$ GeV. Both bands demonstrate the luminosity for two different coupling strengths: $\epsilon g_D|U_D|^2 = 10^{-8}$ and $\epsilon g_D|U_D|^2 = 10^{-4}$. Note that when the coupling is too small, the curves correspond to the SM scenario. The maximum luminosity from new interactions in the neutrino emission rate is about one order of magnitude greater than the SM. This suggests that dark photons, like the one proposed in the DS scenario, may contribute to the evolution and behavior of WDs in ways not accounted

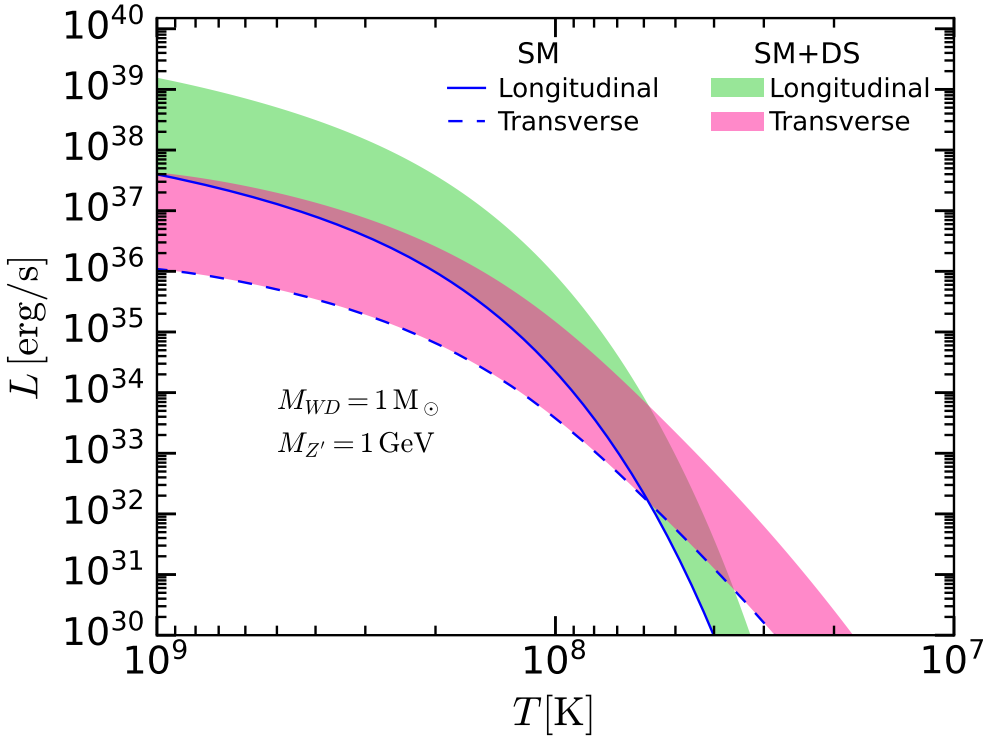

Figure 3.3: Luminosity of a $1M_\odot$ young WD with respect to its temperature for different BSM scenarios. The solid (dashed) line represents the longitudinal (transverse) components. The green (pink) bandwidth of the DS longitudinal (transverse) contribution considers the values: $\epsilon g_D |U_D|^2 = [10^{-8} - 10^{-4}]$. The axial contribution is not just shown since no contribution comes from the new physics.

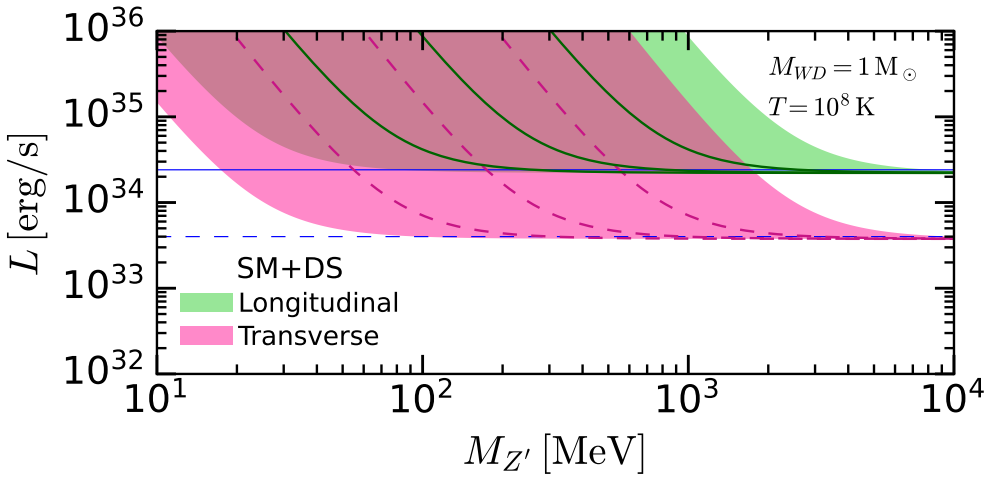

Figure 3.4: Luminosity of a $1M_\odot$ young WD with a temperature of $T = 10^8$ K, as a function of the dark photon mass for different BSM scenarios. The solid (dashed) line represents the longitudinal (transverse) components. The axial contribution is not shown since there is no contribution from new physics. The bandwidth of the DS contribution considers the values: $\epsilon g_D |U_D|^2 = [10^{-8} - 10^{-4}]$.

for by the SM. As the WD cools down, the contributions from plasmons decrease until they essentially disappear. Before reaching a temperature of 10^8 K, the main source of energy loss is from the longitudinal contribution (solid line). At lower temperatures, the transverse contribution (dashed line) dominates. Here, we do not show the axial contribution in our analysis since it is suppressed several orders of magnitude compared to the longitudinal and transverse contributions.

Figure 3.4 shows the luminosity of the WD, at a temperature of $T = 10^8$ K, as a function of the dark photon mass $M_{Z'}$. Again, the solid (dashed) blue line represents the SM longitudinal (transverse) contribution. The green and pink areas correspond to the emission rates, including the dark photon, and the bands represent various fixed values of $\epsilon g_D |U_D|^2 = [10^{-8} - 10^{-4}]$. As expected, for each set of couplings, there is an upper bound on the dark photon

mass above, which the new physics does not visibly contribute, and the luminosity curve is just a horizontal line approaching the SM. As the dark photon mass decreases, the contribution to the luminosity grows exponentially, with the dominant contribution coming from the longitudinal photon states (solid lines). For instance, when the product of couplings is $\epsilon g_D |U_D|^2 = 10^{-8}$, and the dark photon has a mass of ~ 10 MeV, the luminosity of the WD can be up to ~ 2 orders of magnitude higher than the SM case. This effect becomes insignificant for $M_{Z'} \sim 100$ MeV and above. On the other hand, in the case of $\epsilon g_D |U_D|^2 = 10^{-4}$, the effect of the new interaction in the WD luminosity becomes irrelevant around 10 GeV. Notice that as the product $\epsilon g_D |U_D|^2$ increases, the impact of the new physics in the luminosity is visible for heavier dark photon states. This can be seen from the green solid and pink dashed lines showing, from left to right, $\epsilon g_D |U_D|^2 = 10^{-7}, 10^{-6}$ and 10^{-5}.

3.4.2 Results

Finally, we present a comprehensive investigation of the parameter space associated with the dark photon in the context of the cooling of WDs. Here, we express the contribution of dark photons as a fraction of the total SM luminosity,

$$F_{\rm DS} = \frac{\mathcal{L}_{\rm DS+SM} - \mathcal{L}_{\rm SM}}{\mathcal{L}_{\rm SM}} \times 100\%. \tag{3.39}$$

Therefore, we can perform estimations and projections of the allowed parameter space regarding the cooling of WD mediated by dark photons.

By imposing the condition that the luminosity generated through the presence of dark photons constitutes a maximum of 1%, 10%, and 30% of the total SM luminosity, we can determine the excluded parameter space.

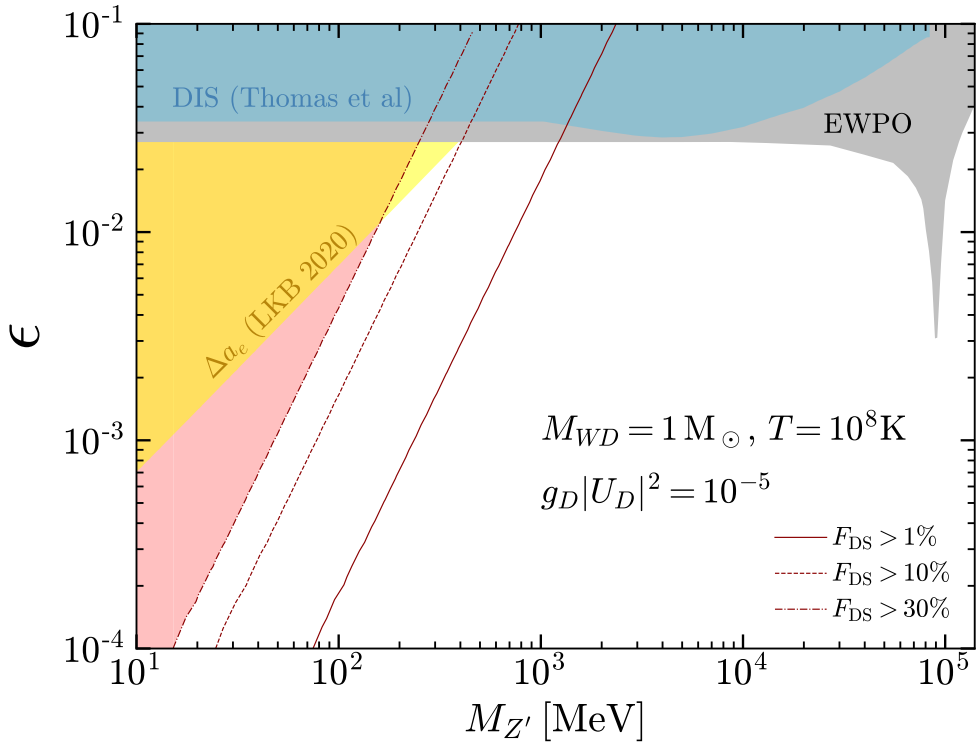

Figure 3.5: Limits on ϵ for dark photons decaying into neutrinos, obtained with a young WD assuming $T = 10^8$ K and a dark sector parameter of $g_D|U_D|^2 = 10^{-5}$. The luminosity due to dark photons constitutes a maximum of $F_{DS} = 1\%$, 10%, and 30% of the total SM luminosity. For comparison, we also show the bounds from DIS [428], electron $(g-2)$ (LKB) [429] and [430] proportioned in Ref. [385].

Current limits on WD cooling through neutrinos exclude more than 30% of extra luminosity with respect to the SM (see Appendix E for the extraction of this limit based on Ref. [431]). In Fig. 3.5, we set reasonable dark sector parameters $g_D|U_D|^2 = 10^{-5}$, and show the estimated bounds on ϵ. The bounds are depicted as red lines, corresponding to 1%, 10%, and 30% maximum values of F_{DS}, respectively. For comparison, we also show the bounds given by Deep-inelastic scattering (DIS) [428], electron $(g-2)$ (LKB) [429] and electroweak precision observables (EWPO) [430], revised and presented in [385] as model-independent limits.

We notice that in all cases, the estimated bounds significantly surpass the existing constraints. As the contribution of dark photons decreases, the bound becomes progressively more stringent. This behavior can be attributed to the fact that, in order to achieve a smaller DS contribution, the coupling parameter ϵ must decrease accordingly. The obtained bounds are up to one and two orders of magnitude, larger than those given by precision measurements of the electron anomalous magnetic moment when considering a maximum fraction of $F_{DS} = 30\%$ and 10%, respectively. However, the most compelling result emerges when we restrict the luminosity to only 1% of the SM luminosity. In this scenario, the range where the bound exhibits its greatest strength extends from 10 MeV to 1 GeV. Future measurements of CASTOR [432, 433] could push the bounds of [431] to 1%. It is important to note that we are unable to extend our bounds beyond 10 GeV since the validity of the dark photon interactions taken into account relies on the assumption that $\left(M_{Z\prime}/M_Z\right)^2 \ll 1$. Hence, for $M_{Z'} > 10^4$ MeV, the strongest bounds are still given by EWPO and DIS.

There are certainly additional constraints on this parameter space [434, 435]. However, in order to translate these bounds, we would need more

specific considerations on the model, especially those that affect the visible, semi-visible and invisible decays of the dark photon. Since our computation is independent of those regards, we are not showing them here. Finally, it is worth noting that electron-neutrino scattering can be mediated through the exchange of a dark photon. In the context of B-L models, the constraints imposed on this process are more stringent compared to those derived from white dwarf cooling. This is primarily due to the fact that in B-L models, the vector boson couples with the same strength to the SM and the DS. On the other hand, in the case of the three-portal model, the couplings are independent, resulting in weaker constraints from the electron-neutrino scattering process.

3.5 Conclusions

In the present chapter, we have computed the total luminosity of a white dwarf due to plasmon decay and present various scenarios involving a dark photon with different masses and couplings, within the Three Portal model. We found that for a $M_{Z'} = 1$ GeV, the maximum luminosity from new interactions, corresponding to $\epsilon g_D |U_D|^2 = 10^{-4}$, exceeds that of the SM by approximately one order of magnitude. Additionally, we have examined the upper bound on the dark photon mass for each set of couplings. Above this mass, the new physics has a minimal visible contribution, and the luminosity from new interactions aligns with the SM one. We found that in the case of $\epsilon g_D |U_D|^2 = 10^{-4}$, the dark photon mass at which the luminosity becomes only SM luminosity is around 10 GeV.

Finally, by imposing the condition that the luminosity attributed to dark photons should not exceed 1%, 10%, and 30% of the total Standard Model

luminosity, we estimated bounds on the coupling parameter ϵ for reasonable dark sector parameters $g_D|U_D|^2 = 10^{-5}$. Remarkably, our estimated bounds consistently surpass the existing constraints, becoming increasingly stringent as the contribution of dark photons decreases. This is due to the need for smaller coupling values of ϵ to achieve a reduced dark sector contribution. Notably, when restricting the luminosity to only 1% of the SM luminosity, our bounds exhibit their strongest range from 10 MeV to 1 GeV. Therefore, the cooling behavior of WDs presents a promising avenue to probe the existence and properties of dark photons. In this way, white dwarfs are an open possibility to study and look for dark sector that interact with the SM.

Chapter 4

Wide mass range DS and WDs

As we have seen, white dwarfs are a powerful test for dark sectors. Here, we broaden the mass range and provide strong bounds from WD cooling. The study is of particular interest as it allows to gain deeper insight on the process of plasmon decay, in regimes in which the dark photons are ultra-light as well as with masses that are resonant with respect to the plasma frequency of the star.

4.1 Introduction

A particularly simple and well-motivated extension of the SM that considers a dark vector mediator is given by a new gauged $U(1)_{L_\mu - L_\tau}$ symmetry [436–439]. These models can solve very prominent problems in particle physics. They not only allow to accommodate neutrino masses [440–443] and DM [444–450], but can also help to explain the muon $(g-2)_\mu$ anomaly [451–454], the Hubble tension [455–457] and the $b \to s\,\mu\mu$ anomaly [458–462].[1]

[1]There still persists a discrepancy between the observed value of the branching ratio of the decay $B^+ \to K^+\mu\mu$ and its SM prediction, which favours BSM contributions [463]. However, in light of the recent LHCb result on lepton universality [464, 465], a careful

In the absence of elementary kinetic mixing, the associated gauge boson only couples to second- and third-generation leptons. This makes $U(1)_{L_\mu - L_\tau}$ models generically hard to test at earth-based laboratory experiments, since couplings to conventional matter, i.e. quarks and electrons, are only induced at the one-loop level via kinetic mixing with the photon. However, its gauge couplings to mu- and tau-flavoured neutrinos render neutrino interactions an excellent way of searching for $U(1)_{L_\mu - L_\tau}$ bosons [466]. In particular, for $U(1)_{L_\mu - L_\tau}$ bosons lighter than the dimuon threshold all leading constraints are due to tests of neutrino physics, like neutrino trident production [458], neutrino oscillation measurements at Borexino [467, 468], the number of effective neutrino degrees of freedom N_{eff} during big bang nucleosynthesis (BBN) [455, 469, 470], or neutrino cooling of supernovae (SN) [471–473].

Studying these models in the process of cooling of a white dwarf is particularly useful because these stars constitute a theoretically very clean astrophysical environment to study neutrino physics. As we have already pointed out, their behaviour is well understood and the various existing equations of state (EoS) for modeling WDs reproduce identical results for the same conditions [474–478]. An additional $U(1)_{L_\mu - L_\tau}$ boson can in principle enhance the plasmon decay into neutrinos via its kinetic mixing with the photon and thus modify the evolution of WDs, just as the dark photon from the Three Portal model. This will ultimately lead to a modification of the WD luminosities compared to the SM prediction. Previously, the resulting constraint on the $U(1)_{L_\mu - L_\tau}$ parameter space has been estimated [403] via an effective field theory (EFT) analysis of modified plasmon decays in WDs [404]. In this chapter, however, we will perform an *ab initio* calculation of the modified WD luminosities due to a $U(1)_{L_\mu - L_\tau}$ gauge boson correctly taking into

reevaluation of an explanation in terms of a $U(1)_{L_\mu - L_\tau}$ boson seems to be warranted.

account transverse, axial and longitudinal emissivities as well as the fully gauge-invariant kinetic mixing.

The remainder of this chapter is organised as follows. In Section 4.2, we introduce the theoretical framework of the minimal $U(1)_{L_\mu - L_\tau}$ model studied in this paper. In Section 4.3, we present the computation of the neutrino luminosities responsible for WD cooling within $U(1)_{L_\mu - L_\tau}$. Finally, we present our results in Section 4.4 before presenting our conclusions in Section 4.5.

4.2 The $U(1)_{L_\mu - L_\tau}$ Model

The Lagrangian of the SM exposes some accidental global symmetries like baryon number, $U(1)_B$, and the lepton family numbers, $U(1)_{L_i}$ with $i = e, \mu, \tau$. Remarkably, the combinations $U(1)_{B-L}$ and $U(1)_{L_i - L_j}$ with $i, j = e, \mu, \tau$ can be promoted to anomaly-free gauge symmetries with only the SM field content.[2] Among these anomaly-free groups $U(1)_{L_\mu - L_\tau}$ is of special phenomenological interest as it allows for the explanation of several experimental anomalies. For example, it can accommodate the observed excess in the anomalous magnetic moment of the muon $(g-2)_\mu$, as well as the tension arising from determining the Hubble constant H_0 from early-time cosmology via the cosmic microwave background (CMB) [69] contrasted with the value obtained from local measurements via standard candles like type-Ia supernovae and cepheid variable stars [479].[3]

[2] Cancelling the gauge anomalies of $U(1)_{B-L}$ requires the addition of three right-handed, SM-singlet neutrinos. The groups $U(1)_{L_i - L_j}$ are already anomaly-free without the addition of right-handed neutrinos (if Majorana mass terms for the neutrinos are forbidden [442]).

[3] As noted in Ref. [480], however, explanations of the H_0 tension by light vector mediators are not able to account for the less severe tension in the cosmological parameter σ_8 linked to the small scale power spectrum of the universe.

The relevant parts of Lagrangian of an extra $U(1)_{L_\mu - L_\tau}$ symmetry can be compactly written in matrix form as

$$\begin{aligned}\mathcal{L} \supset & -\frac{1}{4}\left(B_{\alpha\beta}, W^3_{\alpha\beta}, X_{\alpha\beta}\right)\begin{pmatrix} 1 & 0 & \epsilon_B \\ 0 & 1 & \epsilon_W \\ \epsilon_B & \epsilon_W & 1 \end{pmatrix}\begin{pmatrix} B^{\alpha\beta} \\ W^{3\alpha\beta} \\ X^{\alpha\beta} \end{pmatrix} \\ & + \frac{1}{2}\left(B_\alpha, W^3_\alpha, X_\alpha\right)\frac{v^2}{4}\begin{pmatrix} g'^2 & g'\,g & 0 \\ g'\,g & g^2 & 0 \\ 0 & 0 & \frac{4\,M_X^2}{v^2} \end{pmatrix}\begin{pmatrix} B^\alpha \\ W^{3\alpha} \\ X^\alpha \end{pmatrix} \\ & - \left(g'\,j_Y^\alpha,\ g\,j_3^\alpha,\ g_{\mu\tau}\,j_{\mu\tau}^\alpha\right)\begin{pmatrix} B_\alpha \\ W^3_\alpha \\ X_\alpha \end{pmatrix} . \end{aligned} \tag{4.1}$$

Here, X_α denotes the new $U(1)_{L_\mu - L_\tau}$ gauge boson, while $B_{\alpha\beta}$, $W^3_{\alpha\beta}$ and $X_{\alpha\beta}$ are the hypercharge, neutral $SU(2)_L$ and $U(1)_{L_\mu - L_\tau}$ field strengths, respectively. Furthermore, $g_{\mu\tau}$ is the $U(1)_{L_\mu - L_\tau}$ gauge coupling, and ϵ_B and ϵ_W are the kinetic mixing parameters with the hypercharge and neutral weak boson, respectively. Note that the mixing of the $U(1)_{L_\mu - L_\tau}$ boson with the neutral weak component, $\epsilon_W/2\, W^3_{\alpha\beta}X^{\alpha\beta}$, is generated at the one-loop level from the $SU(2)_L$ lepton doublets running in the loop [481]. The new gauge boson X_α couples to SM leptons through the gauge current

$$j_{\mu\tau}^\alpha = \bar{L}_2\gamma^\alpha L_2 + \bar{\mu}_R\gamma^\alpha\mu_R - \bar{L}_3\gamma^\alpha L_3 - \bar{\tau}_R\gamma^\alpha\tau_R\,. \tag{4.2}$$

The lack of any gauge interactions with conventional matter composed of electrons and quarks (and thus hadrons) sets this gauge group apart from

other anomaly-free $U(1)$ extensions. At the one-loop level, however, the coupling of the leptophilic gauge boson to the leptons induces an interaction with all SM fermions via a kinetic mixing term with the SM photon and Z boson. At energies $E \sim T_{\rm WD} \ll m_{\mu,\tau}$, we find for these mixings (cf. Appendix D.1 for details)

$$\epsilon_A = \frac{e\, g_{\mu\tau}}{6\pi^2}\, \log\left(\frac{m_\mu}{m_\tau}\right) \;\sim\; -\frac{g_{\mu\tau}}{70}\,, \tag{4.3}$$

$$\epsilon_Z = -\frac{1}{2}\frac{s_W}{c_W}\epsilon_A\,, \tag{4.4}$$

where s_W and c_W are the sine and cosine of the Weinberg angle θ_W. These irreducible loop-induced kinetic mixings are finite and effectively lead to loop-suppressed interactions of the $U(1)_{L_\mu - L_\tau}$ boson with quarks and electrons.

In the physical mass basis of the hidden photon A', we can express the interactions of the new mediator as (cf. Appendix D.2),

$$\mathcal{L}_{\rm int} = -g_{\mu\tau}\, j^\alpha_{\mu\tau}\, A'_\alpha + e\,\epsilon_A \left(j^\alpha_{\rm EM} - \frac{1}{2}\tan^2\theta_W\, j^\alpha_Z\right) A'_\alpha\,, \tag{4.5}$$

with the electromagnetic and Z current defined as

$$j^\alpha_{\rm EM} = \sum_f Q^{\rm EM}_f\, \bar f \gamma^\alpha f\,, \tag{4.6}$$

$$j^\alpha_Z = \sum_f \bar f\, \gamma^\alpha\, \frac{1}{2}\left[(T^3_f - 2\, s^2_W\, Q^{\rm EM}_f) - T^3_f\, \gamma^5\right]\, f\,. \tag{4.7}$$

From Eq. (4.5) we see that the mass eigenstate of the $U(1)_{L_\mu - L_\tau}$ boson acquires couplings to the SM electromagnetic and Z currents suppressed by the kinetic mixing parameter ϵ_A.

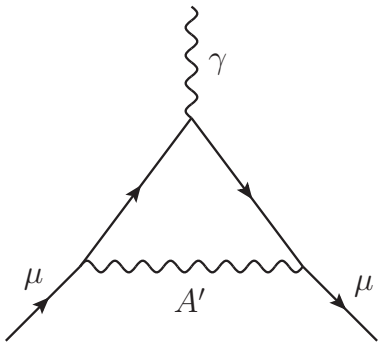

Figure 4.1: Loop contribution of the $U(1)_{L_\mu - L_\tau}$ boson to the muon anomalous magnetic moment $(g-2)_\mu$.

4.2.1 Muon anomalous magnetic moment

Due to its gauge interactions with the second-generation leptons the $U(1)_{L_\mu - L_\tau}$ gauge boson A' contributes to the anomalous magnetic moment of the muon, $a_\mu = (g-2)_\mu/2$, via the loop process displayed in Fig. 4.1. For any neutral gauge boson with vectorial couplings to muons (as in $U(1)_{L_\mu - L_\tau}$), the additional contribution to a_μ can be expressed in the compact form [382, 482],

$$\Delta a_\mu = Q'^2_\mu \, \frac{\alpha'}{\pi} \int_0^1 du \, \frac{(1-u)\,u^2}{u^2 + \dfrac{(1-u)}{x_\mu^2}} \,, \tag{4.8}$$

where $\alpha' = g^2_{\mu\tau}/4\pi$, $x_\mu = m_\mu/m_{A'}$ and Q'_μ denotes the $U(1)_{L_\mu - L_\tau}$ charge of the muon.

In recent years, there has been significant theoretical effort to improve the precision of the SM prediction of $(g-2)_\mu$ [483], with the current theoretical result being

$$a_\mu^{\rm SM} = 116\ 591\ 810(43) \times 10^{-11} \,. \tag{4.9}$$

At the same time, the E989 experiment at Fermilab has recently reported

results from their runs 2 and 3, determining the value of $(g-2)_\mu$ with unprecedented levels of precision [484]. Combined with their run-1 result [381] and the previous BNL result [485], the current experimental world average amounts to

$$a_\mu^{\text{exp}} = 116\ 592\ 059(22) \times 10^{-11}\,. \tag{4.10}$$

This leads to a $\sim 5.2\sigma$ excess of the experimentally observed value from the theoretical prediction in Eq. (4.9) captured by the total deviation of

$$\Delta a_\mu = 249(48) \times 10^{-11}\,. \tag{4.11}$$

The preferred region in parameter space, where the contribution of a $U(1)_{L_\mu - L_\tau}$ boson to $(g-2)_\mu$ can account for this excess is shown by the green band in Fig. 4.5.

It should be noted that a recent lattice result of the leading-order hadronic vacuum polarisation [486] significantly decreases the above tension. This, however, comes at the cost of worsening fits to other electroweak precision observables [487].

4.3 White Dwarf Cooling

In our computation, we will consider the general framework presented in Chapter 3, but now applied to the $U(1)_{L_\mu - L_\tau}$ model: we regard a $U(1)_{L_\mu - L_\tau}$ leptophilic dark photon that contributes to the plasmon decay. This novel vector mediator has different contributions for each flavour of neutrino-antineutrino pairs that are emitted in the plasmon decay process. In order to obtain more compact expressions, we will introduce the following definitions encapsulat-

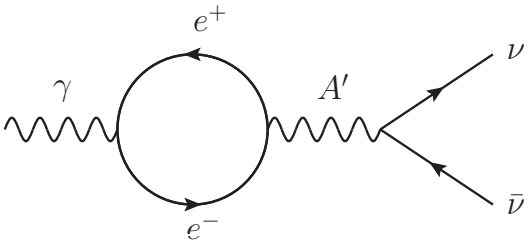

Figure 4.2: Plasmon decay contribution via $U(1)_{L_\mu - L_\tau}$ boson coupling to electrons via kinetic mixing.

ing the A' couplings to electrons and neutrinos,

$$d_V^e = e\,\epsilon_A\Big(1 - \tan^2\theta_W(1 - 4\sin^2\theta_W)/8\Big)\,, \tag{4.12}$$

$$d_A^e = e\,\epsilon_A\ \tan^2\theta_W/8\,, \tag{4.13}$$

$$k_\nu^\alpha = s_\alpha\, g_{\mu\tau}/2 + d_A^e\,, \tag{4.14}$$

where $s_\alpha = 0, 1, -1$ for $\alpha = e, \mu, \tau$, respectively. The contribution to the neutrino emissivity of a WD due to a novel $U(1)_{L_\mu - L_\tau}$ boson originates from the diagram of Fig. 4.2, which is identical to the SM neutral current contribution but with a dark photon A' instead of the SM Z. Due to the kinetic mixing coupling of the dark photon to electrons in this model, the BSM contribution can be calculated exactly analogous to the SM Z. Hence, we only need to redefine the values of C_V and C_A for each neutrino flavour in Eqs. (36-38) of Ref. [421] and consider the full expression for the dark photon propagator to allow for A' masses comparable to the WD plasma frequency,

$$C_a^{\alpha,\mathrm{SM+BSM}}(q) \to C_a^\alpha + b_a\,\frac{\sqrt{2}}{G_F}\frac{k_\nu^\alpha\, d_a^e}{q^2 - m_{A'}^2}\,, \tag{4.15}$$

where $a = V, A$ are the vectorial and axial components with $b_V = 1$ and $b_A = -1$. Here, q is the 4-momentum of the plasmon, α denotes the flavour

of the SM neutrino final states, and C_a^α are the coefficients obtained from the SM plasmon decay diagrams: the vectorial ones are equal to $2\sin^2\theta_W + 0.5$ (for e) and $2\sin^2\theta_W - 0.5$ (for μ and τ), and the axial are 0.5 (for e) and -0.5 (for μ and τ). With this, the WD emissivities into neutrino / antineutrino pairs can be written as

$$\begin{aligned}\mathcal{Q}_L =& \frac{G_F^2}{96\pi^4\alpha}\int_0^\infty dq \sum_\alpha (C_V^{\alpha,\mathrm{SM+BSM}}(q))^2\, q^2\, Z_l(q) \\ & \times \left(\omega_l(q)^2 - q^2\right)^2 \omega_l(q)^2\, n_B(\omega_l(q))\,, \end{aligned} \tag{4.16}$$

$$\begin{aligned}\mathcal{Q}_T =& \frac{G_F^2}{48\pi^4\alpha}\int_0^\infty dq \sum_\alpha (C_V^{\alpha,\mathrm{SM+BSM}}(q))^2\, q^2\, Z_t(q) \\ & \times \left(\omega_t(q)^2 - q^2\right)^3 n_B(\omega_t(q))\,, \end{aligned} \tag{4.17}$$

$$\begin{aligned}\mathcal{Q}_A =& \frac{G_F^2}{48\pi^4\alpha}\int_0^\infty dq \sum_\alpha (C_A^{\alpha,\mathrm{SM+BSM}}(q))^2\, q^2\, Z_t(q) \\ & \times \left(\omega_t(q)^2 - q^2\right) \Pi_A\left(\omega_t(q), q\right)^2\, n_B(\omega_t(q))\,, \end{aligned} \tag{4.18}$$

where as in the previous chapter q denotes the 3−momentum of the dark photon and $n_B(\omega)$ is the Bose-Einstein distribution function. For our computations, we have chosen a representative value of $M_{\mathrm{WD}} = 1\, M_\odot$ for the mass of the WD, which is the same used in the previous chapter. However, the results are not altered by picking smaller values. If the star has a temperature of $T_{\mathrm{WD}} \gtrsim 10^{7.8}$ K then the photon luminosity is just $L_\gamma \gtrsim 10^{-0.5} L_\odot$ [488] and the main cooling mechanism is the plasmon decay inside the star. Therefore, at these temperatures, extra contributions to plasmon decay have an impact on the overall cooling. The limits are computed by estimating the relative excess contribution, F_{DS}, defined in Eq. (3.39) of the novel $U(1)_{L_\mu - L_\tau}$ boson over the SM one.

In the following we discuss the three regimes of dark photon masses with

respect to the WD temperatures: (i) the heavy regime with $m_{A'} \gg T_{\rm WD}$, (ii) the resonant regime with $m_{A'} \sim T_{\rm WD}$, and (iii) the ultra-light regime with $m_{A'} \ll T_{\rm WD}$.

4.3.1 Heavy dark photons

A WD cannot reach temperatures for which the energies of the plasmon decay are substantially greater than $\mathcal{O}(10)$ MeV. Therefore, in the heavy regime of $m_{A'} \gtrsim 10$ MeV the dark photon propagator entering the momentum-integral in the emissivity can be well approximated as $1/(q^2 - m_{A'}^2) \sim -1/m_{A'}^2$. Hence, $C_V^{\alpha,\rm SM+BSM}$ and $C_A^{\alpha,\rm SM+BSM}$ no longer depend on q and we can directly compute $F_{\rm DS}$ since the axial contribution is negligible,

$$\begin{aligned} F_{\rm DS} &= \sum_\alpha \left(C_V^{\alpha,\rm SM+BSM}\right)^2 / \sum_\alpha \left(C_V^{\alpha,\rm SM}\right)^2 - 1 \\ &\simeq 1.50 \times 10^{17} \left(\frac{g_{\mu\tau}}{m_{A'}/1\ \text{MeV}}\right)^4 \\ &\quad - 1.66 \times 10^5 \left(\frac{g_{\mu\tau}}{m_{A'}/1\ \text{MeV}}\right)^2 . \end{aligned} \tag{4.19}$$

This quantity is also independent of the exact temperature of the WD, but is only valid for masses that are much greater than the plasma frequency of the WD[4]. Due to the relative smallness of ϵ_Z compared to ϵ_A, the results are also unaltered if we neglect the dark photon coupling to the Z current in Eq. (4.5).

4.3.2 Ultra-light dark photons

In the case of an ultra-light dark photon mediator, effects due to the self energy correction to the propagator become relevant when computing its

[4]See Eq. (3.17) for the full expression of the plasma frequency.

propagation in the stellar medium and the subsequent plasmon decay. The dark photon self energy is given by

$$\begin{aligned}\Pi^{\mu\nu}_{A'}(Q) = &-\int \frac{d^4K}{(2\pi)^4}\ \mathrm{tr}\big[\gamma^\mu(d^e_V + d^e_A\gamma^5)(\not{K} + m_e)\\ &\times \gamma^\nu(d^e_V + d^e_A\gamma^5)(\not{Q} - \not{K} - m_e)\big]\\ &\times \left\{\frac{i}{K^2 - m_e^2} - 2\pi\big[\theta(-k^0)\right.\\ &\left.+ \mathrm{sign}(k^0)\,\tilde{f}(k^0 - \mu_e)\big]\delta\big(k^2 - m_e^2\big)\right\}\\ &\times \left\{\frac{i}{(Q-K)^2 - m_e^2} - 2\pi\big[\theta(-q^0 + k^0)\right.\\ &+ \mathrm{sign}(q^0 - k^0)\,\tilde{f}(q^0 - k^0 + \mu_e)\big]\\ &\left.\times\,\delta\big((Q-K)^2 - m_e^2\big)\right\}.\end{aligned} \tag{4.20}$$

where $\tilde{f}(x) \equiv (e^{\beta x} + 1)^{-1}$ with $\beta = 1/(k_B\,T)$.

We can conveniently express this in terms of the plasmon self energy $\Pi^{\mu\nu}_\gamma$. To do so, we note that $(d^e_A)^2/(d^e_V)^2 \sim \mathcal{O}(10^{-3})$ is negligible, as well as the axial contribution to the self-energy, which is $\sim d^e_V\,d^e_A\,\Pi_{A,\gamma}$. This is warranted since the axial contribution to the plasmon self-energy $\Pi_{A,\gamma}$ appearing is typically four to six orders of magnitude smaller than the longitudinal and transverse ones. Taking this into account, the final expression for the dark photon self energy reads

$$\Pi^{\mu\nu}_{A'}(Q) = \frac{(d^e_V)^2 + (d^e_A)^2}{4\pi\alpha}\,\Pi^{\mu\nu}_\gamma(Q)\,, \tag{4.21}$$

with $\Pi^{\mu\nu}_\gamma$ the plasmon self-energy. Next, we need to compute the full propagator, $D^{\mu\nu}_{A'}$, up to the same order, $\mathcal{O}(\alpha)$, used for the plasmon decay computation. To compute this quantity, we need to expand the self-energy into its

longitudinal and transverse components. We can work with the same projectors as used for the photon since, as we saw, the dark photon self-energy is proportional to that of the photon. Hence, we can write

$$\Pi^{\mu\nu}_{A'} = F_{A'} P^{\mu\nu}_{L} + G_{A'} P^{\mu\nu}_{T} \,, \tag{4.22}$$

with the transverse and longitudinal projectors given by

$$\begin{aligned} P^{\mu\nu}_{T} &= \left(\delta^{ij} - \hat{q}^i \hat{q}^j\right) \delta^{\mu}_{i} \delta^{\nu}_{j} \,, \\ P^{\mu\nu}_{L} &= \left(- g^{\mu\nu} + \frac{q^\mu q^\nu}{Q^2} \right) - P^{\mu\nu}_{T} \,. \end{aligned} \tag{4.23}$$

Here, the factors $F_{A'}$ and $G_{A'}$ are obtained analogously to the photon case, by contracting $\Pi^{\mu\nu}_{A'}$ with the projectors of Eq. (4.23). Formally, we can write this as

$$F_{A'} \equiv \Pi^{00}_{A'} \frac{Q^2}{q^2} \,, \qquad G_{A'} \equiv \Pi^{xx}_{A'} \,, \tag{4.24}$$

where x is any transverse direction to the propagation of the dark photon with 4−momentum $Q = (\omega, q)$.

Importantly, we note that since $\Pi^{\mu\nu}_{A'}$ is proportional to the plasmon self-energy, its contraction with Q^μ vanishes. Hence it is respecting the Ward identity, even though the gauge symmetry is broken. In our computation, the full propagator $D^{\mu\nu}_{A'}$ is contracted with the plasmon self-energy $\Pi^{\mu\nu}_{\gamma}$. Thus, we will neglect any term proportional to q^μ. Furthermore, we remind ourselves that for the projectors $P^{\mu}_{T\lambda} P^{\lambda\nu}_{T} = P^{\mu\nu}_{T}$, $P^{\mu}_{L\lambda} P^{\lambda\nu}_{L} = P^{\mu\nu}_{L}$, and $P^{\mu}_{L\lambda} P^{\lambda\nu}_{T} = P^{\mu}_{T\lambda} P^{\lambda\nu}_{L} = 0$. With these preparations, we can write the expression for the

full propagator of the dark photon as

$$
\begin{aligned}
D^{\mu\nu}_{A'} &= \frac{-i\,(g^{\mu\nu} - q^\mu q^\nu/m^2_{A'})}{Q^2 - m^2_{A'}} + \frac{-i\,(g^\mu_\lambda - q^\mu q_\lambda/m^2_{A'})}{Q^2 - m^2_{A'}}\,(i\,\Pi^{\lambda\sigma}_{A'})\,\frac{-i\,(g^\nu_\sigma - q_\sigma q^\nu/m^2_{A'})}{Q^2 - m^2_{A'}} + \ldots \\
&= \frac{-i\,g^{\mu\lambda}}{Q^2 - m^2_{A'}}\left[\delta^\nu_\lambda + \sum_{n=1}^{\infty}\left(\frac{F_{A'}}{Q^2 - m^2_{A'}}\right)^n P^\nu_{L\lambda} + \sum_{n=1}^{\infty}\left(\frac{G_{A'}}{Q^2 - m^2_{A'}}\right)^n P^\nu_{T\lambda}\right] \\
&= \frac{-i\,g^{\mu\lambda}}{Q^2 - m^2_{A'} - F_{A'}}\,P^\nu_{L\lambda} + \frac{-i\,g^{\mu\lambda}}{Q^2 - m^2_{A'} - G_{A'}}\,P^\nu_{T\lambda}\,,
\end{aligned}
\tag{4.25}
$$

where finally we have

$$
F_{A'} \equiv \frac{(d^e_V)^2 + (d^e_A)^2}{4\pi\alpha}\,\frac{Q^2}{q^2}\,\Pi^\gamma_L\,, \tag{4.26}
$$

$$
G_{A'} \equiv \frac{(d^e_V)^2 + (d^e_A)^2}{4\pi\alpha}\,\Pi^\gamma_T\,. \tag{4.27}
$$

where Π^γ_L and Π^γ_T are the plasmon longitudinal and transverse self-energies, that can be found in [489] in Eqs. (18) and (19). To obtain the last line of Eq. (4.25), we have made use of the identity

$$
\delta^{\lambda\nu} = P^{\lambda\nu}_L + P^{\lambda\nu}_T + q^\lambda q^\nu/Q^2\,. \tag{4.28}
$$

In the computation of the emissivities the full A' propagator $D^{\mu\nu}_{A'}$ is contracted with the plasmon self-energy $\Pi^{\mu\nu}_\gamma$. Hence, we find that only the longitudinal component of $D^{\mu\nu}_{A'}$ enters the longitudinal emissivity and only its transverse component enters the transverse and axial emissivities. Furthermore, since the A' self-energy can be expressed in terms of the photon self-energy and the 4-momentum at which it is evaluated is the on-shell plasmon momentum (due to momentum conservation), we can use the standard plasmon relations to evaluate $P^{\mu\nu}_L$ and $P^{\mu\nu}_T$ for the dark photon. Taking this

into consideration, the expression for the full propagator finally simplifies to

$$D^{\mu\nu}_{A'} = \frac{-i\,P^{\mu\nu}_L}{Q^2 - m^2_{A'} - \dfrac{(d^e_V)^2 + (d^e_A)^2}{4\pi\alpha}\left(\omega_l(q)^2 - q^2\right)} + \frac{-i\,P^{\mu\nu}_T}{Q^2 - m^2_{A'} - \dfrac{(d^e_V)^2 + (d^e_A)^2}{4\pi\alpha}\left(\omega_t(q)^2 - q^2\right)}\,. \tag{4.29}$$

This expression for the full propagator has to be used instead of the naive tree-level propagator $\frac{-i}{Q^2-m^2_{A'}}$ in computing the coupling coefficients in Eq. (4.15). Effectively, this means that in the computation of the longitudinal emissivity the denominator of the coefficient $C_V^{\alpha,\mathrm{SM+BSM}}(q)$ has to be replaced by the one of the first term in Eq. (4.29). Similarly, for the transverse and axial components the denominator of the coupling coefficients $C_V^{\alpha,\mathrm{SM+BSM}}(q)$ and $C_A^{\alpha,\mathrm{SM+BSM}}(q)$ have to be replaced by the denominator of the second term in Eq. (4.29).

In the very low mass region, where $m^2_{A'} \ll Q^2$, the luminosities become approximately independent of the mass. To see this, let us consider the denominator of the propagator in Eq. (4.29). This has the form $(1-r_{\mathrm{BSM}})\,Q^2 - m^2_{A'}$, where $r_{\mathrm{BSM}} \equiv \left[(d^e_V)^2 + (d^e_A)^2\right]/4\pi\alpha$. Since $r_{\mathrm{BSM}} \ll 1$, in this region the denominator of the propagator can be approximated as $\sim 1/Q^2$. The luminosity in this region is then obtained by integrating the emissivities in Eqs. (4.16) to (4.18) with the replacements,

$$\begin{aligned}
\sum_\alpha (C_V^{\alpha,\mathrm{SM+BSM}}(q))^2 &= \frac{d^V_e}{G_F^2\,(q_r^2)^2}\Big(d^V_e\left(6\,(d^A_e)^2 + g^2_{\mu\tau}\right) + \sqrt{2}\,G_F\,q_r^2\Big[2\,d^A_e\sum_\alpha C_V^{\alpha,\mathrm{SM}} \\
&\quad + g_{\mu\tau}\left(C_V^{\mu,\mathrm{SM}} - C_V^{\tau,\mathrm{SM}}\right)\Big]\Big) \\
\sum_\alpha (C_A^{\alpha,\mathrm{SM+BSM}}(q))^2 &= \frac{d^A_e}{G_F^2(q_r^2)^2}\Big(6\,(d^A_e)^3 - \sqrt{2}\,G_F\,g_{\mu\tau}(C_A^{\mu,\mathrm{SM}} - C_A^{\tau,\mathrm{SM}})\,q_r^2 \\
&\quad + G_F\,d^A_e\Big[g^2_{\mu\tau} - 2\sqrt{2}\,G_F\,q_r^2\sum_\alpha C_A^{\alpha,\mathrm{SM}}\Big]\Big)
\end{aligned} \tag{4.30}$$

where we have defined $q_r^2 \equiv (1 - r_{\rm BSM})\, Q^2$.

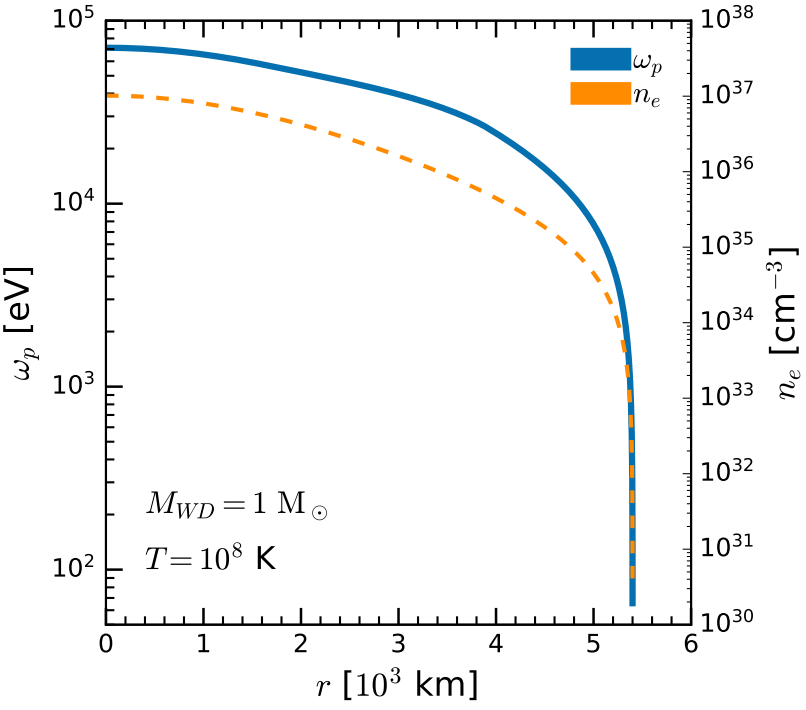

Figure 4.3: Plasma frequency ω_p (blue line) and electron density n_e (orange dashed line) of a WD with $M_{\rm WD} = 1 M_\odot$ at $T_{\rm WD} = 10^8$ K as a function of the distance to the centre of the star in km.

4.3.3 Resonant dark photons

When the dark photon mass is roughly of the same order as the WD temperature of $\mathcal{O}$(keV)[5] the A' contribution to the WD emissivities are significantly enhanced due to a resonance in the A' propagator. More precisely, this happens when the dark photon mass hits the plasma frequency, which is defined as [421] (see Eq. (3.17)).

When computing this frequency, we are integrating over the 3−momentum

[5]In the computations a temperature of $T_{\rm WD}$ =10^8 K was used.

of the electrons and positrons in the plasma with energy $E_k \equiv \sqrt{k^2 + m_e^2}$ and velocity $v \equiv k/E_k$. The plasma frequency ω_p depends on the temperature $T_{\rm WD}$ and the chemical potential μ_e, which depends on the distance r from the centre of the WD.

In Fig. 4.3, we show the plasma frequency ω_p and electron density n_e as a function of the WD radius r. We can see that the plasma frequency reaches its maximum at the centre of the star and decreases roughly over an order of magnitude throughout the interior of the star before it rapidly drops in the outer layers. This behaviour can be readily understood by looking at the electron density profile since the plasma frequency ω_p is directly proportional to it.

Thus, the resonance region consists of a whole range of dark photon masses for which a pole arises in the A' propagator due to the scanning of the plasma frequency ω_p in the range $0 \leq r \leq R_{\rm WD}$. This effect, if not cured, leads to a continuous curve of divergences of the integrands in Eqs. (4.16) to (4.18) in the $q - r$ plane, where q is the 3−momentum of the external plasmon and r the distance from the centre of the WD.

However, these divergences are non-physical and can be cured by considering the Breit-Wigner (BW) propagator [490]. This takes into account the imaginary component of the self-energy, which is directly related to the instability of the particle, and therefore is closely related to its decay width. The BW propagator takes the form [491]

$$\begin{aligned} G^{\mu\nu}_{\rm BW}(Q^2) = & \frac{-i(g^{\mu\lambda} - q^\mu q^\lambda/m^2)}{Q^2 - m^2 - {\rm Re}(F) - i\,{\rm Im}(F)} P^\nu_{L\lambda} \\ & + \frac{-i(g^{\mu\lambda} - q^\mu q^\lambda/m^2)}{Q^2 - m^2 - {\rm Re}(G) - i\,{\rm Im}(G)} P^\nu_{T\lambda}\,, \end{aligned} \tag{4.31}$$

where the self-energy of the vector is $\Pi^{\mu\nu} = F\,P_L^{\mu\nu} + G\,P_T^{\mu\nu}$, in terms of the

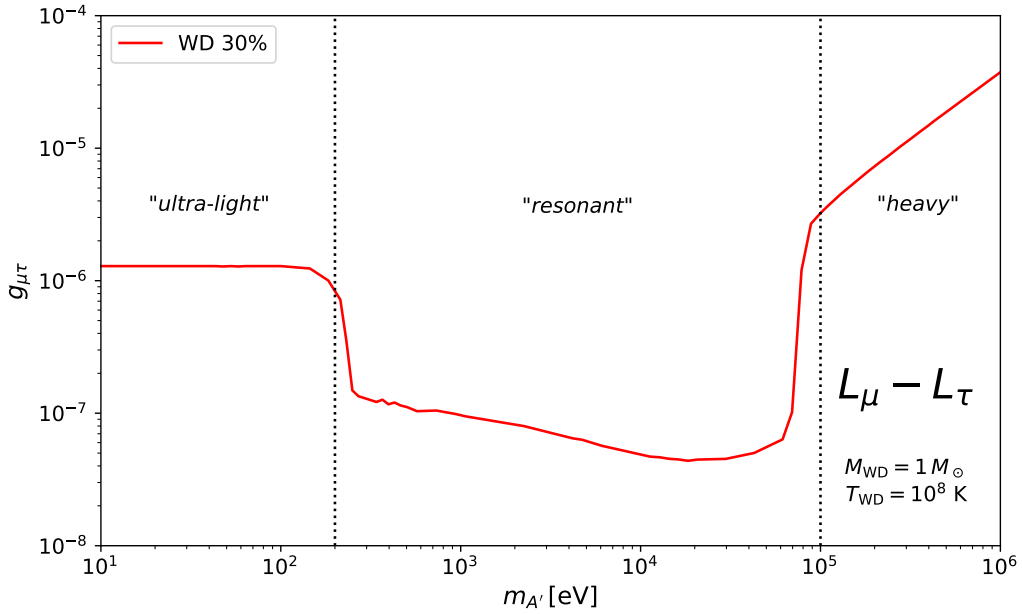

Figure 4.4: WD cooling bounds on sub-MeV $U(1)_{L_\mu - L_\tau}$ bosons. At high dark photon masses of $m_{A'} \gtrsim 100$ keV, the A' propagator in the WD emissivities is dominated by the A' mass and is to good approximation independent of the plasma frequency ω_p. Below this threshold the A' mass scans the plasma frequency in different phase space regions, leading to a resonance behaviour in the window of 0.2 keV $\lesssim m_{A'} \lesssim 100$ keV. At the low-mass end of this window the resonance peaks of the BW propagator start slowly moving outside the integration domain of the luminosity $L_{\rm WD}$ towards higher radii $r > R_{\rm WD}$ resulting in an attenuation of the resonance. Below $m_{A'} \lesssim 200$ eV the integrand no longer exposes any resonance behaviour in the integration domain and the integrand is dominated by the plasma frequency and approximately independent of the A' mass.

projectors $P_L^{\mu\nu}$ and $P_T^{\mu\nu}$ given in Eq. (4.23).

For the case of a vector mediator, it takes a similar form. There are, in principle, two main contributions to the imaginary part of the dark photon self energy $\mathrm{Im}(\Pi_{A'})$. The first one is due to a thermal loop of electrons, while the second one is due to a zero-temperature loop of neutrinos, since neutrinos are not thermalized inside the WD star. In the resonance region of masses

$m_{A'} \ll 1$ MeV, there is no imaginary contribution from the electron loop since the dark photon is not massive enough to decay into an electron-positron pair. It can, however, decay into a pair of neutrino-antineutrino, which for the corresponding A' masses and WD temperatures can be considered to be massless. We have to include the imaginary contributions $i\,\mathrm{Im}(\Pi_{A',\lambda})$ in the propagators of each polarisation $\lambda = T, L$ in Eq. (4.29).

After renormalizing the self-energy with internal neutrinos of flavour α using the $\overline{\mathrm{MS}}$ scheme, we obtain the following expressions,

$$\begin{aligned}\bar{\Pi}^{\mu\nu}_{A'}(Q^2) = -\frac{\left(k^\alpha_\nu\right)^2}{4\pi^2} Q^2 g^{\mu\nu} \int_0^1 dx\, x\,(1-x) \\ \times \log\left(\frac{m_\alpha^2}{m_\alpha^2 - x(1-x)Q^2}\right),\end{aligned} \tag{4.32}$$

where k^α_ν is the coefficient defined in Eq. (4.12). In the limit of massless neutrinos, the imaginary part of this self-energy is easily found as the argument of the logarithm is always negative in the region of integration, since the momentum of the thermal on-shell plasmon, Q^2, is always positive. Hence, we find

$$\begin{aligned}\mathrm{Im}(\bar{\Pi}^{\mu\nu}_{A'})(Q^2) &= \frac{\left(k^\alpha_\nu\right)^2}{24\pi} Q^2 g^{\mu\nu} \\ &= \frac{\left(k^\alpha_\nu\right)^2}{24\pi} \frac{(\omega_l^2 - q^2)^2}{q^2} P_L^{\mu\nu} \\ &\quad - \frac{\left(k^\alpha_\nu\right)^2}{24\pi} (\omega_t^2 - q^2) P_T^{\mu\nu}\,,\end{aligned} \tag{4.33}$$

where we have replaced Q^2 by its explicit value for the two polarizations.

Finally, the quantities entering the denominator of the dark photon propagator following the same procedure as in Section 4.3.2, are $\mathrm{Im}(\bar{\Pi}^{00}_{A'}) \times Q^2/q^2$ and $\mathrm{Im}(\bar{\Pi}^{xx}_{A'})$ for the longitudinal and transverse polarisation, respectively.

The projectors are absorbed when multiplied by those of the electronic loop of the plasmon. To obtain the full expression we still have to sum over the different neutrino flavours α in $\mathrm{Im}(\bar{\Pi}^{\mu\nu}_{A'})$, $k^{\alpha}_{\nu} \to \sum_{\alpha} k^{\alpha}_{\nu}$.

This prescription regulates the divergences in the dark photon propagator and leads to finite expressions in the whole parameter space. Nevertheless, the curve of very narrow peaks in the $q - r$ plane of integration remains. To reliably evaluate the luminosity integrals, we have to thoroughly sample these narrow peaks, for which we were relying on the `VEGAS+` algorithm [492] for adaptive multidimensional Monte Carlo integration in our calculations.

4.4 Results

In the following, we present our results for WD cooling via plasmon decay in presence of a $U(1)_{L_\mu - L_\tau}$ gauge boson. The results were derived for a representative WD with a mass of $M_{\mathrm{WD}} = 1\ M_{\odot}$, a temperature of $T_{\mathrm{WD}} = 10^8$ K, and the profiles of the electron number density n_e and chemical potential μ obtained from solving the Salpeter EoS [475]. For the numerical computation of the self-energy, we have considered two main approximations. For the inner layers of the WD, we considered a degenerate regime, where the chemical potential μ dominates over the temperature T_{WD} and the electron mass m_e. The quantities depend mainly on the Fermi momentum in this regime. For the outer layers, we regarded the classical regime, where the mass of the electron dominates over the temperature and over the sum of the chemical potential and temperature. In this regime, the quantities depend mainly on the electron number density n_e. More details on these limits and their respective expressions can also be found in [475].

In **??** we present the general behaviour of the WD cooling limits due to

plasmon decay via an extra $U(1)_{L_\mu - L_\tau}$ boson obtained by the computations outlined in Section 4.3. Current best fits of the hot WD neutrino luminosity function allow for a variation in the neutrino cooling with respect to the SM by a relative factor of $0.66 \lesssim f_s \lesssim 1.31$ at the 90 % confidence level (CL) (see Appendix E for the extraction of this limit based on Ref. [431]). Therefore, we can exclude parameter space leading to more than 30 % (red line) WD excess cooling in neutrinos. We show the limit of $\varepsilon^{\rm BSM} = 0.3$ extra cooling relative to the SM in the $m_{A'} - g_{\mu\tau}$ plane. This plot illustrates well the three qualitatively different domains of WD cooling depending on the A' mass already outlined throughout the paper.

For heavy dark photon masses of $m_{A'} \gtrsim 10^5$ eV, we observe a linear scaling of the sensitivity line. This is readily explained by looking at the WD plasma frequency in Fig. 4.3. Throughout the star the plasma frequency assumes its maximum value at $\omega_{p,\rm max} \lesssim 10^5$ eV. Hence, for dark photon masses above $\omega_{p,\rm max}$ the A' propagator in the emissivity is entirely dominated by its mass and scales as $\sim 1/m_{A'}^2$. The linear increase can be understood from the solution of the approximation in Eq. (4.19).

On the other hand, for ultra-light dark photons instead, we see a constant scaling of the sensitivity independent of the dark photon mass. This can be understood by an inspection of the propagator of the dark photon. As we stated in section Section 4.3.2, for ultra-light dark photons with $m_{A'} \ll q$ much smaller than the typical momenta in the stellar interior, we can well approximate the propagator in the WD emissivities by $\sim 1/q^2$. Hence, in this very light regime the WD sensitivity becomes independent of the A' mass to excellent approximation.

Finally, we will discuss the central region of the plot where the resonance behaviour dominates. For masses of the order of the plasma frequency, ω_p,

there is a resonance in the propagator between the dark photon mass $m_{A'}$ and the momentum transfer q. As can be seen in Fig. 4.3, as soon as the dark photon masses fall below the maximum plasma frequency of $\omega_{p,\max} \lesssim 10^5$ eV, resonance will occur in some region in the interior of the star. This explains why the transition between the linear and resonant regime is so abrupt. Employing the Breit-Wigner prescription, this will result in narrow but regulated peaks in the emissivities. Since these peaks contribute significantly to the integral, they are largely enhancing the sensitivity of WD cooling to a new $U(1)_{L_\mu - L_\tau}$ boson. As the dark photon masses decrease, the location of these peaks within the integration domain will shift towards higher and higher radii. For masses below about ~ 300 eV these peaks will start moving past the WD radius $R_{\rm WD}$ and out of the integration domain. Hence, their contribution becomes less and less important until no resonance occurs at all for masses of $m_{A'} \lesssim 200$ eV and the ultra-light regime is reached.

In Fig. 4.5 we show the WD cooling limit on a $U(1)_{L_\mu - L_\tau}$ boson in the MeV mass window, where a solution of the muon $(g-2)_\mu$ anomaly is still allowed. For comparison, we show the current best limits in grey. At masses below $\mathcal{O}(10)$ MeV the dark photon A' contributes significantly to the heating of the neutrino gas in the early universe resulting in a too large number of neutrino degrees of freedom, $\Delta N_{\rm eff}$, during BBN [455]. However, in the mass window of $m_{A'} \sim 10 - 20$ MeV the same effect leads to a milder contribution to $N_{\rm eff}$, which could explain the Hubble tension [455]. The corresponding favored region is depicted by the blue band labelled H_0. In turn, the green band shows the region of parameter space preferred by the $(g-2)_\mu$ anomaly as measured at the E989 experiment [484] and explained in Section 4.2.1. The most stringent existing constraint on the $(g-2)_\mu$ favored region is due to the recently reported result of the invisible search at the NA64μ exper-

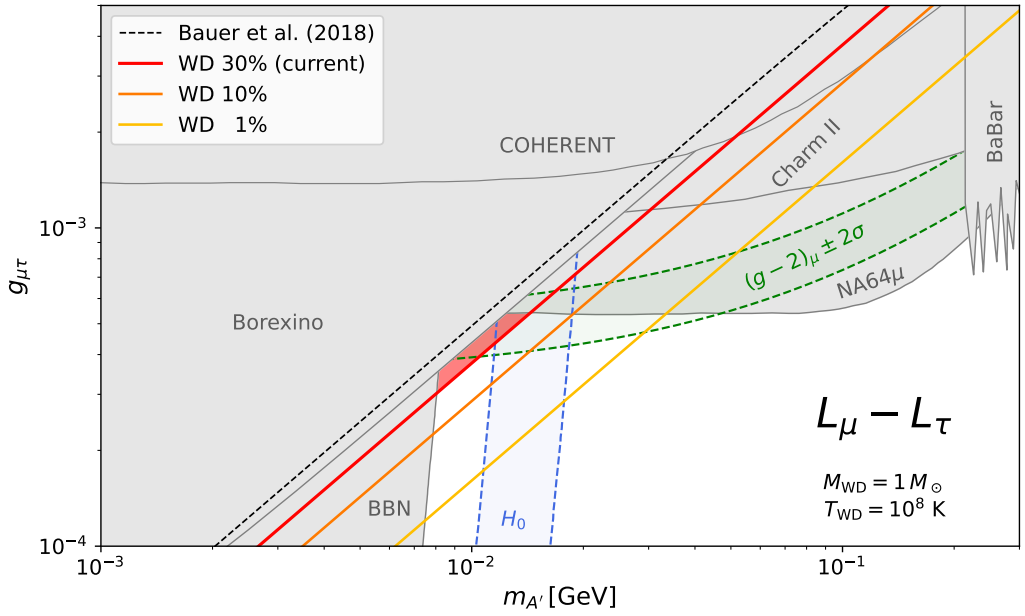

Figure 4.5: Limits on MeV-mass $U(1)_{L_\mu - L_\tau}$ gauge bosons. The grey shaded areas show the current constraints (see text for explanations). The green and blue bands depict the regions of parameter space preferred by the $(g-2)_\mu$ and H_0 anomaly, respectively. We show our constraints from white dwarf cooling via plasmon decay for an excess of 30% (red), 10% (orange) and 1% (yellow) over the SM neutrino cooling rate. The red colored area shows newly excluded parameter space from the 30% excess cooling limit of this analysis. For comparison, the black dashed line shows the previously estimated WD cooling bound of Ref. [403].

iment [493]. At low masses constraints from the measurement of the ^{7}Be solar neutrino flux at the Borexino experiment [468, 494, 495] exclude a solution below A' masses of $m_{A'} \sim 10$ MeV. At high masses, we also show the limit obtained from resonance searches in four-muon production by the BaBar collaboration [496]. For comparison, we also show the resulting bound from measurements of coherent elastic neutrino-nucleus scattering (CEνNS) with a CsI[Na] target at the COHERENT experiment [497, 498]. Similarly, a strong constraint arises from the search for neutrino trident production [499]. We show the leading bound by the CHARM-II experiment [500].[6]

The solid red line is the novel constraint derived in this work from excluding $\varepsilon^{\rm BSM} = 30\,\%$ extra WD neutrino cooling. For comparison, the black dashed line shows the estimate of the WD cooling bound that has been obtained in Ref. [403] from matching to the EFT coefficients used in the analysis of [404], which in turn assumed a 100% excess cooling constraint. We note that the current 30% WD cooling limit excludes part of the parameter space favored by a simultaneous explanation of $(g-2)_\mu$ and H_0, which previously has not been tested (red area).

We also show the sensitivities of a future measurement of the hot WD neutrino luminosity function excluding extra cooling at the 10% (orange line) and 1% (yellow line) level. The future space-based CASTOR experiment [432] is planning to observe approximately 8 million hot young WDs [433]. Hence, CASTOR is expected to collect a factor of $\sim 10^3$ more statistics as compared to the sample used in Ref. [431], which was used to extract the current 30% excess cooling bound. CASTOR is expected to be launched as early as 2027 with a minimum lifetime of the spacecraft of 5 years [502], so that an order

[6] In principle, a more stringent bound can be derived from the CCFR results [499]. However, some doubts have been shed on the correct incorporation of a background due to diffractive charm production in the relevant analysis [501] and hence we abstain from showing the corresponding limit.

of magnitude improvement in the WD excess cooling bound within the next decade seems feasible. Improved sensitivities at the level of 10% (orange line) excess cooling could rule out almost all of the joint $(g-2)_\mu$ and H_0 explanation, while sensitivities at the level of 1% (yellow line) could exclude almost the entire parameter space favored by the $(g-2)_\mu$ anomaly.

4.5 Conclusions

In this chapter, we have performed for the first time an *ab initio* computation of the WD luminosity due to plasmon decay into neutrinos in presence of an extra new $U(1)_{L_\mu - L_\tau}$ gauge boson. We have performed the calculations for a representative WD star with a mass of $M_{\rm WD} = 1 M_\odot$ and temperature of $T_{\rm WD} = 10^8$ K. Following [421], we have considered two main approximations: the degenerate regime (for the inner layers of the WD) and the classical regime (for the outer ones).

Our main result is a careful derivation of the neutrino luminosity for the entire mass range of a $U(1)_{L_\mu - L_\tau}$ boson resulting in the limits shown in Fig. 4.4. In particular, we have also performed the computation in the resonant regime where the A' masses are comparable to the plasma frequency ω_p. We have demonstrated that the varying profile of the electron density n_e and chemical potential μ in the interior of the star result in a broad range of A' masses of 100 eV $\lesssim m_{A'} \lesssim$ 100 keV, in which plasma resonance effects become important and lead to a significantly increased cooling contribution of the A'.

We have further demonstrated that the current bound of 30% extra WD cooling is the leading constraint on the region of parameter space favored by a simultaneous explanation of the $(g-2)_\mu$ and H_0 anomaly (cf. red line

in Fig. 4.5). A future precision observation of the WD neutrino luminosity function with CASTOR at the 10% or even 1% level could exclude a large fraction or even the entire remaining parameter space favored by $(g-2)_\mu$.

A straightforward extension of this work would be to perform the same calculations for neutron stars. However, the lack of knowledge of the precise equation of state for these stars makes it fundamentally more difficult to obtain robust results for the corresponding luminosities. Nevertheless, compared to WDs these objects exhibit much higher densities and at their birth also much higher temperatures of up to $T \sim 50$ MeV. This could significantly enhance the effect of neutrino cooling through a novel $U(1)_{L_\mu - L_\tau}$ boson and in particular improve sensitivities at higher boson masses. Furthermore, resonances at a higher mass range could result in limits improving over current ones for mediators like leptophilic dark photons.

Conclusions

In this thesis we have explored different strategies to test dark sectors, with emphasis on dark photons and heavy neutral leptons, especifically for the "Three portal model" and $L_\mu - L_\tau$ gauge extensions. We have addressed one particular anomaly: MiniBooNE low energy excess. We also took the solution we fitted in MiniBooNE to look for effects in a very different scenario: white dwarf cooling. We have also tested the $L_\mu - L_\tau$ dark photon in these compact stars. The main idea underneath this test was to realize and show how astrophysics can also constrain the models we use to explain terrestrial anomalies. In this way, dark sectors can be inspected from various different approaches and sub-fields, from neutrino to astro-particle physics.

Dark sectors in MiniBooNE As we have seen in Chapter 2, anomalies in experiments like MiniBooNE open the door to a rich world of possibilities from dark sectors, since there are many final states that could be misreconstructed as signal events in the detector. We discussed a vast array of dark sector models that could produce those states and consequently that could explain the excess. Thanks to this richness we were able to propose a LEE explanation exploiting the production of an e^-e^+ pair from the decay of HNLs, upscattered by neutrinos in the detector itself. We have discussed how this solution is a successful alternative to the sterile neutrino oscilla-

tion ones, that are strongly disfavored as they produce an excess in both disappearance and appearance experiments and they have not been seen in MicroBooNE [222–225, 229, 271, 275].

The process we fitted, namely an up-scattering to an HNL through a dark photon, has other challenges: the HNLs can be long-lived in some regions of parameter space. Therefore, they can interact with the dirt before the detector and decay inside it, as well as escape from the detector not leaving a single trace of their presence. These subtleties were carefully worked and studied, so that the correct amount of events was computed. The best solutions involved non-prompt lifetimes, such that the higher energy HNLs could escape the detector before decaying.

This model fits better than the sterile neutrino oscillation explanation, with a χ^2 of 14%. However, it also shares the difficulty of a tension in fitting the neutrino and anti-neutrino mode simultaneously. Another challenge is to reproduce the angular distribution of the excess which, although is forward, it exhibits events along a broad angular spectrum. The HNLs are usually produced very close to the direction of the beam. A dark sector that would fit even better is one with a scalar or axial coupling to matter, though a vector coupling for the decay, though these models are more constrained by direct searches.

The "Three portal model" regions that better fit MiniBooNE can also be tested in the SBN program. We showed that $\mathcal{O}(10^3)$ events would be seen in MicroBooNE and $\mathcal{O}(10^4)$ events in ICARUS and SBND, without considering the detector responses and (mis-)reconstruction capacities. In principle, we would expect to observe these kinds of events in the future years and be able to constrain or exclude parts of the parameter region of the model. In principle any dark sector model fitting MiniBooNE can be tested at these

experiments.

Testing the dark photon in WDs Any model with a mediator that can connect a photon or an electromagnetic current with a neutrino current, such as the dark photon from the "Three portal model", could in principle leave traces in the cooling rate of hot WDs. Therefore, this dark boson is a suitable candidate to study a contribution to plasmon decay in WDs, which is the main source of cooling for those stars with temperatures beyond $10^{7.8} - 10^{8}$ K.

Even though the constrained couplings from the model are usually weaker than the electroweak ones, the region of masses of the order of 10s MeV to 1 GeV of the dark photon gives a stronger contribution through its propagator. For the temperatures considered, $\ll 1$ MeV, the propagator takes the form of $1/m_{Z'}^2$, which can be several orders of magnitude greater than the SM ones: $1/m_W^2$ or $1/m_Z^2$.

The constraints found by this search do not depend on the number of HNLs added to the model. The only parameter that comes into the computation from the neutrino sector of the model is the neutrino mixing. Light sterile neutrino mass states could even make the limits stronger: no extra state would relax the limits obtained in Chapter 3. The constraints calculated in the present work are stronger that the general model - independent limits from DIS [428], LKB [429] and EWPO [430].

The general behavior of the limits are as expected: lower masses of the dark photon are more constrained than higher masses due to the impact of its propagator, while higher values of the kinetic mixing ε are more excluded. In the region studied, where the propagator is approximated to a constant, the temperature does not have a direct impact in the limits. The indirect

effect of the temperature would be on the stars observed and the statistics and sensitivity of their measurement, which is beyond the scope of this work.

In the case of the $L_\mu - L_\tau$, this model has a strong advantage: it just adds one field to the SM. The dark photon that arises from this model is directly connected to the second and third generation of leptons, which makes it less constrained than models where interactions with electrons are at tree level. This dark photon, as we have shown, can interact with the first generation of leptons through a kinetic mixing with the photon and the Z boson at a 1-loop level. This possibility lets this dark photon to contribute to WD cooling.

In Chapter 4, we have performed a computation of the luminosities in this BSM scenario for a full range of masses. These whole-range limits may not be important if we consider other ones. However, they allow us to better understand the effect of having an extra boson of any mass in a WD and to visualize a region which would in principle enable to observe new physics in any hot object: the resonant region. Hotter and denser objects could more stringently exclude regions. That is why a further study in neutron stars could also be of great interest for researchers working in dark sectors.

The limits come from the heavy sector of the mass range, for which we have shown a better constraint than the existing ones, especially on the region where the $L_\mu - L_\tau$ model could in principle solve the Hubble tension and the muon $(g-2)_\mu$ simultaneously. The sensitivities that set the limits were obtained thanks to the statistical fit done by [431] and the χ^2 values the authors found for hot WD luminosities deviating from just the SM contribution. A careful inspection into the values was needed to find the 90% C.L., which is the same level considered by the other limits. There is still a region from which this model could solve the two anomalous measurements,

though near future observations by CASTOR may exclude the whole region.

Astrophysics as a testing scenario As we have shown from a WD cooling context, astrophysical scenarios may be fruitful places to search for dark sectors and to test the models, especially when they play a role in explaining observed anomalies. Astrophysics can constrain the models used to explain terrestrial experimental anomalies, as we showed in Chapter 3. There are some conclusions and future prospects that we can extract from the work presented here.

Open questions and future developments First, low mass mediators are more strongly excluded by cooling stars because of their higher contribution to cooling through their propagators. If these masses are well above the plasma frequencies in the star core, then the effect is simply a linear one on the space of the mass and couplings of the dark vector. We have not computed a case in which a non-excluded mass for a mediator can be in resonance with the star plasma ferquencies, since the computations done for the resonant region in the present thesis set limits for already excluded parameter regions. This was out of the scope of our work, but it is a promising challenge to find such a case. Neutron stars (NSs) could offer fruitful opportunities to exclude broader ranges of parameter regions for $\sim \mathcal{O}(\text{MeV})$ bosons under this resonant regime, due to their higher masses and densities. The difficulties for these computations are related to the modeling of the equation of state of the NSs: unless we know with more precision what happens inside these stars, we will not be able to set stronger limits than the current ones.

Second, WDs, as degenerate scenarios, are sensitive to BSM physics. In our case, an electron degenerate gas makes leptonic processes visible.

Hadronic degenerate cases could also have a strong impact, though we would need to be very careful about the regime in which form factors can be used for the computations. The formulae used in the present thesis regard the degenerate approximation in order to compute quantities that would be numerically too expensive without these degenerate assumptions. A full computation of plasmon decay emissivities is also a challenge to face in the future in order to have a better control of the different regimes found in stars. This is especially relevant when we get closer to their atmospheres and farther from the center of the degenerate core.

Third, dark sectors offer a rich a vast phenomenology that can explain many of the current experimental anomalies with just some simple new ingredients added to the SM. We have mainly worked with dark photons, so other kinds of mediators are a challenge for the future. In the case of scalars in WD cooling, they have a suppressed contribution because they couple to the difference of electrons and positrons distributions. Unless other kinds of diagrams are made possible, this would be analogous to the axial contribution in the case presented here. Furthermore, pseudo-scalar vanish if we are forced to attach them to electron-positron loops. Axions and ALPs in general could be good candidates to be studied, as they can directly be connected to photons. Hot WDs are also sensitive to more exotic interactions, though that was out of the scope of this work and remains as a future challenge.

Finally, there are many other astrophysical (and cosmological) scenarios that can help in the search of dark sectors, such as black holes, Active Galactic Nuclei (AGNs), phase transitions, inflation, topological defects, etc. The collaboration between these contexts and terrestrial experiments is certainly of great importance and can in principle give a feedback to the solutions that are being regarded for many of the current experimental anomalies. This is

precisely what we wanted to show along the thesis.

Appendix A

MiniBooNE signal selection

The MiniBooNE signal selection focused on a $\nu_\mu \to \nu_e$ signal from oscillations. The data released by the collaboration [66] includes data and background distributions in reconstructed quantities like visible shower energy, shower angles, and reconstructed neutrino energy under the assumption of CCQE scattering. The collaboration also released Monte-Carlo events with true and reconstructed variables and selection efficiencies for electron and photon final states. These data releases are best suited for studies of single-electron, positron, or photon final states. Other models based on misidentifying multiple electromagnetic showers into one require greater care since they depend on the detector response and signal reconstruction specifics. The two main challenges are i) obtaining realistic distributions of reconstructed quantities without a detailed detector simulation and ii) evaluating the signal efficiency without access to high-level reconstructed variables. For instance, part of the signal selection in MiniBooNE is performed using particle identification likelihoods, which quantify the compatibility of an observed event with the hypothesis that it consists of an electron, muon, or pion final state. Without a detector simulation, obtaining the distributions of these abstract quanti-

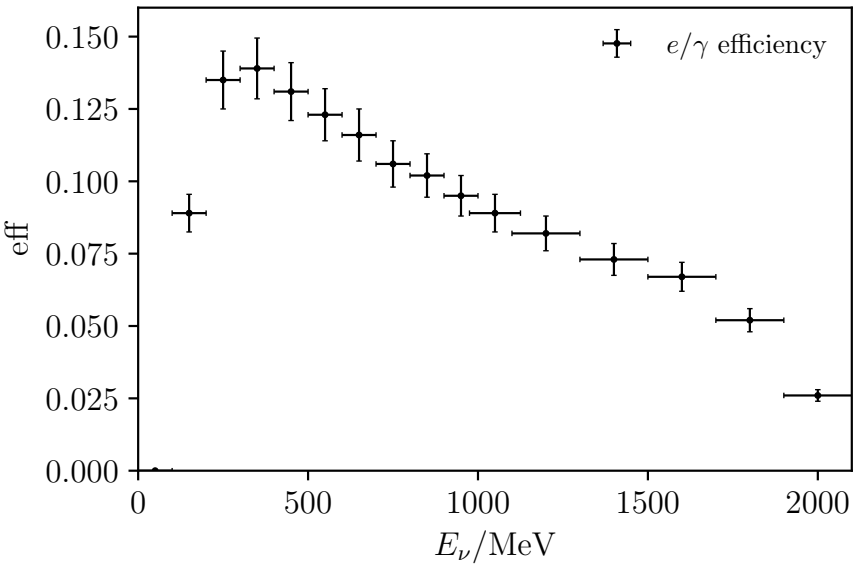

Figure A.1: MiniBooNE single electron/photon efficiencies as a function of energy [60] used in this work.

ties and the selection efficiency of the respective cuts in these variables is not realistic. As a result, phenomenological studies of models that rely on the misidentification of final states are subject to more uncertainties than those based on oscillation signatures, for example.

In the absence of dedicated studies of exotic e^+e^- and $\gamma\gamma$ final states by the collaboration, we turn to simplified signal selection criteria. As the main benchmark of this chapter, we focus on the dark neutrino model that arises from the Three Portal model, where the main source of uncertainty in the analysis is the probability that an e^+e^- final state is selected as an electron-like event in the LEE region. We also turn to the study in Ref. [198], where the authors attempted to reproduce the MiniBooNE π^0 signal selection without a complete detector simulation. In our own fits, we implement a procedure analogous to theirs and compare the final signal efficiency obtained under different selection and reconstruction assumptions.

We divide the selection criteria into two steps.

- Pre-selection: requirements that the e^+e^- pair is reconstructed as a single electromagnetic shower.
- Selection: fiducialization, PID, and energy requirements.

To evaluate the efficiency of the second step, we apply the official MiniBooNE reconstruction efficiencies shown in Fig. A.1 for each event given its E_{vis}. Since we apply fiducial volume cuts ourselves, we divide the official MiniBooNE efficiencies by 55% [54]. The efficiencies also include the cut on $E_{\text{vis}} > 140$ MeV, so we extend our prediction down to $E_{\text{vis}} < 100$ MeV. This is also an approximation since the shape of CCQE events and dark-neutrino events within this low-energy bin can differ. Also implicit is the assumption that the PID cuts have the same efficiency for CCQE events and e^+e^- ones. These cuts account for approximately a factor of two reduction in the overall efficiency [54]. This number may vary for e^+e^- events due to the different topology, but it cannot be estimated here without access to the reconstructed electron, muon, and pion likelihoods for each event. Finally, other cuts aimed at reducing external (dirt and wall) events and comics are also included in Fig. A.1 and are assumed to have the same effect on e^+e^- events.

We now describe two simplified pre-selection procedures and compare their efficiencies in Figs. A.3 and A.4.

A.1 Simplified hard cuts pre-selection

A dark neutrino event can be reconstructed as a single shower for sufficiently energy-asymmetric or collimated e^+e^- pairs. A simplified approach adopted in Refs. [196, 230] was to define an energy-asymmetric e^+e^- pair as one where

the energy of one of the particles was below 30 MeV (after smearing). Events were classified as overlapping when the opening angle between the leptons was at most 13° (after smearing). In addition, a cut on the *true* invariant mass of all events was performed, simulating the selection criterion in Table 12.1 of Ref. [391],

$$m^{\text{true}}_{e^+e^-} < \left[32.03 + 7.417\left(\frac{E_{e^+}+E_{e^-}}{\text{GeV}}\right) + 27.38\left(\frac{E_{e^+}+E_{e^-}}{\text{GeV}}\right)^2\right] \text{ MeV}. \tag{A.1}$$

In the MiniBooNE analysis, this cut is applied to the invariant mass obtained under the two-photon reconstruction hypothesis. Without such a reconstructed variable, we apply the cut to the true invariant mass of the e^+e^- pair. This implicitly assumes that the MiniBooNE two-photon reconstruction correctly reconstructs the e^+e^- invariant mass, which is less likely to be the case for events that appear more single-shower-like. While a crude approximation, this cut ensures that heavy parent particles do not contribute significantly to the LEE, since the daughter e^+e^- pair will typically be well separated. As we will see, this cut tends to produce much smaller efficiencies than the method implemented in the analysis of the main text.

A.2 Simplified π^0-based pre-selection

This method is the one we adopt for our dark neutrino fits and is adapted from Ref. [198]. The authors implement an energy-dependent cut on the plane of the π^0 kinematics: $\cos\theta_{\gamma\gamma}$ vs $E_{\text{max}}/E_{\text{vis}}$. This is achieved with a cut on r, the distance between points in the π^0 kinematic plane and the most-overlapping and most-energy-asymmetric region. The selection criterion is

designed to reproduce the correct π^0-background distribution, and it was shown to be mostly independent of the exact choice of the abstract variable r. Due to the similarity between the topology of dark neutrino and π^0 events, we readily adapt the selection for e^+e^- events. For concreteness, we choose to work with the variable r_{circ1}, defined here as

$$r_{\text{circ1}}^2 = \left(\frac{1-\cos\theta_{ee}}{2}\right)^2 + \left(1-\frac{E_{\max}}{E_{\text{vis}}}\right)^2 . \tag{A.2}$$

We then apply an energy-dependent cut on r_{circ1} following the data release of Ref. [198]. The three different r variables defined in Ref. [198], namely, r_{circ1}, r_{circ0}, and r_{diag}, lead to very similar results.

A comparison of the efficiency for the two pre-selection methods discussed above is shown in Fig. A.2. We generate upscattering events exclusively inside the detector and enforce the N_4 decays to be prompt. In this way, the shape of the efficiencies as a function of the reconstructed visible energy $E_{\text{vis}}^{\text{reco}}$ depends uniquely on the kinematics and not on the HNL lifetime. The fiducial volume cut is included in our pre-selection efficiency but does not depend on the kinematics. The comparison shows that the cut in Eq. (A.1) significantly impacts the true-variable selection method. In addition, the methods of Appendix A.1 and Appendix A.2 can differ significantly in shape and overall normalization. The discrepancy is also significant for $m_{Z'} \simeq m_\pi$, indicating that the true-variable method would most likely not reproduce the correct π^0 spectrum at MiniBooNE if applied to single π^0 background events. This further motivates us to work with the simplified π^0 method of Ref. [198].

We also compare our pre-selection method (circ1) with the misidentification of π^0 backgrounds at MiniBooNE. In Fig. A.3, we show the pre-selection efficiencies for a few dark neutrino models and compare them with

the misidentification probabilities for genuine π^0 events quoted in Fig. 11.8 of Ref.[391]. Although we refer to the latter as an efficiency, it should not be confused with the efficiency of reconstructing well-separated 2γ event from π^0s. We convert the true e^+e^- total energy $E_{\rm tot}$ into a mock π^0 momentum variable according to $p_\pi = \sqrt{E_{\rm tot}^2 - m_{\pi^0}^2}$. The differences in shapes are due to the different boost factors of the parent particle. Light mediators produced on-shell are more likely to be misidentified as a single shower at much lower momenta than π^0 simply due to their larger boosts. In the case of off-shell mediators, the HNLs are misidentified as a single shower more often across the entire energy region. Finally, we also compare our preselection with the efficiency in [198], as a function of the reconstructed visible energy $E_{\rm vis}^{\rm reco}$.

A comparison of the final signal selection efficiencies for various points in the parameter space of dark neutrino events is shown in Figs. A.5 and A.6. We do not include the geometrical acceptance in order to isolate the effects of the kinematics on the efficiency. However, we do include the official MiniBooNE e/γ efficiencies.

For ease of comparison with previous literature, we compare our own dark neutrino fit for 3+1 model with $m_{Z'} = 30$ MeV with the fit in Ref. [194]. While the set of phenomenological parameters used in their work is not the same, we assume that $|U_{D4}| = 1$, instead of our own value of $|U_{D4}| = 1/\sqrt{2}$. Good agreement is observed between the two cases.

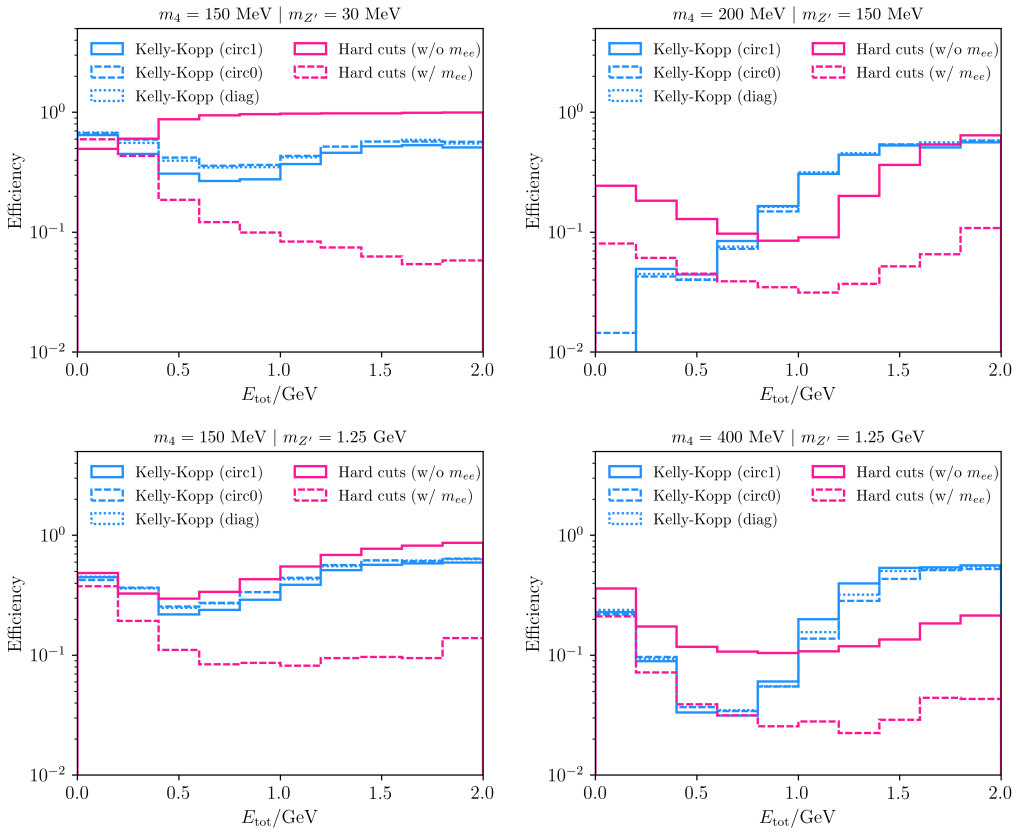

Figure A.2: The final signal efficiency using different pre-selection methods. The true-variable method, discussed in Appendix A.1, is shown with and without applying the cut on the e^+e^- invariant mass m_{ee}. The simplified π^0 method, discussed in Appendix A.2, is referred to as Kelly-Kopp. We show the different methods based on the choice of the r variable, as defined in [198]. In all cases, we generate upscattering inside the detector and enforce N_4 to decay promptly. The fits in the main text are based on the Kelly-Kopp (circ1) method.

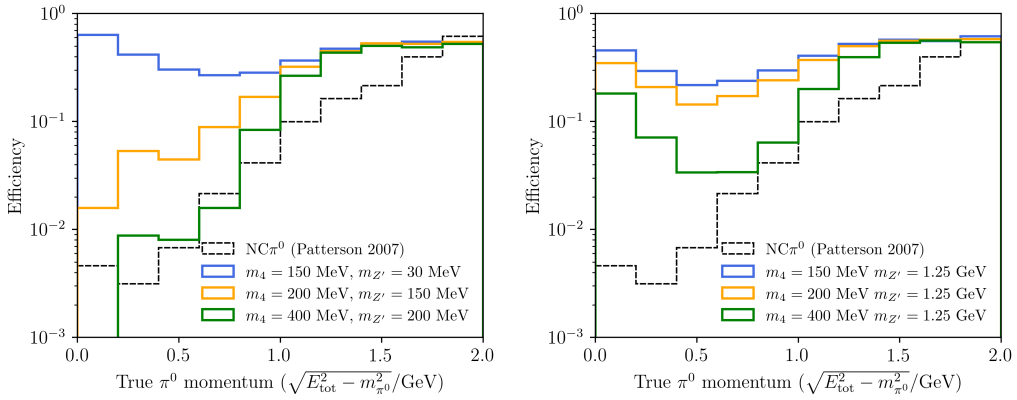

Figure A.3: A comparison between the MiniBooNE signal selection efficiency for dark neutrino events and the misidentification probability for π^0 background events (from [391]) in the true π^0 momentum variable. The latter is defined as $\sqrt{E^2_{\rm tot} - m^2_{\pi^0}}$ for e^+e^- events.

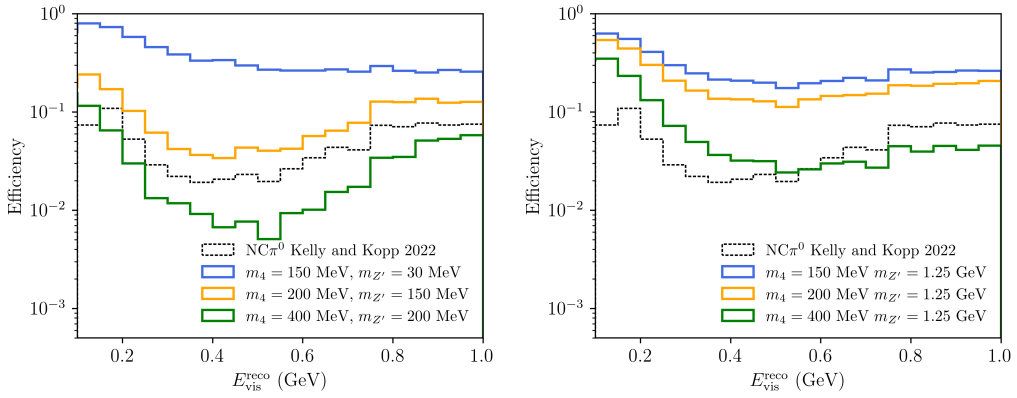

Figure A.4: A comparison between the pre-selection (circ1) efficiency for dark neutrino events and the misidentification probability for π^0 background events (from [198]) in the reconstructed visible energy variable.

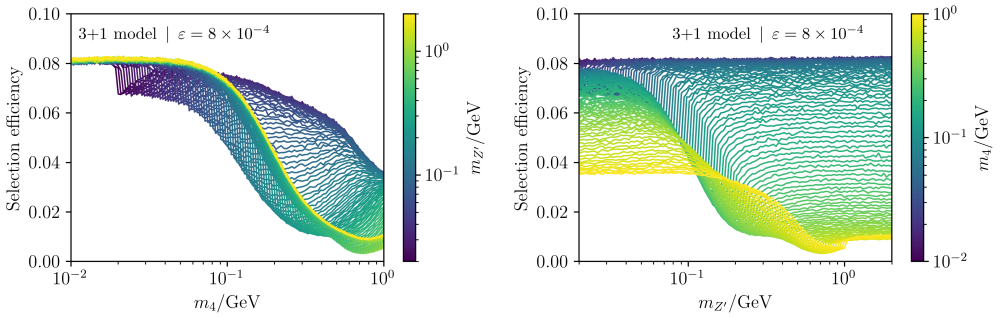

Figure A.5: The signal selection efficiency of our simulation for dark neutrino events in MiniBooNE for the 3+1 model. On the left, we show the efficiency as a function of the heavy neutrino mass m_4 for fixed values of the mediator mass, $m_{Z'}$. On the right, we show the same efficiency, now as a function of $m_{Z'}$ for fixed values of m_4. The geometric acceptance is not included.

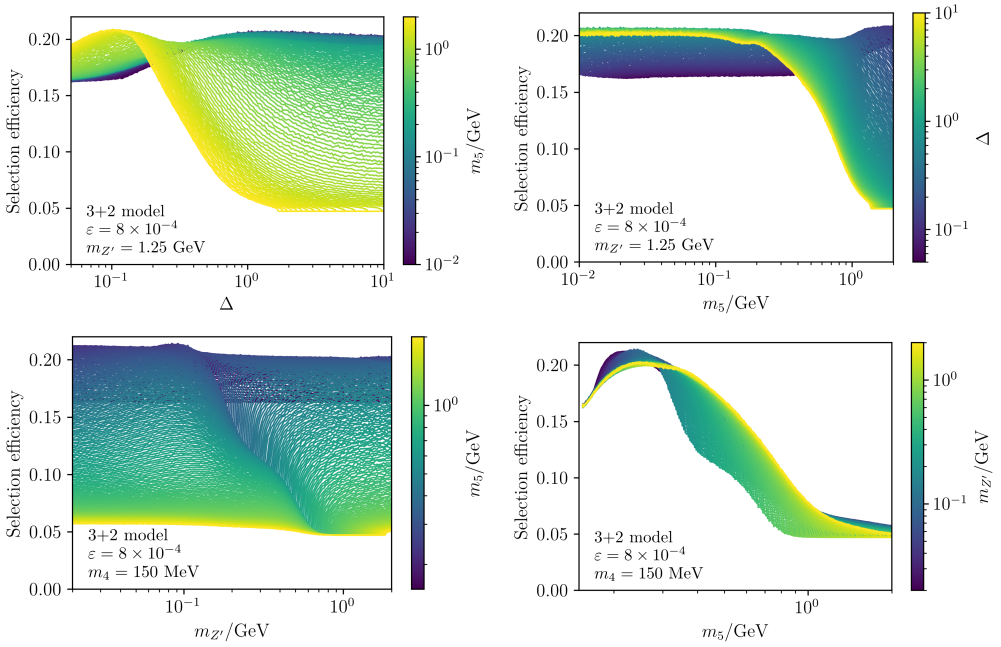

Figure A.6: The signal selection efficiency of our simulation for dark neutrino events in MiniBooNE for the 3+2 model. The upper panels show the efficiency as a function of the HNL mass splitting Δ (left) and the parent HNL mass m_5 (right) for a single fixed value of $m_{Z'}$. The lower panels show the efficiency as a function of the mediator mass $m_{Z'}$ (left) and the parent HNL mass m_5 (right) for a single fixed value of m_4. The geometric acceptance is not included.

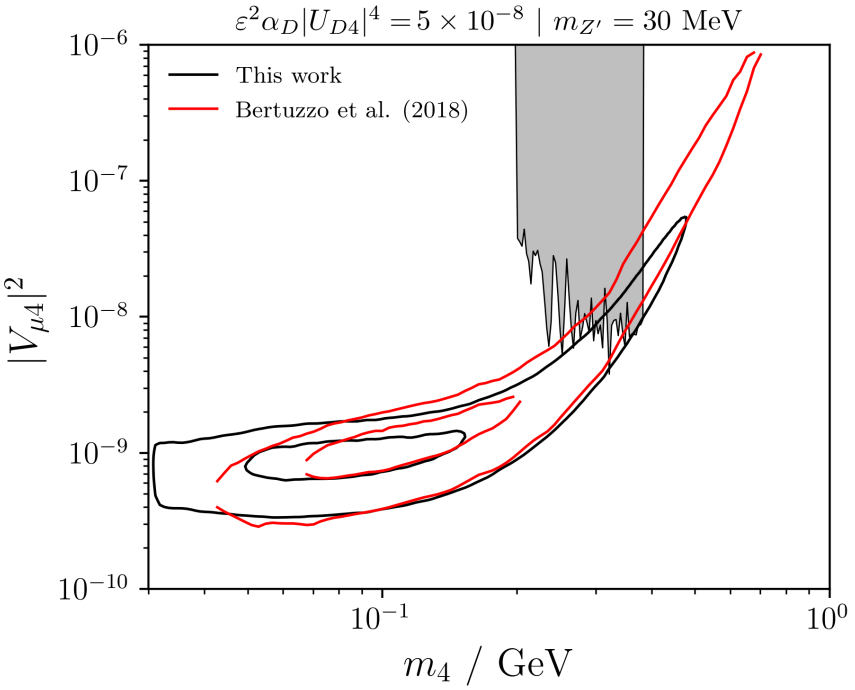

Figure A.7: A comparison of the LEE neutrino energy spectrum fit in this work and that of Ref. [194] for the choice of $m_{Z'} = 30$ MeV. The 1σ and 2σ regions are shown are shown as smaller and larger closed regions, respectively. We assume that the results in Ref. [194] are quoted for $|U_{D4}|^2 = 1$.

Appendix B

Kinematics of events in MiniBooNE

To understand the properties of the e^+e^- showers produced in dark neutrino events, we show the median of kinematical variables across the parameter space.

For the 3+1 model, Fig. B.1 shows the median of various kinematical observables as a function of $m_{Z'}$ and m_4. We can observe that on-shell regions exhibit more forward events than off-shell ones. Lower values of $m_{Z'}$ and m_4 produce more forward showers because of the larger boost characterizing the events. In those regions, the misreconstruction of the two showers is dominated by asymmetric events, which can have a larger separation angle than those in regions dominated by overlapping showers, which by definition, have small angles. Higher HNL masses favor higher showers' total energy, particularly in the on-shell region, where more energy goes to the e^+e^- pair rather than to the outgoing invisible neutrino.

Figure B.2 shows the same study for the 3+2 model. In this case, we only show the off-shell region considered for this model. The median angle of

showers relative to the neutrino incoming beam increases with higher values of m_5 and Δ. Close to the off and on-shell decay limits of HNLs, a resonance due to interactions with dirt produces highly forward events. Conversely, the angle increases in two directions: for lower m_5 and higher Δ. The higher m_5 region is naturally explained by the high mass of the decaying HNLs that produce the showers. The lower m_5 region results from filtering highly boosted events due to long decay, leaving showers with larger angles. The separation angle between showers mainly depends on the mass of N_5, with higher masses leading to larger angles. However, very high masses approaching the on-shell region exhibit a reverting effect due to resonance and boosted effect near the change of regimes on the on-shell side. Apart from this effect, the region with the highest separation angle is around $m_5 \sim 700$ MeV, where the energy asymmetry is also larger due to misreconstructed events being dominated by asymmetric showers. The total energy of showers is highly dependent on the regime, with energies significantly higher very close to the on-shell region. Additionally, higher Δ values lead to less massive outgoing N_4, translating into more energy going into the showers. Hence, regions with large m_5 exhibit a maximum as they approach the on-shell mediator region.

Figure B.3 shows an additional study on the 3+2 model obtained by varying $m_{Z'}$ and m_5, while fixing $m_4 = 150$ MeV and $\varepsilon = 0.01$. There is a clear separation between off and on-shell regimes In the on-shell region, angles are less forward for lighter mediators and higher m_5, while in the off-shell region, events are less forward for heavier mediators and higher m_5. The angular separation between pairs exhibits the opposite behavior: less forward events result in more separated e^+e^- pairs. This region of high separation is also the most asymmetric one. Moreover, heavier N_5 mediators in the on-shell region lead to significantly higher shower energies, and a similar trend

can be observed for other cases with fixed m_4.

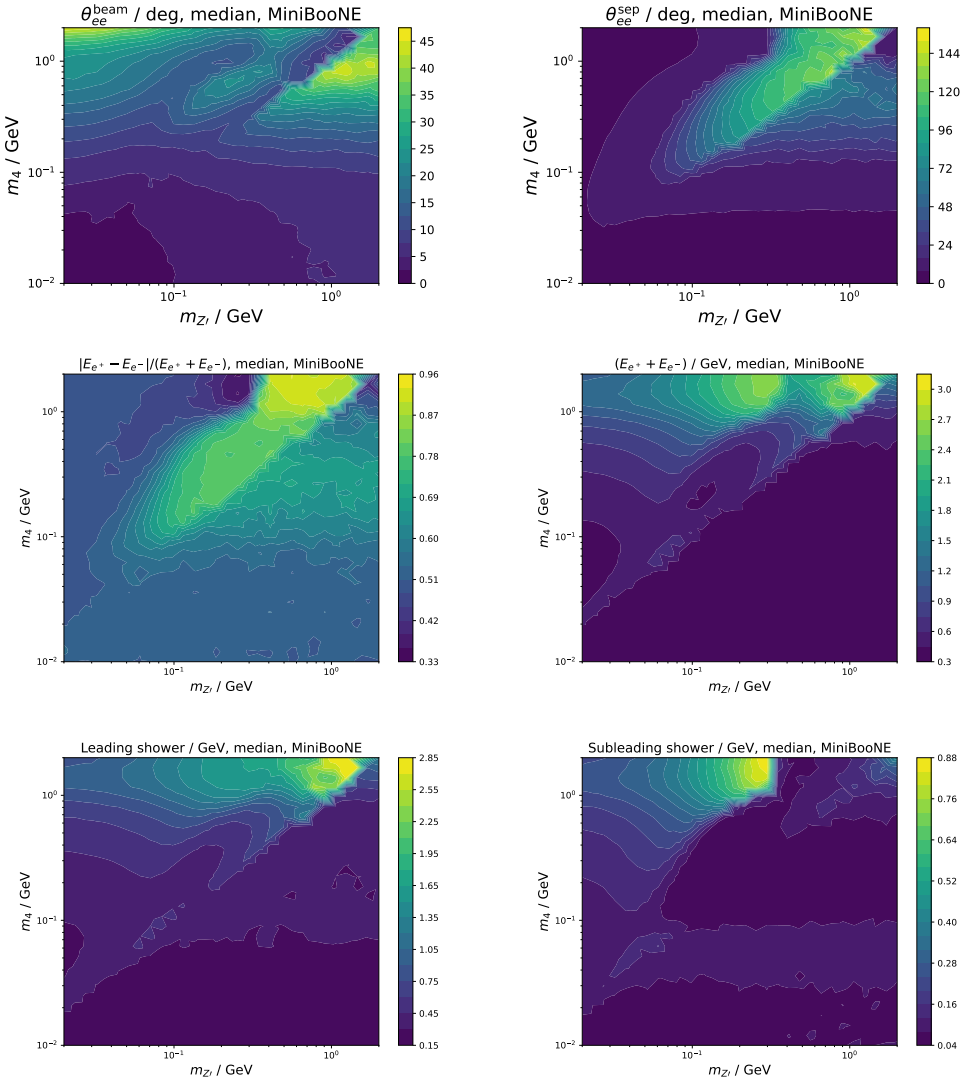

Figure B.1: The median of kinematical variables in dark neutrino events at MiniBooNE for the 3+1 model. We show the median of (1) the angle between the shower and beam, (2) the angle between the two showers, (3) the asymmetry of the showers, (4) the total energy of the showers, and the energy of the leading (5) and subleading (6) showers.

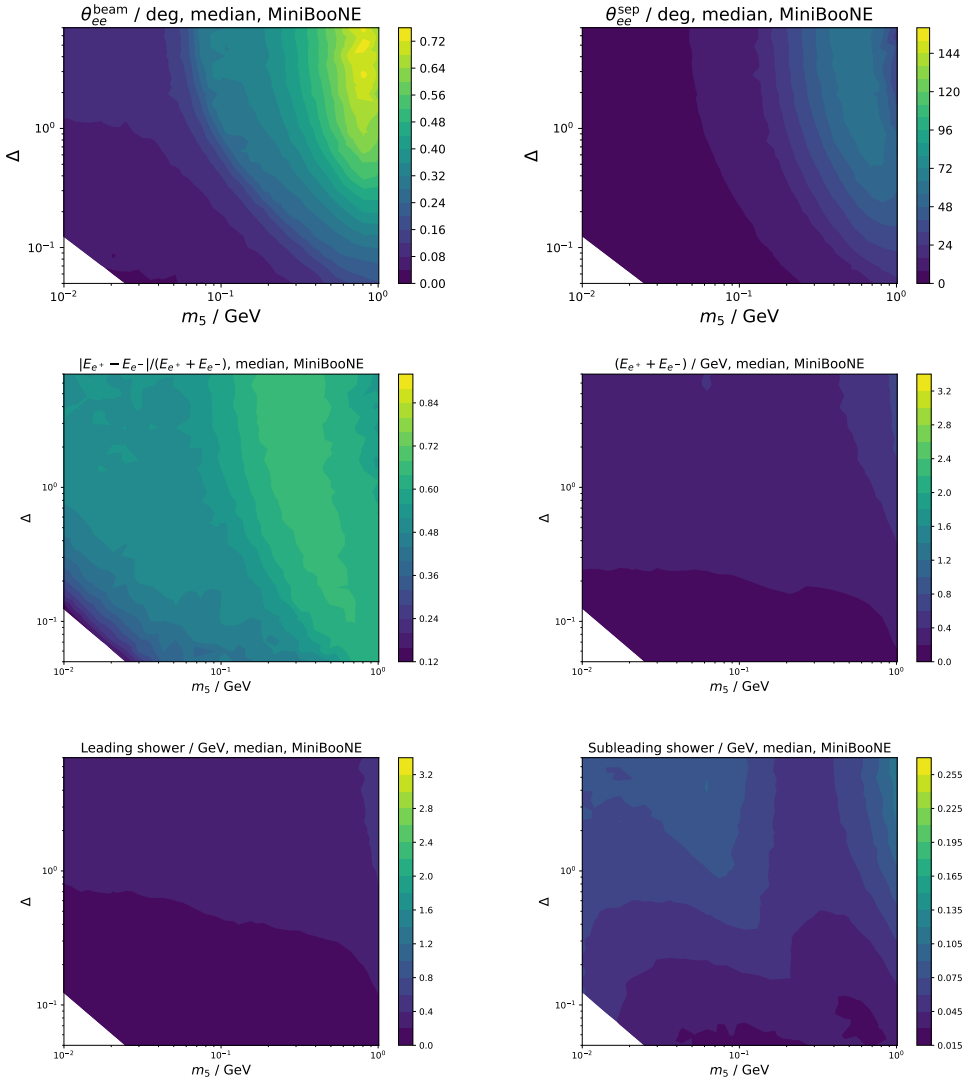

Figure B.2: The median of kinematical variables in dark neutrino events at MiniBooNE for the 3+2 model with $m_{Z'} = 1.25$ GeV. We show the median of (1) the angle between the shower and beam, (2) the angle between the two showers, (3) the asymmetry of the showers, (4) the total energy of the showers, and the energy of the leading (5) and subleading (6) showers.

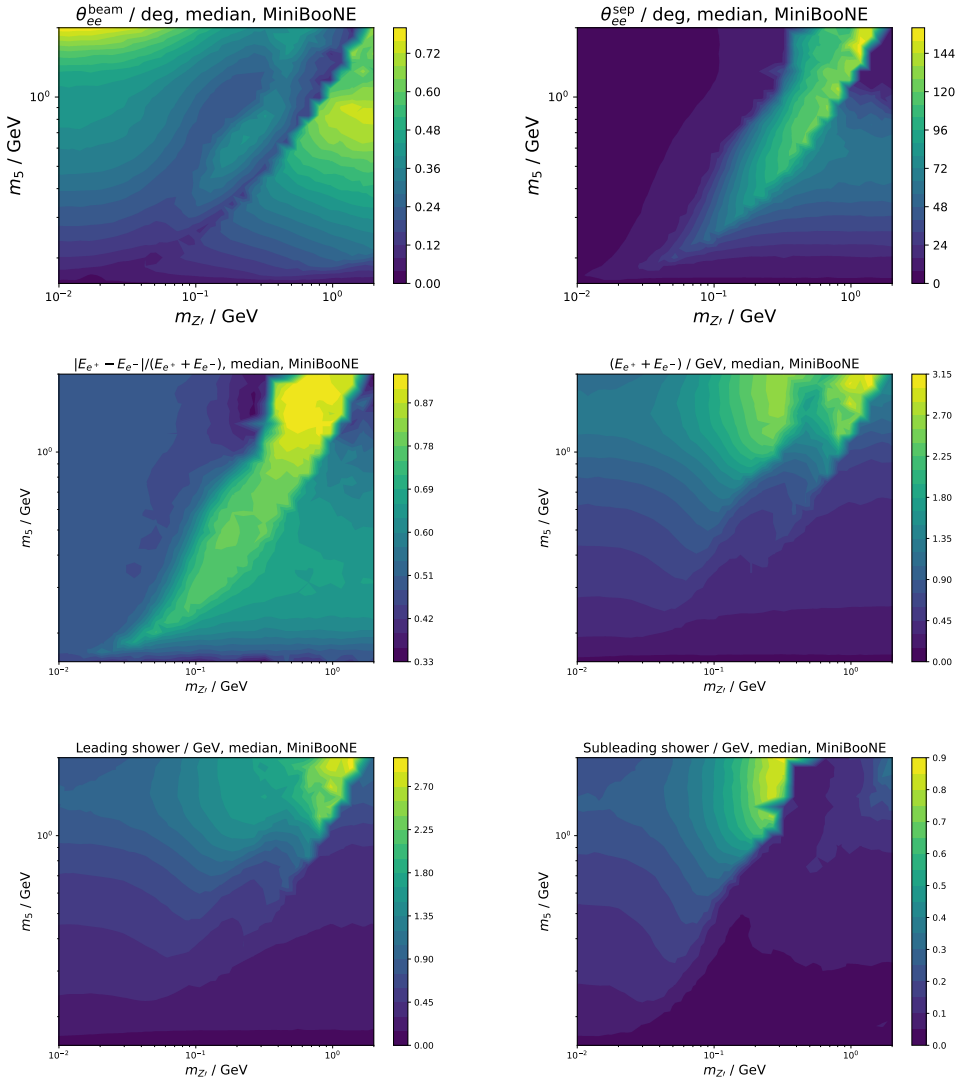

Figure B.3: The median of kinematical variables in dark neutrino events at MiniBooNE. We show the median of (1) the angle between the shower and beam, (2) the angle between the two showers, (3) the asymmetry of the showers, (4) the total energy of the showers, and the energy of the leading (5) and subleading (6) showers. We fix $m_4 = 150$ MeV and $\epsilon = 0.01$.

Appendix C

Plasmon decay computation

C.1 General expression of the photon self-energy

Introduction We want to compute the photon self-energy in a QED plasma. We will mainly consider a plasma of electrons and positrons. The quantity we are interested in is $\Pi^{\mu\nu}$, defined through the following diagram:

$\Pi^{\mu\nu}$ is equal to i times this diagram. We will compute the diagram using the real time formalism of Thermal Field Theory.

Initial expression Following the thermal Feynman rules, we have:

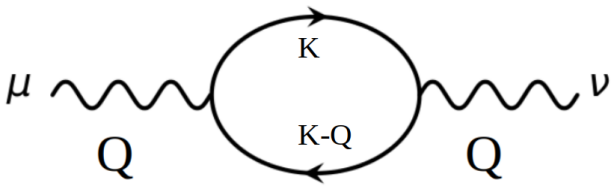

Figure C.1: Feynman diagram under consideration.

$$
\begin{aligned}
\Pi^{\mu\nu} =& -ie^2 \int \frac{d^4K}{(2\pi)^4} \mathrm{tr}[\gamma^\mu S_\beta^F(K)\gamma^\nu S_\beta^F(Q-K)] \\
=& -ie^2 \int \frac{d^4K}{(2\pi)^4} \mathrm{tr}[\gamma^\mu(\not{K}+m_e)\gamma^\nu(\not{Q}-\not{K}-m_e)] \\
&\times \left[\frac{i}{K^2-m_e^2} - 2\pi\big(\theta(-k^0)+\mathrm{sgn}(k^0)\tilde{f}(k^0-\mu_e)\big)\delta(K^2-m_e^2)\right] \\
&\times \left[\frac{i}{(Q-K)^2-m_e^2} - 2\pi\big(\theta(-q^0+k^0)\right. \\
&\left. + \mathrm{sgn}(Q^0-k^0)\tilde{f}(q^0-k^0+\mu_e)\big)\delta((Q-K)^2-m_e^2)\right]
\end{aligned}
\tag{C.1}
$$

where:

$$
\tilde{f}(x) = \frac{1}{e^{\beta x}+1} \tag{C.2}
$$

The function θ is the step function and $\beta \equiv 1/T$ using natural units. It is important to notice that after performing the product of the 2 factors in square brackets, we obtain 4 terms that we need to analyze. One of them is exactly the self-energy of the photon at $T = 0$, so we do not need to compute it because it will be absorbed after the renormalization is taken into account. The term with the 2 deltas is not relevant for our computation because the both conditions in the deltas taken simultaneously force the photon to be on-shell and, consequently, no decay is allowed. Therefore, we are left with 2 terms with just one delta that makes the computation be on-shell.

$$\begin{aligned}\Pi^{\mu\nu} = &- e^2 \int \frac{d^4K}{(2\pi)^3} \mathrm{tr}[\gamma^\mu(\not{K} + m_e)\gamma^\nu(\not{Q} - \not{K} - m_e)] \\ &\times \left[\frac{\theta(-k^0) + \mathrm{sgn}(k^0)\tilde{f}(k^0 - \mu_e)}{(Q-K)^2 - m_e^2}\delta(K^2 - m_e^2)\right] \\ &\times \left[\frac{\theta(-q^0 + k^0) + \mathrm{sgn}(q^0 - k^0)\tilde{f}(q^0 - k^0 + \mu_e)}{K^2 - m_e^2}\delta((Q-K)^2 - m_e^2)\right]\end{aligned} \tag{C.3}$$

First term First, we will work on the first term. In order to do so, we need to compute the trace.

$$\begin{aligned}\mathrm{tr}[\gamma^\mu(\not{K} + m_e)\gamma^\nu(\not{Q} - \not{K} - m_e)] &= 4(k^\mu q^\nu + k^\nu q^\mu - 2k^\mu k^\nu - K\cdot Q g^{\mu\nu}) \\ &\equiv 4A^{\mu\nu}\end{aligned} \tag{C.4}$$

We expect the self-energy to obey the Ward identity, so that: $Q_\mu \Pi^{\mu\nu} = 0$. That also implies that $Q_\mu A^{\mu\nu} = 0$, which implies that $Q^2 = 2Q\cdot K$. Therefore, we can express $A^{\mu\nu}$ as:

$$A^{\mu\nu} = \frac{(K\cdot Q)(k^\mu q^\nu + k^\nu q^\mu) - Q^2 k^\mu k^\nu - (K\cdot Q)^2 g^{\mu\nu}}{K\cdot Q} \tag{C.5}$$

Since the delta forces K^2 to be equal to m_e^2, then the denominator of the same term would be: $(Q-K)^2 - m_e^2 = Q^2 - 2Q\cdot K$.

Finally, the rest of the factors can be reduced using the properties of the delta:

$$\theta(-k^0) + \mathrm{sgn}(k^0)\tilde{f}(k^0-\mu_e)\delta(K^2-m_e^2) = \frac{1}{2E_K}\Big[\tilde{f}(k^0-\mu_e)\delta^+ + \big(1-\tilde{f}(k^0-\mu_e)\big)\delta^-\Big] \tag{C.6}$$

where $E_K \equiv \sqrt{\vec{K}^2+m_e^2}$ and $\delta^\pm \equiv \delta(k^0 \mp E_K)$. Therefore, the first term yields:

$$\frac{2A^{\mu\nu}}{E_K}\frac{\tilde{f}(k^0-\mu_e)\delta^+ + \big(1-\tilde{f}(k^0-\mu_e)\big)\delta^-}{Q^2-2Q\cdot K} \tag{C.7}$$

Second term For the second term, we will use a trick: we will change the integration variable just with a translation: $K \to K+Q$, so that d^4K remains invariant. After that change and performing the same computation done for the first term, the second term is:

$$\begin{aligned}\mathrm{tr}[\gamma^\mu(\not{K}+\not{Q}+m_e)\gamma^\nu(-\not{K}+m_e)] &= -4(k^\mu q^\nu + k^\nu q^\mu + 2k^\mu k^\nu - K\cdot Q g^{\mu\nu}) \\ &\equiv -4B^{\mu\nu}\end{aligned} \tag{C.8}$$

The Ward identity, $Q_\mu B^{\mu\nu}=0$, gives us a similar relation as the previous one: $Q^2 = -2Q\cdot K$. So we find that:

$$B^{\mu\nu} = \frac{(K\cdot Q)(k^\mu q^\nu + k^\nu q^\mu) - Q^2 k^\mu k^\nu - (K\cdot Q)^2 g^{\mu\nu}}{K\cdot Q} = A^{\mu\nu} \tag{C.9}$$

The delta gives us again the relation $K^2 = m_e^2$ after considering the transformation $K \to K + Q$. If we follow the same procedure as with the first term, the second term is found to be:

$$\frac{-2A^{\mu\nu}}{E_K}\frac{\big(1-\tilde{f}(-k^0+\mu_e)\big)\delta^+ + \tilde{f}(-k^0+\mu_e)\delta^-}{Q^2+2Q\cdot K} \tag{C.10}$$

Final expression Now, we just need to add the two terms. It is worth noting that, under the transformation $k^\mu \to -k^\mu$, then $A^{\mu\nu} \to -A^{\mu\nu}$ and $\int d^4K \to \int d^4K$. Then, we just need to perform this transformation of the k^μ just for the terms containing δ^-, which turns into δ^+. In this way and after integrating over k^0 with the use of the Dirac deltas, we find the final expression for the photon self-energy at finite temperature:

$$\begin{aligned}\Pi^{\mu\nu} =& 4e^2\int\frac{d^3k}{(2\pi)^3}\frac{f_e(E_K)+f_{\bar{e}}(E_K)}{2E_K}\\ &\times\frac{Q\cdot K(k^\mu q^\nu + k^\nu q^\mu) - Q^2k^\mu k^\nu - (Q\cdot K)^2 g^{\mu\nu}}{(Q\cdot K)^2-(Q^2)^2/4}\end{aligned} \tag{C.11}$$

Canceling the unphysical decay into e^+e^- According to Braaten and Segel [421], it is necessary to cancel the unphysical process: $\gamma \to e^+e^-$, which is forbidden because the thermal masses of the electron and positron also grow together with the thermal mass of the photon in such a way that this channel is forbidden. Because of that, it contributes to an imaginary part of the self-energy, whose value is proportional to the decay width, which is precisely forbidden. Therefore, the expression to be used for the self-energy computations is:

$$\begin{aligned}\Pi^{\mu\nu} =& 4e^2 \int \frac{d^3k}{(2\pi)^3} \frac{f_e(E_K) + f_{\overline{e}}(E_K)}{2E_K} \\ & \times \frac{Q\cdot K(k^\mu q^\nu + k^\nu q^\mu) - Q^2 k^\mu k^\nu - (Q\cdot K)^2 g^{\mu\nu}}{(Q\cdot K)^2}\end{aligned} \tag{C.12}$$

C.2 Projection onto L and T components

C.2.1 Introduction

The self-energy tensor can be projected onto a longitudinal and a transverse component using the following projectors:

$$\Pi^{\mu\nu} = F P_L^{\mu\nu} + G P_T^{\mu\nu} \tag{C.13}$$

where the projectors are:

$$\begin{aligned} P_T^{\mu\nu} &= \left(\delta^{ij} - \hat{q}^i \hat{q}^j\right) \delta_i^\mu \delta_j^\nu \\ P_L^{\mu\nu} &= \left(- g^{\mu\nu} + \frac{q^\mu q^\nu}{Q^2} \right) - P_T^{\mu\nu} \\ \text{where:} \quad & Q = (q_0, \vec{q}) \end{aligned} \tag{C.14}$$

For the following computations, we will assume without loss of generality that the photon momentum points towards the Z-axis, so that: $\vec{q} = q\hat{z}$. To obtain F, we just need to compute Π^{00}:

$$\begin{aligned}\Pi^{00} &= FP_L^{00} + GP_T^{00} \\ &= F\left[\left(-1+\frac{q_0^2}{Q^2}\right)-0\right]+G\cdot 0 \\ &= F\frac{q^2}{Q^2}\end{aligned} \tag{C.15}$$

Therefore, $F = \frac{Q^2}{q^2}\Pi^{00}$. To obtain G, we need to pick up a direction perpendicular to Z, any transverse direction. We will choose X:

$$\begin{aligned}\Pi^{xx} &= FP_L^{xx} + GP_T^{xx} \\ &= F\left[\left(1+\frac{0}{Q^2}\right)-\big(1-0\big)\right]+G\big(1-0\big) \\ &= G\end{aligned} \tag{C.16}$$

Therefore, $G = \Pi^{xx}$, such that $\vec{q} = q\hat{z}$.

C.2.2 Computing Π^{00}

Considering that under our assumptions: $Q \cdot k = q_0 E_k - k_3 q$, we plug in everything to compute Π^{00} and then change it into spherical coordinates, such that $k_3 = k\cos\theta \equiv kx$, where we will call x to $\cos\theta$:

$$\begin{aligned}\Pi^{00} &= 4e^2\int\frac{d^3k}{(2\pi)^3}\frac{f_e(E_k)+f_{\bar{e}}(E_k)}{2E_k}\frac{(q_0E_k-k_3q)(2q_0E_k)-Q^2E_k^2-(q_0E_k-k_3q)^2}{(q_0E_k-k_3q)^2-Q^4/2} \\ &= \frac{e^2}{2\pi^2}\int\frac{k^2dk}{E_k}(f_e(E_k)+f_{\bar{e}}(E_k))\int dx\Bigg(2E_kq_0\frac{E_kq_0-kqx}{(E_kq_0-kqx)^2-Q^4/4} \\ &\qquad -Q^2E_k^2\frac{1}{(E_kq_0-kqx)^2-Q^4/4}-\frac{(E_kq_0-kqx)^2}{(E_kq_0-kqx)^2-Q^4/4}\Bigg)\end{aligned} \tag{C.17}$$

Each of the terms inside the integration over x can be easily performed and the logarithms can be grouped so as to obtain the final expression:

$$\begin{aligned}\Pi^{00} = &-\frac{e^2}{2\pi^2 q}\int \frac{kdk}{E_k}(f_e(E_k)+f_{\bar{e}}(E_k))\Bigg[2qk \\ &+\frac{Q^2+4E_k(E_k-q_0)}{4}\ln\left(\frac{Q^2-2kq-2E_kq_0}{Q^2+2kq-2E_kq_0}\right) \\ &+\frac{Q^2+4E_k(E_k+q_0)}{4}\ln\left(\frac{Q^2-2kq+2E_kq_0}{Q^2+2kq+2E_kq_0}\right)\Bigg]\end{aligned} \tag{C.18}$$

C.2.3 Computing Π^{xx}

To compute Π^{xx} we need to consider that: $k_x = k(1-x^2)^{1/2}\cos\varphi$ and that $q^x = 0$:

$$\begin{aligned}\Pi^{xx} &= 4e^2\int\frac{d^3k}{(2\pi)^3}\frac{f_e(E_k)+f_{\bar{e}}(E_k)}{2E_k}\frac{-Q^2k^2(1-x^2)\cos^2\varphi+(q_0E_k-kqx)^2}{(q_0E_k-kqx)^2-Q^4/2} \\ &= \frac{e^2}{4\pi^3}\int\frac{k^2dk}{E_k}(f_e(E_k)+f_{\bar{e}}(E_k))\int dxd\varphi\Bigg(-\frac{Q^2k^2(1-x^2)}{(q_0E_k-kqx)^2-Q^4/2}\cos^2\varphi \\ &\quad +1+\frac{Q^4}{4}\frac{1}{(q_0E_k-kqx)^2-Q^4/2}\Bigg)\end{aligned} \tag{C.19}$$

The integration over φ is quite simple and, then, the one over x, when rearranging the terms leads us to the following final form:

$$\Pi^{xx} = \frac{e^2}{2\pi^2 q}\int \frac{kdk}{E_k}(f_e(E_k)+f_{\bar{e}}(E_k))\Bigg[2qk\left(1+\frac{Q^2}{2q^2}\right) + \frac{1}{2}\left(\frac{(Q^2/2-E_kq_0)^2}{q^2}+\frac{Q^2}{2}-k^2\right)\ln\left(\frac{Q^2-2kq-2E_kq_0}{Q^2+2kq-2E_kq_0}\right) + \frac{1}{2}\left(-\frac{(Q^2/2+E_kq_0)^2}{q^2}-\frac{Q^2}{2}+k^2\right)\ln\left(\frac{Q^2+2kq+2E_kq_0}{Q^2-2kq+2E_kq_0}\right)\Bigg] \tag{C.20}$$

C.3 Propagators, Polarization 4-vectors and Dispersion relations

C.3.1 Propagators

First, let us compute the longitudinal propagator, which is found by considering:

$$D^{00} = \frac{1}{q^2-\Pi_L(Q)} \tag{C.21}$$

If $\omega_l(q)$ is the energy of the longitudinally polarized photon on-shell, we know that:

$$\lim_{q_0\to\omega_l(q)} D^{00} = \frac{\omega_l^2(q)}{q^2}\frac{Z_l(q)}{q_0^2-\omega_l(q)^2} \tag{C.22}$$

$\omega_l(q)$ is the pole of the propagator, so that $\Pi_L(\omega_l(q),q)=q^2$. To find the expression for $Z_l(q)$, we will do a perturbation on q_0^2: $q_0^2=\omega_l(q)^2+\lambda$, being λ a small parameter which will subsequently be sent to 0. Under these conditions: $\Pi_L(q_0,q)\approx\Pi_L(\omega_l(q),q)+\lambda\frac{\partial\Pi_L}{\partial q_0^2}\Big|_{\omega_l(q)^2} = q^2+\lambda\frac{\partial\Pi_L}{\partial q_0^2}\Big|_{\omega_l(q)^2}$. Therefore, in the vicinity of $\omega_l(q)$, we can solve the equality:

$$\begin{aligned}\frac{1}{q^2-\Pi_L(\sqrt{\omega_l(q)^2+\lambda},q)} &= \frac{\omega_l(q)^2}{q^2}\frac{Z_l(q)}{\omega_l(q)^2+\lambda-\omega_l(q)^2}\\ Z_l(q) &= \frac{q^2}{\omega_l(q)^2}\lambda\frac{1}{q^2-(q^2+\lambda\frac{\partial\Pi_L}{\partial q_0^2}\Big|_{\omega_l(q)^2})}\\ Z_l(q) &= \frac{q^2}{\omega_l(q)^2}\Big[-\frac{\partial\Pi_L}{\partial q_0^2}(\omega_l(q),q)\Big]^{-1}\end{aligned} \tag{C.23}$$

For the transverse, we can work on the X direction, being Z the direction of the photon momentum:

$$D^{xx} = \frac{1}{q_0^2-q^2-\Pi_T(Q)} \tag{C.24}$$

Now, the pole of the propagator is $\omega_t(q)$ and on its vicinity the propagator takes the form:

$$\lim_{q_0\to\omega_t(q)} D^{xx} = \frac{Z_t(q)}{q_0^2-\omega_t(q)^2} \tag{C.25}$$

Now our perturbation will be: $q_0^2=\omega_t(q)^2+\lambda$ and $\Pi_T(q_0,q)\approx\Pi_T(\omega_t(q),q)+\lambda\frac{\partial\Pi_T}{\partial q_0^2}\Big|_{\omega_t(q)^2} = q_0^2-q^2+\lambda\frac{\partial\Pi_T}{\partial q_0^2}\Big|_{\omega_t(q)^2}$. Therefore, in the vicinity of $\omega_t(q)$, we can solve the equality:

$$\begin{aligned}\frac{1}{q_0^2-q^2-\Pi_T(\sqrt{\omega_t(q)^2+\lambda},q)} &= \frac{Z_t(q)}{\omega_t(q)^2+\lambda-\omega_t(q)^2}\\ Z_t(q) &= \frac{\omega_t(q)^2+\lambda-\omega_t(q)^2}{\omega_t(q)^2+\lambda-q^2-\Pi_T(\omega_t(q),q)-\lambda\frac{\partial\Pi_T}{\partial q_0^2}\Big|_{\omega_t(q)^2}}\\ Z_t(q) &= \Big[1-\frac{\partial\Pi_T}{\partial q_0^2}(\omega_t(q),q)\Big]^{-1}\end{aligned} \tag{C.26}$$

C.3.2 Polarization 4-vectors

The residue of a pole in q_0^2 of $D^{\mu\nu}(q_0, q)$ can be identified with $\varepsilon^\mu(q)\varepsilon^\nu(q)^*$. So we have:

$$\begin{aligned} \mathrm{Res}D^{00} &= \mathrm{Res}\left(\frac{\omega_l(q)^2}{q^2}\frac{Z_l(q)}{q_0^2-\omega_l(q)^2}\right) = \frac{\omega_l(q)^2}{q^2}Z_l(q) \\ \mathrm{Res}D^{xx} &= \mathrm{Res}D^{yy} = \mathrm{Res}\left(\frac{Z_t(q)}{q_0^2-\omega_t(q)^2}\right) = Z_t(q) \end{aligned} \tag{C.27}$$

From these expressions, we can find the polarization 4-vectors:

$$\begin{aligned} \varepsilon^\mu(q,\lambda=0) &= \frac{\omega_l(q)}{q}\sqrt{Z_l(q)}(1,0)^\mu \\ \varepsilon^\mu(q,\lambda=\pm1) &= \sqrt{Z_t(q)}(0,\varepsilon_\pm(q))^\mu \end{aligned} \tag{C.28}$$

C.3.3 Dispersion Relations

The dispersion relations are simply the ones in which there is a pole on the denominators of the propagators. Therefore, we have:

$$\begin{aligned} \omega_l(q)^2 &= \frac{\omega_l(q)^2}{q^2}\Pi_L(\omega_l(q),q) \\ \omega_t(q)^2 &= q^2 + \Pi_T(\omega_t(q),q) \end{aligned} \tag{C.29}$$

C.4 Limiting Cases

In the following, we will obtain approximate expressions for certain cases of interest. We need to take into account the results obtained for the projections of the self-energy and the plasma frequency.

C.4.1 Classical limit

In this limit, we have a non-relativistic ($T \ll m_e$) and non-degenerate ($T \ll m_e - \mu_e$) plasma. That means $\beta\mu \gg \mu/(m_e - \mu_e)$. Therefore, the distributions take the following form:

$$\begin{aligned} f_e(E_k) &= \left[e^{\beta(E_k-\mu_e)} + 1\right]^{-1} \cong \left[e^{\beta(E_k-\mu_e)}\right]^{-1} = e^{\frac{\mu_e - E_k}{T}} \\ f_{\bar{e}}(E_k) &= \left[e^{\beta(E_k+\mu_e)} + 1\right]^{-1} \cong 0 \end{aligned} \tag{C.30}$$

Because $f_{\bar{e}}(E_k)$ is negligible, under this regime we will just consider a plasma of electrons. The number density is given by:

$$\begin{aligned} n_e(T,\mu_e) &= \frac{1}{\pi^2}\int dk k^2 \big(f_e(E_k) - f_{\bar{e}}(E_k)\big) \\ &= \frac{e^{\mu_e/T}}{\pi^2}\int dk k^2 e^{-\frac{\sqrt{k^2+m_e^2}}{T}} \\ &\cong \frac{e^{(\mu_e - m_e)/T}}{\sqrt{2\pi^3}}\big(mT\big)^{3/2}\left(1 + \frac{15}{8}\frac{T}{m_e}\right) \end{aligned} \tag{C.31}$$

On the other hand, the plasma frequency is:

$$\begin{aligned} \omega_p^2 &= \frac{4\alpha}{\pi}\int dk \frac{k^2}{E_k}\left(1 - \frac{1}{3}\frac{k^2}{\sqrt{k^2+m_e^2}}\right)e^{\mu_e/T}e^{-\frac{\sqrt{k^2+m_e^2}}{T}} \\ &\cong e^{(\mu_e - m_e)/T}\sqrt{\frac{8}{\pi}}\alpha\big(mT^3\big)^{1/2}\left(1 - \frac{5}{8}\frac{T}{m_e}\right) \\ &= \frac{4\pi\alpha n_e}{m_e}\left(1 - \frac{5}{2}\frac{T}{m_e}\right) \end{aligned} \tag{C.32}$$

When doing the same process for Π_L and Π_T, we find:

$$\begin{aligned}\Pi_L &\cong \omega_p^2\left(\frac{q^2}{q_0^2}+3\frac{q^4}{q_0^4}\frac{T}{m_e}\right)\\ \Pi_T &\cong \omega_p^2\left(1+\frac{q^2}{q_0^2}\frac{T}{m_e}\right)\end{aligned} \tag{C.33}$$

With this expressions, we can also compute the dispersion relations:

$$\begin{aligned}\omega_l^2 &= \omega_p^2\left(1+3\frac{q^2}{\omega_l^2}\frac{T}{m_e}\right), \qquad 0\le q<\sqrt{1+3\frac{T}{m_e}}\\ \omega_t^2 &= q^2+\omega_p^2\left(1+\frac{q^2}{\omega_t^2}\frac{T}{m_e}\right)\end{aligned} \tag{C.34}$$

and:

$$\begin{aligned}Z_l(q) &= \frac{\omega_l^2}{\omega_p^2}\left(1-6\frac{q^2}{\omega_l^2}\frac{T}{m_e}\right)\\ Z_t(q) &= 1-\frac{\omega_p^2 q^2}{\omega_t^4}\frac{T}{m_e}\end{aligned} \tag{C.35}$$

C.4.2 Degenerate limit

In the degenerate limit of the electrons, $\mu_e - m_e \gg T$. Therefore, the positron distribution vanishes and the electron one approximates to:

$$f_e(E_k) \cong \begin{cases}1, & E_k < m_e\\ 0, & E_k > m_e\end{cases} \tag{C.36}$$

So, the number density is easily found:

$$\begin{aligned} n_e(T \sim 0, \mu) &= \frac{1}{\pi^2} \int dk k^2 f_e(E_k) \\ &\cong \frac{1}{\pi^2} \int_0^{(\mu^2 - m_e^2)^{1/2}} dk k^2 f_e(E_k) \\ &= \frac{1}{3\pi^2} (\mu^2 - m_e^2)^{3/2} \equiv \frac{1}{3\pi^2} p_F^3 \end{aligned} \tag{C.37}$$

For the plasma frequency:

$$\begin{aligned} \omega_p^2 &\cong \frac{4\alpha}{\pi} \int_0^{p_F} dk \frac{k^2}{\sqrt{k^2 + m_e^2}} \left(1 - \frac{1}{3} \frac{k^2}{\sqrt{k^2 + m_e^2}} \right) \\ &= \frac{4\alpha}{\pi} \left(\frac{p_F E_F}{3} - \frac{m_e^2 p_F}{3 E_F} \right) \\ &= \frac{4\alpha}{3\pi} p_F^2 v_F \end{aligned} \tag{C.38}$$

where $v_F \equiv p_F / E_F$. We can also compute Π_L and Π_T, by integrating over p or v, depending on the term:

$$\begin{aligned} \Pi_L &\cong \omega_p^2 \frac{3}{v_F^2} \left(\frac{q_0}{2 v_f q} \ln \frac{q_0 + v_F q}{q_0 - v_F q} - 1 \right) \\ \Pi_T &\cong \omega_p^2 \frac{3 q_0^2}{2 v_F^2 q^2} \left(1 - \frac{q_0^2 - q^2 v_F^2}{q_0^2} \frac{q_0}{2 v_f q} \ln \frac{q_0 + v_F q}{q_0 - v_F q} \right) \end{aligned} \tag{C.39}$$

From these expressions we can find the transverse photon mass:

$$m_t = \lim_{q \to \infty} \Pi_T^{1/2} = \left[\frac{3}{2 v_F^2} \left(1 - \frac{1 - v_F^2}{2 v_F} \ln \frac{1 + v_F}{1 - v_F} \right) \right]^{1/2} \omega_p \tag{C.40}$$

and finally:

$$
\begin{aligned}
Z_l^{-1} &= \frac{3}{2}\frac{\omega_p^2}{v_F^2 q^2}\left[\frac{\omega_l^2}{\omega_l^2 - q^2 v_F^2} - \frac{\omega_l}{2v_F q}\ln\frac{\omega_l + qv_F}{\omega_l - qv_F}\right] \\
Z_t^{-1} &= 1 - \frac{3}{2}\frac{\omega_p^2}{v_F^2 q^2}\left[\frac{3}{2} - \frac{3\omega_t^2 - q^2 v_F^2}{2\omega_t^2}\frac{\omega_t}{2v_F q}\ln\frac{\omega_t + qv_F}{\omega_t - qv_F}\right]
\end{aligned}
\tag{C.41}
$$

C.4.3 Relativistic limit

In the relativistic regime, $T, \mu \gg m_e$, so we will assume $m_e \sim 0$. So, the number density is:

$$
\begin{aligned}
n_e(T,\mu) &\cong \frac{1}{\pi^2}\int dk k^2 \left[\frac{1}{e^{\beta(k-\mu)}} - \frac{1}{e^{\beta(k+\mu)}}\right] \\
&= \frac{1}{3\pi^2}\mu\big(\mu^2 + \pi^2 T^2\big)
\end{aligned}
\tag{C.42}
$$

In this particular case, we can solve it for μ:

$$
\mu = \left(\frac{p_F^3}{2} + \sqrt{\left(\frac{p_F^3}{2}\right)^2 + \left(\frac{\pi^2}{3}T^2\right)^3}\right)^{1/3} - \left(-\frac{p_F^3}{2} + \sqrt{\left(\frac{p_F^3}{2}\right)^2 + \left(\frac{\pi^2}{3}T^2\right)^3}\right)^{1/3}
\tag{C.43}
$$

The plasma frequency is:

$$
\begin{aligned}
\omega_p^2 &\cong \frac{4\alpha}{\pi}\int dk k\left(1 - \frac{1}{3}\right)\left[\frac{1}{e^{\beta(k-\mu)}} - \frac{1}{e^{\beta(k+\mu)}}\right] \\
&= \frac{4\alpha}{\pi}\frac{2}{3}\left(\frac{3\mu^2 + \pi^2 T^2}{6}\right) = \frac{4\alpha}{3\pi}\left(\mu^2 + \frac{1}{3}\pi^2 T^2\right)
\end{aligned}
\tag{C.44}
$$

The values for Π_L and Π_T are also obtained straightforwardly by setting

v_F equal to 1 on the previous result for the degenerate case:

$$\begin{aligned}\Pi_L &\cong 3\omega_p^2\left(\frac{q_0}{2q}\ln\frac{q_0+q}{q_0-q}-1\right)\\ \Pi_T &\cong \omega_p^2\frac{3q_0^2}{2q^2}\left(1-\frac{q_0^2-q^2}{q_0^2}\frac{q_0}{2q}\ln\frac{q_0+q}{q_0-q}\right)\end{aligned} \tag{C.45}$$

and to conclude:

$$\begin{aligned}Z_l^{-1} &= \frac{3}{2}\frac{\omega_p^2}{q^2}\left[\frac{\omega_l^2}{\omega_l^2-q^2}-\frac{\omega_l}{2q}\ln\frac{\omega_l+q}{\omega_l-q}\right]\\ Z_t^{-1} &= 1-\frac{3}{2}\frac{\omega_p^2}{q^2}\left[\frac{3}{2}-\frac{3\omega_t^2-q^2}{2\omega_t^2}\frac{\omega_t}{2q}\ln\frac{\omega_t+q}{\omega_t-q}\right]\end{aligned} \tag{C.46}$$

C.4.4 Analytical Approximation

We can obtain useful approximations to better perform numerical computations. We first need to integrate Π_L and Π_T by parts. We will first work with Π_T, which has the form $\Pi_T = \frac{4\alpha}{\pi}\int dk\mathcal{F}(k)(f_e(E_k)+f_{\bar{e}}(E_k))$. We will compute the indefinite integral $\int\mathcal{F}(k)dk$ to perform the whole integration. We will define $w \equiv q/q_0$ just to have a shorter notation. Since it is an indefinite integral, we might neglect constant terms.

$$\begin{aligned}\int \mathcal{F}(k)dk &= \frac{1}{w^2}\int dk \frac{k^2}{\sqrt{k^2+m_e^2}} - \frac{Q^2}{q^2}\frac{1}{2w}\sum_{b=\pm 1} b\int dk k \ln\left(1+\frac{bwk}{\sqrt{k^2+m_e^2}}\right) \\ &= \frac{1}{w^2}\Big(\frac{E_k k}{2} - \frac{m_e^2}{2}\ln(E_k+k)\Big) \\ &\quad \frac{1-w^2}{2q^2w^3}\sum_{b=\pm 1} b\frac{m_e^2}{2}\Big[\Big(\frac{1}{1-v^2}-\frac{w^2}{1-w^2}\Big)\ln(1+bwv) \\ &\quad \frac{\ln(1-v)}{2(1+bw)} + \frac{\ln(1+v)}{2(1+-w)}\Big] \\ &= \frac{q_0^2}{2q^2}E_k k - \frac{q_0^3 E_k^2 - k^2 q^2 q_0}{4q^3}\ln\frac{q_0+vq}{q_0-vq}\end{aligned} \tag{C.47}$$

On the other hand, since the integration is performed from 0 to ∞, we see that the surface terms that arises from the integration by parts vanish identically. Therefore, we finally obtain:

$$\begin{aligned}\Pi_T = -\frac{4\alpha}{\pi}\int dk \frac{k^3}{E_k}\left[\frac{1}{2v^2}\left(\frac{q_0^2}{q^2} - \frac{q_0^2-v^2q^2}{q^2}\frac{q_0}{2vq}\ln\frac{q_0+vq}{q_0-vq}\right)\right] \\ \times \frac{d}{dk}\big(f_e(E_k)+f_{\bar{e}}(E_k)\big)\end{aligned} \tag{C.48}$$

Now we will do the same with Π_L, which has the form $\Pi_L = \frac{4\alpha}{\pi}\int dk \mathcal{G}(k)(f_e(E_k)+ f_{\bar{e}}(E_k))$. We need to compute the indefinite integral $\int \mathcal{G}(k)dk$:

$$\begin{aligned}\int \mathcal{G}(k)dk &= \frac{1}{w}\sum_{b=\pm 1} b\int dk k\ln(1+bwv) - \int dk\frac{k^2}{E_k} - (1-w^2)\int dk\frac{kv}{1-w^2v^2} \\ &= \frac{1}{w}\left(\frac{E_k^2-k^2w^2}{2(1-w^2)}\ln\frac{1+wv}{1-wv} - \frac{m_e^2 w}{2(1-w^2)}\ln\frac{1+v}{1-v}\right) \\ &\quad \left(\frac{kE_k}{2}+\frac{m_e^2}{4}\ln\frac{1-v}{1+v}\right) \\ &\quad (1-w^2)\left(\frac{m_e^2 w}{2(1-w^2)^2}\ln\frac{1+wv}{1-wv} + \frac{m_e^2 v}{2(1-w^2)(1-v^2)}\right. \\ &\quad \left.\frac{m_e^2}{4}\frac{1+w^2}{(1-w^2)^2}\ln\frac{1+v}{1-v}\right) \\ &= \frac{k^3}{E_k}\left[\frac{1}{v^2}\left(\frac{q_0}{2vq}\ln\frac{q_0+qv}{q_0-qv}-1\right)\right]\end{aligned} \tag{C.49}$$

The surface terms also vanish identically. Therefore, we finally obtain:

$$\begin{aligned}\Pi_L = &-\frac{4\alpha}{\pi}\int dk\frac{k^3}{E_k}\left[\frac{1}{v^2}\left(\frac{q_0}{2vq}\ln\frac{q_0+vq}{q_0-vq}-1\right)\right] \\ &\times\frac{d}{dk}\big(f_e(E_k)+f_{\bar{e}}(E_k)\big)\end{aligned} \tag{C.50}$$

For many cases of interest, v can be regarded as being dominated by a value v_*. For the limiting cases considered above, this value is equal to 0 (classical limit), 1 (relativistic limit) and v_F (degenerate limit, because df_e/dk us peaked at v_F). Under such consideration, we can pull out the factors depending just on v out of the integral and perform it in a very simple way. What we are going to do first, is to uncover the relation between that result and the plasma frequency. In order to do that, we will do the same process we did for Π_L and Π_T, but for ω_p^2, which has the form $\omega_p^2 =$

$\frac{4\alpha}{\pi}\int dk\mathcal{H}(k)(f_e(E_k)+f_{\bar{e}}(E_k))$. Let us compute $\int\mathcal{H}(k)dk$:

$$\begin{aligned}\int\mathcal{H}(k)dk &= \int dk\frac{k^2}{E_k}-\frac{1}{3}\int dv\frac{m_e^2v^4}{(1-v^2)^2}\\ &= \left(\frac{kE_k}{2}+\frac{m_e^2}{4}\ln\frac{1-v}{1+v}\right)-\frac{1}{3}\left(m_e^2v-\frac{3}{4}m_e^2\ln\ln\frac{1+v}{1-v}+\frac{E_k^2v}{2}\right)\\ &= \frac{1}{3}\frac{k^3}{E_k}\end{aligned} \tag{C.51}$$

Since the surface terms also vanish, we finally obtain:

$$\omega_p^2 = -\frac{4\alpha}{3\pi}\int dk\frac{k^3}{E_k}\times\frac{d}{dk}\big(f_e(E_k)+f_{\bar{e}}(E_k)\big) \tag{C.52}$$

So the final approximations are:

$$\begin{aligned}\Pi_L &= \omega_p^2\frac{3}{v_*^2}\left(\frac{q_0}{2v_*q}\ln\frac{q_0+v_*q}{q_0-v_*q}-1\right)\\ \Pi_T &= \omega_p^2\frac{3}{2v_*^2}\left(\frac{q_0^2}{q^2}-\frac{q_0^2-v_*^2q^2}{q^2}\frac{q_0}{2v_*q}\ln\frac{q_0+v_*q}{q_0-v_*q}\right)\end{aligned} \tag{C.53}$$

With those approximations, we can also find Z_l and Z_t:

$$\begin{aligned}Z_l^{-1} &= \frac{3\omega_p^2}{2v_*^2q^2}\left(\frac{\omega_l^2}{\omega_l^2-v_*^2q^2}-\frac{\omega_l}{2v_*q}\ln\frac{\omega_l+v_*q}{\omega_l-v_*q}-1\right)\\ Z_t^{-1} &= 1-\frac{3\omega_p^2}{2v_*^2q^2}\left(\frac{3}{2}-\frac{3\omega_t^2-v_*^2q^2}{2\omega_t^2}\frac{\omega_t}{2v_*q}\ln\frac{\omega_t+v_*q}{\omega_t-v_*q}\right)\end{aligned} \tag{C.54}$$

C.5 Computation of axial self-energy of the photon

C.5.1 Axial self-energy

One expression that will be of great importance to compute the decay of photons into neutrino pairs is the same diagram that we previously calculated, the photon self-energy, but with a γ_5 matrix. The expression is as follows:

$$\begin{aligned}\Pi_A^{\mu\nu} =& -ie^2\int\frac{d^4K}{(2\pi)^4}\mathrm{tr}[\gamma^\mu S^F(K)\gamma^\nu\gamma^5 S^F(K-Q)]\\ =& -ie^2\int\frac{d^4K}{(2\pi)^4}\mathrm{tr}[\gamma^\mu(\not{K}+m_e)\gamma^\nu\gamma^5(\not{Q}-\not{K}-m_e)]\\ &\times\left[\frac{i}{K^2-m_e^2}-2\pi\big(\theta(-k^0)+\mathrm{sgn}(k^0)\tilde{f}(k^0-\mu_e)\big)\delta(K^2-m_e^2)\right]\\ &\times\left[\frac{i}{(Q-K)^2-m_e^2}-2\pi\big(\theta(-q^0+k^0)\right.\\ &\left.+\mathrm{sgn}(q^0-k^0)\tilde{f}(q^0-k^0+\mu_e)\big)\delta((Q-K)^2-m_e^2)\right]\end{aligned} \tag{C.55}$$

We will follow the same procedure. The two terms, after transforming the second by doing $k^\mu\to k^\mu+q^\mu$, yield the same trace:

$$\mathrm{tr}[\gamma^\mu(\not{K}+m_e)\gamma^\nu\gamma_5(\not{Q}-\not{K}-m_e)]=4i\varepsilon^{\mu\nu\lambda\sigma}Q_\lambda K_\sigma \tag{C.56}$$

In the last line, the symmetric factors vanish due to the antisymmetric nature of the Levi-Civita symbol. This expression already vanishes when contracted with Q_μ. The rest of the computation is quite similar to the one

we have already done. When we do $K \to K + Q$ to work on the second term of the last factor, the trace remains the same, as it is easy to show. Finally we find:

$$\begin{aligned}\Pi_A^{\mu\nu} = 4e^2 i\varepsilon^{\mu\nu\lambda\sigma} \int \frac{d^4K}{(2\pi)^3} \frac{K_\lambda Q_\sigma}{2E_k} \\ \times \left[\frac{\tilde{f}(k^0 - \mu_e)\delta^+ + \big(1 - \tilde{f}(k^0 - \mu_e)\big)\delta^-}{Q^2 - 2Q \cdot K} \right. \\ \left. + \frac{\big(1 - \tilde{f}(-k^0 + \mu_e)\big)\delta^+ + \tilde{f}(-k^0 + \mu_e)\delta^-}{Q^2 + 2Q \cdot K} \right]\end{aligned} \tag{C.57}$$

This can be easily solved by transforming the δ^- into δ^+ by doing $k^\mu \to -k^\mu$. Then we are left with:

$$\Pi_A^{\mu\nu} = 2e^2 i\varepsilon^{\mu\nu\lambda\sigma} \int \frac{d^3k}{(2\pi)^3} \frac{f_e(E_K) - f_{\bar{e}}(E_K)}{2E_K} \frac{Q^2 K_\lambda Q_\sigma}{(Q \cdot K)^2 - (Q^2)^2/4} \tag{C.58}$$

After a manipulation of this expression, we could discover that is purely transverse and that it has the following form:

$$\begin{aligned}\Pi_A^{\mu\nu} &= g^{\mu i} g^{\nu j} [\Pi_A(Q)(i\varepsilon^{ijm}\hat{q}^m)] \\ \Pi_A(Q) &= 8\pi\alpha \frac{Q^2}{q} \int \frac{d^3k}{(2\pi)^3} \frac{f_e(E_k) - f_{\bar{e}}(E_k)}{2E_k} \frac{Q \cdot K q_0 - Q^2 E_k}{(Q \cdot K)^2 - (Q^2)^2/4}\end{aligned} \tag{C.59}$$

We can perform the angular integration of $\Pi_A(Q)$. φ is straightforwardly done, while with $x \equiv \cos\theta$ we need to integrate term by term:

$$\Pi_A(Q) = \frac{\alpha}{\pi}\frac{Q^2}{q}\int k^2 dk \frac{f_e(E_k) - f_{\bar{e}}(E_k)}{E_k}\left(q_0 \int \frac{dx}{q_0 E_k - qkx} - Q^2 E_k \int \frac{dx}{(q_0 E_k - qkx)^2}\right)$$
$$= \frac{2\alpha}{\pi}\frac{Q^2}{q}\int dk \frac{k^2}{E_k^2}\left(\frac{q_0}{2qv}\ln\frac{q_0+vq}{q_0-vq} - \frac{Q^2}{q_0^2 - v^2q^2}\right)\left[f_e(E_k) - f_{\bar{e}}(E_k)\right] \tag{C.60}$$

C.5.2 Limits

Classical limit:

$$\Pi_A(Q) = e^{(\mu - m_e)/T}\sqrt{\frac{2}{\pi}}\alpha\left(\frac{T^3}{m_e}\right)^{1/2}\frac{Q^2}{q_0^2} = \frac{\omega_p^2}{2m_e}\frac{qQ^2}{q_0^2} \tag{C.61}$$

Degenerate limit:

$$\Pi_A(Q) = \frac{2\alpha}{\pi}k_F\frac{Q^2}{q}\left(\frac{q_0}{2v_F q}\ln\frac{q_0 + v_F q}{q_0 - v_F q} - 1\right) \tag{C.62}$$

Relativistic limit:

$$\Pi_A(Q) = \frac{2\alpha}{\pi}\frac{Q^2}{q}\left(\frac{q_0}{2q}\ln\frac{q_0+q}{q_0-q} - 1\right) \tag{C.63}$$

C.5.3 Analytic approximation

By doing a similar process than that done for Pi_L and Pi_T, we would find the following equality:

$$\Pi_A(Q) = -\frac{2\alpha}{\pi}\frac{Q^2}{q}\int dk \frac{k^3}{E_k^2}\left[\frac{1}{v^2}\left(\frac{q_0}{2qv}\ln\frac{q_0+vq}{q_0-vq} - 1\right)\right]\frac{d}{dk}\left[f_e(E_k) - f_{\bar{e}}(E_k)\right] \tag{C.64}$$

In the limits considered above, there is usually a value v_* that dominates.

But together with this, we need an axial frequency to absorb the derivative above. We will define this to be ω_A:

$$\lim_{q\to 0}\Pi_A(Q) = \omega_A q \tag{C.65}$$

We now can compute this frequency, neglecting some terms by considering that $q \to 0$:

$$\begin{aligned}
\omega_A &= \frac{2\alpha}{\pi}\frac{q_0^2}{q^2}\int dk \frac{k^2}{E_k^2}\left(\frac{q_0}{2qv}\ln\frac{1+(v/q_0)q}{1-(v/q_0)q} - \frac{Q^2}{q_0^2}\Big(1+(v^2/q_0^2)q^2\Big)\right)\big[f_e(E_k) - f_{\bar{e}}(E_k)\big] \\
&= \frac{2\alpha}{\pi}\frac{q_0^2}{q^2}\int dk \frac{k^2}{E_k^2}\left(\Big(1+\frac{v^2q^2}{3q_0^2}\Big) - \Big(1-(1-v^2)\frac{q^2}{q_0^2}\Big)\right)\big[f_e(E_k) - f_{\bar{e}}(E_k)\big] \\
&= \frac{2\alpha}{\pi}\int dk \frac{k^2}{E_k^2}\left(1-\frac{2}{3}v^2\right)\big[f_e(E_k) - f_{\bar{e}}(E_k)\big]
\end{aligned} \tag{C.66}$$

Also, considering that $\int \frac{k^2}{E_k^2}\left(1-\frac{2}{3}v^2\right) = \frac{k^3}{E_k^2} + C$, we find the following:

$$\omega_A = -\frac{2\alpha}{3\pi}\int dk \frac{k^3}{E_k^2}\frac{d}{dk}\big[f_e(E_k) - f_{\bar{e}}(E_k)\big] \tag{C.67}$$

Finally, we can express $\Pi_A(Q)$ in terms of ω_A and, by considering a dominant v_*, we obtain:

$$\Pi_A(Q) = \omega_A\frac{Q^2}{q}\frac{3}{v_*^2}\left(\frac{q_0}{2qv_*}\ln\frac{q_0+v_*q}{q_0-v_*q} - 1\right) \tag{C.68}$$

C.6 Decay of the plasmon

C.6.1 Amplitude

We need to compute two main diagrams by which the photons decay into a pair of neutrino-antineutrino. The first one is through the Z boson, while the second through the W one. What we will see is that these diagrams can be computed in terms of the photon self-energy and axial self-energy. We will consider that M_Z^2 and M_W^2 are much larger than the square 4-momenta of the propagators involved. The decay can take place mediated by the Z boson:

$$\begin{aligned}\mathcal{M}_Z = \varepsilon_\mu(Q)\int \frac{d^4k}{(2\pi)^4}\mathrm{tr}\big[\gamma^\mu S^F(K)\gamma^\nu(C_V^{(e)}-C_A^{(e)}\gamma_5)S^F(K-Q)\big]\frac{e}{4}\frac{e^2}{\sin^2\theta_W\cos^2\theta_W M_Z^2}\\ \times\overline{u}(p_1)\gamma_\nu(1-\gamma_5)v(p_2)\\ = \frac{G_F}{\sqrt{2}}\frac{1}{\sqrt{4\pi\alpha}}\varepsilon_\mu(Q)\big[C_V^{(e)}\Pi^{\mu\nu}-C_A^{(e)}\Pi_A^{\mu\nu}\big]\overline{u}(p_1)\gamma_\nu(1-\gamma_5)v(p_2)\end{aligned} \tag{C.69}$$

The other diagram that contributes to the process is mediated by the W boson:

$$\begin{aligned}\mathcal{M}_W = \varepsilon_\mu(Q)ie\int \frac{d^4k}{(2\pi)^4}\frac{-ig_W}{2\sqrt{2}}\mathrm{tr}\big[\gamma^\mu S^F(K)\gamma^\nu(1-\gamma_5)S^F(K-Q)\big]\frac{-ig_W}{2\sqrt{2}}\frac{i}{M_W^2}\\ \times\overline{u}(p_1)\gamma_\nu(1-\gamma_5)v(p_2)\\ = \frac{G_F}{\sqrt{2}}\frac{1}{\sqrt{4\pi\alpha}}\varepsilon_\mu(Q)\big[\Pi^{\mu\nu}-\Pi_A^{\mu\nu}\big]\overline{u}(p_1)\gamma_\nu(1-\gamma_5)v(p_2)\end{aligned} \tag{C.70}$$

Here, the final states can just be ν_e and $\overline{\nu}_e$. We can sum both diagrams

to obtain:

$$\mathcal{M} = \frac{G_F}{\sqrt{2}} \frac{1}{\sqrt{4\pi\alpha}} \varepsilon_\mu(Q) \left[C_V \Pi^{\mu\nu} - C_A \Pi_A^{\mu\nu} \right] \overline{u}(p_1) \gamma_\nu (1 - \gamma_5) v(p_2) \tag{C.71}$$

where C_V is equal to $2\sin^2\theta_W + 1/2$ for ν_e and $2\sin^2\theta_W - 1/2$ for the other neutrino species, while C_A is equal to $1/2$ for ν_e and $-1/2$ for the rest. Now, we need to see how we can carefully separate that part that belongs to the longitudinal polarization to that of the transverse, because the photon polarization vector and its dispersion relation is differently defined with respect to each of them. $\Pi^{\mu\nu}$, when $\vec{q} = q\hat{q}$, is:

$$\Pi^{\mu\nu} = \begin{pmatrix} \Pi_L & 0 & 0 & \frac{q_0}{q}\Pi_L \\ 0 & \Pi_T & 0 & 0 \\ 0 & 0 & \Pi_T & 0 \\ \frac{q_0}{q}\Pi_L & 0 & 0 & \frac{q_0^2}{q^2}\Pi_L \end{pmatrix} = \Pi_L \Big(1, \frac{q_0}{q}\hat{q}\Big)^\mu \Big(1, \frac{q_0}{q}\hat{q}\Big)^\nu + \Pi_T \Big(\delta^{ij} - \hat{q}^i\hat{q}^j\Big) g^{\mu i} g^{\nu j} \tag{C.72}$$

Therefore, the final expression for $\mathcal{M}$ would be:

$$\begin{aligned} \mathcal{M} = & \frac{G_F}{\sqrt{2}} \frac{1}{\sqrt{4\pi\alpha}} \Bigg[\varepsilon_\mu(\omega_l, q) C_V \Big(\Pi_L(\omega_l, q) \Big(1, \frac{\omega_l}{q}\hat{q}\Big)^\mu \Big(1, \frac{\omega_l}{q}\hat{q}\Big)^\nu \Big) \\ & + \varepsilon_\mu(\omega_t, q) g^{\mu i} \Big(C_V \Pi_T(\omega_t, q) \Big(\delta^{ij} - \hat{q}^i\hat{q}^j\Big) \\ & + C_A \Pi_A(\omega_t, q) (i\varepsilon^{ijm}\hat{q}^m) \Big) g^{\nu j} \Bigg] \overline{u}(p_1) \gamma_\nu (1 - \gamma_5) v(p_2) \end{aligned} \tag{C.73}$$

If λ stands for the polarization, the previous equation can be expressed in a short hand notation:

$$\mathcal{M} = \frac{G_F}{\sqrt{2}}\Big(\Gamma^{\mu\nu}_{\lambda}\varepsilon_{\nu}(\vec{q},\lambda)\Big)\overline{u}(p_1)\gamma_{\nu}(1-\gamma_5)v(p_2) \tag{C.74}$$

where a sum over polarizations is assumed.

C.6.2 Decay width

The previous process has the following effective diagram:

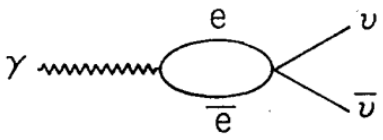

The decay width of the process given a specific polarization λ is:

$$\Gamma_{\lambda}(q) = \frac{1}{2\omega_{\lambda}(q)}\int\frac{d^3p_1}{(2\pi)^3}\frac{1}{2p_1}\int\frac{d^3p_2}{(2\pi)^3}\frac{1}{2p_2}(2\pi)^4\delta^{(4)}(P_1+P_2-Q)|\mathcal{M}|^2 \tag{C.75}$$

We are assuming that the number density of neutrinos is negligible, so that no Pauli blocking factors need to be considered. We can see that the integration is just of $|\overline{u}(p_1)\gamma_{\nu}(1-\gamma_5)v(p_2)|^2$. We can sum over final states to obtain:

$$\sum_{\text{spins}}|\overline{u}(p_1)\gamma_{\nu}(1-\gamma_5)v(p_2)|^2 = 8\Big(P_1^{\mu}P_2^{\nu}+P_1^{\nu}P_2^{\mu}-P_1\cdot P_2 g^{\mu\nu}-i\varepsilon^{\mu\nu\lambda\sigma}P_{1\lambda}P_{2\sigma}\Big) \tag{C.76}$$

So the integrals over p_1 and p_2 give us a tensor, $I^{\mu\nu}$:

$$I^{\mu\nu} = \frac{1}{2\pi^2}\int \frac{d^3p_1}{p_1}\frac{d^3p_2}{p_2}\delta^{(4)}(Q - P_1 - P_2)\Big[P_1^\mu P_2^\nu + P_1^\nu P_2^\mu - P_1 \cdot P_2 g^{\mu\nu} - i\varepsilon^{\mu\nu\lambda\sigma}P_{1\lambda}P_{2\sigma}\Big] \tag{C.77}$$

To compute this tensor, we will just need to compute I^{00} and I^{03}, as we will see. Before starting to compute it, let us analyze what happens to the last term in the square brackets when we consider $P_2 \to Q - P_1$. We will have just one apparently non vanishing term: the one that contains $\varepsilon^{\mu\nu\lambda\sigma}P_{1\lambda}Q_\sigma$. But, if we consider Z to be the direction of $\vec{q}$, we see that this term also vanishes for our computation: for I^{00} the Levi-Civita symbol vanishes, and for I^{03}, since Q only has non-vanishing for 0 and 3, its contraction with $\varepsilon^{00\lambda\sigma}$ vanishes identically. Therefore, we just need to compute $I_0^{\mu\nu}$:

$$I_0^{\mu\nu} = \frac{1}{2\pi^2}\int \frac{d^3p_1}{p_1}\frac{d^3p_2}{p_2}\delta^{(4)}(Q - P_1 - P_2)\Big[P_1^\mu P_2^\nu + P_1^\nu P_2^\mu - P_1 \cdot P_2 g^{\mu\nu}\Big] \tag{C.78}$$

The interesting fact about $I_0^{\mu\nu}$ is that it is symmetric in $\mu\nu$, so that we can express it in the following way:

$$\begin{aligned} I_0^{\mu\nu} &= A(Q^2)q^\mu q^\nu + B(Q^2)g^{\mu\nu} \\ I_0^{03} &= A(Q^2)q_0 q \\ I_0^{00} &= A(Q^2)q_0^2 + B \end{aligned} \tag{C.79}$$

It is important to note that, considering kinematics, the value of $p_1 \equiv |\vec{p_1}|$ is:

$$p_1 = \frac{Q^2}{2(q_0 - qx)} \tag{C.80}$$

where $x \equiv \cos\theta$, and θ is the angle between $\vec{p_1}$ and $\vec{q}$. On the other hand, after performing the integral for the spatial part of the Dirac delta, we remain with the following:

$$\delta(q_0 - p_1 - p_2) = \frac{q_0 - p_1}{q_0 - qx}\delta\left(p_1 - \frac{Q^2}{2(q_0 - qx)}\right) \tag{C.81}$$

Now, we can compute I_0^{03}

$$\begin{aligned} I_0^{03} &= \frac{1}{2\pi^2}\int \frac{d^3p_1}{p_1}\frac{d^3p_2}{p_2}\delta^{(4)}(Q - P_1 - P_2)\Big[p_1 p_2^z + p_1^z p_2\Big] \\ &= \frac{1}{2\pi^2}\int \frac{p_1 dp_1 d\varphi dx}{q_0 - qx}\delta\left(p_1 - \frac{Q^2}{2(q_0 - qx)}\right)\Big[p_1 q - + p_1 x(2p_1 - q_0)\Big] \\ &= \frac{q_0 q}{3\pi} \end{aligned} \tag{C.82}$$

Therefore, $A = \frac{1}{3\pi}$. Now, we need to compute I_0^{00}:

$$\begin{aligned} I_0^{00} &= \frac{1}{2\pi^2}\int \frac{d^3p_1}{p_1}\frac{d^3p_2}{p_2}\delta^{(4)}(Q - P_1 - P_2)\Big[p_1 p_2 + p_1 \cdot p_2\Big] \\ &= \frac{1}{2\pi^2}\int \frac{p_1 dp_1 d\varphi dx}{q_0 - qx}\delta\left(p_1 - \frac{Q^2}{2(q_0 - qx)}\right)\Big[p_1 q_0 - + p_1 x q - 2p_1^2\Big] \\ &= \frac{q^2}{3\pi} \end{aligned} \tag{C.83}$$

Therefore, $B = I_0^{00} - Aq_0^2 = -\frac{Q^2}{3\pi}$. So, for our case, $I^{\mu\nu} \equiv I_0^{\mu\nu}$:

$$I^{\mu\nu} = \frac{1}{3\pi}\Big(q^\mu q^\nu - Q^2 g^{\mu\nu}\Big) \tag{C.84}$$

However, if we remember that $Q_\mu \Gamma^{\mu\nu} = 0$, the effective tensor we need to consider is:

$$I^{\mu\nu}_{\text{eff}} = -\frac{1}{3\pi} Q^2 g^{\mu\nu} \tag{C.85}$$

So, we obtain for the decay width:

$$\Gamma_\lambda(q) = -\frac{G_F^2}{12\pi} \frac{\omega_\lambda(q)^2 - q^2}{\omega_\lambda(q)} \Big(\Gamma^{\alpha\mu} \varepsilon_\mu(q,\lambda)\Big) \Big(\Gamma_{\alpha\rho} \varepsilon^\rho(q,\lambda)\Big)^* \tag{C.86}$$

C.6.3 Longitudinal case

We need to compute the terms contracting and keep in mind that $\Pi_L(\omega_l, q) = q^2$:

$$\begin{aligned} \Gamma^{\alpha\mu}(\omega_l(q), q)\varepsilon_\mu(q,0) &= \frac{1}{\sqrt{4\pi\alpha}} C_V \Pi_L \Big(1, \frac{\omega_l}{q}\hat{q}\Big)^\alpha \Big(1, \frac{\omega_l}{q}\hat{q}\Big)^\mu \frac{\omega_l(q)}{q} \sqrt{Z_l(q)} (1,0)_\mu \\ &= C_V \frac{1}{\sqrt{4\pi\alpha}} q \omega_l(q) \sqrt{Z_l(q)} \Big(1, \frac{\omega_l}{q}\hat{q}\Big)^\alpha \end{aligned} \tag{C.87}$$

If we plug this into the expression for the decay width, we find:

$$\Gamma_l(q) = C_V^2 \frac{G_F^2}{48\pi^2\alpha} Z_l(q) \Big(\omega_l(q)^2 - q^2\Big)^2 \omega_l(q) \tag{C.88}$$

C.6.4 Transverse case

This case is a bit more subtle in the computation. We need to remember that $\Pi_T(\omega_t, q) = \omega_t(q)^2 - q^2$.

$$\begin{aligned}\Gamma^{\alpha\mu}(\omega_t(q),q)\varepsilon_\mu(q,\pm1) &= \frac{1}{\sqrt{4\pi\alpha}}\Bigg(C_V\Big(\delta^{ij}-\hat{q}^i\hat{q}^j\Big)g^{\alpha i}g^{\mu j}\Pi_T \\ &\qquad + C_A g^{\alpha i}g^{\mu j}\Pi_A\Big(i\varepsilon^{ijm}\hat{q}^m\Big)\Bigg)\sqrt{Z_t(q)}\big(0,\vec{\varepsilon}_\pm(q)\big)_\mu \\ &= \frac{1}{\sqrt{4\pi\alpha}}\sqrt{Z_t(q)}\Bigg(C_V\Big(\omega_t(q)^2-q^2\Big)\big(0,\vec{\varepsilon}_\pm(q)\big)^\alpha \\ &\qquad - C_A\Pi_A\big(0,i\hat{q}\times\vec{\varepsilon}_\pm(q)\big)^\alpha\Bigg)\end{aligned} \tag{C.89}$$

It is important to notice that the first and second terms in the parenthesis represent perpendicular vectors, so that their contraction vanishes. Keeping this in mind, we can finally obtain the decay width for this case:

$$\Gamma_t(q) = \frac{G_F^2}{48\pi^2\alpha}Z_t(q)\frac{\omega_t(q)^2-q^2}{\omega_t(q)}\Bigg(C_V^2\Big(\omega_t(q)^2-q^2\Big)^2 + C_A^2\Pi_A(\omega_t(q),q)^2\Bigg) \tag{C.90}$$

C.6.5 Including plasma effects from protons

If we made all the computations considering the thermal bath of protons too in such a way that the plasma frequency is much less than 700 MeV, so that form factors do not need to be included, we would straightforwardly obtain the following results:

$$\Gamma_l(q) = \frac{G_F^2}{48\pi^2\alpha} Z_l(q) \frac{\Big(\omega_l(q)^2 - q^2\Big)^2 \omega_l(q)}{q^4} \Big[C_V \Pi_L^{(e)}(\omega_l, q) - h_V \Pi_L^{(p)}(\omega_l, q) \Big]^2$$
$$\Gamma_t(q) = \frac{G_F^2}{48\pi^2\alpha} Z_t(q) \frac{\omega_t(q)^2 - q^2}{\omega_t(q)} \Bigg[\Big(C_V \Pi_T^{(e)}(\omega_t, q) - h_V \Pi_T^{(p)}(\omega_t, q) \Big)^2 + \Big(C_A \Pi_A^{(e)}(\omega_t, q) - h_A \Pi_A^{(p)}(\omega_t, q) \Big)^2 \Bigg] \tag{C.91}$$

where wherever we find a (p) we must substitute $m_e \to m_p$ in the previous expressions. On the other hand, $h_V = -2\sin^2\theta_W + 1/2$ and $h_A = g_A/2$, where $g_A \approx 1.26$. Finally, the dispersion equations are now:

$$\begin{aligned} \omega_t^2 &= q^2 + \Pi_T^{(e)}(\omega_t, q) + \Pi_T^{(p)}(\omega_t, q) \\ \omega_l^2 &= \frac{\omega_l^2}{q^2} \Big(\Pi_L^{(e)}(\omega_l, q) + \Pi_L^{(p)}(\omega_l, q) \Big) \end{aligned} \tag{C.92}$$

C.7 Emissivity of the plasma

We want to compute the emissivity $\mathcal{Q}$ of the plasma, namely, the rate of energy loss per unit volume. What we need to do is integrate the decay rate over the phase space of the photon, weighted by the number density and energy and summing over the polarization states of the photon and the different species of neutrinos. The full expression is:

$$\mathcal{Q} = \sum_\nu \int \frac{d^3q}{(2\pi)^3} \Big[2 n_B\big(\omega_t(q)\big) \omega_t(q) \Gamma_t(q) + n_B\big(\omega_l(q)\big) \omega_l(q) \Gamma_l(q) \Big] \tag{C.93}$$

where n_B is the boson distribution of the photons:

$$n_B(\omega) = \frac{1}{e^{\omega/T} - 1} \tag{C.94}$$

If we plug in the expressions already found, we obtain the following emissivity for each type of polarization:

$$\begin{aligned}
\mathcal{Q}_t &= 2\Big(\sum_\nu C_V^2\Big)\frac{G_F^2}{96\pi^4\alpha}\int_0^\infty dq q^2 Z_t(q)\Big(\omega_t(q)^2 - q^2\Big)^3 n_B(\omega_t(q)) \\
\mathcal{Q}_A &= 2\Big(\sum_\nu C_A^2\Big)\frac{G_F^2}{96\pi^4\alpha}\int_0^\infty dq q^2 Z_t(q)\Big(\omega_t(q)^2 - q^2\Big)\Pi_A(\omega_t(q), q)^2 n_B(\omega_t(q)) \\
\mathcal{Q}_l &= \Big(\sum_\nu C_V^2\Big)\frac{G_F^2}{96\pi^4\alpha}\int_0^\infty dq q^2 Z_l(q)\omega_l(q)^2\Big(\omega_l(q)^2 - q^2\Big)^2 n_B(\omega_l(q))
\end{aligned} \tag{C.95}$$

where $\sum_\nu C_V^2 = 3/4 - 2\sin^2\theta_W + 12\sin^4\theta_W \approx 0.911$ and $\sum_\nu C_A^2 = 3/4$, for the standard number of species of light neutrinos.

C.8 Dark Sectors and Plasmon Decay

C.8.1 Dark Photon from the Three portal model

We can consider the effects of a dark photon, such as in the model of the Three Portal dark sectors. For the energies we are considering, we have an effective interaction of the dark photon of the following form:

$$\mathcal{L}_I = -\epsilon e J_\mu^{\mathrm{EM}} Z'^\mu + g_D J_\mu^{\mathrm{D}} Z'^\mu \tag{C.96}$$

where $J_\mu^{\rm EM}$ is an electromagnetic current, $J_\mu^{\rm D}$ is a dark current that consists of dark neutrino states: $\bar{\nu}_{\rm D}\gamma_\mu\nu_{\rm D}$, and Z'^μ is a dark photon. We consider ϵ to be a small number, while g_D is not highly constrained. This interaction allows the dark photon to couple to the fermion loop the plasmon decay, on one side, and to neutrino dark states, on the other. The dark neutrinos are mixed with the SM neutrinos in such a way that the dark photon would be effectively coupled to these SM neutrino states. We consider the non-SM states to have masses well above the limit of what can be produced by the decay of a plasmon.

The contribution to the amplitude of the plasmon decay is exactly the same diagram of the Z-contribution, but with a dark photon instead of that heavy boson state. In this case, we will not use an effective propagator of the boson (dark photon) due to its heavy mass. The amplitude to neutrino mass states i and j is:

$$\begin{aligned}\mathcal{M}_{Z'}^{ij} = -\varepsilon_\mu(Q)\int\frac{d^4k}{(2\pi)^4}\mathrm{tr}\big[\gamma^\mu S^F(K)\gamma^\nu S^F(K-Q)\big] \\ \times\epsilon e^2\frac{1}{Q^2-M_{Z'}^2}\frac{g_{\rm D}}{2}U_{i{\rm D}}^*U_{j{\rm D}} \\ \times\overline{u}_j(p_1)\gamma_\nu(1-\gamma_5)v_i(p_2) \\ = \frac{G_F}{2}\frac{1}{\sqrt{4\pi\alpha}}\Big[C_{\nu,ij}^{\rm D}\Pi^{\mu\nu}\Big]\overline{u}_j(p_1)\gamma_\nu(1-\gamma_5)v_i(p_2)\end{aligned} \tag{C.97}$$

where U is the mixing matrix for neutrino states and:

$$C_{\nu,ij}^{\rm D} = \frac{\sqrt{2\pi\alpha}}{G_F}\frac{\epsilon g_{\rm D}U_{i{\rm D}}^*U_{j{\rm D}}}{M_{Z'}^2-Q^2} \tag{C.98}$$

Now, this effective C is purely vector in nature, but depends on Q. We

can just add it to the SM contribution, but it is important to notice that we must sum over all contributions. We need to project the SM results on different mass states, final i and j states. Then, we need to sum over all possible combinations of light mass states:

$$\begin{aligned} C_{V,ij} =& \sum_{\alpha} C_{V,\alpha}^{\mathrm{SM}} U_{\alpha i}^{*} U_{\alpha j} + \frac{\sqrt{2\pi\alpha}}{G_F} \frac{\epsilon g_{\mathrm{D}} U_{i\mathrm{D}}^{*} U_{j\mathrm{D}}}{M_{Z'}^2 - Q^2} \\ C_{V,ij}^2 =& \Big| \sum_{\alpha} C_{V,\alpha}^{\mathrm{SM}} U_{\alpha i}^{*} U_{\alpha j} \Big|^2 \\ &+ \frac{\sqrt{8\pi\alpha}}{G_F} \frac{\epsilon g_{\mathrm{D}} U_{i\mathrm{D}}^{*} U_{j\mathrm{D}}}{M_{Z'}^2 - Q^2} \,\mathrm{Re}\Big(\sum_{\alpha} C_{V,\alpha}^{\mathrm{SM}} U_{\alpha i}^{*} U_{\alpha j} \Big) \\ &+ \frac{2\pi\alpha}{G_F^2} \frac{\epsilon^2 g_{\mathrm{D}}^2 \big|U_{i\mathrm{D}}\big|^2 \big|U_{j\mathrm{D}}\big|^2}{(M_{Z'}^2 - Q^2)^2} \end{aligned} \tag{C.99}$$

where $C_{V,\alpha}^{\mathrm{SM}}$ is $2\sin^2\theta_W + 0.5$ for ν_e and $2\sin^2\theta_W - 0.5$ for the other flavors.

Now, we perform the sums over all possible final mass eigenstates to compute the decay width:

$$\begin{aligned} \sum_{ij} C_V^2 =& \sum_{\alpha} \big(C_V^{\mathrm{SM}}\big)^2 \\ &+ \frac{\sqrt{8\pi\alpha}}{G_F} \frac{\epsilon g_{\mathrm{D}} \big|U_{i\mathrm{D}}\big|^2}{M_{Z'}^2 - Q^2} \,\mathrm{Re}\Big(\sum_{\alpha,i,j} C_{V,\alpha}^{\mathrm{SM}} U_{\alpha i}^{*} U_{\alpha j} \Big) \\ &+ \frac{18\pi\alpha}{G_F^2} \frac{\epsilon^2 g_{\mathrm{D}}^2 \big|U_{\mathrm{D}}\big|^4}{(M_{Z'}^2 - Q^2)^2} \end{aligned} \tag{C.100}$$

where, to simplify the computation, we have assumed that $U_{i\mathrm{D}} \equiv U_{\mathrm{D}}$ is equal for every i and $\sum_{\alpha} \big(C_V^{\mathrm{SM}}\big) = 6\sin^2\theta_W - 1/2$.

With this change, we alter the transverse and longitudinal emissivities:

$$\begin{aligned}\mathcal{Q}_t =& 2\frac{G_F^2}{96\pi^4\alpha}\int_0^\infty dq q^2 Z_t(q) \\ &\times \Big(\sum_{\alpha\beta}\big(C_V(\omega_t(q),q)\big)^2\Big)\Big(\omega_t(q)^2-q^2\Big)^3 n_B(\omega_t(q)) \\ \mathcal{Q}_l =& \frac{G_F^2}{96\pi^4\alpha}\int_0^\infty dq q^2 Z_l(q)\Big(\sum_{\alpha\beta}\big(C_V(\omega_l(q),q)\big)^2\Big) \\ &\times \omega_l(q)^2\Big(\omega_l(q)^2-q^2\Big)^2 n_B(\omega_l(q))\end{aligned} \tag{C.101}$$

where we have added an explicit dependence of C_V on $Q \equiv (\omega_i(q), q)$, such that $i = t, l$. $\mathcal{Q}_A$ remains unchanged.

C.8.2 Dark Photon from $U(1)_{L_i-L_j}$

In the case of the $U(1)_{L_i-L_j}$ model, the computation is straightforward, since the final states that couple to the dark photon are exactly the same from the ones that couple to the SM Weak forces. That is why we just need to reformulate the values of the vector and axial coefficients, as shown before:

$$C_a^{\alpha,\mathrm{SM+BSM}}(Q) \to C_a^\alpha + b_a\,\frac{\sqrt{2}}{G_F}\frac{k_\nu^\alpha\, d_a^e}{Q^2-m_{A'}^2} \tag{C.102}$$

where $a = V, A$ are the vector and axial components with $b_V = 1$ and $b_A = -1$, α is the flavor.

The final formula would be the same as the SM one, with the coefficients inside the integral, as in Eqs. (4.16) to (4.18).

Appendix D

$L_\mu - L_\tau$: Model details

D.1 Loop-induced kinetic mixing in $U(1)_{L_i - L_j}$

In this section, we discuss the computation of the one-loop induced kinetic mixing. In this work we are mainly interested in $U(1)_{L_\mu - L_\tau}$, however, this discussion is generic for all $U(1)_{L_i - L_j}$ with $i, j = e, \mu, \tau$.

Since part of the SM leptons are charged under both the SM hypercharge $U(1)_Y$ and the new leptophilic gauge group $U(1)_{L_i - L_j}$, a kinetic mixing term between the new gauge boson and the hypercharge boson as well as the neutral $SU(2)_L$ boson is induced at the one-loop level [481],

$$\epsilon_B^{ij}(q^2) = \frac{g'\, g_{ij}}{8\pi^2} \int_0^1 dx\, x(1-x) \left[3 \log \left(\frac{m_i^2 - x(1-x)q^2}{m_j^2 - x(1-x)q^2} \right) \right. \tag{D.1}$$

$$\left. + \log \left(\frac{m_{\nu_i}^2 - x(1-x)q^2}{m_{\nu_j}^2 - x(1-x)q^2} \right) \right], \tag{D.2}$$

$$\epsilon_W^{ij}(q^2) = \frac{g\, g_{ij}}{8\pi^2} \int_0^1 dx\, x(1-x) \left[\log \left(\frac{m_i^2 - x(1-x)q^2}{m_j^2 - x(1-x)q^2} \right) \right. \tag{D.3}$$

$$\left. - \log \left(\frac{m_{\nu_i}^2 - x(1-x)q^2}{m_{\nu_j}^2 - x(1-x)q^2} \right) \right]. \tag{D.4}$$

In the physical basis of neutral photon and Z boson, the mixings with the new leptophilic gauge boson read

$$\epsilon_A^{ij}(q^2) = \frac{e\, g_{ij}}{2\pi^2} \int_0^1 dx\, x(1-x)\ \log \left(\frac{m_i^2 - x(1-x)q^2}{m_j^2 - x(1-x)q^2} \right), \tag{D.5}$$

$$\epsilon_Z^{ij}(q^2) = -\frac{g_z\, g_{ij}}{4\pi^2} \int_0^1 dx\, x(1-x) \left[\log \left(\frac{m_i^2 - x(1-x)q^2}{m_j^2 - x(1-x)q^2} \right) \right. \tag{D.6}$$

$$\left. + \log \left(\frac{m_{\nu_i}^2 - x(1-x)q^2}{m_{\nu_j}^2 - x(1-x)q^2} \right) \right]. \tag{D.7}$$

Since the typical core temperature of a white dwarf is of the order of ~ 10 keV, it is safe to assume that the typical energy transfer q^2 at which the plasmon decay is happening, is much larger than the neutrino masses, $q^2 \gg m_\nu^2$. Thus, we can expand the second term in Eq. (D.7),

$$\log \left(\frac{m_{\nu_i}^2/q^2 - x(1-x)}{m_{\nu_j}^2/q^2 - x(1-x)} \right) \approx \log \left(\frac{x(1-x)}{x(1-x)} \right) = 0\,, \tag{D.8}$$

where the first approximation is valid almost everywhere in the interval $x \in [0, 1]$.

At the same time, the masses of the charged leptons are much larger than the WD temperatures, $q^2 \ll m_\ell^2$. Hence, we can also expand the logarithms containing the charged lepton masses in Eqs. (D.5) and (D.7),

$$\log\left(\frac{m_i^2/m_j^2 - x(1-x)\ q^2/m_j^2}{1 - x(1-x)\ q^2/m_j^2}\right) \approx \log\left(\frac{m_i^2}{m_j^2}\right)\,, \tag{D.9}$$

In summary, at typical WD temperatures, we can work with the q^2-independent approximations,

$$\epsilon_A^{ij} \approx \frac{e\, g_{ij}}{6\pi^2}\ \log\left(\frac{m_i}{m_j}\right)\,, \tag{D.10}$$

$$\epsilon_Z^{ij} \approx -\frac{g_z\, g_{ij}}{12\pi^2}\ \log\left(\frac{m_i}{m_j}\right) = -\frac{1}{2}\frac{s_W}{c_W}\,\epsilon_A^{ij}\,. \tag{D.11}$$

D.2 Interaction terms of the boson mass eigenstates

In order to obtain the interaction terms of the physical mass eigenstates of the neutral gauge bosons, we have to diagonalise both the kinetic and the mass terms in Eq. (4.1). Applying the full diagonalisation to the interaction terms, we obtain

$$\mathcal{L}_{\text{int}} = -(A_\mu, Z_\mu, A'_\mu) \begin{pmatrix} e\, j^\mu_{\text{EM}} \\ \frac{1}{\tau}\sqrt{\frac{\kappa-1}{2\,\kappa}}\left[g_x\, j^\mu_x - e\,\epsilon_A\, j^\mu_{\text{EM}} - g_z\left(\epsilon_Z - \tau\sqrt{\frac{\kappa+1}{\kappa-1}}\right) j^\mu_Z\right] \\ \frac{1}{\tau}\sqrt{\frac{\kappa+1}{2\,\kappa}}\left[g_x\, j^\mu_x - e\,\epsilon_A\, j^\mu_{\text{EM}} - g_z\left(\epsilon_Z + \tau\sqrt{\frac{\kappa-1}{\kappa+1}}\right) j^\mu_Z\right] \end{pmatrix}, \tag{D.12}$$

with the definitions

$$\tau = \sqrt{1 - \epsilon_A^2 - \epsilon_Z^2}\,, \tag{D.13}$$

$$\kappa = \sqrt{1 + 4\left(\frac{\epsilon_Z}{\delta - 1}\right)^2}\,, \tag{D.14}$$

$$\delta = \left(\frac{M_X}{M_Z}\right)^2. \tag{D.15}$$

Since we are considering the mass range $M_X \ll M_Z$ we can approximate $\delta \approx 0$. Furthermore, we are mostly interested in the parameter space where $g_x < 10^{-2}$, such that $\epsilon_A \lesssim 10^{-4}$. To linear order in the the small parameters ϵ_A and ϵ_Z, we then get

$$\mathcal{L}_{\text{int}} \approx -(A_\mu, Z_\mu, A'_\mu) \begin{pmatrix} e\, j^\mu_{\text{EM}} \\ g_z\, j^\mu_Z \\ g_x\, j^\mu_x - e\,\epsilon_A\, j^\mu_{\text{EM}} - g_z\,\epsilon_Z\, j^\mu_Z \end{pmatrix}. \tag{D.16}$$

Hence, we recover the familiar SM photon and Z interactions with the electromagnetic and Z currents as defined in Eqs. (4.6) and (4.7), respectively.

The mass eigenstate of the $U(1)_{L_\mu - L_\tau}$ gauge boson A', however, not only couples to the $U(1)_{L_\mu - L_\tau}$ current but picks up an additional interaction with the electromagnetic and Z current suppressed by the kinetic mixings ϵ_A and ϵ_Z, respectively.

Appendix E

Limit extraction for WD cooling

To set a limit on extra WD cooling through neutrinos, we utilise the χ^2 function provided in Fig. 10 of Ref. [431]. The plot in Fig. E.1 shows $\Delta\chi^2$ as a function of the linear scaling parameter f_s quantifying extra neutrino cooling relative to the SM. The original limit provided in [431] was set at the 95% CL and resulted in an allowed interval of $0.6 \lesssim f_s^{95} \lesssim 1.7$. However, in order to be consistent with the literature on dark photons, where limits in the coupling-versus-mass plane are typically set at the 90% CL, we also extract the 90% CL limit on the scaling parameter f_s by setting $\Delta\chi^2 = 2.7$ (for 1 dof) in the χ^2 function of [431]. As illustrated by the two blue vertical lines in Fig. E.1, this results in an interval of $0.66 \lesssim f_s^{90} \lesssim 1.31$. Hence, we can exclude 30% extra neutrino cooling at the 90% CL (cf. red line in Figs. 4.4 and 4.5) given the analysis of [431].

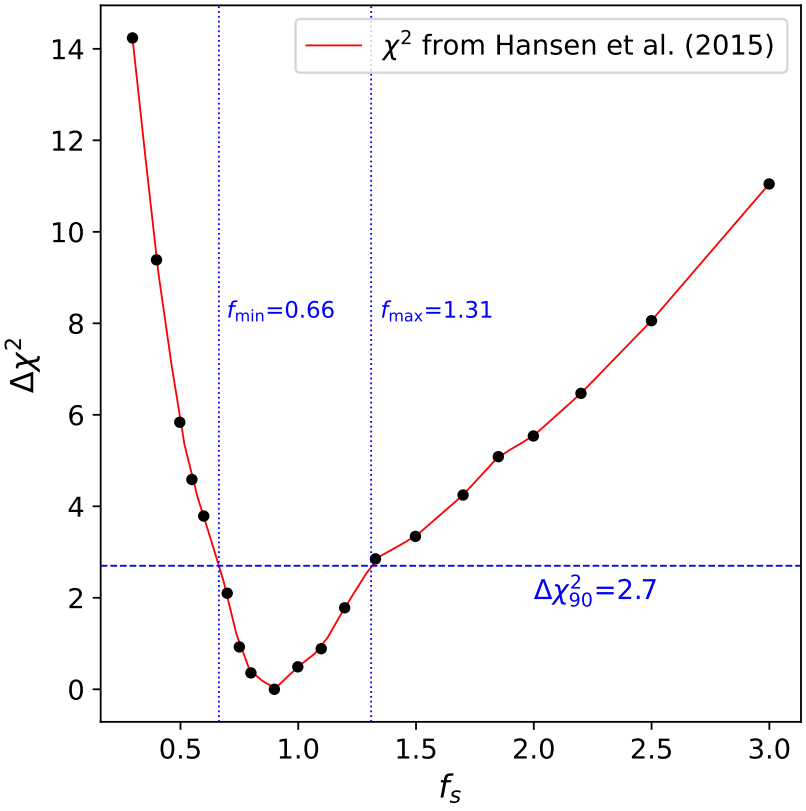

Figure E.1: We use the χ^2 function computed in Ref. [431] to extract the limit at the 90% CL ($\Delta\chi^2 = 2.7$) for modified cooling by a factor of f_s relative to the SM.

Bibliography

[1] Sheldon L Glashow. Partial-symmetries of weak interactions. *Nuclear physics*, 22(4):579–588, 1961.

[2] Steven Weinberg. A model of leptons. *Physical review letters*, 19(21):1264, 1967.

[3] Abdus Salam and John Clive Ward. Weak and electromagnetic interactions. *Il Nuovo Cimento (1955-1965)*, 11:568–577, 1959.

[4] Murray Gell-Mann. A schematic model of baryons and mesons. In *Murray Gell-Mann: Selected Papers*, pages 151–152. World Scientific, 2010.

[5] George Zweig. An su _3 model for strong interaction symmetry and its breaking. Technical report, CM-P00042884, 1964.

[6] Martinus Veltman et al. Regularization and renormalization of gauge fields. *Nuclear Physics B*, 44(1):189–213, 1972.

[7] Peter W Higgs. Broken symmetries and the masses of gauge bosons. *Physical review letters*, 13(16):508, 1964.

[8] François Englert and Robert Brout. Broken symmetry and the mass of gauge vector mesons. *Physical review letters*, 13(9):321, 1964.

[9] Bruno Pontecorvo. Inverse *beta* processes and nonconservation of lepton charge. *Zhur. Eksptl'. i Teoret. Fiz.*, 34, 1958.

[10] Ziro Maki, Masami Nakagawa, and Shoichi Sakata. Remarks on the unified model of elementary particles. *Progress of Theoretical Physics*, 28(5):870–880, 1962.

[11] John N Bahcall and Raymond Davis Jr. An account of the development of the solar neutrino problem. *Essays in Nuclear Astrophysics*, pages 243–285, 1982.

[12] SP Mikheyev and A Yu Smirnov. Resonant amplification of ν oscillations in matter and solar-neutrino spectroscopy. *Il Nuovo Cimento C*, 9:17–26, 1986.

[13] Lincoln Wolfenstein. Neutrino oscillations in matter. In *Solar neutrinos*, pages 294–299. CRC Press, 2018.

[14] Yoshiyuki Fukuda, T Hayakawa, E Ichihara, K Inoue, K Ishihara, Hirokazu Ishino, Y Itow, T Kajita, J Kameda, S Kasuga, et al. Evidence for oscillation of atmospheric neutrinos. *Physical review letters*, 81(8):1562, 1998.

[15] Art McDonald. Measurement of cc interactions produced by^ 8b solar neutrinos at sno. *PoS*, page 186, 2001.

[16] AB McDonald, QR Ahmad, RC Allen, TC Andersen, JD Anglin, JC Barton, EW Beier, M Bercovitch, J Bigu, SD Biller, et al. Direct evidence for neutrino flavor transformation from neutral-current interactions in sno. In *AIP Conference Proceedings*, volume 646, pages 43–58. AIP Publishing, 2002.

[17] KamLAND& Eguchi, S Enomoto, K Furuno, J Goldman, H Hanada, H Ikeda, K Ikeda, K Inoue, K Ishihara, W Itoh, et al. First results from kamland: evidence for reactor antineutrino disappearance. *Physical review letters*, 90(2):021802, 2003.

[18] Fritz Zwicky. Die rotverschiebung von extragalaktischen nebeln. *Helvetica Physica Acta, Vol. 6, p. 110-127*, 6:110–127, 1933.

[19] Albert Einstein. Lens-like action of a star by the deviation of light in the gravitational field. *Science*, 84(2188):506–507, 1936.

[20] Vera C Rubin and W Kent Ford Jr. Rotation of the andromeda nebula from a spectroscopic survey of emission regions. *Astrophysical Journal, vol. 159, p. 379*, 159:379, 1970.

[21] Philip JE Peebles and JT Yu. Primeval adiabatic perturbation in an expanding universe. *Astrophysical Journal, vol. 162, p. 815*, 162:815, 1970.

[22] Alan H Guth. Inflationary universe: A possible solution to the horizon and flatness problems. *Physical Review D*, 23(2):347, 1981.

[23] Vera C Rubin. Dark matter in spiral galaxies. *Scientific American*, 248(6):96–109, 1983.

[24] Dark Matter Bright Galaxies. Beyond: The life of astronomer vera rubin by: Doi: Isbn (electronic): Publisher: Published: Ashley jean yeager the mit press 2023 10.7551/mitpress/13374.001. 0001 9780262366885 page 2 in the spring of 1952, vera, pregnant with her second child, climbed into the car with bob to drive to the carnegie institu-tion's department of terrestrial magnetism. founded in 1904,

the research department, nestled on the west side of washing-ton, dc's famous rock creek park, was originally focused on mapping the earth's geomagnetic field. *No part of this book may be reproduced in any form by any electronic or mechanical means (including photocopy-ing, record-ing, or information storage and retrieval) without permis-sion in writ-ing from the publisher. This book was set in Stone Serif and Stone Sans by Westchester Pub*, 2007.

[25] George F Smoot, Charles L Bennett, A Kogut, EL Wright, J Aymon, NW Boggess, ES Cheng, G De Amici, S Gulkis, MG Hauser, et al. Structure in the cobe differential microwave radiometer first-year maps. *Astrophysical Journal, Part 2-Letters (ISSN 0004-637X), vol. 396, no. 1, Sept. 1, 1992, p. L1-L5. Research supported by NASA.*, 396:L1–L5, 1992.

[26] David N Schramm. Dark matter and cosmology. *Nuclear Physics B-Proceedings Supplements*, 28(1):243–253, 1992.

[27] WMAP Collaboration, DN Spergel, et al. First year wilkinson microwave anisotropy probe (wmap) observations: determination of cosmological parameters. *Astrophys. J. Suppl.*, 148:175–194, 2003.

[28] Planck Collaboration, PAR Ade, N Aghanim, C Armitage-Caplan, M Arnaud, M Ashdown, F Atrio-Barandela, J Aumont, C Baccigalupi, AJ Banday, et al. Planck 2013 results. xvi. cosmological parameters. *A&A*, 571:A16, 2014.

[29] Scott Dodelson and Fabian Schmidt. *Modern cosmology*. Academic press, 2020.

[30] Andrei D Sakharov. Violation of cp-invariance, c-asymmetry, and baryon asymmetry of the universe. In *In The Intermissions... Collected Works on Research into the Essentials of Theoretical Physics in Russian Federal Nuclear Center, Arzamas-16*, pages 84–87. World Scientific, 1998.

[31] Kuzmin VA. uzm in, va r ubakov and me shaposhnikov. *Phys. Lett. B*, 155:36, 1985.

[32] Masataka Fukugita and Tsutomu Yanagida. Barygenesis without grand unification. *Physics Letters B*, 174(1):45–47, 1986.

[33] Ian Affleck and Michael Dine. A new mechanism for baryogenesis. *Nuclear Physics B*, 249(2):361–380, 1985.

[34] Licia Verde, HV Peiris, DN Spergel, MR Nolta, CL Bennett, M Halpern, G Hinshaw, N Jarosik, A Kogut, M Limon, et al. First-year wilkinson microwave anisotropy probe (wmap)* observations: parameter estimation methodology. *The Astrophysical Journal Supplement Series*, 148(1):195, 2003.

[35] Freeman J Dyson. The radiation theories of tomonaga, schwinger, and feynman. *Physical Review*, 75(3):486, 1949.

[36] R. P. Feynman. Quantum theory of gravitation. *Acta Physica Polonica*, 24:697, 1963.

[37] B. S. DeWitt. Quantum theory of gravity. i. the canonical theory. *Physical Review*, 160(5):1113–1148, 1967.

[38] S. Weinberg. Infrared photons and gravitons. *Physical Review*, 140(2B):B516–B524, 1965.

[39] M. B. Green, J. H. Schwarz, and E. Witten. *Superstring Theory*. Cambridge University Press, 1987.

[40] A. Ashtekar. New variables for classical and quantum gravity. *Physical Review Letters*, 57(18):2244–2247, 1986.

[41] B. P. Abbott, others (LIGO Scientific Collaboration, and Virgo Collaboration). Observation of gravitational waves from a binary black hole merger. *Physical Review Letters*, 116(6):061102, 2016.

[42] J. Bailey and others (CERN-Mainz-Daresbury Collaboration). Final report on the cern muon storage ring including the anomalous magnetic moment and the electric dipole moment of the muon, and a direct test of relativistic time dilation. *Nuclear Physics B*, 150:1–75, 1979.

[43] J. Schwinger. On quantum-electrodynamics and the magnetic moment of the electron. *Physical Review*, 73(4):416–417, 1948.

[44] H. N. Brown and others (Muon g 2 Collaboration). Precise measurement of the positive muon anomalous magnetic moment. *Physical Review Letters*, 86(22):2227–2231, 2001.

[45] A. Czarnecki and W. J. Marciano. The muon anomalous magnetic moment: A harbinger for "new physics". *Physics Today*, 54(6):35–41, 2001.

[46] F. Jegerlehner and A. Nyffeler. The muon g-2. *Physics Reports*, 477(1-3):1–110, 2009.

[47] T. Aoyama et al. The anomalous magnetic moment of the muon in the standard model. *Physics Reports*, 887:1–166, 2020.

[48] B. Abi and others (Muon g 2 Collaboration). Measurement of the positive muon anomalous magnetic moment to 0.46 ppm. *Physical Review Letters*, 126(14):141801, 2021.

[49] C. Athanassopoulos and others (LSND Collaboration). Evidence for $\bar{\nu}_\mu \to \bar{\nu}_e$ oscillations from the lsnd experiment at the los alamos meson physics facility. *Physical Review Letters*, 77(15):3082–3085, 1996.

[50] C. Athanassopoulos and others (LSND Collaboration). Further evidence for neutrino oscillations from the lsnd experiment. *Physical Review C*, 55(4):2075–2084, 1997.

[51] A. Aguilar and others (LSND Collaboration). Evidence for neutrino oscillations from the observation of $\bar{\nu}_e$ appearance in a $\bar{\nu}_\mu$ beam. *Physical Review D*, 64(11):112007, 2001.

[52] A. Aguilar and others (LSND Collaboration). A combined ν_μ disappearance ν_e appearance search at the los alamos meson physics facility. *Physical Review D*, 64(9):112007, 2002.

[53] A. A. Aguilar-Arevalo and others (LSND Collaboration). Evidence for $\bar{\nu}_\mu \to \bar{\nu}_e$ oscillations from lsnd and miniboone. *Physical Review D*, 81(7):072002, 2010.

[54] A. A. Aguilar-Arevalo et al. A Search for Electron Neutrino Appearance at the $\Delta m^2 \sim 1eV^2$ Scale. *Phys. Rev. Lett.*, 98:231801, 2007.

[55] A. A. Aguilar-Arevalo et al. The Neutrino Flux Prediction at MiniBooNE. *Phys. Rev. D*, 79:072002, 2009.

[56] A. A. Aguilar-Arevalo et al. First Observation of Coherent π^0 Produc-

tion in Neutrino Nucleus Interactions with $E_\nu < 2$ GeV. *Phys. Lett. B*, 664:41–46, 2008.

[57] A. A. Aguilar-Arevalo et al. Unexplained Excess of Electron-Like Events From a 1-GeV Neutrino Beam. *Phys. Rev. Lett.*, 102:101802, 2009.

[58] Alexis A. Aguilar-Arevalo et al. Measurement of ν_μ and $\bar{\nu}_\mu$ induced neutral current single π^0 production cross sections on mineral oil at $E_\nu \sim \mathcal{O}(1\text{GeV})$. *Phys. Rev. D*, 81:013005, 2010.

[59] A. A. Aguilar-Arevalo et al. Event Excess in the MiniBooNE Search for $\bar{\nu}_\mu \to \bar{\nu}_e$ Oscillations. *Phys. Rev. Lett.*, 105:181801, 2010.

[60] A. A. Aguilar-Arevalo et al. A Combined $\nu_\mu \to \nu_e$ and $\bar{\nu}_\mu \to \bar{\nu}_e$ Oscillation Analysis of the MiniBooNE Excesses. 7 2012.

[61] G. Cheng et al. Dual baseline search for muon antineutrino disappearance at $0.1\text{eV}^2 < \Delta m^2 < 100\text{eV}^2$. *Phys. Rev. D*, 86:052009, 2012.

[62] A. A. Aguilar-Arevalo et al. Improved Search for $\bar{\nu}_\mu \to \bar{\nu}_e$ Oscillations in the MiniBooNE Experiment. *Phys. Rev. Lett.*, 110:161801, 2013.

[63] A. A. Aguilar-Arevalo et al. Significant Excess of ElectronLike Events in the MiniBooNE Short-Baseline Neutrino Experiment. *Phys. Rev. Lett.*, 121(22):221801, 2018.

[64] A. A. Aguilar-Arevalo et al. Dark Matter Search in Nucleon, Pion, and Electron Channels from a Proton Beam Dump with MiniBooNE. *Phys. Rev. D*, 98(11):112004, 2018.

[65] A. A. Aguilar-Arevalo et al. Updated MiniBooNE neutrino oscillation results with increased data and new background studies. *Phys. Rev. D*, 103(5):052002, 2021.

[66] A. A. Aguilar-Arevalo et al. MiniBooNE Data Releases. 10 2021.

[67] A. A. Aguilar-Arevalo et al. MiniBooNE and MicroBooNE Combined Fit to a 3+1 Sterile Neutrino Scenario. *Phys. Rev. Lett.*, 129(20):201801, 2022.

[68] A. G. Riess et al. A 2.4% determination of the local value of the hubble constant. *The Astrophysical Journal*, 826(1):56, 2016.

[69] N. Aghanim et al. Planck 2018 results. VI. Cosmological parameters. *Astron. Astrophys.*, 641:A6, 2020. [Erratum: Astron.Astrophys. 652, C4 (2021)].

[70] W. L. Freedman et al. The carnegie-chicago hubble program. viii. an independent determination of the hubble constant based on the tip of the red giant branch. *The Astrophysical Journal*, 858(2):L15, 2021.

[71] E. Di Valentino, A. Melchiorri, and J. Silk. The cosmic discordance: Planck and hubble tensions. *Physics Reports*, 873:1–70, 2021.

[72] L. Verde, T. Treu, and A. G. Riess. Tensions between the early and late universe. *Nature Astronomy*, 3(7):589–599, 2019.

[73] P. W. Gorham and others (ANITA Collaboration). Observation of an unusual upward-going cosmic-ray-like event in the third flight of anita. *Physical Review Letters*, 117(7):071101, 2016.

[74] P. W. Gorham and others (ANITA Collaboration). Observation of ultra-high-energy cosmic rays with the anita balloon-borne radio interferometer. *Physical Review D*, 98(2):022001, 2018.

[75] P. Allison and others (ANITA Collaboration). Measurement of the cosmic ray spectrum above 4×10^{18} ev using 60,000 radio pulses detected by the anita experiment. *Physical Review Letters*, 124(7):071101, 2020.

[76] A. Romero-Wolf and others (ANITA Collaboration). Recent results from the anita experiment. *Nuclear Instruments and Methods in Physics Research Section A: Accelerators, Spectrometers, Detectors and Associated Equipment*, 936:321–325, 2019.

[77] A. Romero-Wolf and others (ANITA Collaboration). Report on the anita experiment's implications for ultra-high-energy cosmic-ray physics. *Journal of Physics G: Nuclear and Particle Physics*, 48(8):085201, 2021.

[78] R. Brandenberger and C. Vafa. Superstrings in the early universe. *Nuclear Physics B*, 316(3):391–410, 1989.

[79] J. Polchinski. *String Theory*. Cambridge University Press, 1998.

[80] T. Banks and M. Dine. Quantum moduli spaces of quasi-finite superstring vacua. *Physical Review D*, 68(4):043512, 2003.

[81] M. R. Douglas. The statistics of string / m theory vacua. *Journal of High Energy Physics*, 2003(5):046, 2003.

[82] J. Wess and J. Bagger. *Supersymmetry and Supergravity*. Princeton University Press, 1992.

[83] S. P. Martin. A supersymmetry primer. *arXiv preprint hep-ph/9709356*, 1997.

[84] S. Weinberg. *The Quantum Theory of Fields, Vol. 3: Supersymmetry*. Cambridge University Press, 2000.

[85] H. Baer and X. Tata. Supersymmetry phenomenology: With 120 problems and solutions. *Cambridge University Press*, 2020.

[86] ATLAS Collaboration. Search for supersymmetry in final states with two same-sign or three leptons and jets using 139 fb^{-1} of pp collision data at $\sqrt{s} = 13$ tev with the atlas detector. *Physical Review D*, 104(1):012005, 2021.

[87] Karl Popper. *Conjectures and Refutations: The Growth of Scientific Knowledge*. Routledge, London, 1963.

[88] Peter Ballett, Matheus Hostert, and Silvia Pascoli. Dark Neutrinos and a Three Portal Connection to the Standard Model. *Phys. Rev. D*, 101(11):115025, 2020.

[89] Andrea Caputo, Alexander J. Millar, Ciaran A. J. O'Hare, and Edoardo Vitagliano. Dark photon limits: A handbook. *Phys. Rev. D*, 104:095029, Nov 2021.

[90] Bob Holdom. Searching for ϵ Charges and a New U(1). *Phys. Lett.*, B178:65–70, 1986.

[91] F. del Aguila, M. Masip, and M. Perez-Victoria. Physical parameters and renormalization of U(1)-a x U(1)-b models. *Nucl. Phys.*, B456:531–549, 1995.

[92] Sacha Davidson, Steen Hannestad, and Georg Raffelt. Updated bounds on millicharged particles. *JHEP*, 05:003, 2000.

[93] E. C. G. Stueckelberg. Interaction energy in electrodynamics and in the field theory of nuclear forces. *Helv. Phys. Acta*, 11:225–244, 1938.

[94] Henri Ruegg and Marti Ruiz-Altaba. The Stueckelberg field. *Int. J. Mod. Phys.*, A19:3265–3348, 2004.

[95] Boris Körs and Pran Nath. A stueckelberg extension of the standard model. *Physics Letters B*, 586(3–4):366–372, Apr 2004.

[96] B. Grzadkowski, M. Iskrzynski, M. Misiak, and J. Rosiek. Dimension-Six Terms in the Standard Model Lagrangian. *JHEP*, 10:085, 2010.

[97] Lotty Ackerman, Matthew R. Buckley, Sean M. Carroll, and Marc Kamionkowski. Dark Matter and Dark Radiation. *Phys. Rev.*, D79:023519, 2009. [,277(2008)].

[98] Francis-Yan Cyr-Racine and Kris Sigurdson. Cosmology of atomic dark matter. *Phys. Rev.*, D87(10):103515, 2013.

[99] Prateek Agrawal, Francis-Yan Cyr-Racine, Lisa Randall, and Jakub Scholtz. Make Dark Matter Charged Again. *JCAP*, 1705(05):022, 2017.

[100] C. Boehm and Pierre Fayet. Scalar dark matter candidates. *Nucl. Phys. B*, 683:219–263, 2004.

[101] Thomas Hambye, Michel H.G. Tytgat, Jérôme Vandecasteele, and Laurent Vanderheyden. Dark matter from dark photons: a taxonomy of dark matter production. *Phys. Rev. D*, 100(9):095018, 2019.

[102] C. Boehm, T.A. Ensslin, and J. Silk. Can Annihilating dark matter be lighter than a few GeVs? *J. Phys. G*, 30:279–286, 2004.

[103] Eder Izaguirre, Gordan Krnjaic, Philip Schuster, and Natalia Toro. Analyzing the Discovery Potential for Light Dark Matter. *Phys. Rev. Lett.*, 115(25):251301, 2015.

[104] Ann E. Nelson and Jakub Scholtz. Dark Light, Dark Matter and the Misalignment Mechanism. *Phys. Rev.*, D84:103501, 2011.

[105] Itay M. Bloch, Rouven Essig, Kohsaku Tobioka, Tomer Volansky, and Tien-Tien Yu. Searching for Dark Absorption with Direct Detection Experiments. *JHEP*, 06:087, 2017.

[106] Steven Weinberg. *Gravitation and cosmology: principles and applications of the general theory of relativity.* 1972.

[107] Maurizio Giannotti, Igor Irastorza, Javier Redondo, and Andreas Ringwald. Cool WISPs for stellar cooling excesses. *JCAP*, 05:057, 2016.

[108] Brian D. Fields, Keith A. Olive, Tsung-Han Yeh, and Charles Young. Big-Bang Nucleosynthesis After Planck. *JCAP*, 2003(03):010, 2020.

[109] Bogdan A. Dobrescu. Massless gauge bosons other than the photon. *Phys. Rev. Lett.*, 94:151802, 2005.

[110] Emidio Gabrielli and Martti Raidal. Exponentially spread dynamical Yukawa couplings from nonperturbative chiral symmetry breaking in the dark sector. *Phys. Rev.*, D89(1):015008, 2014.

[111] Marco Fabbrichesi, Emidio Gabrielli, and Gaia Lanfranchi. *The physics of the dark photon: a primer.* Springer, 2021.

[112] Emidio Gabrielli, Barbara Mele, Martti Raidal, and Elena Venturini. FCNC decays of standard model fermions into a dark photon. *Phys. Rev.*, D94(11):115013, 2016.

[113] D. Barducci, M. Fabbrichesi, and E. Gabrielli. Neutral Hadrons Disappearing into the Darkness. *Phys. Rev.*, D98(3):035049, 2018.

[114] Albert M Sirunyan et al. Search for a narrow resonance decaying to a pair of muons in proton-proton collisions at 13 TeV. 8 2019.

[115] R. Barbieri, C. Braggio, G. Carugno, C. S. Gallo, A. Lombardi, A. Ortolan, R. Pengo, G. Ruoso, and C. C. Speake. Searching for galactic axions through magnetized media: the QUAX proposal. *Phys. Dark Univ.*, 15:135–141, 2017.

[116] So Chigusa, Takeo Moroi, and Kazunori Nakayama. Detecting Light Boson Dark Matter through Conversion into Magnon. 2020.

[117] Paola Arias, Davide Cadamuro, Mark Goodsell, Joerg Jaeckel, Javier Redondo, and Andreas Ringwald. WISPy Cold Dark Matter. *JCAP*, 06:013, 2012.

[118] S. J. Asztalos, G. Carosi, C. Hagmann, D. Kinion, K. van Bibber, M. Hotz, L. J Rosenberg, G. Rybka, J. Hoskins, J. Hwang, P. Sikivie, D. B. Tanner, R. Bradley, and J. Clarke. Squid-based microwave cavity search for dark-matter axions. *Phys. Rev. Lett.*, 104:041301, Jan 2010.

[119] N. Du, N. Force, R. Khatiwada, E. Lentz, R. Ottens, L. J Rosenberg, G. Rybka, G. Carosi, N. Woollett, D. Bowring, A. S. Chou, A. Sonnenschein, W. Wester, C. Boutan, N. S. Oblath, R. Bradley, E. J. Daw, A. V. Dixit, J. Clarke, S. R. O'Kelley, N. Crisosto, J. R. Gleason,

S. Jois, P. Sikivie, I. Stern, N. S. Sullivan, D. B Tanner, and G. C. Hilton. Search for invisible axion dark matter with the axion dark matter experiment. *Phys. Rev. Lett.*, 120:151301, Apr 2018.

[120] T. Braine, R. Cervantes, N. Crisosto, N. Du, S. Kimes, L. J. Rosenberg, G. Rybka, J. Yang, D. Bowring, A. S. Chou, R. Khatiwada, A. Sonnenschein, W. Wester, G. Carosi, N. Woollett, L. D. Duffy, R. Bradley, C. Boutan, M. Jones, B. H. LaRoque, N. S. Oblath, M. S. Taubman, J. Clarke, A. Dove, A. Eddins, S. R. O'Kelley, S. Nawaz, I. Siddiqi, N. Stevenson, A. Agrawal, A. V. Dixit, J. R. Gleason, S. Jois, P. Sikivie, J. A. Solomon, N. S. Sullivan, D. B. Tanner, E. Lentz, E. J. Daw, J. H. Buckley, P. M. Harrington, E. A. Henriksen, and K. W. Murch. Extended search for the invisible axion with the axion dark matter experiment. *Phys. Rev. Lett.*, 124:101303, Mar 2020.

[121] C. Boutan, M. Jones, B. H. LaRoque, N. S. Oblath, R. Cervantes, N. Du, N. Force, S. Kimes, R. Ottens, L. J. Rosenberg, G. Rybka, J. Yang, G. Carosi, N. Woollett, D. Bowring, A. S. Chou, R. Khatiwada, A. Sonnenschein, W. Wester, R. Bradley, E. J. Daw, A. Agrawal, A. V. Dixit, J. Clarke, S. R. O'Kelley, N. Crisosto, J. R. Gleason, S. Jois, P. Sikivie, I. Stern, N. S. Sullivan, D. B. Tanner, P. M. Harrington, and E. Lentz. Piezoelectrically tuned multimode cavity search for axion dark matter. *Phys. Rev. Lett.*, 121:261302, Dec 2018.

[122] L. Zhong, S. Al Kenany, K. M. Backes, B. M. Brubaker, S. B. Cahn, G. Carosi, Y. V. Gurevich, W. F. Kindel, S. K. Lamoreaux, K. W. Lehnert, S. M. Lewis, M. Malnou, R. H. Maruyama, D. A. Palken, N. M. Rapidis, J. R. Root, M. Simanovskaia, T. M. Shokair, D. H. Speller, I. Urdinaran, and K. A. van Bibber. Results from phase 1 of the

haystac microwave cavity axion experiment. *Phys. Rev. D*, 97:092001, May 2018.

[123] Kelly M Backes, Daniel A Palken, S Al Kenany, Benjamin M Brubaker, SB Cahn, A Droster, Gene C Hilton, Sumita Ghosh, H Jackson, Steve K Lamoreaux, et al. A quantum enhanced search for dark matter axions. *Nature*, 590(7845):238–242, 2021.

[124] S. Lee, S. Ahn, J. Choi, B. R. Ko, and Y. K. Semertzidis. Axion dark matter search around 6.7 μeV. *Phys. Rev. Lett.*, 124:101802, Mar 2020.

[125] Junu Jeong, SungWoo Youn, Sungjae Bae, Jihngeun Kim, Taehyeon Seong, Jihn E. Kim, and Yannis K. Semertzidis. Search for invisible axion dark matter with a multiple-cell haloscope. *Phys. Rev. Lett.*, 125:221302, Nov 2020.

[126] Ohjoon Kwon, Doyu Lee, Woohyun Chung, Danho Ahn, HeeSu Byun, Fritz Caspers, Hyoungsoon Choi, Jihoon Choi, Yonuk Chong, Hoyong Jeong, Junu Jeong, Jihn E. Kim, Jinsu Kim, Ça ğlar Kutlu, Jihnhwan Lee, MyeongJae Lee, Soohyung Lee, Andrei Matlashov, Seonjeong Oh, Seongtae Park, Sergey Uchaikin, SungWoo Youn, and Yannis K. Semertzidis. First results from an axion haloscope at capp around 10.7 μeV. *Phys. Rev. Lett.*, 126:191802, May 2021.

[127] D. Alesini, C. Braggio, G. Carugno, N. Crescini, D. D'Agostino, D. Di Gioacchino, R. Di Vora, P. Falferi, U. Gambardella, C. Gatti, G. Iannone, C. Ligi, A. Lombardi, G. Maccarrone, A. Ortolan, R. Pengo, A. Rettaroli, G. Ruoso, L. Taffarello, and S. Tocci. Search

for invisible axion dark matter of mass $m_a = 43$ μeV with the quax–$a\gamma$ experiment. *Phys. Rev. D*, 103:102004, May 2021.

[128] David Alesini, Danilo Babusci, Daniele Di Gioacchino, Claudio Gatti, Gianluca Lamanna, and Carlo Ligi. The klash proposal, 2017.

[129] S. DePanfilis, A. C. Melissinos, B. E. Moskowitz, J. T. Rogers, Y. K. Semertzidis, W. U. Wuensch, H. J. Halama, A. G. Prodell, W. B. Fowler, and F. A. Nezrick. Limits on the abundance and coupling of cosmic axions at 4.5lt;$m_a$lt;5.0 μev. *Phys. Rev. Lett.*, 59:839–842, Aug 1987.

[130] C. Hagmann, P. Sikivie, N. S. Sullivan, and D. B. Tanner. Results from a search for cosmic axions. *Phys. Rev. D*, 42:1297–1300, Aug 1990.

[131] Ben T. McAllister, Graeme Flower, Eugene N. Ivanov, Maxim Goryachev, Jeremy Bourhill, and Michael E. Tobar. The organ experiment: An axion haloscope above 15 ghz. *Physics of the Dark Universe*, 18:67–72, 2017.

[132] A. Álvarez Melcón, S. Arguedas Cuendis, J. Baier, K. Barth, H. Bräuninger, S. Calatroni, G. Cantatore, F. Caspers, J. F. Castel, S. A. Cetin, C. Cogollos, T. Dafni, M. Davenport, A. Dermenev, K. Desch, A. Díaz-Morcillo, B. Döbrich, H. Fischer, W. Funk, J. D. Gallego, J. M. García Barceló, A. Gardikiotis, J. G. Garza, B. Gimeno, S. Gninenko, J. Golm, M. D. Hasinoff, D. H. H. Hoffmann, I. G. Irastorza, K. Jakovčić, J. Kaminski, M. Karuza, B. Lakić, J. M. Laurent, A. J. Lozano-Guerrero, G. Luzón, C. Malbrunot, M. Maroudas, J. Miralda-Escudé, H. Mirallas, L. Miceli, P. Navarro, A. Ozbey, K. Özbozduman, C. Peña Garay, M. J. Pivovaroff, J. Redondo, J. Ruz, E. Ruiz Chóliz,

S. Schmidt, M. Schumann, Y. K. Semertzidis, S. K. Solanki, L. Stewart, I. Tsagris, T. Vafeiadis, J. K. Vogel, E. Widmann, W. Wuensch, and K. Zioutas. First results of the CAST-RADES haloscope search for axions at 34.67 eV. *Journal of High Energy Physics*, 2021(10), oct 2021.

[133] N. Crisosto, P. Sikivie, N. S. Sullivan, D. B. Tanner, J. Yang, and G. Rybka. Admx slic: Results from a superconducting lc circuit investigating cold axions. *Phys. Rev. Lett.*, 124:241101, Jun 2020.

[134] Jonathan L. Ouellet, Chiara P. Salemi, Joshua W. Foster, Reyco Henning, Zachary Bogorad, Janet M. Conrad, Joseph A. Formaggio, Yonatan Kahn, Joe Minervini, Alexey Radovinsky, Nicholas L. Rodd, Benjamin R. Safdi, Jesse Thaler, Daniel Winklehner, and Lindley Winslow. First results from abracadabra-10 cm: A search for sub-μeV axion dark matter. *Phys. Rev. Lett.*, 122:121802, Mar 2019.

[135] Alexander V Gramolin, Deniz Aybas, Dorian Johnson, Janos Adam, and Alexander O Sushkov. Search for axion-like dark matter with ferromagnets. *Nature Physics*, 17(1):79–84, 2021.

[136] Matthew Lawson, Alexander J. Millar, Matteo Pancaldi, Edoardo Vitagliano, and Frank Wilczek. Tunable axion plasma haloscopes. *Phys. Rev. Lett.*, 123:141802, Oct 2019.

[137] Allen Caldwell, Gia Dvali, Béla Majorovits, Alexander Millar, Georg Raffelt, Javier Redondo, Olaf Reimann, Frank Simon, and Frank Steffen. Dielectric haloscopes: A new way to detect axion dark matter. *Phys. Rev. Lett.*, 118:091801, Mar 2017.

[138] Masha Baryakhtar, Junwu Huang, and Robert Lasenby. Axion and hidden photon dark matter detection with multilayer optical haloscopes. *Phys. Rev. D*, 98:035006, Aug 2018.

[139] Javier De Miguel. A dark matter telescope probing the 6 to 60 GHz band. *Journal of Cosmology and Astroparticle Physics*, 2021(04):075, apr 2021.

[140] BRASS.

[141] Jan Schütte-Engel, David J.E. Marsh, Alexander J. Millar, Akihiko Sekine, Francesca Chadha-Day, Sebastian Hoof, Mazhar N. Ali, Kin Chung Fong, Edward Hardy, and Libor Šmejkal. Axion quasiparticles for axion dark matter detection. *Journal of Cosmology and Astroparticle Physics*, 2021(08):066, aug 2021.

[142] C. Antel et al. Feebly-interacting particles: FIPs 2022 Workshop Report. *Eur. Phys. J. C*, 83(12):1122, 2023.

[143] A. Blondel et al. Searches for long-lived particles at the future FCC-ee. *Front. in Phys.*, 10:967881, 2022.

[144] Subir Sarkar. Big bang nucleosynthesis and physics beyond the standard model. *Rept. Prog. Phys.*, 59:1493–1610, 1996.

[145] A. D. Dolgov, S. H. Hansen, G. Raffelt, and D. V. Semikoz. Heavy sterile neutrinos: Bounds from big bang nucleosynthesis and SN1987A. *Nucl. Phys. B*, 590:562–574, 2000.

[146] Oleg Ruchayskiy and Artem Ivashko. Restrictions on the lifetime of sterile neutrinos from primordial nucleosynthesis. *JCAP*, 10:014, 2012.

[147] Marco Hufnagel, Kai Schmidt-Hoberg, and Sebastian Wild. BBN constraints on MeV-scale dark sectors. Part I. Sterile decays. *JCAP*, 02:044, 2018.

[148] A. Boyarsky, M. Ovchynnikov, O. Ruchayskiy, and V. Syvolap. Improved big bang nucleosynthesis constraints on heavy neutral leptons. *Phys. Rev. D*, 104:023517, 2021.

[149] Nashwan Sabti, James Alvey, Miguel Escudero, Malcolm Fairbairn, and Diego Blas. Refined Bounds on MeV-scale Thermal Dark Sectors from BBN and the CMB. *JCAP*, 01:004, 2020.

[150] P. Abratenko, M. Alrashed, R. An, J. Anthony, J. Asaadi, A. Ashkenazi, S. Balasubramanian, B. Baller, C. Barnes, G. Barr, V. Basque, S. Berkman, A. Bhanderi, A. Bhat, M. Bishai, A. Blake, T. Bolton, L. Camilleri, D. Caratelli, I. Caro Terrazas, R. Castillo Fernandez, F. Cavanna, G. Cerati, Y. Chen, E. Church, D. Cianci, E. O. Cohen, J. M. Conrad, M. Convery, L. Cooper-Troendle, J. I. Crespo-Anadón, M. Del Tutto, D. Devitt, L. Domine, K. Duffy, S. Dytman, B. Eberly, A. Ereditato, L. Escudero Sanchez, J. J. Evans, R. S. Fitzpatrick, B. T. Fleming, N. Foppiani, D. Franco, A. P. Furmanski, D. Garcia-Gamez, S. Gardiner, V. Genty, D. Goeldi, S. Gollapinni, O. Goodwin, E. Gramellini, P. Green, H. Greenlee, L. Gu, W. Gu, R. Guenette, P. Guzowski, P. Hamilton, O. Hen, C. Hill, G. A. Horton-Smith, A. Hourlier, E.-C. Huang, R. Itay, C. James, J. Jan de Vries, X. Ji, L. Jiang, J. H. Jo, R. A. Johnson, J. Joshi, Y.-J. Jwa, G. Karagiorgi, W. Ketchum, B. Kirby, M. Kirby, T. Kobilarcik, I. Kreslo, R. LaZur, I. Lepetic, Y. Li, A. Lister, B. R. Littlejohn, S. Lockwitz, D. Lorca, W. C. Louis, M. Luethi, B. Lundberg, X. Luo, A. Mar-

chionni, S. Marcocci, C. Mariani, J. Marshall, J. Martin-Albo, D. A. Martinez Caicedo, K. Mason, A. Mastbaum, N. McConkey, V. Meddage, T. Mettler, K. Miller, J. Mills, K. Mistry, A. Mogan, T. Mohayai, J. Moon, M. Mooney, C. D. Moore, J. Mousseau, R. Murrells, D. Naples, R. K. Neely, P. Nienaber, J. Nowak, O. Palamara, V. Pandey, V. Paolone, A. Papadopoulou, V. Papavassiliou, S. F. Pate, A. Paudel, Z. Pavlovic, E. Piasetzky, D. Porzio, S. Prince, G. Pulliam, X. Qian, J. L. Raaf, V. Radeka, A. Rafique, L. Ren, L. Rochester, H. E. Rogers, M. Ross-Lonergan, C. Rudolf von Rohr, B. Russell, G. Scanavini, D. W. Schmitz, A. Schukraft, W. Seligman, M. H. Shaevitz, R. Sharankova, J. Sinclair, A. Smith, E. L. Snider, M. Soderberg, S. Söldner-Rembold, S. R. Soleti, P. Spentzouris, J. Spitz, M. Stancari, J. St. John, T. Strauss, K. Sutton, S. Sword-Fehlberg, A. M. Szelc, N. Tagg, W. Tang, K. Terao, R. T. Thornton, M. Toups, Y.-T. Tsai, S. Tufanli, M. A. Uchida, T. Usher, W. Van De Pontseele, R. G. Van de Water, B. Viren, M. Weber, H. Wei, D. A. Wickremasinghe, Z. Williams, S. Wolbers, T. Wongjirad, K. Woodruff, M. Wospakrik, W. Wu, T. Yang, G. Yarbrough, L. E. Yates, G. P. Zeller, J. Zennamo, and C. Zhang. Search for heavy neutral leptons decaying into muon-pion pairs in the microboone detector. *Phys. Rev. D*, 101:052001, Mar 2020.

[151] Moritz Breitbach, Luca Buonocore, Claudia Frugiuele, Joachim Kopp, and Lukas Mittnacht. Searching for physics beyond the Standard Model in an off-axis DUNE near detector. *JHEP*, 01:048, 2022.

[152] Tommaso Boschi. Nushock: Bunch of tools to study sensitivity of heavy neutrinos. 2019. (2019) https://github.com/tboschi/NuShock,

repository cloned on September 15, 2020.

[153] Peter Ballett, Tommaso Boschi, and Silvia Pascoli. Heavy Neutral Leptons from low-scale seesaws at the DUNE Near Detector. *JHEP*, 03:111, 2020.

[154] Pilar Coloma, Pedro A. N. Machado, Ivan Martinez-Soler, and Ian M. Shoemaker. Double-Cascade Events from New Physics in Icecube. *Phys. Rev. Lett.*, 119(20):201804, 2017.

[155] Ryan Plestid. Luminous solar neutrinos I: Dipole portals. *Phys. Rev. D*, 104:075027, 2021.

[156] Ryan Plestid. Luminous solar neutrinos II: Mass-mixing portals. *Phys. Rev. D*, 104:075028, 2021. [Erratum: Phys.Rev.D 105, 099901 (2022), Erratum: Phys.Rev.D 105, 099901 (2022)].

[157] R. Andrew Gustafson, Ryan Plestid, and Ian M. Shoemaker. Neutrino portals, terrestrial upscattering, and atmospheric neutrinos. *Phys. Rev. D*, 106(9):095037, 2022.

[158] Thomas Schwetz, Albert Zhou, and Jing-Yu Zhu. Constraining active-sterile neutrino transition magnetic moments at DUNE near and far detectors. *JHEP*, 21:200, 2020.

[159] Guo-yuan Huang, Sudip Jana, Manfred Lindner, and Werner Rodejohann. Probing Heavy Sterile Neutrinos at Ultrahigh Energy Neutrino Telescopes via the Dipole Portal. 4 2022.

[160] Carlos Argüelles, Pilar Coloma, Pilar Hernández, and Víctor Muñoz. Searches for Atmospheric Long-Lived Particles. *JHEP*, 02:190, 2020.

[161] Pilar Coloma, Pilar Hernández, Víctor Muñoz, and Ian M. Shoemaker. New constraints on Heavy Neutral Leptons from Super-Kamiokande data. *Eur. Phys. J. C*, 80(3):235, 2020.

[162] Alexander Kusenko, Silvia Pascoli, and Dmitry Semikoz. New bounds on MeV sterile neutrinos based on the accelerator and Super-Kamiokande results. *JHEP*, 11:028, 2005.

[163] Takehiko Asaka and Atsushi Watanabe. Atmospheric Sterile Neutrinos. *JHEP*, 07:112, 2012.

[164] Manuel Masip. A sterile neutrino at MiniBooNE and IceCube. *AIP Conf. Proc.*, 1606(1):59–65, 2015.

[165] A. Aguilar-Arevalo et al. Search for heavy neutrinos in $\pi \to \mu\nu$ decay. *Phys. Lett. B*, 798:134980, 2019.

[166] Dinko Počanić et al. Experimental study of rare charged pion decays. *J. Phys. G*, 41(11):114002, 2014.

[167] J. P. Lees et al. Search for Heavy Neutral Leptons Using Tau Lepton Decays at BABAR. 7 2022.

[168] The ATLAS Collaboration. The atlas experiment at the cern large hadron collider. *Journal of Instrumentation*, 3(08):S08003, aug 2008.

[169] The CMS Collaboration. The cms experiment at the cern lhc. *Journal of Instrumentation*, 3(08):S08004, aug 2008.

[170] Armen Tumasyan et al. Search for long-lived heavy neutral leptons with displaced vertices in proton-proton collisions at $\sqrt{\mathrm{s}}$ =13 TeV. *JHEP*, 07:081, 2022.

[171] Georges Aad et al. Search for Heavy Neutral Leptons in Decays of W Bosons Using a Dilepton Displaced Vertex in s=13 TeV pp Collisions with the ATLAS Detector. *Phys. Rev. Lett.*, 131(6):061803, 2023.

[172] Armen Tumasyan et al. Probing Heavy Majorana Neutrinos and the Weinberg Operator through Vector Boson Fusion Processes in Proton-Proton Collisions at s=13 TeV. *Phys. Rev. Lett.*, 131(1):011803, 2023.

[173] Georges Aad et al. Search for type-III seesaw heavy leptons in leptonic final states in pp collisions at $\sqrt{s} = 13$ TeV with the ATLAS detector. *Eur. Phys. J. C*, 82(11):988, 2022.

[174] Search for Z′ bosons decaying to pairs of heavy Majorana neutrinos in proton-proton collisions at $\sqrt{s} = 13$ TeV. 2022.

[175] Albert M Sirunyan et al. Search for heavy neutral leptons in events with three charged leptons in proton-proton collisions at $\sqrt{s} = 13$ TeV. *Phys. Rev. Lett.*, 120(22):221801, 2018.

[176] Albert M Sirunyan et al. Search for heavy Majorana neutrinos in same-sign dilepton channels in proton-proton collisions at $\sqrt{s} = 13$ TeV. *JHEP*, 01:122, 2019.

[177] A. M. Cooper-Sarkar, S. J. Haywood, M. A. Parker, S. Sarkar, K. W. J. Barnham, P. Bostock, M. L. Faccini-Turluer, H. Grässler, J. Guy, P. O. Hulth, K. Hultqvist, U. Idschok, H. Klein, H. Kreutzmann, J. Krstic, M. M. Mobayyen, D. R. O. Morrison, B. Nellen, M. Talebzadeh, W. Venus, D. Vignaud, H. Wachsmuth, W. Wittek, and B. Wünsch. Search for heavy neutrino decays in the BEBC beam dump experiment. *Physics Letters B*, 160:207–211, 1985.

[178] Giacomo Marocco and Subir Sarkar. Blast from the past: Constraints on the dark sector from the BEBC WA66 beam dump experiment. *SciPost Phys.*, 10(2):043, 2021.

[179] H. Grassler et al. Prompt Neutrino Production in 400-GeV Proton Copper Interactions. *Nucl. Phys. B*, 273:253–274, 1986.

[180] P. Marage et al. OBSERVATION OF COHERENT DIFFRACTIVE CHARGED CURRENT INTERACTIONS OF ANTI-NEUTRINOS ON NEON NUCLEI. *Phys. Lett. B*, 140:137–141, 1984.

[181] Kyrylo Bondarenko, Alexey Boyarsky, Juraj Klaric, Oleksii Mikulenko, Oleg Ruchayskiy, Vsevolod Syvolap, and Inar Timiryasov. An allowed window for heavy neutral leptons below the kaon mass. *JHEP*, 07:193, 2021.

[182] Carlos A. Argüelles, Nicolò Foppiani, and Matheus Hostert. Heavy neutral leptons below the kaon mass at hodoscopic neutrino detectors. *Phys. Rev. D*, 105(9):095006, 2022.

[183] Martina Mongillo, Asli Abdullahi, Benjamin Banto Oberhauser, Paolo Crivelli, Matheus Hostert, Daniele Massaro, Laura Molina Bueno, and Silvia Pascoli. Constraining Light Thermal Inelastic Dark Matter with NA64. 2 2023.

[184] Masahiro Ibe, Shin Kobayashi, Yuhei Nakayama, and Satoshi Shirai. Cosmological constraints on dark scalar. *JHEP*, 03:198, 2022.

[185] R. S. Chivukula, Andrew G. Cohen, H. Georgi, and A. V. Manohar. Couplings of a Light Higgs Boson. *Phys. Lett. B*, 222:258–262, 1989.

[186] H. Leutwyler and Mikhail A. Shifman. GOLDSTONE BOSONS GENERATE PECULIAR CONFORMAL ANOMALIES. *Phys. Lett. B*, 221:384–388, 1989.

[187] H. Leutwyler and Mikhail A. Shifman. Light Higgs Particle in Decays of K and η Mesons. *Nucl. Phys. B*, 343:369–397, 1990.

[188] N. Ishizuka and M. Yoshimura. Axion and Dilaton Emissivity From Nascent Neutron Stars. *Prog. Theor. Phys.*, 84:233–250, 1990.

[189] Gordan Krnjaic. Probing Light Thermal Dark-Matter With a Higgs Portal Mediator. *Phys. Rev. D*, 94(7):073009, 2016.

[190] P. S. Bhupal Dev, Rabindra N. Mohapatra, and Yongchao Zhang. Revisiting supernova constraints on a light CP-even scalar. *JCAP*, 08:003, 2020. [Erratum: JCAP 11, E01 (2020)].

[191] James B. Dent, Francesc Ferrer, and Lawrence M. Krauss. Constraints on Light Hidden Sector Gauge Bosons from Supernova Cooling. 1 2012.

[192] M. Aaboud et al. Search for scalar resonances decaying into $\mu^+\mu^-$ in events with and without b-tagged jets produced in proton-proton collisions at $\sqrt{s} = 13$ TeV with the ATLAS detector. *JHEP*, 07:117, 2019.

[193] Adeela Afzal et al. The NANOGrav 15 yr Data Set: Search for Signals from New Physics. *Astrophys. J. Lett.*, 951(1):L11, 2023.

[194] Enrico Bertuzzo, Sudip Jana, Pedro A. N. Machado, and Renata Zukanovich Funchal. Dark Neutrino Portal to Explain MiniBooNE excess. *Phys. Rev. Lett.*, 121(24):241801, 2018.

[195] Peter Ballett, Tommaso Boschi, and Silvia Pascoli. Heavy Neutral Leptons from low-scale seesaws at the DUNE Near Detector. *Journal of High Energy Physics*, 2020, 3 2020.

[196] Asli Abdullahi, Matheus Hostert, and Silvia Pascoli. A dark seesaw solution to low energy anomalies: MiniBooNE, the muon (g−2), and BaBar. *Phys. Lett. B*, 820:136531, 2021.

[197] Vedran Brdar and Joachim Kopp. Can standard model and experimental uncertainties resolve the MiniBooNE anomaly? *Phys. Rev. D*, 105(11):115024, 2022.

[198] Kevin J. Kelly and Joachim Kopp. More ingredients for an Altarelli cocktail at MiniBooNE. *JHEP*, 05:113, 2023.

[199] et al. Keshavarzi, Alexander. Muon g 2 and connection. *Phys. Rev. D*, 102(3):033002, 2020.

[200] Pierre Fayet. U-boson production in e+ e annihilations, and decays, and Light Dark Matter. *Phys. Rev. D*, 75(11):115017, 2007.

[201] Maxim Pospelov. Secluded U (1) below the weak scale. *Phys. Rev. D*, 80(9):095002, 2009.

[202] Gopolang Mohlabeng. Revisiting the dark photon explanation of the muon anomalous magnetic moment. *Phys. Rev. D*, 99(11):115001, 2019.

[203] A. Aguilar et al. Evidence for neutrino oscillations from the observation of $\bar{\nu}_e$ appearance in a $\bar{\nu}_\mu$ beam. *Phys. Rev. D*, 64:112007, 2001.

[204] P. Anselmann et al. First results from the Cr-51 neutrino source experiment with the GALLEX detector. *Phys. Lett. B*, 342:440–450, 1995.

[205] W. Hampel et al. Final results of the Cr-51 neutrino source experiments in GALLEX. *Phys. Lett. B*, 420:114–126, 1998.

[206] F. Kaether, W. Hampel, G. Heusser, J. Kiko, and T. Kirsten. Reanalysis of the GALLEX solar neutrino flux and source experiments. *Phys. Lett. B*, 685:47–54, 2010.

[207] Dzh. N. Abdurashitov et al. The Russian-American gallium experiment (SAGE) Cr neutrino source measurement. *Phys. Rev. Lett.*, 77:4708–4711, 1996.

[208] J. N. Abdurashitov et al. Measurement of the response of the Russian-American gallium experiment to neutrinos from a Cr-51 source. *Phys. Rev. C*, 59:2246–2263, 1999.

[209] J. N. Abdurashitov et al. Measurement of the response of a Ga solar neutrino experiment to neutrinos from an Ar-37 source. *Phys. Rev. C*, 73:045805, 2006.

[210] J. N. Abdurashitov et al. Measurement of the solar neutrino capture rate with gallium metal. III: Results for the 2002–2007 data-taking period. *Phys. Rev. C*, 80:015807, 2009.

[211] Jan Hamann, Steen Hannestad, Georg G. Raffelt, and Yvonne Y. Y. Wong. Sterile neutrinos with eV masses in cosmology: How disfavoured exactly? *JCAP*, 09:034, 2011.

[212] Maria Archidiacono, Nicolao Fornengo, Carlo Giunti, Steen Hannestad, and Alessandro Melchiorri. Sterile neutrinos: Cosmology versus short-baseline experiments. *Phys. Rev. D*, 87(12):125034, 2013.

[213] Steffen Hagstotz, Pablo F. de Salas, Stefano Gariazzo, Martina Gerbino, Massimiliano Lattanzi, Sunny Vagnozzi, Katherine Freese, and Sergio Pastor. Bounds on light sterile neutrino mass and mixing from cosmology and laboratory searches. *Phys. Rev. D*, 104(12):123524, 2021.

[214] P. Adamson et al. Improved Constraints on Sterile Neutrino Mixing from Disappearance Searches in the MINOS, MINOS+, Daya Bay, and Bugey-3 Experiments. *Phys. Rev. Lett.*, 125(7):071801, 2020.

[215] M. G. Aartsen et al. eV-Scale Sterile Neutrino Search Using Eight Years of Atmospheric Muon Neutrino Data from the IceCube Neutrino Observatory. *Phys. Rev. Lett.*, 125(14):141801, 2020.

[216] M. G. Aartsen et al. Searching for eV-scale sterile neutrinos with eight years of atmospheric neutrinos at the IceCube Neutrino Telescope. *Phys. Rev. D*, 102(5):052009, 2020.

[217] Mona Dentler, Álvaro Hernández-Cabezudo, Joachim Kopp, Pedro A. N. Machado, Michele Maltoni, Ivan Martinez-Soler, and Thomas Schwetz. Updated Global Analysis of Neutrino Oscillations in the Presence of eV-Scale Sterile Neutrinos. *JHEP*, 08:010, 2018.

[218] A. Diaz, C. A. Argüelles, G. H. Collin, J. M. Conrad, and M. H. Shaevitz. Where Are We With Light Sterile Neutrinos? *Phys. Rept.*, 884:1–59, 2020.

[219] M. A. Acero et al. White Paper on Light Sterile Neutrino Searches and Related Phenomenology. 3 2022.

[220] R. Acciarri et al. A Proposal for a Three Detector Short-Baseline

Neutrino Oscillation Program in the Fermilab Booster Neutrino Beam. 3 2015.

[221] Pedro AN Machado, Ornella Palamara, and David W Schmitz. The Short-Baseline Neutrino Program at Fermilab. *Ann. Rev. Nucl. Part. Sci.*, 69:363–387, 2019.

[222] P. Abratenko et al. Search for an Excess of Electron Neutrino Interactions in MicroBooNE Using Multiple Final-State Topologies. *Phys. Rev. Lett.*, 128(24):241801, 2022.

[223] P. Abratenko et al. Search for an anomalous excess of charged-current quasielastic νe interactions with the MicroBooNE experiment using Deep-Learning-based reconstruction. *Phys. Rev. D*, 105(11):112003, 2022.

[224] P. Abratenko et al. Search for an anomalous excess of charged-current νe interactions without pions in the final state with the MicroBooNE experiment. *Phys. Rev. D*, 105(11):112004, 2022.

[225] P. Abratenko et al. Search for an anomalous excess of inclusive charged-current ν_e interactions in the MicroBooNE experiment using Wire-Cell reconstruction. *Phys. Rev. D*, 105(11):112005, 2022.

[226] C. A. Argüelles, I. Esteban, M. Hostert, Kevin J. Kelly, J. Kopp, P. A. N. Machado, I. Martinez-Soler, and Y. F. Perez-Gonzalez. MicroBooNE and the νe Interpretation of the MiniBooNE Low-Energy Excess. *Phys. Rev. Lett.*, 128(24):241802, 2022.

[227] P. Abratenko et al. First Constraints on Light Sterile Neutrino Oscillations from Combined Appearance and Disappearance Searches with the MicroBooNE Detector. *Phys. Rev. Lett.*, 130(1):011801, 2023.

[228] Peter B. Denton. Sterile Neutrino Search with MicroBooNE's Electron Neutrino Disappearance Data. *Phys. Rev. Lett.*, 129(6):061801, 2022.

[229] P. Abratenko et al. Search for Neutrino-Induced Neutral-Current Δ Radiative Decay in MicroBooNE and a First Test of the MiniBooNE Low Energy Excess under a Single-Photon Hypothesis. *Phys. Rev. Lett.*, 128:111801, 2022.

[230] Peter Ballett, Silvia Pascoli, and Mark Ross-Lonergan. U(1)' mediated decays of heavy sterile neutrinos in MiniBooNE. *Phys. Rev. D*, 99:071701, 2019.

[231] Bhaskar Dutta, Sumit Ghosh, and Tianjun Li. Explaining $(g-2)_{\mu,e}$, the KOTO anomaly and the MiniBooNE excess in an extended Higgs model with sterile neutrinos. *Phys. Rev. D*, 102(5):055017, 2020.

[232] Alakabha Datta, Saeed Kamali, and Danny Marfatia. Dark sector origin of the KOTO and MiniBooNE anomalies. *Phys. Lett. B*, 807:135579, 2020.

[233] Waleed Abdallah, Raj Gandhi, and Samiran Roy. Understanding the MiniBooNE and the muon and electron $g2$ anomalies with a light Z and a second Higgs doublet. *JHEP*, 12:188, 2020.

[234] A. Hammad, Ahmed Rashed, and S. Moretti. The dark Z' and sterile neutrinos behind current anomalies. *Phys. Lett. B*, 827:136945, 2022.

[235] Waleed Abdallah, Raj Gandhi, and Samiran Roy. Requirements on common solutions to the LSND and MiniBooNE excesses: a post-MicroBooNE study. *JHEP*, 06:160, 2022.

[236] Asli M. Abdullahi, Jaime Hoefken Zink, Matheus Hostert, Daniele Massaro, and Silvia Pascoli. DarkNews: a Python-based event generator for heavy neutral lepton production in neutrino-nucleus scattering. 7 2022.

[237] G. Cheng et al. Measurement of K^+ production cross section by 8 GeV protons using high energy neutrino interactions in the SciBooNE detector. *Phys. Rev. D*, 84:012009, 2011.

[238] K. B. M. Mahn et al. Dual baseline search for muon neutrino disappearance at $0.5\text{eV}^2 < \Delta m^2 < 40\text{eV}^2$. *Phys. Rev. D*, 85:032007, 2012.

[239] E. Wang, L. Alvarez-Ruso, and J. Nieves. Single photon events from neutral current interactions at MiniBooNE. *Phys. Lett. B*, 740:16–22, 2015.

[240] Johnathon R. Jordan, Yonatan Kahn, Gordan Krnjaic, Matthew Moschella, and Joshua Spitz. Severe Constraints on New Physics Explanations of the MiniBooNE Excess. *Phys. Rev. Lett.*, 122(8):081801, 2019.

[241] Sebastian Böser, Christian Buck, Carlo Giunti, Julien Lesgourgues, Livia Ludhova, Susanne Mertens, Anne Schukraft, and Michael Wurm. Status of Light Sterile Neutrino Searches. *Prog. Part. Nucl. Phys.*, 111:103736, 2020.

[242] Basudeb Dasgupta and Joachim Kopp. Sterile Neutrinos. *Phys. Rept.*, 928:1–63, 2021.

[243] Zander Moss, Marjon H. Moulai, Carlos A. Argüelles, and Janet M. Conrad. Exploring a nonminimal sterile neutrino model involving decay at IceCube. *Phys. Rev. D*, 97(5):055017, 2018.

[244] M. H. Moulai, C. A. Argüelles, G. H. Collin, J. M. Conrad, A. Diaz, and M. H. Shaevitz. Combining Sterile Neutrino Fits to Short Baseline Data with IceCube Data. *Phys. Rev. D*, 101(5):055020, 2020.

[245] E. Kh. Akhmedov and T. Schwetz. New MiniBooNE results and non-standard neutrino interactions. *Nucl. Phys. B Proc. Suppl.*, 217:217–219, 2011.

[246] Joseph Bramante. Sterile Neutrino Production Through a Matter Effect Enhancement at Long Baselines. *Int. J. Mod. Phys. A*, 28:1350067, 2013.

[247] G. Karagiorgi, M. H. Shaevitz, and J. M. Conrad. Confronting the Short-Baseline Oscillation Anomalies with a Single Sterile Neutrino and Non-Standard Matter Effects. 2 2012.

[248] J. Asaadi, E. Church, R. Guenette, B. J. P. Jones, and A. M. Szelc. New light Higgs boson and short-baseline neutrino anomalies. *Phys. Rev. D*, 97(7):075021, 2018.

[249] Alexei Y. Smirnov and Victor B. Valera. Resonance refraction and neutrino oscillations. *JHEP*, 09:177, 2021.

[250] Daniele S. M. Alves, William C. Louis, and Patrick G. deNiverville. Quasi-sterile neutrinos from dark sectors. Part I. BSM matter effects in neutrino oscillations and the short-baseline anomalies. *JHEP*, 08:034, 2022.

[251] Jeffrey M. Berryman, André De Gouvêa, Kevin J. Kelly, and Yue Zhang. Lepton-Number-Charged Scalars and Neutrino Beamstrahlung. *Phys. Rev. D*, 97(7):075030, 2018.

[252] Sergio Palomares-Ruiz, Silvia Pascoli, and Thomas Schwetz. Explaining LSND by a decaying sterile neutrino. *JHEP*, 09:048, 2005.

[253] Yang Bai, Ran Lu, Sida Lu, Jordi Salvado, and Ben A. Stefanek. Three Twin Neutrinos: Evidence from LSND and MiniBooNE. *Phys. Rev. D*, 93(7):073004, 2016.

[254] André de Gouvêa, O. L. G. Peres, Suprabh Prakash, and G. V. Stenico. On The Decaying-Sterile Neutrino Solution to the Electron (Anti)Neutrino Appearance Anomalies. *JHEP*, 07:141, 2020.

[255] Mona Dentler, Ivan Esteban, Joachim Kopp, and Pedro Machado. Decaying Sterile Neutrinos and the Short Baseline Oscillation Anomalies. *Phys. Rev. D*, 101(11):115013, 2020.

[256] Matheus Hostert and Maxim Pospelov. Constraints on decaying sterile neutrinos from solar antineutrinos. *Phys. Rev. D*, 104(5):055031, 2021.

[257] Oliver Fischer, Álvaro Hernández-Cabezudo, and Thomas Schwetz. Explaining the MiniBooNE excess by a decaying sterile neutrino with mass in the 250 MeV range. *Phys. Rev. D*, 101(7):075045, 2020.

[258] Chia-Hung Vincent Chang, Chuan-Ren Chen, Shu-Yu Ho, and Shih-Yen Tseng. Explaining the MiniBooNE anomalous excess via a leptophilic ALP-sterile neutrino coupling. *Phys. Rev. D*, 104(1):015030, 2021.

[259] Waleed Abdallah, Raj Gandhi, and Samiran Roy. Two-Higgs doublet solution to the LSND, MiniBooNE and muon g-2 anomalies. *Phys. Rev. D*, 104(5):055028, 2021.

[260] S. N. Gninenko. The MiniBooNE anomaly and heavy neutrino decay. *Phys. Rev. Lett.*, 103:241802, 2009.

[261] Sergei N. Gninenko. A resolution of puzzles from the LSND, KARMEN, and MiniBooNE experiments. *Phys. Rev. D*, 83:015015, 2011.

[262] S. N. Gninenko. New limits on radiative sterile neutrino decays from a search for single photons in neutrino interactions. *Phys. Lett. B*, 710:86–90, 2012.

[263] Manuel Masip, Pere Masjuan, and Davide Meloni. Heavy neutrino decays at MiniBooNE. *JHEP*, 01:106, 2013.

[264] Alexander Radionov. Constraints on electromagnetic properties of sterile neutrinos from MiniBooNE results. *Phys. Rev. D*, 88(1):015016, 2013.

[265] Gabriel Magill, Ryan Plestid, Maxim Pospelov, and Yu-Dai Tsai. Dipole Portal to Heavy Neutral Leptons. *Phys. Rev. D*, 98(11):115015, 2018.

[266] Stefano Vergani, Nicholas W. Kamp, Alejandro Diaz, Carlos A. Argüelles, Janet M. Conrad, Michael H. Shaevitz, and Melissa A. Uchida. Explaining the MiniBooNE excess through a mixed model of neutrino oscillation and decay. *Phys. Rev. D*, 104(9):095005, 2021.

[267] Luis Alvarez-Ruso and Eduardo Saul-Sala. Neutrino interactions with matter and the MiniBooNE anomaly. *Eur. Phys. J. ST*, 230(24):4373–4389, 2021.

[268] Nicholas W. Kamp, Matheus Hostert, Austin Schneider, Stefano Vergani, Carlos A. Argüelles, Janet M. Conrad, Michael H. Shaevitz, and

Melissa A. Uchida. Dipole-coupled heavy-neutral-lepton explanations of the MiniBooNE excess including constraints from MINERvA data. *Phys. Rev. D*, 107(5):055009, 2023.

[269] Saurabh Bansal, Gil Paz, Alexey Petrov, Michele Tammaro, and Jure Zupan. Enhanced neutrino polarizability. *JHEP*, 05:142, 2023.

[270] Bhaskar Dutta, Doojin Kim, Adrian Thompson, Remington T. Thornton, and Richard G. Van de Water. Solutions to the MiniBooNE Anomaly from New Physics in Charged Meson Decays. *Phys. Rev. Lett.*, 129(11):111803, 2022.

[271] P. Abratenko et al. First Constraints on Light Sterile Neutrino Oscillations from Combined Appearance and Disappearance Searches with the MicroBooNE Detector. *Phys. Rev. Lett.*, 130(1):011801, 2023.

[272] Nicholas W. Kamp, Matheus Hostert, Carlos A. Argüelles, Janet M. Conrad, and Michael H. Shaevitz. Implications of MicroBooNE's low sensitivity to electron antineutrino interactions in the search for the MiniBooNE excess. *Phys. Rev. D*, 107(9):092002, 2023.

[273] P. Abratenko et al. Differential cross section measurement of charged current νe interactions without final-state pions in MicroBooNE. *Phys. Rev. D*, 106(5):L051102, 2022.

[274] P. Abratenko et al. Measurement of the flux-averaged inclusive charged-current electron neutrino and antineutrino cross section on argon using the NuMI beam and the MicroBooNE detector. *Phys. Rev. D*, 104(5):052002, 2021.

[275] P. Abratenko et al. First measurement of inclusive electron-neutrino and antineutrino charged current differential cross sections in charged

lepton energy on argon in MicroBooNE. *Phys. Rev. D*, 105(5):L051102, 2022.

[276] G. Mention, M. Fechner, Th. Lasserre, Th. A. Mueller, D. Lhuillier, M. Cribier, and A. Letourneau. The Reactor Antineutrino Anomaly. *Phys. Rev. D*, 83:073006, 2011.

[277] Th. A. Mueller et al. Improved Predictions of Reactor Antineutrino Spectra. *Phys. Rev. C*, 83:054615, 2011.

[278] Patrick Huber. On the determination of anti-neutrino spectra from nuclear reactors. *Phys. Rev. C*, 84:024617, 2011. [Erratum: Phys.Rev.C 85, 029901 (2012)].

[279] C. Giunti, Y. F. Li, C. A. Ternes, and Z. Xin. Reactor antineutrino anomaly in light of recent flux model refinements. *Phys. Lett. B*, 829:137054, 2022.

[280] V. Kopeikin, M. Skorokhvatov, and O. Titov. Reevaluating reactor antineutrino spectra with new measurements of the ratio between U235 and Pu239 β spectra. *Phys. Rev. D*, 104(7):L071301, 2021.

[281] K. Schreckenbach, H. R. Faust, F. von Feilitzsch, A. A. Hahn, K. Hawerkamp, and J. L. Vuilleumier. Absolute measurement of the beta spectrum from 235 U fission as a basis for reactor antineutrino experiments. *Phys. Lett. B*, 99:251–256, 1981.

[282] F. Von Feilitzsch, A. A. Hahn, and K. Schreckenbach. EXPERIMENTAL BETA SPECTRA FROM PU-239 AND U-235 THERMAL NEUTRON FISSION PRODUCTS AND THEIR CORRELATED ANTINEUTRINOS SPECTRA. *Phys. Lett. B*, 118:162–166, 1982.

[283] K. Schreckenbach, G. Colvin, W. Gelletly, and F. Von Feilitzsch. DETERMINATION OF THE ANTI-NEUTRINO SPECTRUM FROM U-235 THERMAL NEUTRON FISSION PRODUCTS UP TO 9.5-MEV. *Phys. Lett. B*, 160:325–330, 1985.

[284] A. A. Hahn, K. Schreckenbach, G. Colvin, B. Krusche, W. Gelletly, and F. Von Feilitzsch. Anti-neutrino Spectra From $^{2}41Puand^{239}$Pu Thermal Neutron Fission Products. *Phys. Lett. B*, 218:365–368, 1989.

[285] C. Augier et al. Fast neutron background characterization of the future Ricochet experiment at the ILL research nuclear reactor. *Eur. Phys. J. C*, 83(1):20, 2023.

[286] H. Almazán et al. STEREO neutrino spectrum of ^{235}U fission rejects sterile neutrino hypothesis. *Nature*, 613(7943):257–261, 2023.

[287] J. Ashenfelter et al. First search for short-baseline neutrino oscillations at HFIR with PROSPECT. *Phys. Rev. Lett.*, 121(25):251802, 2018.

[288] M. Andriamirado et al. Improved short-baseline neutrino oscillation search and energy spectrum measurement with the PROSPECT experiment at HFIR. *Phys. Rev. D*, 103(3):032001, 2021.

[289] H. Almazán et al. Sterile Neutrino Constraints from the STEREO Experiment with 66 Days of Reactor-On Data. *Phys. Rev. Lett.*, 121(16):161801, 2018.

[290] H. Almazán et al. Improved sterile neutrino constraints from the STEREO experiment with 179 days of reactor-on data. *Phys. Rev. D*, 102(5):052002, 2020.

[291] I Alekseev et al. Search for sterile neutrinos at the DANSS experiment. *Phys. Lett. B*, 787:56–63, 2018.

[292] Z. Atif et al. Search for sterile neutrino oscillations using RENO and NEOS data. *Phys. Rev. D*, 105(11):L111101, 2022.

[293] A. P. Serebrov et al. First Observation of the Oscillation Effect in the Neutrino-4 Experiment on the Search for the Sterile Neutrino. *Pisma Zh. Eksp. Teor. Fiz.*, 109(4):209–218, 2019.

[294] M. Andriamirado et al. Note on arXiv:2005.05301, 'Preparation of the Neutrino-4 experiment on search for sterile neutrino and the obtained results of measurements'. 6 2020.

[295] C. Giunti, Y. F. Li, C. A. Ternes, and Y. Y. Zhang. Neutrino-4 anomaly: oscillations or fluctuations? *Phys. Lett. B*, 816:136214, 2021.

[296] Mario A. Acero, Carlo Giunti, and Marco Laveder. Limits on nu(e) and anti-nu(e) disappearance from Gallium and reactor experiments. *Phys. Rev. D*, 78:073009, 2008.

[297] Carlo Giunti and Marco Laveder. Statistical Significance of the Gallium Anomaly. *Phys. Rev. C*, 83:065504, 2011.

[298] V. V. Barinov et al. Results from the Baksan Experiment on Sterile Transitions (BEST). *Phys. Rev. Lett.*, 128(23):232501, 2022.

[299] Kim Goldhagen, Michele Maltoni, Shayne E. Reichard, and Thomas Schwetz. Testing sterile neutrino mixing with present and future solar neutrino data. *Eur. Phys. J. C*, 82(2):116, 2022.

[300] C. Giunti, Y. F. Li, C. A. Ternes, O. Tyagi, and Z. Xin. Gallium Anomaly: critical view from the global picture of ν_e and $\overline{\nu}_e$ disappearance. *JHEP*, 10:164, 2022.

[301] C. Giunti, Y. F. Li, C. A. Ternes, and Z. Xin. Inspection of the detection cross section dependence of the Gallium Anomaly. *Phys. Lett. B*, 842:137983, 2023.

[302] Vedran Brdar, Julia Gehrlein, and Joachim Kopp. Towards resolving the gallium anomaly. *JHEP*, 05:143, 2023.

[303] Jeffrey M. Berryman, Pilar Coloma, Patrick Huber, Thomas Schwetz, and Albert Zhou. Statistical significance of the sterile-neutrino hypothesis in the context of reactor and gallium data. *JHEP*, 02:055, 2022.

[304] F. Dydak et al. A Search for Muon-neutrino Oscillations in the Delta m**2 Range 0.3-eV**2 to 90-eV**2. *Phys. Lett. B*, 134:281, 1984.

[305] W. C. Louis. Problems With the MINOS/MINOS+ Sterile Neutrino ν_μ Result. 3 2018.

[306] E. Eskut et al. Final results on nu(mu) —> nu(tau) oscillation from the CHORUS experiment. *Nucl. Phys. B*, 793:326–343, 2008.

[307] N. Agafonova et al. Limits on muon-neutrino to tau-neutrino oscillations induced by a sterile neutrino state obtained by OPERA at the CNGS beam. *JHEP*, 06:069, 2015.

[308] Benjamin R. Smithers, Benjamin J. P. Jones, Carlos A. Argüelles, Janet M. Conrad, and Alejandro Diaz. Cascade appearance signatures of sterile neutrinos at 1–100 TeV. *Phys. Rev. D*, 105(5):052001, 2022.

[309] S. Aiello et al. Sensitivity to light sterile neutrino mixing parameters with KM3NeT/ORCA. *JHEP*, 10:180, 2021.

[310] P. Adamson et al. Search for active-sterile neutrino mixing using neutral-current interactions in NOvA. *Phys. Rev. D*, 96(7):072006, 2017.

[311] M. A. Acero et al. Search for Active-Sterile Antineutrino Mixing Using Neutral-Current Interactions with the NOvA Experiment. *Phys. Rev. Lett.*, 127(20):201801, 2021.

[312] Andrew P. Furmanski and Christopher Hilgenberg. Neutrino energy estimation in neutral current interactions and prospects for sterile neutrino searches. *Phys. Rev. D*, 103(11):112011, 2021.

[313] M. Aker et al. Improved eV-scale sterile-neutrino constraints from the second KATRIN measurement campaign. *Phys. Rev. D*, 105(7):072004, 2022.

[314] Matthew Adams, Fedor Bezrukov, Jack Elvin-Poole, Justin J. Evans, Pawel Guzowski, Brían Ó. Fearraigh, and Stefan Söldner-Rembold. Direct comparison of sterile neutrino constraints from cosmological data, ν_e disappearance data and $\nu_\mu \to \nu_e$ appearance data in a $3+1$ model. *Eur. Phys. J. C*, 80(8):758, 2020.

[315] Basudeb Dasgupta and Joachim Kopp. Cosmologically Safe eV-Scale Sterile Neutrinos and Improved Dark Matter Structure. *Phys. Rev. Lett.*, 112(3):031803, 2014.

[316] Steen Hannestad, Rasmus Sloth Hansen, and Thomas Tram. How Self-Interactions can Reconcile Sterile Neutrinos with Cosmology. *Phys. Rev. Lett.*, 112(3):031802, 2014.

[317] Xiaoyong Chu, Basudeb Dasgupta, Mona Dentler, Joachim Kopp, and Ninetta Saviano. Sterile neutrinos with secret interactions—cosmological discord? *JCAP*, 11:049, 2018.

[318] Carlos E. Yaguna. Sterile neutrino production in models with low reheating temperatures. *JHEP*, 06:002, 2007.

[319] Ninetta Saviano, Alessandro Mirizzi, Ofelia Pisanti, Pasquale Dario Serpico, Gianpiero Mangano, and Gennaro Miele. Multi-momentum and multi-flavour active-sterile neutrino oscillations in the early universe: role of neutrino asymmetries and effects on nucleosynthesis. *Phys. Rev. D*, 87:073006, 2013.

[320] Massimo Giovannini, Hannu Kurki-Suonio, and Elina Sihvola. Big bang nucleosynthesis, matter antimatter regions, extra relativistic species, and relic gravitational waves. *Phys. Rev. D*, 66:043504, 2002.

[321] F. Bezrukov, A. Chudaykin, and D. Gorbunov. Hiding an elephant: heavy sterile neutrino with large mixing angle does not contradict cosmology. *JCAP*, 06:051, 2017.

[322] Yasaman Farzan. Ultra-light scalar saving the 3 + 1 neutrino scheme from the cosmological bounds. *Phys. Lett. B*, 797:134911, 2019.

[323] James M. Cline. Viable secret neutrino interactions with ultralight dark matter. *Phys. Lett. B*, 802:135182, 2020.

[324] Maria Archidiacono, Stefano Gariazzo, Carlo Giunti, Steen Hannestad, and Thomas Tram. Sterile neutrino self-interactions: H_0 tension and short-baseline anomalies. *JCAP*, 12:029, 2020.

[325] Eleonora Di Valentino, Stefano Gariazzo, Carlo Giunti, Olga Mena, Supriya Pan, and Weiqiang Yang. Minimal dark energy: Key to sterile neutrino and Hubble constant tensions? *Phys. Rev. D*, 105(10):103511, 2022.

[326] Graciela Gelmini, Sergio Palomares-Ruiz, and Silvia Pascoli. Low reheating temperature and the visible sterile neutrino. *Phys. Rev. Lett.*, 93:081302, 2004.

[327] C. Giunti and E. M. Zavanin. Appearance–disappearance relation in $3 + N_s$ short-baseline neutrino oscillations. *Mod. Phys. Lett. A*, 31(01):1650003, 2015.

[328] Carlo Giunti and Marco Laveder. 3+1 and 3+2 Sterile Neutrino Fits. *Phys. Rev. D*, 84:073008, 2011.

[329] J. M. Conrad, C. M. Ignarra, G. Karagiorgi, M. H. Shaevitz, and J. Spitz. Sterile Neutrino Fits to Short Baseline Neutrino Oscillation Measurements. *Adv. High Energy Phys.*, 2013:163897, 2013.

[330] Joachim Kopp, Pedro A. N. Machado, Michele Maltoni, and Thomas Schwetz. Sterile Neutrino Oscillations: The Global Picture. *JHEP*, 05:050, 2013.

[331] C. Giunti, M. Laveder, Y. F. Li, and H. W. Long. Pragmatic View of Short-Baseline Neutrino Oscillations. *Phys. Rev. D*, 88:073008, 2013.

[332] Davio Cianci, Andy Furmanski, Georgia Karagiorgi, and Mark Ross-Lonergan. Prospects of Light Sterile Neutrino Oscillation and CP Violation Searches at the Fermilab Short Baseline Neutrino Facility. *Phys. Rev. D*, 96(5):055001, 2017.

[333] *Neutrino Non-Standard Interactions: A Status Report*, volume 2, 2019.

[334] Evgeny Akhmedov and Thomas Schwetz. MiniBooNE and LSND data: Non-standard neutrino interactions in a (3+1) scheme versus (3+2) oscillations. *JHEP*, 10:115, 2010.

[335] Zhuojun Hu. Improved Limits on Sterile Neutrino Mixing from a Joint Search of the MINOS, MINOS+, Daya Bay, and Bugey-3 Experiments. *PoS*, ICHEP2020:201, 2021.

[336] Austin Schneider, Barbara Skrzypek, Carlos A. Argüelles, and Janet M. Conrad. Closing the neutrino BSM gap: Physics potential of atmospheric through-going muons at DUNE. *Phys. Rev. D*, 104(9):092015, 2021.

[337] Arman Esmaili and Hiroshi Nunokawa. On the robustness of IceCube's bound on sterile neutrinos in the presence of non-standard interactions. *Eur. Phys. J. C*, 79(1):70, 2019.

[338] Jiajun Liao and Danny Marfatia. Impact of nonstandard interactions on sterile neutrino searches at IceCube. *Phys. Rev. Lett.*, 117(7):071802, 2016.

[339] Jiajun Liao, Danny Marfatia, and Kerry Whisnant. MiniBooNE, MINOS+ and IceCube data imply a baroque neutrino sector. *Phys. Rev. D*, 99(1):015016, 2019.

[340] Peter B. Denton, Yasaman Farzan, and Ian M. Shoemaker. Activating the fourth neutrino of the 3+1 scheme. *Phys. Rev. D*, 99(3):035003, 2019.

[341] Marjon H. Moulai. *Light, Unstable Sterile Neutrinos: Phenomenology, a Search in the IceCube Experiment, and a Global Picture*. PhD thesis, MIT, 2021.

[342] R. Abbasi et al. Search for Unstable Sterile Neutrinos with the IceCube Neutrino Observatory. *Phys. Rev. Lett.*, 129(15):151801, 2022.

[343] J. M. Hardin, I. Martinez-Soler, A. Diaz, M. Jin, N. W. Kamp, C. A. Argüelles, J. M. Conrad, and M. H. Shaevitz. New Clues About Light Sterile Neutrinos: Preference for Models with Damping Effects in Global Fits. 11 2022.

[344] Carlos A. Argüelles, Toni Bertólez-Martínez, and Jordi Salvado. Impact of wave packet separation in low-energy sterile neutrino searches. *Phys. Rev. D*, 107(3):036004, 2023.

[345] Evgeny Akhmedov and Alexei Y. Smirnov. Damping of neutrino oscillations, decoherence and the lengths of neutrino wave packets. *JHEP*, 11:082, 2022.

[346] B. J. P. Jones, E. Marzec, and J. Spitz. Width of a beta-decay-induced antineutrino wave packet. *Phys. Rev. D*, 107(1):013008, 2023.

[347] B. J. P. Jones. Comment on "Damping of neutrino oscillations, decoherence and the lengths of neutrino wave packets". 9 2022.

[348] Evgeny Akhmedov and Alexei Y. Smirnov. Reply to "Comment on "Damping of neutrino oscillations, decoherence and the lengths of neutrino wave packets"". 10 2022.

[349] Thomas Schwetz. LSND versus MiniBooNE: Sterile neutrinos with energy dependent masses and mixing? *JHEP*, 02:011, 2008.

[350] K. S. Babu, Vedran Brdar, André de Gouvêa, and Pedro A. N. Machado. Addressing the short-baseline neutrino anomalies with energy-dependent mixing parameters. *Phys. Rev. D*, 107(1):015017, 2023.

[351] Heinrich Pas, Sandip Pakvasa, and Thomas J. Weiler. Sterile-active neutrino oscillations and shortcuts in the extra dimension. *Phys. Rev. D*, 72:095017, 2005.

[352] Sebastian Hollenberg, Octavian Micu, Heinrich Pas, and Thomas J. Weiler. Baseline-dependent neutrino oscillations with extra-dimensional shortcuts. *Phys. Rev. D*, 80:093005, 2009.

[353] Marcela Carena, Ying-Ying Li, Camila S. Machado, Pedro A. N. Machado, and Carlos E. M. Wagner. Neutrinos in Large Extra Dimensions and Short-Baseline ν_e Appearance. *Phys. Rev. D*, 96(9):095014, 2017.

[354] Dominik Döring and Heinrich Päs. Sterile Neutrino Shortcuts in Asymmetrically Warped Extra Dimensions. *Eur. Phys. J. C*, 79(7):604, 2019.

[355] Dominik Döring, Heinrich Päs, Philipp Sicking, and Thomas J. Weiler. Sterile neutrinos with altered dispersion relations as an explanation for neutrino anomalies. *Eur. Phys. J. C*, 80(12):1202, 2020.

[356] V. Alan Kostelecky and Matthew Mewes. Lorentz violation and short-baseline neutrino experiments. *Phys. Rev. D*, 70:076002, 2004.

[357] Jorge S. Diaz and V. Alan Kostelecky. Three-parameter Lorentz-violating texture for neutrino mixing. *Phys. Lett. B*, 700:25–28, 2011.

[358] Jorge S. Diaz and Alan Kostelecky. Lorentz- and CPT-violating models for neutrino oscillations. *Phys. Rev. D*, 85:016013, 2012.

[359] Gabriela A Barenboim, Pablo Martínez-Miravé, Christoph Andreas Ternes, and Maria Amparo Tórtola. Sterile neutrinos with altered dispersion relations revisited. *JHEP*, 03:070, 2020.

[360] Ian M. Shoemaker and Jason Wyenberg. Direct Detection Experiments at the Neutrino Dipole Portal Frontier. *Phys. Rev. D*, 99(7):075010, 2019.

[361] Arnab Dasgupta, Sin Kyu Kang, and Jihn E. Kim. Probing neutrino dipole portal at COHERENT experiment. *JHEP*, 11:120, 2021.

[362] Patrick D. Bolton, Frank F. Deppisch, Kåre Fridell, Julia Harz, Chandan Hati, and Suchita Kulkarni. Probing active-sterile neutrino transition magnetic moments with photon emission from CEνNS. *Phys. Rev. D*, 106(3):035036, 2022.

[363] Mack Atkinson, Pilar Coloma, Ivan Martinez-Soler, Noemi Rocco, and Ian M. Shoemaker. Heavy Neutrino Searches through Double-Bang Events at Super-Kamiokande, DUNE, and Hyper-Kamiokande. *JHEP*, 04:174, 2022.

[364] Guo-yuan Huang, Sudip Jana, Manfred Lindner, and Werner Rodejohann. Probing new physics at future tau neutrino telescopes. *JCAP*, 02(02):038, 2022.

[365] Ahmed Ismail, Sudip Jana, and Roshan Mammen Abraham. Neutrino up-scattering via the dipole portal at forward LHC detectors. *Phys. Rev. D*, 105(5):055008, 2022.

[366] Vedran Brdar, Admir Greljo, Joachim Kopp, and Toby Opferkuch. The Neutrino Magnetic Moment Portal: Cosmology, Astrophysics, and Direct Detection. *JCAP*, 01:039, 2021.

[367] M. B. Voloshin. On Compatibility of Small Mass with Large Magnetic Moment of Neutrino. *Sov. J. Nucl. Phys.*, 48:512, 1988.

[368] Riccardo Barbieri and Rabindra N. Mohapatra. A Neutrino With a Large Magnetic Moment and a Naturally Small Mass. *Phys. Lett. B*, 218:225–229, 1989.

[369] K. S. Babu and R. N. Mohapatra. Supersymmetry and Large Transition Magnetic Moment of the Neutrino. *Phys. Rev. Lett.*, 64:1705, 1990.

[370] K. S. Babu and R. N. Mohapatra. Model for Large Transition Magnetic Moment of the ν_e. *Phys. Rev. Lett.*, 63:228, 1989.

[371] Miriam Leurer and Neil Marcus. A Model for a Large Neutrino Magnetic Transition Moment and Naturally Small Mass. *Phys. Lett. B*, 237:81–87, 1990.

[372] K. S. Babu, Sudip Jana, and Manfred Lindner. Large Neutrino Magnetic Moments in the Light of Recent Experiments. *JHEP*, 10:040, 2020.

[373] David McKeen and Maxim Pospelov. Muon Capture Constraints on Sterile Neutrino Properties. *Phys. Rev. D*, 82:113018, 2010.

[374] J. Park et al. Measurement of Neutrino Flux from Neutrino-Electron Elastic Scattering. *Phys. Rev. D*, 93(11):112007, 2016.

[375] E. Valencia et al. Constraint of the MINERνA medium energy neutrino flux using neutrino-electron elastic scattering. *Phys. Rev. D*, 100(9):092001, 2019.

[376] L. Zazueta et al. Improved constraint on the MINERνA medium energy neutrino flux using ν^{-}e-$\rightarrow\nu^{-}$e- data. *Phys. Rev. D*, 107(1):012001, 2023.

[377] Carlos A. Argüelles, Matheus Hostert, and Yu-Dai Tsai. Testing New Physics Explanations of the MiniBooNE Anomaly at Neutrino Scattering Experiments. *Phys. Rev. Lett.*, 123(26):261801, 2019.

[378] K. Abe et al. Search for heavy neutrinos with the T2K near detector ND280. *Phys. Rev. D*, 100(5):052006, 2019.

[379] Carlos A. Argüelles, Nicolò Foppiani, and Matheus Hostert. Efficiently exploring multidimensional parameter spaces beyond the Standard Model. *Phys. Rev. D*, 107(3):035027, 2023.

[380] Enrico Bertuzzo, Sudip Jana, Pedro A. N. Machado, and Renata Zukanovich Funchal. Neutrino Masses and Mixings Dynamically Generated by a Light Dark Sector. *Phys. Lett. B*, 791:210–214, 2019.

[381] B. Abi et al. Measurement of the Positive Muon Anomalous Magnetic Moment to 0.46 ppm. *Phys. Rev. Lett.*, 126(14):141801, 2021.

[382] Maxim Pospelov. Secluded U(1) below the weak scale. *Phys. Rev. D*, 80:095002, 2009.

[383] J. P. Lees et al. Search for Invisible Decays of a Dark Photon Produced in $e^{+}e^{-}$ Collisions at BaBar. *Phys. Rev. Lett.*, 119(13):131804, 2017.

[384] D. Banerjee et al. Dark matter search in missing energy events with NA64. *Phys. Rev. Lett.*, 123(12):121801, 2019.

[385] Asli M. Abdullahi, Matheus Hostert, Daniele Massaro, and Silvia Pascoli. Semi-Visible Dark Photons below the Electroweak Scale. 2 2023.

[386] André de Gouvêa, Patrick J. Fox, Roni Harnik, Kevin J. Kelly, and Yue Zhang. Dark Tridents at Off-Axis Liquid Argon Neutrino Detectors. *JHEP*, 01:001, 2019.

[387] Babette Döbrich, Joerg Jaeckel, Felix Kahlhoefer, Andreas Ringwald, and Kai Schmidt-Hoberg. ALPtraum: ALP production in proton beam dump experiments. *JHEP*, 02:018, 2016.

[388] Enrique Fernández-Martínez, Manuel González-López, Josu Hernández-García, Matheus Hostert, and Jacobo López-Pavón. Effective portals to heavy neutral leptons. 4 2023.

[389] R. B. Patterson, E. M. Laird, Y. Liu, P. D. Meyers, I. Stancu, and H. A. Tanaka. The Extended-track reconstruction for MiniBooNE. *Nucl. Instrum. Meth. A*, 608:206–224, 2009.

[390] Robert Wilson. Fermilab Short-Baseline Neutrino Program. Snowmass Community Summer Study 2022.

[391] Ryan Benton Patterson. *A Search for Muon Neutrino to Electron Neutrino Oscillations at $\delta(m^2) > 0.1\ eV^2$*. PhD thesis, Princeton U., 2007.

[392] Joshua Isaacson, William I. Jay, Alessandro Lovato, Pedro A. N. Machado, and Noemi Rocco. Introducing a novel event generator for electron-nucleus and neutrino-nucleus scattering. *Phys. Rev. D*, 107(3):033007, 2023.

[393] C. Andreopoulos et al. The GENIE Neutrino Monte Carlo Generator. *Nucl. Instrum. Meth. A*, 614:87–104, 2010.

[394] Maxim Pospelov. Neutrino Physics with Dark Matter Experiments and the Signature of New Baryonic Neutral Currents. *Phys. Rev. D*, 84:085008, 2011.

[395] Roni Harnik, Joachim Kopp, and Pedro A. N. Machado. Exploring nu Signals in Dark Matter Detectors. *JCAP*, 07:026, 2012.

[396] Brian Batell, Maxim Pospelov, and Brian Shuve. Shedding Light on Neutrino Masses with Dark Forces. *JHEP*, 08:052, 2016.

[397] Yasaman Farzan and Julian Heeck. Neutrinophilic nonstandard interactions. *Phys. Rev. D*, 94(5):053010, 2016.

[398] Valentina De Romeri, Enrique Fernandez-Martinez, Julia Gehrlein, Pedro A. N. Machado, and Viviana Niro. Dark Matter and the elusive Z in a dynamical Inverse Seesaw scenario. *JHEP*, 10:169, 2017.

[399] Peter Ballett, Matheus Hostert, and Silvia Pascoli. Neutrino Masses from a Dark Neutrino Sector below the Electroweak Scale. *Phys. Rev. D*, 99(9):091701, 2019.

[400] Pilar Coloma. Icecube/DeepCore tests for novel explanations of the MiniBooNE anomaly. *Eur. Phys. J. C*, 79(9):748, 2019.

[401] E. M. Kantor and M. E. Gusakov. The neutrino emission due to plasmon decay and neutrino luminosity of white dwarfs. *Mon. Not. Roy. Astron. Soc.*, 381:1702, 2007.

[402] D. E. Winget, D. J. Sullivan, T. S. Metcalfe, S. D. Kawaler, and M. H. Montgomery. A Strong Test of Electroweak Theory Using Pulsating

DB White Dwarf Stars as Plasmon Neutrino Detectors. *Astrophys. J. Lett.*, 602(2):L109–L112, February 2004.

[403] Martin Bauer, Patrick Foldenauer, and Joerg Jaeckel. Hunting All the Hidden Photons. *JHEP*, 07:094, 2018.

[404] Herbert K. Dreiner, Jean-François Fortin, Jordi Isern, and Lorenzo Ubaldi. White Dwarfs constrain Dark Forces. *Phys. Rev. D*, 88:043517, 2013.

[405] V. Canuto, C. Chiuderi, and C. K. Chou. Plasmon Neutrinos Emission in a Strong Magnetic Field. I: Transverse Plasmons. *Astrophys. Space Sci.*, 7(3):407–415, June 1970.

[406] V. Canuto, C. Chiuderi, and C. K. Chou. Plasmon Neutrinos Emission in a Strong Magnetic Field. II: Longitudinal Plasmons. *Astrophys. Space Sci.*, 9(3):453–460, December 1970.

[407] Lester L. DeRaad, Jr., Kimball A. Milton, and N. D. Hari Dass. Photon Decay Into Neutrinos in a Strong Magnetic Field. *Phys. Rev. D*, 14:3326, 1976.

[408] VV Skobelev. Reaction whereby a photon decays into a neutrino-antineutrino pair and a neutrino decays into a photon-neutrino pair in a strong magnetic field. *Zhurnal Eksperimentalnoi i Teoreticheskoi Fiziki*, 71:1263–1267, 1976.

[409] DV Galtsov and NS Nikitina. Photoneutrino processes in a strong field. *Sov. Phys. JETP*, 35:1047, 1972.

[410] M. P. Kennett and D. B. Melrose. Neutrino emission via the plasma process in a magnetized plasma. *Phys. Rev. D*, 58:093011, 1998.

[411] John Darlington Landstreet. Synchrotron Radiation of Neutrinos and Its Astrophysical Significance. *Phys. Rev.*, 153:1372–1377, 1967.

[412] Probhas Ray Chaudhuri. Neutrino synchrotron radiation: I: Application to white dwarfs. *Astrophysics and Space Science*, 8:432–447, 1970.

[413] D. G. Iakovlev and R. Tschaepe. Synchrotron neutrino-pair radiation in neutron stars. *Astronomische Nachrichten*, 302(4):167–176, January 1981.

[414] A. D. Kaminker, K. P. Levenfish, D. G. Yakovlev, P. Amsterdamski, and P. Haensel. Neutrino emissivity from e- synchrotron and e- e+ annihilation processes in a strong magnetic field: General formalism and nonrelativistic limit. *Phys. Rev. D*, 46:3256–3264, 1992.

[415] I. Bhattacharyya. Neutrino synchrotron radiation in electro-weak interaction. *Astropart. Phys.*, 24:100–106, 2005.

[416] Marco Drewes, Jamie McDonald, Loïc Sablon, and Edoardo Vitagliano. Neutrino Emissivities as a Probe of the Internal Magnetic Fields of White Dwarfs. *Astrophys. J.*, 934:99, 2022.

[417] E. E. Salpeter. Energy and Pressure of a Zero-Temperature Plasma. *Astrophys. J.* , 134:669, November 1961.

[418] V. Canuto, C. Chiuderi, and C. K. Chou. Plasmon neutrinos emission in a strong magnetic field. i: Transverse plasmons. *Astrophys. Space Sci.*, 7:407–415, 1970.

[419] V. Canuto, C. Chiuderi, and C. K. Chou. Plasmon neutrinos emission

in a strong magnetic field. ii: Longitudinal plasmons. *Astrophys. Space Sci.*, 7:453–460, 1970.

[420] D. G. Yakovlev and R. Tschaepe. Synchrotron neutrino-pair radiation in neutron stars. *Astronomische Nachrichten*, 302(4):167–176, 1981.

[421] Eric Braaten and Daniel Segel. Neutrino energy loss from the plasma process at all temperatures and densities. *Phys. Rev. D*, 48:1478–1491, 1993.

[422] Michel Le Bellac. *Thermal Field Theory*. Cambridge Monographs on Mathematical Physics. Cambridge University Press, 1996.

[423] Irving Langmuir. Oscillations in ionized gases. *Proceedings of the National Academy of Sciences*, 14(8):627–637, 1928.

[424] Arun Mathew and Malay K Nandy. General relativistic calculations for white dwarf stars. *arXiv preprint arXiv:1401.0819*, 2014.

[425] A. Bédard, P. Bergeron, P. Brassard, and G. Fontaine. On the Spectral Evolution of Hot White Dwarf Stars. I. A Detailed Model Atmosphere Analysis of Hot White Dwarfs from SDSS DR12. *Astrophys. J.*, 901(2):93, October 2020.

[426] Wojciech Flieger, Janusz Gluza, and Kamil Porwit. New limits on neutrino non-unitary mixings based on prescribed singular values. *JHEP*, 03:169, 2020.

[427] Julien Billard, Joseph Johnston, and Bradley J. Kavanagh. Prospects for exploring New Physics in Coherent Elastic Neutrino-Nucleus Scattering. *JCAP*, 11:016, 2018.

[428] A. W. Thomas, X. G. Wang, and A. G. Williams. Constraints on the dark photon from deep inelastic scattering. *Phys. Rev. D*, 105(3):L031901, 2022.

[429] Richard H. Parker, Chenghui Yu, Weicheng Zhong, Brian Estey, and Holger Müller. Measurement of the fine-structure constant as a test of the Standard Model. *Science*, 360(6385):191–195, April 2018.

[430] David Curtin, Rouven Essig, Stefania Gori, and Jessie Shelton. Illuminating Dark Photons with High-Energy Colliders. *JHEP*, 02:157, 2015.

[431] Brad M. S. Hansen, Harvey Richer, Jason Kalirai, Ryan Goldsbury, Shane Frewen, and Jeremy Heyl. Constraining Neutrino Cooling using the Hot White Dwarf Luminosity Function in the Globular Cluster 47 Tucanae. *Astrophys. J.*, 809(2):141, 2015.

[432] Patrick Côté et al. CASTOR: the Cosmological Advanced Survey Telescope for Optical and Ultraviolet Research. In Mark C. Clampin, Giovanni G. Fazio, Howard A. MacEwen, and Jacobus M. Oschmann Jr., editors, *Space Telescopes and Instrumentation 2012: Optical, Infrared, and Millimeter Wave*, volume 8442, page 844215. International Society for Optics and Photonics, SPIE, 2012.

[433] Nicholas J. Fantin, Patrick Côté, and Alan W. McConnachie. White Dwarfs in the Era of the LSST and Its Synergies with Space-based Missions. *The Astrophysical Journal*, 900(2):139, 2020.

[434] Rouven Essig, Roni Harnik, Jared Kaplan, and Natalia Toro. Discovering New Light States at Neutrino Experiments. *Phys. Rev. D*, 82:113008, 2010.

[435] Philip Ilten, Yotam Soreq, Mike Williams, and Wei Xue. Serendipity in dark photon searches. *JHEP*, 06:004, 2018.

[436] Robert Foot. New Physics From Electric Charge Quantization? *Mod. Phys. Lett. A*, 6:527–530, 1991.

[437] X. G. He, Girish C. Joshi, H. Lew, and R. R. Volkas. NEW Z-prime PHENOMENOLOGY. *Phys. Rev. D*, 43:22–24, 1991.

[438] Xiao-Gang He, Girish C. Joshi, H. Lew, and R. R. Volkas. Simplest Z-prime model. *Phys. Rev. D*, 44:2118–2132, 1991.

[439] Robert Foot, X. G. He, H. Lew, and R. R. Volkas. Model for a light Z-prime boson. *Phys. Rev. D*, 50:4571–4580, 1994.

[440] Julian Heeck and Werner Rodejohann. Gauged $L_\mu - L_\tau$ Symmetry at the Electroweak Scale. *Phys. Rev. D*, 84:075007, 2011.

[441] Kento Asai, Koichi Hamaguchi, Natsumi Nagata, Shih-Yen Tseng, and Koji Tsumura. Minimal Gauged $\mathrm{U}(1)_{L_\alpha - L_\beta}$ Models Driven into a Corner. *Phys. Rev. D*, 99(5):055029, 2019.

[442] Martin Bauer, Patrick Foldenauer, and Martin Mosny. Flavor structure of anomaly-free hidden photon models. *Phys. Rev. D*, 103(7):075024, 2021.

[443] Chayan Majumdar, Sudhanwa Patra, Prativa Pritimita, Supriya Senapati, and Urjit A. Yajnik. Neutrino mass, mixing and muon g − 2 explanation in $\mathrm{U}(1)_{L_\mu - L_\tau}$ extension of left-right theory. *JHEP*, 09:010, 2020.

[444] Seungwon Baek and Pyungwon Ko. Phenomenology of U(1)(L(mu)-L(tau)) charged dark matter at PAMELA and colliders. *JCAP*, 10:011, 2009.

[445] Seungwon Baek. Dark matter and muon $(g-2)$ in local $U(1)_{L_\mu - L_\tau}$-extended Ma Model. *Phys. Lett. B*, 756:1–5, 2016.

[446] Anirban Biswas, Sandhya Choubey, and Sarif Khan. Neutrino Mass, Dark Matter and Anomalous Magnetic Moment of Muon in a $U(1)_{L_\mu - L_\tau}$ Model. *JHEP*, 09:147, 2016.

[447] Anirban Biswas, Sandhya Choubey, and Sarif Khan. FIMP and Muon $(g-2)$ in a $U(1)_{L_\mu - L_\tau}$ Model. *JHEP*, 02:123, 2017.

[448] Patrick Foldenauer. Light dark matter in a gauged $U(1)_{L_\mu - L_\tau}$ model. *Phys. Rev. D*, 99(3):035007, 2019.

[449] Nobuchika Okada and Osamu Seto. Inelastic extra $U(1)$ charged scalar dark matter. *Phys. Rev. D*, 101(2):023522, 2020.

[450] Ian Holst, Dan Hooper, and Gordan Krnjaic. Simplest and Most Predictive Model of Muon g-2 and Thermal Dark Matter. *Phys. Rev. Lett.*, 128(14):141802, 2022.

[451] Seungwon Baek, N. G. Deshpande, X. G. He, and P. Ko. Muon anomalous g-2 and gauged L(muon) - L(tau) models. *Phys. Rev. D*, 64:055006, 2001.

[452] Ernest Ma, D. P. Roy, and Sourov Roy. Gauged L(mu) - L(tau) with large muon anomalous magnetic moment and the bimaximal mixing of neutrinos. *Phys. Lett. B*, 525:101–106, 2002.

[453] Keisuke Harigaya, Takafumi Igari, Mihoko M. Nojiri, Michihisa Takeuchi, and Kazuhiro Tobe. Muon g-2 and LHC phenomenology in the $L_\mu - L_\tau$ gauge symmetric model. *JHEP*, 03:105, 2014.

[454] Wolfgang Altmannshofer, Chien-Yi Chen, P. S. Bhupal Dev, and Amarjit Soni. Lepton flavor violating Z' explanation of the muon anomalous magnetic moment. *Phys. Lett. B*, 762:389–398, 2016.

[455] Miguel Escudero, Dan Hooper, Gordan Krnjaic, and Mathias Pierre. Cosmology with A Very Light $L_\mu - L_\tau$ Gauge Boson. *JHEP*, 03:071, 2019.

[456] Jose Alonso Carpio, Kohta Murase, Ian M. Shoemaker, and Zahra Tabrizi. High-energy cosmic neutrinos as a probe of the vector mediator scenario in light of the muon g-2 anomaly and Hubble tension. *Phys. Rev. D*, 107(10):103057, 2023.

[457] Takeshi Araki, Kento Asai, Kei Honda, Ryuta Kasuya, Joe Sato, Takashi Shimomura, and Masaki J. S. Yang. Resolving the Hubble tension in a $\mathrm{U}(1)_{L_\mu - L_\tau}$ model with the Majoron. *PTEP*, 2021(10):103B05, 2021.

[458] Wolfgang Altmannshofer, Stefania Gori, Maxim Pospelov, and Itay Yavin. Quark flavor transitions in $L_\mu - L_\tau$ models. *Phys. Rev. D*, 89:095033, 2014.

[459] Andreas Crivellin, Giancarlo D'Ambrosio, and Julian Heeck. Explaining $h \to \mu^\pm \tau^\mp$, $B \to K^* \mu^+ \mu^-$ and $B \to K \mu^+ \mu^- / B \to K e^+ e^-$ in a two-Higgs-doublet model with gauged $L_\mu - L_\tau$. *Phys. Rev. Lett.*, 114:151801, 2015.

[460] Wolfgang Altmannshofer, Stefania Gori, Stefano Profumo, and Farinaldo S. Queiroz. Explaining dark matter and B decay anomalies with an $L_\mu - L_\tau$ model. *JHEP*, 12:106, 2016.

[461] Chuan-Hung Chen and Takaaki Nomura. Penguin $b \to s\ell'^+\ell'^-$ and B-meson anomalies in a gauged $L_\mu - L_\tau$. *Phys. Lett. B*, 777:420–427, 2018.

[462] Seungwon Baek. Dark matter contribution to $b \to s\mu^+\mu^-$ anomaly in local $U(1)_{L_\mu - L_\tau}$ model. *Phys. Lett. B*, 781:376–382, 2018.

[463] Wolfgang Altmannshofer, Sri Aditya Gadam, and Stefano Profumo. Probing new physics with μ+μ-→bs at a muon collider. *Phys. Rev. D*, 108(11):115033, 2023.

[464] R. Aaij et al. Test of lepton universality in $b \to s\ell^+\ell^-$ decays. *Phys. Rev. Lett.*, 131(5):051803, 2023.

[465] R. Aaij et al. Measurement of lepton universality parameters in $B^+ \to K^+\ell^+\ell^-$ and $B^0 \to K^{*0}\ell^+\ell^-$ decays. *Phys. Rev. D*, 108(3):032002, 2023.

[466] D. W. P. Amaral, D. G. Cerdeno, A. Cheek, and P. Foldenauer. Confirming $U(1)_{L_\mu - L_\tau}$ as a solution for $(g-2)_\mu$ with neutrinos. *Eur. Phys. J. C*, 81(10):861, 2021.

[467] Yuya Kaneta and Takashi Shimomura. On the possibility of a search for the $L_\mu - L_\tau$ gauge boson at Belle-II and neutrino beam experiments. *PTEP*, 2017(5):053B04, 2017.

[468] Dorian Warren Praia do Amaral, David G. Cerdeno, Patrick Folde-

nauer, and Elliott Reid. Solar neutrino probes of the muon anomalous magnetic moment in the gauged $U(1)_{L_\mu - L_\tau}$. *JHEP*, 12:155, 2020.

[469] Ayuki Kamada and Hai-Bo Yu. Coherent Propagation of PeV Neutrinos and the Dip in the Neutrino Spectrum at IceCube. *Phys. Rev. D*, 92(11):113004, 2015.

[470] Ayuki Kamada, Kunio Kaneta, Keisuke Yanagi, and Hai-Bo Yu. Self-interacting dark matter and muon $g-2$ in a gauged $U(1)_{L_\mu - L_\tau}$ model. *JHEP*, 06:117, 2018.

[471] Djuna Croon, Gilly Elor, Rebecca K. Leane, and Samuel D. McDermott. Supernova Muons: New Constraints on Z' Bosons, Axions and ALPs. *JHEP*, 01:107, 2021.

[472] David G. Cerdeño, Marina Cermeño, and Yasaman Farzan. Constraints from the duration of supernova neutrino burst on on-shell light gauge boson production by neutrinos. *Phys. Rev. D*, 107(12):123012, 2023.

[473] Kensuke Akita, Sang Hui Im, Mehedi Masud, and Seokhoon Yun. Limits on heavy neutral leptons, Z' bosons and majorons from high-energy supernova neutrinos. 12 2023.

[474] R. P. Feynman, N. Metropolis, and E. Teller. Equations of State of Elements Based on the Generalized Fermi-Thomas Theory. *Phys. Rev.*, 75:1561–1573, 1949.

[475] E. E. Salpeter. Energy and Pressure of a Zero-Temperature Plasma. *Astrophys. J.*, 134:669–682, 1961.

[476] Michael Rotondo, Jorge A. Rueda, Remo Ruffini, and She-Sheng Xue.

The Relativistic Feynman-Metropolis-Teller theory for white dwarfs in general relativity. *Phys. Rev. D*, 84:084007, 2011.

[477] Arun Mathew and Malay K. Nandy. General relativistic calculations for white dwarfs. *Research in Astronomy and Astrophysics*, 17(6):061, 2017.

[478] Riccardo Fantoni. White-dwarf equation of state and structure: the effect of temperature. *J. Stat. Mech.*, 1711(11):113101, 2017.

[479] Adam G. Riess, Stefano Casertano, Wenlong Yuan, Lucas M. Macri, and Dan Scolnic. Large Magellanic Cloud Cepheid Standards Provide a 1% Foundation for the Determination of the Hubble Constant and Stronger Evidence for Physics beyond ΛCDM. *Astrophys. J.*, 876(1):85, 2019.

[480] Nikita Blinov, Kevin James Kelly, Gordan Z Krnjaic, and Samuel D McDermott. Constraining the Self-Interacting Neutrino Interpretation of the Hubble Tension. *Phys. Rev. Lett.*, 123(19):191102, 2019.

[481] Martin Bauer and Patrick Foldenauer. Consistent Theory of Kinetic Mixing and the Higgs Low-Energy Theorem. *Phys. Rev. Lett.*, 129(17):171801, 2022.

[482] Kevin R. Lynch. A Note on one loop electroweak contributions to g-2: A Companion to BUHEP-01-16. 8 2001.

[483] T. Aoyama et al. The anomalous magnetic moment of the muon in the Standard Model. *Phys. Rept.*, 887:1–166, 2020.

[484] D. P. Aguillard et al. Measurement of the Positive Muon Anomalous Magnetic Moment to 0.20 ppm. *Phys. Rev. Lett.*, 131(16):161802, 2023.

[485] G. W. Bennett et al. Final Report of the Muon E821 Anomalous Magnetic Moment Measurement at BNL. *Phys. Rev. D*, 73:072003, 2006.

[486] Sz. Borsanyi et al. Leading hadronic contribution to the muon magnetic moment from lattice QCD. *Nature*, 593(7857):51–55, 2021.

[487] Andreas Crivellin, Martin Hoferichter, Claudio Andrea Manzari, and Marc Montull. Hadronic Vacuum Polarization: $(g-2)_\mu$ versus Global Electroweak Fits. *Phys. Rev. Lett.*, 125(9):091801, 2020.

[488] S. L. Shapiro and S. A. Teukolsky. *Black holes, white dwarfs, and neutron stars: The physics of compact objects*. 1983.

[489] Jaime Hoefken Zink and Maura E. Ramirez-Quezada. Exploring the dark sectors via the cooling of white dwarfs. *Phys. Rev. D*, 108(4):043014, 2023.

[490] G. Breit and E. Wigner. Capture of Slow Neutrons. *Phys. Rev.*, 49:519–531, 1936.

[491] H. Arthur Weldon. Simple Rules for Discontinuities in Finite Temperature Field Theory. *Phys. Rev. D*, 28:2007, 1983.

[492] G. Peter Lepage. Adaptive multidimensional integration: VEGAS enhanced. *J. Comput. Phys.*, 439:110386, 2021.

[493] Yu. M. Andreev et al. Exploration of the Muon $g-2$ and Light Dark Matter explanations in NA64 with the CERN SPS high energy muon beam. 1 2024.

[494] G. Bellini et al. Precision measurement of the 7Be solar neutrino interaction rate in Borexino. *Phys. Rev. Lett.*, 107:141302, 2011.

[495] M. Agostini et al. First Simultaneous Precision Spectroscopy of *pp*, ^{7}Be, and *pep* Solar Neutrinos with Borexino Phase-II. *Phys. Rev. D*, 100(8):082004, 2019.

[496] J. P. Lees et al. Search for a muonic dark force at BABAR. *Phys. Rev. D*, 94(1):011102, 2016.

[497] D. Akimov et al. The COHERENT Experiment at the Spallation Neutron Source. 9 2015.

[498] D. Akimov et al. Observation of Coherent Elastic Neutrino-Nucleus Scattering. *Science*, 357(6356):1123–1126, 2017.

[499] Wolfgang Altmannshofer, Stefania Gori, Maxim Pospelov, and Itay Yavin. Neutrino Trident Production: A Powerful Probe of New Physics with Neutrino Beams. *Phys. Rev. Lett.*, 113:091801, 2014.

[500] D. Geiregat et al. First observation of neutrino trident production. *Phys. Lett. B*, 245:271–275, 1990.

[501] Gordan Krnjaic, Gustavo Marques-Tavares, Diego Redigolo, and Kohsaku Tobioka. Probing Muonphilic Force Carriers and Dark Matter at Kaon Factories. *Phys. Rev. Lett.*, 124(4):041802, 2020.

[502] Patrick Côté et al. Castor: A flagship canadian space telescope id of associated expression of interest topic area of white paper executive summary of white paper. Zenodo, 10 2019.